Structure and Dynamics of Unfolded Proteins Probed with Advanced Spectroscopic Techniques and Microfluidic Mixing

---

Dissertation
zur
Erlangung der naturwissenschaftlichen Doktorwürde
(Dr. sc. nat.)
vorgelegt der
Mathematisch-naturwissenschaftlichen Fakultät
der
Universität Zürich

von
Armin Hoffmann
aus
Deutschland

Promotionskomitee

Prof. Dr. Benjamin Schuler (Vorsitz)
Prof. Dr. Amedeo Caflisch
PD Dr. Ilian Jelezarov

Zürich, 2010

SUMMARY

The unfolded state has attracted increasing attention due to growing evidence for its importance for the regulation, function, stability, and folding of proteins. The analysis of the unfolded state has been hampered by its properties, as it comprises a distribution of rapidly interconverting configurations rarely populated under physiologically relevant conditions. In this work, two strategies are used to meet the demands of investigating unfolded proteins: in single molecule fluorescence spectroscopy, the unfolded state can be monitored in the presence of the folded state. In kinetic experiments, the unfolded state can be populated transiently and analyzed in the conditions of interest prior to the start of the refolding reaction.

The presented experiments are used to investigate the properties of the unfolded state of the cold shock protein (Csp) from *Thermotoga maritima* under near-physiological conditions, where unfolded Csp has previously been shown to collapse. To understand the implications for the folding process, a more detailed picture of the structure of the collapsed unfolded state is needed. To this end, different variants of Csp were produced and labeled to measure internal Förster resonance energy transfer (FRET) in different parts of the protein. With single molecule FRET spectroscopy, it could be shown that the distance distributions of all variants agree very well with a Gaussian chain model not only in the presence of high concentrations of denaturants, but also in the collapsed state in near-physiological conditions. This observation suggests that there is no preferential collapse of one part of the chain, but that the compaction is rather uniform for the entire polypeptide.

To quantify the secondary structure content in the unfolded state, a microfluidic mixing system was developed, making it possible to perform kinetic experiments with synchrotron radiation circular dichroism (SRCD) spectroscopy. This mixing device in combination with SRCD allows the wavelength range to be extended down to 205 nm, and the dead time to about 200 μs, making it possible to monitor the secondary structure content during kinetic experiments at wavelengths and with a time resolution that are inaccessible with conventional stopped-flow techniques. The performance of the mixer was demonstrated by measuring the folding kinetics of cytochrome c, which showed good agreement with previously published results. Measurements of Csp indicated β-structure content in the collapsed unfolded state of about 20% compared with its folded state. Such secondary structure could have significant influence on the subsequent folding process. This result, together with the findings from the single molecule measurements, is an interesting contribution to the reconciliation problem, i.e. how the observations of random coil behavior from global properties such as the radius of gyration can be reconciled with findings of residual structure in unfolded molecules. Obviously, the existence of secondary structure does not have to affect the overall distance properties of unfolded chains, also under near-physiological conditions. A possible explanation is that the structured elements are rather short in sequence and/or only transiently populated, thus not affecting the overall distance distribution significantly.

The structure in unfolded proteins is directly connected to the proteins' dynamic behavior, since the formation of structure requires the encounter of different parts of the chain. The dynamic properties are thus of great interest, because they determine the time in which a protein can sample its conformational space and are therefore crucial for

understanding both the unfolded state and the folding process. To this end, fluorescence intensity correlation functions for the unfolded subpopulations were measured in the presence of folded molecules with sub-nanosecond time resolution. The dead times of single detectors could be avoided by using a Hanbury Brown and Twiss detection scheme. The analysis of the photon statistics revealed the global reconfiguration time of the polypeptide chain that is about 50 ns for highly denatured Csp and increases with decreasing GdmCl concentrations. As the intrachain distances are available from FRET analysis, the relative diffusion coefficient D of the chain ends can also be calculated. It could be shown that D decreases concomitant with chain collapse under near-physiological conditions. A decrease of D can be interpreted as an increase of intramolecular interactions due to changes in the packing and interaction of the polypeptide backbone and side chains. An example for those interactions could be the formation of secondary structure, as observed in the SRCD experiments. The end-to-end diffusion coefficients of Csp agree very well with results from short unstructured peptides, indicating the absence of strong and specific interactions and correspondingly large energy barriers in the collapsed unfolded state of Csp. Measurements of the Csp variants with different intramolecular distances showed a decrease of D with decreasing separation within the sequence, which might result from a viscous drag of the tail segment.

The significant change of both structural and dynamical properties of unfolded Csp between highly denaturing and near-physiological conditions shows the importance of using single molecule spectroscopy and kinetic experiments to study unfolded proteins. To benefit from the advantages of both techniques, a microfluidic mixer was developed to combine the resolution of single molecule spectroscopy with the capability to populate states out of equilibrium with kinetic measurements. The continuous mixer design decouples the reaction process from the measurement time, enabling measurements for extended periods of times, as required for single molecule detection. Refolding experiments of Csp could be performed with a dead time of about 5 ms and the folding rate was in good agreement with ensemble stopped-flow data. In addition, the system can be used to analyze non-equilibrium states and to monitor complex kinetic processes with the growing set of observables available from single molecule measurements.

Correlation analysis can give important insights into chain dynamics on the nanosecond timescale, but processes such as triplet state decay or translational diffusion contribute to the correlation signal on longer timescales, thus hampering the analysis of slower dynamical processes. Additionally, structural heterogeneity within subpopulations is often difficult to access with single molecule spectroscopy, as the transfer efficiency peak representing a subpopulation is already broadened by shot noise. In order to investigate both structural heterogeneity and slower dynamical processes, a new analysis method was developed, which uses the information of freely diffusing molecules detected a second time, i.e. after they recur to the confocal volume after a first passage. Recurrence analysis of single particles (RASP) can extend the time window available for single molecules in diffusion by more than a factor of ten. The additional information can be employed to extract shot noise-broadened peak shapes and positions, even when subpopulations strongly overlap or when they are only marginally populated. The knowledge of the shot noise width allows the identification of heterogeneity that contributes to peak widths within one subpopulation. Interconversion between subpopulations can be monitored and the corresponding rates can be determined if the process occurs on time scales between hundreds of microseconds and tens of milliseconds. RASP was used to directly observe structural heterogeneity of proline peptides in aqueous buffer and of the unfolded state of Csp in ethylene glycol, with subspecies interconverting on the tens of millisecond timescale and slower. The folding rates of spectrin R15 and the B domain of protein A at equilibrium could be determined in good agreement with stopped-flow and temperature jump data, respectively, showing the potential of RASP to provide quantitative information.

Taken together, this work sheds new light on the structural and dynamical properties of unfolded Csp, especially under the most interesting conditions where the protein is mostly native. To this end, several new techniques were introduced to obtain more detailed information on subpopulations in heterogeneous systems. The range of conditions accessible for the analysis of the unfolded state could be extended by using microfluidic mixing, both with CD at lower wavelengths and with single molecule FRET. The window to monitor dynamic processes could be extended to very short times (picoseconds timescale) by correlation analysis. For single molecule spectroscopy in diffusion, RASP was introduced as a simple but very effective approach to detect structural heterogeneity in subpopulations and to study dynamical processes in the time range between hundreds of microseconds and tens of milliseconds.

ZUSAMMENFASSUNG

Der entfaltete Zustand gewinnt zunehmend an Aufmerksamkeit aufgrund der steigenden Zahl von Belegen für dessen Bedeutung für die Regulation, Funktion, Stabilität und Faltung von Proteinen. Die Untersuchung des entfalteten Zustandes wird erschwert durch dessen besondere Eigenschaften; so ist er durch eine Verteilung von schnell fluktuierenden Konfigurationen charakterisiert, die unter physiologischen Bedingungen nur schwach populiert sind. In der vorliegenden Arbeit werden zwei Strategien verwendet, um die speziellen Anforderungen der Untersuchung von entfalteten Proteinen zu erfüllen: Mit Einzelmolekülfluoreszenzspektroskopie kann der entfaltete Zustand auch in Anwesenheit des gefalteten Zustandes untersucht werden. Mit kinetischen Experimenten kann der entfaltete Zustand transient in interessanten Lösungsbedingungen populiert und untersucht werden, bevor die Rückfaltung startet.

In den hier vorgestellten Experimenten werden die Eigenschaften des entfalteten Zustandes des Kälteschockproteins (*cold shock protein*, Csp) aus *Thermotoga maritima* in der Nähe physiologischer Bedingungen untersucht, wo in vorangegangenen Studien ein Kollaps des entfalteten Csps nachgewiesen werden konnte. Um die Auswirkungen auf den Faltungsprozess verstehen zu können, ist ein detailliertes Bild der kollabierten Struktur von großem Interesse. Zu diesem Zweck wurden verschiedene Varianten von Csp hergestellt und mit Fluoreszenzfarbstoffen markiert, um Förster Resonanzenergietransfer nach Förster (FRET) in verschiedenen Bereichen innerhalb der Proteinmoleküle messen zu können. Mittels Einzelmolekül-FRET-Spektroskopie konnte nachgewiesen werden, dass die Abstände aller Varianten sehr gut mit dem Gaußschen Kettenmodel übereinstimmen, sowohl in Anwesenheit von hohen GdmCl-Konzentrationen als auch in der Nähe physiologischer Bedingungen. Diese Beobachtungen lassen vermuten, dass es keinen bevorzugten Kollaps in bestimmten Kettensegmenten gibt, sondern dass die Kompaktierung gleichmäßig über die gesamte Polypeptidkette stattfindet.

Um den Anteil der Sekundärstruktur im entfalteten Zustand messen zu können, wurde ein Mikrofluidik-Mischsystem entwickelt, welches es ermöglicht, kinetische Experimente mit Synchrotronstrahlungs- Circulardichroismus (*synchrotron radiation circular dichroism*, SRCD) durchführen zu können. In Kombination mit SRCD erweitert diese Mischapparatur den zugänglichen Wellenlängenbereich bis auf 205 nm bei einer Totzeit von ca. 200 μs. Damit kann der Sekundärstrukturgehalt in kinetischen Experimenten untersucht werden, bei Wellenlängen und mit einer Zeitauflösung, die mit kommerziellen *stopped-flow*-Geräten nicht zugänglich sind. Die Leistung des Mischapparates konnte mit Messungen der Faltungskinetik von Cytochrom C gezeigt werden, welche eine gute Übereinstimmung mit bereits veröffentlichten Daten zeigten. Messungen von Csp ergaben einen β-Strukturgehalt von 20% verglichen mit dem gefalteten Zustand. Diese Sekundärstuktur kann einen signifikanten Einfluss auf den folgenden Faltunsgprozess haben. Im Zusammenhang mit den Ergebnissen der Einzelmolekülmessungen sind diese Ergebnisse ein interessanter Beitrag zum *reconciliation problem* („Vereinbarungsproblem“), das heisst zu der Frage, wie die Beobachtungen von globalen Eigenschaften, die denen eines *random coils* (einer Irrflugskette) entsprechen, zu vereinbaren sind mit Nachweisen von Reststruktur in entfalteten Proteinen. Offensichtlich muss die Anwesenheit von Sekundärstruktur nicht die globalen Abstandsverteilungen von entfalteten Proteinen beeinflussen, nicht einmal in der Nähe

physiologischer Bedingungen. Eine mögliche Erklärung hierfür ist, dass die Strukturelemente eher kurze Kettenabschnitte umfassen und/oder nur sehr kurzlebig sind und daher die globale Abstandsverteilung nicht signifikant beeinflussen.

Die Struktur von entfalteten Proteinen ist eng mit ihren dynamischen Eigenschaften verknüpft, da die Bildung von strukturellen Elementen das Zusammentreffen von verschiedenen Teilen der Kette bedingt. Die dynamischen Eigenschaften legen die Zeit fest, in der ein Protein seinen Konfigurationsraum austesten kann und sind somit essential für das Verständnis von entfalteten Proteinen und des Faltungsprozesses. Zu diesem Zweck wurden Fluoreszenzkorrelationsfunktionen in Anwesenheit von gefalteten Molekülen mit einer Zeitauflösungen von unter einer Nanosekunde gemessen. Die Totzeiten der einzelnen Detektoren konnten mittels eines Hanbury Brown und Twiss Aufbaus umgangen werden. Die Analyse der Photonenstatistik ergab eine globale Rekonfigurationszeit der entfalteten Polypeptidkette von ca. 50 ns für stark denaturierte Proteine, die mit Abnahme der GdmCl Konzentration ansteigt. Da die intramolekularen Abstände aus der Analyse der Transfereffizienten verfügbar sind, konnte der relative Diffusionskoeffizient *D* der kettenenden ebenfalls ermittelt werden. Es konnte gezeigt werden, dass *D* mit zunehmender Kettenkompaktierung nahe physiologischer Bedingungen abnimmt. Diese Abnahme kann mit einer Zunahme von intramolekularen Wechselwirkungen aufgrund von Veränderungen der Dichte und Interaktionen des Polypeptid-Rückgrats sowie der Seitenketten interpretiert werden. Ein Beispiel solcher Interaktionen könnte die Bildung von Sekundärstruktur sein, wie sie in den SRCD-Experimenten nachgewiesen wurde. Die intramolekularen Diffusionskoeffizienten von Csp stimmen sehr gut mit denjenigen von kurzen, unstrukturierten Peptiden überein, was auf die Abwesenheit von starken und spezifischen Wechselwirkungen schließen lässt und damit verbundenen größeren Energiebarrieren im kollabierten entfalteten Zustand von Csp. Messungen der verschiedenen Csp Varianten mit unterschiedlichen intramolekularen Abständen ergaben eine Abnahme von *D* mit abnehmendem Abstand innerhalb der Kette, welche möglicherweise von einem viskosen Widerstand des überhängenden Kettenabschnitts verursacht wird.

Die deutlichen Änderungen der strukturellen und dynamischen Eigenschaften von entfaltetem Csp zwischen stark denaturierenden und annähernd physiologischen Bedingungen verdeutlichen, wie wichtig Einzelmolekülspektroskopie und kinetische Experimente für die Untersuchung entfalteter Proteine sind. Um von den Vorteilen beider Methoden zu profitieren wurde ein Mikrofluidik-System entwickelt, mit deren Hilfe Einzelmolekülmessungen in nicht-Gleichgewichtsexperimenten durchgeführt werden können. Durch die kontinuierliche Mischanordnung können längere Messungen zu bestimmten Zeiten der Reaktion durchgeführt werden, wie sie für Einzelmolekül Experimente benötigt werden. Rückfaltungsexperimente mit Csp wurden mit einer Totzeit von ca. 5 ms gemessen und stimmen gut mit *Stopped-Flow* Ergebnissen im Ensemble überein. Insgesamt kann das System eingesetzt werden, um Zustände unter destabilisierenden Bedingungen zu messen oder um kinetische Prozesse zu verfolgen mit den diversen Parametern, die durch Einzelmolekülspektroskopie bestimmbar sind.

Fluoreszenzkorrelationsexperimente ermöglichen wichtige Einblicke in die Kettendynamik auf der Nanosekunden-Zeitskala; schwieriger ist allerdings die Untersuchung langsamerer dynamischer Prozesse, da z.B. der Zerfall des Triplettzustandes der Farbstoffe und die Translationsdiffusion der Moleküle das Signal der Fluoreszenzkorrelation dominieren. Die Heterogenität innerhalb von Subpopulationen ist schwierig zu untersuchen, da die Transfereffizienzverteilungen, die einer Subpopulation entsprechen, bereits durch Schrotrauschen verbreitert werden. Um sowohl die strukturelle Heterogenität als auch langsamere dynamische Prozesse untersuchen zu können, wurde eine neue Analysemethode entwickelt, die die Information von Molekülen ausnutzt, die nach ihrer ersten Detektion ein weiteres Mal detektiert werden. Diese Analyse wiederkehrender Moleküle (*Recurrence Analysis of Single Particles*, RASP) erweitert das Zeitfenster, in dem einzelne Moleküle untersucht werden können, um eine Größenordnung. Die zusätzliche Information kann verwendet werden, um die genauen Schrotrausch-bedingten Peakformen und -positionen zu ermitteln, selbst wenn die Subpopulationen stark überlappen oder nur gering populiert werden. Mit Kenntnis der Schrotrausch-bedingten Breite kann Heterogenität innerhalb der Subpopulationen identifiziert werden, die ebenfalls zur Verbreiterung der Peaks beitragen kann. Umwandlungen zwischen den Subpopulationen können beobachtet und die zugehörigen Reaktionsraten bestimmt werden, sofern die entsprechenden Zeitkonstanten zwischen ca. 100 μs und 20 ms liegen. RASP wurde erfolgreich eingesetzt, um strukturelle Heterogenität von Polyprolinpeptiden in wässrigem Puffer und von ungefaltetem Csp in Ethylenglykol zu charakterisieren, wobei die Subspezies sich mit Raten von 100 s^{-1} (Csp) und langsamer (Prolin-Peptide) ineinander umwandeln. Die Faltungsrate von Spektrin R15 und der B Domäne von Protein A konnten im Gleichgewicht bestimmt werden und stimmen gut mit *Stopped-Flow* Daten bzw. Temperatursprungdaten überein. Dies zeigt, dass RASP auch quantitative Ergebnisse liefern kann.

Insgesamt ermöglicht die vorliegende Arbeit neue Einsichten in die strukturellen und dynamischen Eigenschaften von entfalteten Csp, insbesondere unter Bedingungen wo das Protein hauptsächlich in seiner nativen Form vorliegt. Dazu wurden mehrere Methoden entwickelt, um neue Information über Subpopulationen in heterogenen Gemischen zu erhalten. Der zur Verfügung stehende Zeitbereich, um entfaltete Zustände zu untersuchen, konnte durch Mikrofluidik-Mischsysteme erweitert werden, sowohl für CD-Messungen in niedrigeren Wellenlängenbereichen als auch für Einzelmolekül-Messungen. Der zur Verfügung stehende Zeitbereich, um dynamische Prozesse mittels Fluoreszenzkorrelationsspektroskopie zu untersuchen, konnte auf den Picosekunden-Bereich ausgedehnt werden. RASP wurde als einfache, aber doch sehr effiziente Methode eingeführt, um strukturelle Heterogenität in Subpopulationen zu charakterisieren sowie dynamische Prozesse in der Größenordnung zwischen 100 μs und 10 ms zu untersuchen.

Contents

I. Introduction

1.1 UNFOLDED STATES OF PROTEINS

Proteins take part in the vast majority of processes in living organisms. In a classical view, a protein's ability to fulfill its function is directly linked to its unique, three dimensional structure. For its elucidation, there are routine methods available such as X-ray diffraction crystallography or nuclear magnetic resonance (NMR) spectroscopy. Besides the wealth of information available from the native structure giving important insights into the functional properties of proteins, a full understanding of the function and regulation of proteins has to include their dynamic nature as well. There are various circumstances in cells where proteins are not in their folded state but in states with less or no structure at all (Dill and Shortle, 1991; Prakash and Matouschek, 2004): (i) The first occasion is during the production of a protein on the ribosome, where the polypeptide chain has to obtain its folded structure the first time, a process that might be supported by chaperones in some cases. (ii) In eukaryotes, a considerable fraction of proteins synthesized in the cytosol have to be transferred to other cell compartments across membranes, where the translocation channels are so narrow that only unfolded proteins can pass through. (iii) Degradation of proteins is not only essential during digestion, but also for the regulation of the intracellular concentration of proteins. Prior to degradation, proteins have to be unfolded to be accessible to proteases (Prakash et al., 2004). (iv) A number proteins undergo many folding and unfolding cycles during their lifetime in the cell. (v) Unwanted occasions of protein unfolding can occur when the cell is exposed to stress such as abnormal temperature or high concentrations of stress agents. (vi) Finally, there is a significant fraction of proteins that are “natively unfolded” with unique functional features (Uversky, 2009).

Obviously, the structural characteristics of the unfolded states are very important for understanding the basic steps in a protein's lifecycle. This includes not only folding, but also potential misfolding into nonproductive or even harmful aggregates, or interaction with diverse cellular factors, such as ribosomes and chaperones, members of protein translocation or degradation machineries, and the numerous binding partners of disordered proteins (Dyson and Wright, 2005).

It is not surprising that the structural and dynamical features of the unfolded state are also important for understanding the fundamental mechanisms of protein folding: the unfolded state is the reference state for characterizing the stability of the folded state of a protein, and it is the starting point of folding as well as the competing reactions.

Before the effects of the unfolded state on a protein's function and regulation can be explored, two important steps have to be taken. Firstly, one needs a detailed description of the unfolded state, whose investigation has quite different demands than the folded state. For instance, unfolded chains are not only much more heterogeneous, but also very dynamic, which has to be considered when elucidating structural features. In addition, the structural properties of the unfolded state are more sensitive to the environment than the folded state, which is important to take into account when comparing results from different environments or when drawing conclusions from *in vitro* experiments about the situation *in vivo*.

1.1.1 PROPERTIES OF THE UNFOLDED STATE

Unlike the native state with its rather well-defined structure, the unfolded state is a large ensemble of rapidly interconverting, non- or marginally structured microstates. This necessitates a different way to describe the properties of the unfolded state (Dill and Shortle, 1991).

Models for the unfolded state

The first step is to model the configurational statistics of the polypeptide chain, from which the average properties of the chain can be obtained. In general, the models presented in the following assume random coil chains (Chan and Dill, 1991), i.e. polypeptide chains without long-range interactions. Consequently, experimental results of the average distances of unfolded proteins or protein mutants in different conditions that deviate from the predictions might indicate the presence of long range interactions.

A very simple model is the freely jointed or random-walk chain (Cantor and Schimmel, 1980 pp. 984-991; Flory, 1989 pp. 10-12), in which the amino acids are represented by bonds of defined length and every bond vector is completely uncorrelated from every other bond vector. Here, the mean squared end-to-end distance $\langle R^2 \rangle$ is

$$\left\langle R^2 \right\rangle = n\, l^2 \qquad [1.1]$$

where n is the number of bonds and l is the bond length. For long polymers, i.e. large numbers of n, this value can be directly translated into the radius of gyration R_G by

$$\left\langle R_G^2 \right\rangle = \left\langle R^2 \right\rangle / 6 \qquad [1.2]$$

Besides the mean squared end-to-end distance, the distance distribution can be calculated, i.e. the probability $P(R)$ of a certain distance R between the chain termini to be populated based on a Gaussian distribution of distances:

$$P(R) = \left(\frac{3}{2\pi \left\langle R^2 \right\rangle} \right)^{\frac{2}{3}} e^{\left(\frac{2 \left\langle R^2 \right\rangle}{3 R^2} \right)} 4\pi R^2 \qquad [1.3]$$

Deviations from the dependence of $\langle R^2 \rangle$ on the number of bonds in Eq. 1.1 are expected for real chains, as side chains restrict the available bond vector space. This restriction can be accounted for by introducing a proportionality factor

$$\left\langle R^2 \right\rangle = C_n\, n\, l^2 \qquad [1.4]$$

where C_n is the characteristic ratio, which is a measure for the stiffness of the chain due to restricted bond vectors. When the Kuhn segment[I] ($l\sqrt{C_n}$) is used instead of the bond length, a polymer can be treated again as a freely jointed chain (Kuhn, 1934). Alternatively, for large n, the stiffness can be described as the persistence length l_p, which is related to C_∞ (i.e. the characteristic ratio in the limit $n \to \infty$) by (Doi and Edwards, 1988 p. 317; Flory, 1989 p. 402)

$$l_P = C_\infty \, l/2 \qquad [1.5]$$

The persistence length is preferentially used in the context of an alternative model to describe especially stiff chains (e.g. for double stranded DNA (Murphy et al., 2004)), which is the Porod-Kratky chain model, also known as worm-like chain model. Here, the chain is treated as a continuously curving chain with the direction of the curvature at any point being random.

Next to local correlations due to bond angel restrictions, real chains also experience long-range restrictions due to the excluded volume effect, i.e. that a chain molecule cannot cross its own path, resulting in a perturbation of the random walk model. Therefore, the average chain dimensions will increase as the probability of intersections is higher for more compact configurations. Compared to short-range interactions, i.e. configurational restrictions due to neighboring residues, these long-range interactions depend on n. A more general equation for the dependence of the radius of gyration on the number of monomers is

$$R_G = R_{G,0} \, n^{\upsilon} \qquad [1.6]$$

where $R_{G,0}$ is a constant that includes the Kuhn length and v is the exponential scaling factor. For a random walk chain in the absence of the excluded volume effect, the latter is 0.5, as can be seen from equations 1.1 and 1.2. A theoretical estimate by Flory shows that by taking into account the excluded volume effect, v increases to 0.6 (Flory, 1949; Grosberg et al., 1994 p. 84).

Random Coil versus Residual Structure

Several studies have been conducted to determine v based on measurements of unfolded protein sets under highly denaturing conditions as shown in table 1.1. Although there is some scatter of the scaling factors, the studies summarized in table 1.1 show only very few proteins deviating from the overall trends. Evidently, only the sequence length is needed to describe the mean distances of the unfolded state under highly denaturing conditions. If residual structure was present under these conditions, one may expect it to result in deviations from the excluded volume model, which rarely seems to be the case. This result is especially interesting in view of the increasing amount of studies revealing residual structure in proteins even under highly denaturing conditions. This residual structure ranges from topological similarities to the folded state shown in nuclear magnetic resonance residual dipolar couplings

---

[I] The Kuhn length is also referred to as ‘statistical segment’ (Grosberg et al., 1994 p. 9) or ‘length of a hypothetical bond’ (Flory, 1989 p. 12).

Probe	*v*	condition	Number of proteins[i]	Reference
Intrinsic viscosity	0.66 ± 0.04	5 M GdmCl	11 (8)	(Tanford et al., 1967)
Sedimentation coefficient	0.48	5 M GdmCl	11 (8)	(Tanford et al., 1967)
Stokes radius (DLS)	0.50 ± 0.02	6 M GdmCl	12 (12)	(Damaschun et al., 1998)
Radius of gyration (NMR)	0.57 ± 0.02	diverse[ii]	11 (7)	(Wilkins et al., 1999)
Diverse	0.54	6 M GdmCl	40 (1)	(Tcherkasskaya and Uversky, 2001)
Radius of gyration (SAXS)	0.59 ± 0.028	diverse[iii]	28 (17)	(Kohn et al., 2004)

Table 1.1: Exponential scaling factor calculated for different numbers of unfolded proteins and with different methods. ([i] number in brackets corresponds to the number of proteins measured in the cited work. [ii] High concentrations of urea or guanidine hydrochloride or at extremes of pH. [iii] Conditions range from 2 to 6 M GdmCl and 4 to 8 M urea.)

for staphylococcal nuclease (Shortle and Ackerman, 2001) and eglin C (Ohnishi et al., 2004), electrostatic interactions in ribosomal protein L9 (Cho and Raleigh, 2005), marginal secondary structure in single chain monellin (Kimura et al., 2005), cold shock protein (Magg et al., 2006), or chymotrypsin inhibitor 2 (Kazmirski et al., 2001), to hydrophobic clusters in 434 repressor (Neri et al., 1992) and lysozyme (Klein-Seetharaman et al., 2002). Both non-native and native-like interactions can be found.

How can these findings be reconciled (McCarney et al., 2005)? Apparently, the nature of the structural feature is important for its influence on the overall distance distribution of an unfolded state. First, one can distinguish between local and nonlocal order. The former case is in principle already taken into account when extending the monomer length to the Kuhn length, thus including stiffness arising from local steric constraints. Since proteins are heteropolymers, the segments vary both in length and the extent of angular restriction, thus the Kuhn length corresponds only to an average value. Fitzkee and Rose explored the extreme consequences of this averaging (Fitzkee and Rose, 2004). They showed that even when the chain configurations of 33 proteins are constrained to the native state for more than 90% of all residues, and the remaining residues are evenly distributed in the chain and are flexible, the overall dimensions can still be described surprisingly well with random coil statistics. These Monte Carlo simulations suggest that global properties, such as the radius of gyration and the models used to interpret them are quite insensitive to short-range structure. For nonlocal order, a stronger impact on the overall dimensions is expected, as can be seen in the substantial changes of the radius of gyration of Rnase A and lysozyme upon reduction of their disulfide bonds (Kohn et al. 2004). The absence of hints for long-range interactions in studies estimating the scaling factor (Table 1.1) could be due to the very low abundance of these features and/or their high flexibility resulting in very short lifetimes. Thus, they are not visible in ensemble and time-averaged measurements. Nevertheless, even short-lived or short-range structures might bias folding mechanisms or protein stability substantially. These findings show the importance of high spatial and temporal resolution to analyze the unfolded state.

Solvent Dependence

An important aspect of the unfolded state is the solvent dependence of its properties. For a specific chain, one can differentiate three classes of solvents (Dill and Shortle, 1991): in "good" solvents, the interaction between monomers of the chain is the same as between the monomers and solvent molecules, which is a prerequisite for the random walk model. In a "bad" solvent, the interactions between monomers are more favorable, leading to a collapse of the chain. These conditions influence the scaling factor ν describing the length dependence of the overall chain dimensions, being 0.6 for a good and 0.33 for a bad solvent. Since a continuous shift from "good" to "bad" solvent leads to a continuous shift in the scaling factor, conditions exist where the scaling factor matches the theoretical value for a random walk chain model in the absence of the excluded volume effect, that is 0.5 (see formulas 1.1 and 1.2). These solvents are called "theta" solvents. A decrease of the scaling factor when going to worse solvents results in a decrease of the radius of gyration of a polymer with fixed chain length: the chain collapses.

The interactions between a monomer and a solvent molecule depend on the nature of both the solvent molecule and the chain monomer as well as on the temperature (Schellman, 2002). Obviously, these interactions vary in heteropolymers for the different types of monomers. Classical denaturating agents as GdmCl and urea are good solvents because they solubilize all parts of the protein including the backbone, but also the nonpolar side chains (Fersht, 1999 p. 513). Upon removal of these denaturants, i.e. when changing the solution conditions from a good solvent to a bad solvent, the attraction within the chain prevails resulting in a collapsed globular conformation (Grosberg et al., 1994 p. 84 ff. and 129 ff.). Electrostatic interactions can influence the dimensions of the unfolded state as well (Hofmann et al., 2008). The properties of the unfolded state have also been studied investigating the influence of temperature (Nettels et al., 2009), confinement (Zhou and Dill, 2001), presence of crowding agents (Minton, 2005), viscogens (Silow and Oliveberg, 2003), or external forces (Walther et al., 2007). More difficult to access are the details of the interactions causing the collapse, i.e. whether they are sequence-specific or not, native or non-native-like, and local or nonlocal.

Dynamic Properties

Another fundamental feature discerning the unfolded from the folded state is its dynamic nature. The reconfiguration time of the unfolded chain describes how long it takes a protein to sample its configurational space (Socci et al., 1996). Therefore it sets an upper bound on the rate at which a protein can fold and influences the folding mechanism (Kubelka et al., 2004). The dependence of the reconfiguration time on the protein sequence and the environmental conditions can give valuable insights in the relation between unfolded state dynamics and folding properties.

An important parameter studied in this context is the rate of contact formation k, i.e. the inverse of the average time it takes two residues in a flexible chain to come within a distance a, which is the sum of the van der Waals radii of both residues. For a Gaussian chain it is related to the intra-chain diffusion constant D by (Szabo et al., 1980)

$$k = \frac{3\sqrt{6}}{\sqrt{\pi}} \frac{D\,a}{\left\langle r^2 \right\rangle^{3/2}} \qquad [1.7]$$

Contact formation between two residues is one of the most fundamental steps in protein folding, as elementary structure elements such as α-helices (Chakrabartty and Baldwin, 1995) or β-sheets (Gellman, 1998) require the interaction of non-adjacent residues for stabilization. Measurements of the contact rate within short random coil peptides revealed times on the order of tens of nanoseconds (Bieri et al., 1999; Lapidus et al., 2000). The rates increase with decreasing distances and approach constant values for very short distances due to chain stiffness (Lapidus et al., 2000; Krieger et al., 2003). The logarithm of this rate is inversely proportional to the logarithm of the solvent viscosity (Bieri et al., 1999) and decreases with increasing concentrations of GdmCl for short peptides modeling random coil chains (Krieger et al., 2003) and unfolded proteins such as cold shock protein from *Thermotoga maritima* (Csp*Tm*) (Buscaglia et al., 2003).

As already mentioned, the chain dynamics limit the time an unfolded protein chain needs to adapt to new environments. A prominent example is the collapse of polypeptide chains upon dilution in refolding conditions, i.e. when taken from high to low denaturant concentrations. Therefore, the collapse time can be used to estimate how fast the unfolded chain can rearrange. For cytochrome c, apomyoglobin, and lysozyme, the collapse was estimated to be faster than 20 μs, i.e. in the dead time of fast mixing experiments starting from high GdmCl concentrations (Lapidus et al., 2007). The similarity of collapse times of cytochrome c and analogous peptides, which have the same amino acid composition but are not able to fold, suggests that the collapse time is independent of the subsequent folding process (Qiu et al., 2003).

1.1.2 THE UNFOLDED STATE AS THE REFERENCE FOR THE FOLDED STATE

For understanding how proteins fold into their functional relevant, three-dimensional structure and how this folded state is stabilized compared to the unfolded state is of great interest. Studies to elucidate the basic principles of the folding and stabilization of proteins often neglect possible structural features within the unfolded state. For instance, the absence of secondary structure at high denaturant concentrations is often extrapolated to native buffer conditions, where it is difficult to characterize the unfolded state because it is typically very low populated. Additionally, structural features of the unfolded state might be simple missed because the measurement technique is not sensitive enough (see chapter 1.3). Nevertheless, unfolded state properties might be very important to understand the underlying principles of stability and folding processes.

Protein Stability

Protein stability refers to the free energy difference $\varDelta G$ between the folded and the unfolded state, from which the ratio of their concentrations can be calculated from

$$\varDelta G = -RT \ln \frac{c_F}{c_U} \qquad [1.8]$$

where R is the gas constant, T is the temperature in Kelvin, and c_U and c_F are the concentrations of unfolded and folded molecules, respectively. Since the unfolded molecules are usually not functional and prone to degradation, misfolding, and aggregation, the fraction of the unfolded state is a very crucial parameter in vivo and also in vitro. Altering the stability is important for instance for the adaption of organisms to extreme environments or improvement of protein yields, handling, and applications. It is therefore of substantial interest to understand the relationship between mutations and stability.

Is the stability affected by the unfolded state? Another way to ask this question would be: Is the stability only affected by the native structure? To estimate the stability of a protein has been the aim of various computational methods, which have been developed to predict the influence of mutations based on the structure of the native state and using either physics-based, or knowledge-based potentials, or a combination of them. Tests of the predictive power of six methods have shown (Potapov et al., 2009) that experimental and calculated stabilities have a correlation of at most 0.59. Even qualitative predictions resulted in an accuracy between 69 - 79% for identifying the stabilizing or destabilizing nature of a mutation, and between 38 - 63% for finding a high impact of a mutation on the stability. Also combinations of methods could not improve the predictive power significantly. The reasons of this rather low predictive power based on the native structure might be diverse, including the influence of mutations on intermediates. But obviously, methods based on the native structure alone neglect the influence of mutations on the unfolded state, although its importance has been pointed out (Shortle, 1996; Zhou, 2004). For instance, interactions between charged groups in the unfolded state are important to describe the pH-dependent stability of proteins and can destabilize the unfolded state due to the repulsion of neighboring residues (Zhou and Dong,

2003) or they can stabilize it due to non-native interactions (Cho et al., 2004). In general, mutations reducing the chain entropy are suggested to increase the stability, such as shortening of loop lengths or covalent linkage (Zhou, 2004). These residue-specific effects due to point mutations might be influenced by the overall properties of the unfolded chain, such as the average distance within the unfolded chain and how strong and fast the distances can fluctuate. As pointed out by Dill and Shortle about 20 years ago, the „*denatured state under physiological conditions [...] is the most relevant to an understanding of protein stability”* (Dill and Shortle, 1991).

Protein Folding

To monitor protein folding processes with ensemble methods, non-equilibrium experiments are used most commonly. The unfolded state is populated by adding denaturants or altering the pH, for instance, and is then rapidly diluted into native buffer conditions to start the refolding reaction, which can be monitored by many different spectroscopic techniques. With this procedure, in addition to the folding reaction, also the adaptation of the unfolded state to the native buffer conditions is observed, which in the case of a GdmCl concentration jump is for many proteins a collapse of the chain. For many proteins, folding and collapse occur on separated timescales, as they fold on the order of milliseconds or slower, and the collapse is much faster, i.e. on the nanosecond to microsecond timescale (Agashe et al., 1995; Ballew et al., 1996; Magg and Schmid, 2004; Ratner et al., 2005). For conventional stopped-flow instruments used for kinetic measurements, the collapse happens in the dead time and is revealed by an unresolved signal change, in case the signal is sensitive to the changes in the unfolded state dimensions. As the folding process is usually the rate limiting step, only the final conditions influence the refolding rate, not the initial ones. Obviously, the properties of the unfolded state in the final conditions are the most relevant ones for the influence on the folding mechanism.

The general properties of the unfolded state and especially the presence of structure acting as initiation sites under refolding conditions have direct influence of the folding mechanism and the folding rate. Initiation events in different models (Fersht, 1999) vary from the formation of structure elements at one position acting as a nucleus, either local (nucleation model) or nonlocal (nucleation-condensation model), the formation of all secondary structure elements prior to a diffusive assembly to form the proper tertiary structure (diffusion-collision model), or the formation of hydrophobic clusters in a collapsed conformation followed by rearrangement of the other parts of the protein (hydrophobic-collapse model). The properties of the unfolded chain might not only bias a certain folding mechanism, but also affect misfolding (Jahn and Radford, 2008).

The influence of the dynamic properties of the unfolded state on folding is apparent in studies of the viscosity dependence of the folding reaction. Following Kramers theory (Hänggi et al., 1990), which describes folding as a diffusive crossing over a barrier, the folding rate should depend linearly on the inverse of the microscopic friction. This could be validated for cold shock protein from *Bacillus subtilis* (Jacob et al., 1999a) and the IgG binding domain of protein L (Plaxco and Baker, 1998). However, for fast folding proteins and secondary structure model peptides it was shown that the folding rates (Pabit et al., 2004) or the rate of conformational changes (Ansari et al., 1992) cannot be extrapolated to zero for zero viscosity, i.e. that an additional offset caused by internal friction is needed to describe the folding rate. Accordingly, the viscosity in the pre-exponential factor of a Kramers-like equation can be split into a solvent friction η and an internal friction σ:

$$k = \frac{A}{(\sigma + \eta)} e^{(-E_0/k_B T)} \qquad [1.9]$$

where k is the folding rate, A is a viscosity-independent parameter that depends on the shape of the potential surface, E_0 is the average height of the potential energy barrier separating the protein conformations, k_B is the Boltzmann constant, and T is the temperature (Ansari et al., 1992).

The heterogeneous character of the unfolded state ensemble might raise the question how diverse the folding pathways (Sali et al., 1994) can be among the different substates. A theoretical approach to deal with the heterogeneity of conformations and possible pathways between them is the description of protein folding in terms of free energy landscapes (Bryngelson and Wolynes, 1987; Dill and Chan, 1997; Pande et al., 1998; Dinner et al., 2000), also referred to as the 'new view' in protein folding in contrast to classic chemical kinetics (Baldwin, 1995). According to Dill, „*an energy landscape is just the free energy of each conformation as a function of the degrees of freedom, such as the dihedral bond angles along the peptide backbone*" (Dill and Chan, 1997)

A simple and well-known example of an energy surface is a Ramachandran plot, as shown in figure 1.1 a. The configurational space of a single amino acid in the context of a protein chain can be described by the dihedral angels of the main chain. The configurational space of a polypeptide chain has many more than two dimensions, as a multitude of bond angles and distances define the conformations. Therefore, the configurational complexity is reduced to order parameters, that can describe the system and its main characteristics, such as the population and properties of the states and possible interconversion pathways. Commonly used order parameters are the number or fraction of native contacts or the number of total contacts. The different populated states are represented by local minima, in which similar conformations can interconvert rapidly; they are separated from other states by free energy barriers. The shape of this landscape may change upon alteration of solvent conditions, showing the response of the system. It might also reveal whether a unique folding pathway or multiple pathways may occur. An additional feature of the energy landscape is its roughness (Zwanzig, 1988), i.e. the distribution of small valleys on the surface, influencing the dynamics of the system, that is the time needed to interconvert between different states. Of special interest is the energy landscape under folding conditions (Figure 1.1 b), where the surface shows multiple folding pathways (indicated by arrows), the transition state or states, and possible traps on the way the folded state.

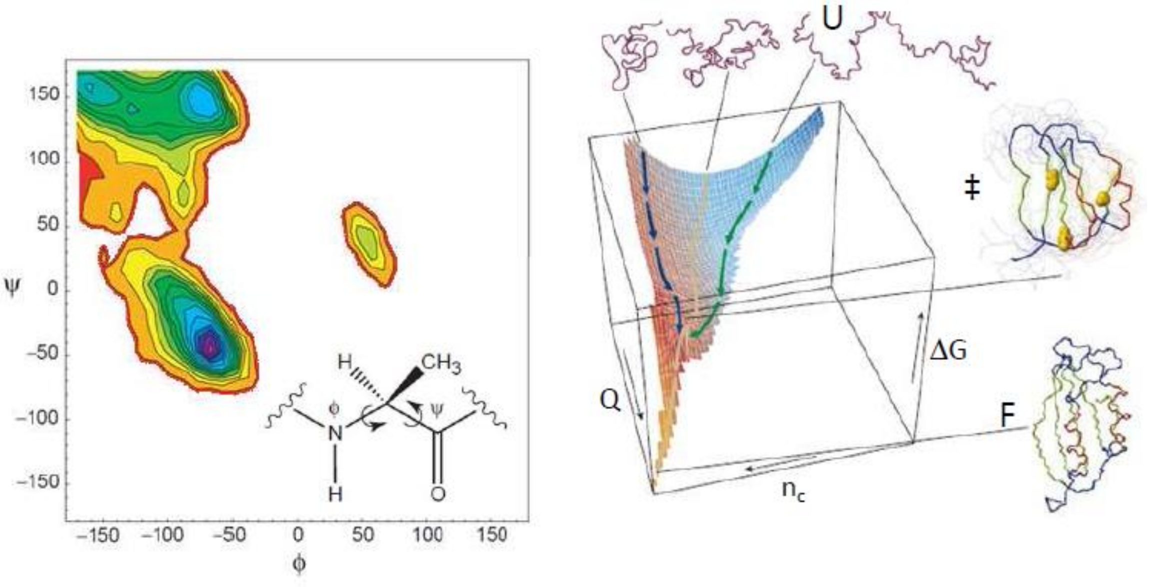

Figure 1.1: Free Energy Landscapes. (a) Ramachandran plot for an alanin residue in a protein environment (inset) showing its low free energy regions (color scale from white/red to purple, representing less and more probable configurations, respectively) in its conformational space, here defined by its main chain dihedral angles ϕ and ψ (adapted from Dinner et al., 2000). (b) Effective free energy (ΔG) surface of a protein as a function of its native contacts (Q) and total number of contacts (n_c) under physiological conditions, forming a funnel-like structure with a heterogeneous unfolded state (U) with high free energy, a transition state (‡) at a saddle point with intermediate effective free energy and the folded state (F) confined at the bottom of the funnel i.e. having the lowest free energy (adapted from Dobson, 2003).

1.2 COLD SHOCK PROTEIN

Cold shock proteins (Csps) are highly expressed in many prokaryotic organisms as a response to a significant temperature drop below the typical growth temperature (Phadtare S. et al., 1999). The main function of Csps is to regulate transcriptional processes via binding to single-stranded nucleic acids and destabilizing unwanted RNA secondary structure (Horn et al., 2007). The cold shock protein from *Thermotoga maritima* (Csp*Tm*) is a typical member of the cold shock protein family: its NMR structure (Kremer et al., 2001) shows that it folds into a Greek key β-barrel consisting of two antiparallel β-sheets formed by three (β1- β3) and two (β4, β5) β-stands (figure 1.2). It consists of 66 amino acids, resulting in a molecular mass of 7474 Da.

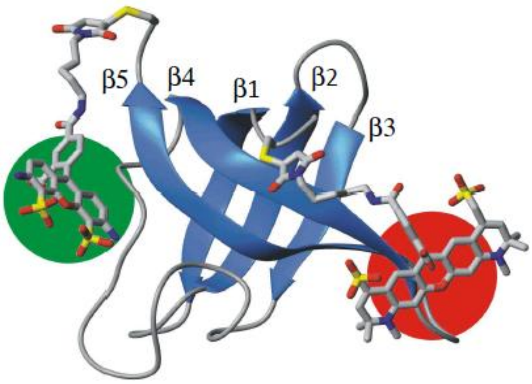

Figure 1.2: Schematic structure of the cold shock protein from *Thermotoga maritima*. As typical for Csps, it consists of 5 β sheets (β1- β5) forming a β-barrel, here shown with fluorophores Alexa 488 (with green circle, C-terminus) and Alexa 594 (with red circle, N-terminus) for FRET measurements (adapted from Schuler et al., 2002))

As a protein from a hyperthermophilic organism, Csp*Tm* shows a high thermodynamic stability (Perl et al., 1998) compared to its homologous proteins from *Bacillus subtilis* (Csp*Bs*) and *Bacillus caldolyticus* (Csp*Bc*), and a melting temperature of about 360 K (Wassenberg et al., 1999). The difference in stability between the homologous proteins is based on different unfolding rates, as the folding rates are very similar and on the order of 1 ms^{-1} at 25° C. All thermodynamic and kinetic properties for these three Csps follow a two-state mechanism, i.e. no evidence for intermediates could be found (Schindler et al., 1995; Perl et al., 1998; Wassenberg et al., 1999; Schuler et al., 2002). One reason of the reduced unfolding rate of Csp*Tm* and its correspondingly higher stability is its increased number of charged residues which form ion-pairs on the surface (Frankenberg et al., 1999). The high stability of Csp*Tm* and the absence of intermediates makes it a well-suited model protein for single molecule FRET spectroscopy to elucidate basic principles of the folding process of small all-β proteins. The thermodynamic and kinetic properties of the variant labeled with Alexa 488 and Alexa 594 are shown in figure 1.3.

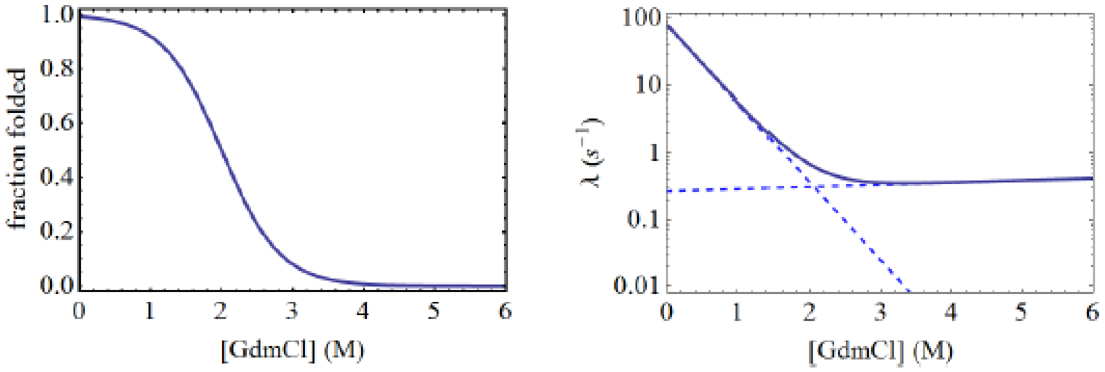

Figure 1.3: Biophysical characterization of a Csp*Tm* variant used for single molecule spectroscopy. (a) Equilibrium folding transition (taken from chapter II) and (b) Kinetic rate constants as a function of GdmCl. (Data taken from Schuler et al., 2002)

The characteristic first step in the folding of Csp starting from high concentrations of GdmCl is the collapse of the unfolded state, as could be shown by single molecule FRET spectroscopy, both in equilibrium (Schuler et al., 2002) and kinetic measurements (Lipman et al., 2003) for Csp*Tm* and by kinetic ensemble FRET measurements for Csp*Bc* (Magg and Schmid, 2004). The folding mechanism of Csp*Bs* was studied by mutational analysis (Garcia-Mira et al., 2004). From kinetic experiments, two characteristic ratios were obtained: the β_T-value[II] is a measure of the compactness of the transition state compared to the native state (Fersht, 1999 p. 545). The high β_T-value of 0.9 for Csp*Bs* indicates an almost native-like transition state, which is true for Csp*Bc* and Csp*Tm* as well (Perl et al., 1998). The Φ-value is the ratio of the folding activation free energy difference and the overall free energy difference between the wild type and a point mutated variant (Perl et al., 1998). This ratio is interpreted as a measure of the importance of the mutated amino acid in the transition state of folding. High Φ-values in the β1 strand of Csp*Bs* suggest that it is already formed in the transition state and that it has established critical non-local interactions with strand β4 in the second sheet. Kinetic experiments of FRET-labeled variants of Csp*Bc* showed that the collapse is faster than 50 μs (dead time of the pressure jump technique (Magg and Schmid, 2004)), and that the β-strands β1 and β2 appear more extended than expected for the collapsed distance under refolding conditions (Magg et al., 2006).

[II] The β_T -value is defined by $\beta_T = m_{UN} / (m_{UN} - m_{NU})$, where m_{UN} and m_{NU} are the kinetic *m*-values for folding or unfolding, respectively.

1.3 TECHNIQUES TO STUDY THE UNFOLDED STATE

The unfolded state of proteins is best described by a number of properties such as the global chain dimensions (expressed e.g. by the radius of gyration), the content and nature of residual structure, and the dynamic behavior (e.g. intra-chain diffusion) of the unfolded chain.

Global chain dimensions are typically studied by small-angle X-ray scattering (SAXS), dynamic light scattering (DLS), or fluorescence spectroscopy like Förster resonance energy transfer (FRET). Except for single molecule fluorescence spectroscopy (see chapter 1.3.1), these techniques are ensemble techniques, i.e. the signal measured is averaged over the whole ensemble of species present in the sample. The ensemble averaging makes it difficult (if not impossible in some cases) to deduce unfolded state properties if the folded state is present as well, as is typically the case close to physiological conditions.

Information about residual structural can be obtained by spectroscopic techniques such as nuclear magnet resonance (NMR), circular dichroism (CD), fluorescence, or infrared and ultraviolet absorbance. These techniques have different averaging properties, which do or do not allow them to differentiate between different possible scenarios:

1. Static residual structure is present in all molecules in a specific part of the chain
2. Residual structure appears temporarily, but only in a specific part of the chain
3. Residual structure appears temporarily in different parts of the chain
4. Static residual structure is present in different parts of the chain

Methods which average over the whole chain and over all molecules can give information about the presence and nature of residual structure, but frequently, they cannot differentiate between the four scenarios, i.e. the dynamic behavior and the location of the residual structure within the chain. FRET can reveal local (but not residue-specific) information and in single molecule mode also temporal information to some extent. NMR can give residue-specific structural information (Dyson and Wright, 1998; Meier et al., 2008) of the unfolded state, including bond angle distributions (Smith et al., 1996), secondary structure content, and even long range interactions.

Dynamic information can be obtained from NMR, AFM (atomic force microscopy (Junker et al., 2009)) and fluorescence-based techniques. The accessible time range for dynamic information in NMR depends on the probe used. For instance backbone motion can be measured by nuclear spin relaxation in the picosecond to nanosecond time range (Palmer, 2001). Residual dipolar couplings reports on long range dynamics on the tens to hundred millisecond timescale (Meier et al., 2008). In single molecule FRET spectroscopy, dynamic information can be obtained in the range of the observation time of a single molecule (Merchant et al. 2007; Gopich & Szabo 2007), which can be on the order of milliseconds for diffusion experiments and can extend to seconds and longer for experiments with immobilized samples (Schuler and Eaton, 2008). Faster timescales, down to the picoseconds range, can be measured using time correlation spectroscopy of FRET-labeled biomolecules (chapter III and Berglund et al., 2002). Other methods utilize the triplet states of chromophores, either by monitoring the transfer between two triplet states of a donor and acceptor (Bieri et al., 1999) or by triplet state quenching of a fluorophore (Lapidus et al., 2000). Both methods are limited to the lifetime of the first excited triplet state, which is usually on the order of tens of microseconds. They require van der Waals contact between the two reporter groups and therefore are limited to distributions of shorter distances.

For all techniques mentioned above, the influence of signal from the folded state has to be considered, especially for measurements under near-physiological conditions, where the properties of the unfolded state are most relevant. The extrapolation of properties from strongly denaturating conditions might be difficult. In the ideal case, the technique is sensitive to the conformational state, like single molecule spectroscopy or NMR (Korzhnev et al., 2004), which means that the signal from unfolded state can be differentiated from the signal of the folded state. A minimal fraction of unfolded molecules is always required. In general, an extension of the accessible range of conditions can be achieved in non-equilibrium experiments (see chapter 1.3.2). Here, the unfolded state is populated under appropriate conditions such as high concentrations of GdmCl, and then rapidly diluted into the conditions of interest. As the adaption of the unfolded state is usually very fast, its properties can be studied in case that the depopulation rate is sufficiently slow, e.g. the rate of folding under native conditions. Alternatively, proteins can be destabilized by altering the amino acid sequence or reducing essential disulfide bonds, so that the unfolded state is populated also under physiological conditions to a sufficient extent. However, the effects of the destabilization on the results have to be considered.

1.3.1 SINGLE MOLECULE FLUORESCENCE SPECTROSCOPY

Single molecules techniques have the unique feature of allowing to measure the properties of different subpopulations in a heterogeneous sample at the same time, instead of getting only the information averaged over the whole ensemble. In combination with Förster resonance energy transfer (FRET), single molecule fluorescence spectroscopy was first applied to immobilized DNA (Ha et al., 1996) and immobilized peptides (Jia et al., 1999) before measuring freely diffusing DNA (Deniz et al., 1999), peptides (Talaga et al., 2000) and proteins (Deniz et al., 2000). Its application range includes the study of conformational changes in dynamic states and upon folding (Bokinsky and Zhuang, 2005; Schuler and Eaton, 2008), as a result of interaction with other molecules or complexes (Abbondanzieri et al., 2008), and during the activities of enzymes (Henzler-Wildman et al., 2007) or larger multi-molecular complexes such as ATP synthase (Diez et al., 2004) or the ribosome (Blanchard et al., 2004).

An inherent advantage of single molecule techniques are the extremely low concentrations of sample needed, making it possible to measure unfolded species at conditions where they are otherwise highly prone to aggregation (Hillger et al., 2007). The high signal resolution also opens possibilities of studying important processes in living cells, as many processes are conducted by macromolecules at low concentrations (Xie et al., 2008).

Förster Resonance Energy Transfer

Fluorescence is the emission of light from a molecule that has absorbed radiation of a different (usually shorter) wavelength (Lakowicz, 2006). Important parameters for describing the fluorescence process are the quantum yield Q and the fluorescence lifetime τ defined by

$$Q = \frac{k_{f'}}{k_{f'} + k_{nf}} \qquad [1.10]$$

$$\tau = \frac{1}{k_{f'} + k_{nf}} \qquad [1.11]$$

where $k_{f'}$ and k_{nf} are the radiative and non-radiative decay rates, respectively. The excitation energy of a fluorophore can also be transferred to another fluorophore through Förster resonance energy transfer (FRET) (Förster, 1948; van der Meer et al., 1994). Here, the energy donating and accepting fluorophores are called donor and acceptor, respectively. The energy transfer efficiency E is defined by

$$E = \frac{k_T}{k_T + k_{D'} + k_{nD}} \qquad [1.12]$$

where k_T is the energy transfer rate and $k_{D'}$ and k_{nD} are the radiative and non-radiative decay rates (excluding FRET) of the donor molecule, respectively. The FRET process is depicted in the Jablonski diagram in Fig. 1.4.

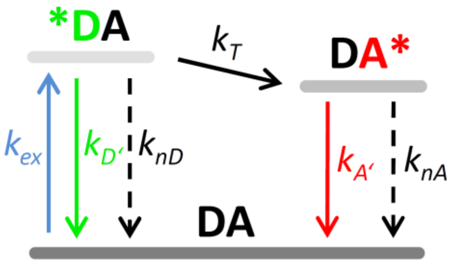

Figure 1.4: Energy level diagram of the FRET process. A donor molecule D that has absorbed light (blue arrow) can lose its excitation energy in a number of ways, including emitting a photon of longer wavelength than the excitation light (fluorescence, green arrow), by non-radiative decay (black dashed arrow), or by Förster resonance energy transfer to an acceptor A (black solid arrow). The excitation energy of the acceptor can again be lost by emitting a photon (red arrow), which typically has a longer wavelength than the donor fluorescent photon, or by non-radiative decay (black dashed arrow).

Using equation 1.11, the transfer efficiency can be expressed as a function of fluorescence lifetimes:

$$E = 1 - \frac{\tau_{DA}}{\tau_D} \qquad [1.13]$$

where τ_{DA} and τ_D are the donor lifetimes in presence and absence of an acceptor, respectively. An alternative expression for E uses the emission rates of donor and acceptor photons. The number of donor photons n_D and acceptor photons n_A per time is proportional to the donor and acceptor emission rates k_D and k_A, respectively. From $k_T = k_{A'} + k_{nA}$ and equation 1.10, the transfer efficiency can be calculated as

$$E = \frac{n_A}{n_A + n_D \left(Q_A / Q_D \right)} \qquad [1.14]$$

where Q_A and Q_D are the quantum yields of the acceptor and the donor dye, respectively. Equations 1.13 and 1.14 reflect the two standard methods for obtaining the transfer efficiency in single molecule spectroscopy, that is either from the donor lifetime or from the ratiometric approach, i.e. from the ratio of acceptor photons over the sum of both donor and acceptor photons detected for the molecule. Calculating E with the ratiometric approach requires knowledge of the quantum yields, which may depend on the solvent conditions or the neighboring chemical groups of the molecule the fluorophores are attached to. In addition, the instrumental detection efficiency of donor and acceptor photons might be different and crosstalk between the detection channels might distort the ratio of donor and acceptor photons. Therefore a careful calibration of the system is required. The lifetime approach is independent of the quantum yields and the detection efficiencies. However, the demands on the instrumentation and data analysis are higher.

Both methods are sensitive to dynamical processes affecting E on the timescale it is determined. For the ratiometric approach, it is the time over which the photons are collected, which for typical single molecule diffusion experiments is about one millisecond. For the lifetime approach, it is the excited state lifetime of the dyes, which is on the order of a few nanoseconds. If all influencing factors are considered sufficiently, both approaches should result in the same mean transfer efficiencies.

The Förster transfer mechanism accounting for k_T is based on near-field dipole-dipole interactions between the two fluorophores, and depends on a number of parameters. The most prominent parameter and the one used most in biochemical applications is the distance R between the fluorophores. The distance dependence of k_T is shown in equation 1.15

$$k_T = \left(k_{D'} + k_{nD}\right)\left(\frac{R_0}{R}\right)^6 \qquad [1.15]$$

where R_0 is the Förster distance. Using equations 1.12 and 1.15, E and R can be directly related by the Förster equation:

$$E = \left(1 + \left(\frac{R}{R_0}\right)^6\right)^{-1} \qquad [1.16]$$

This strong distance dependence makes FRET a very sensitive spectroscopic ruler (Stryer and Haugland, 1967) around the Förster distance, as shown in figure 1.5.

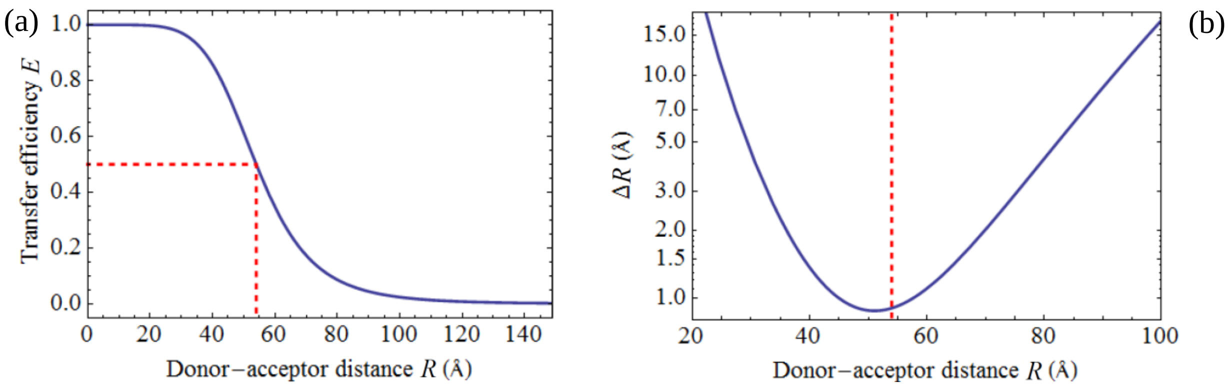

Figure 1.5: (a) Relationship between inter-dye distance R and FRET efficiency E. At the Förster distance R_0 (here 54 Å), E is 0.5 (see red dashed line). (b) Assuming E can be determined with an accuracy of $\Delta E = \pm 0.025$ and $R_0 = 54$ Å, the uncertainty $\Delta R = \left(dR/dE\right)\Delta E$ in the distance is shown as a function of R. Around R_0, the error is about ±1 Å, between 30 Å and 80 Å it is still under ±5 Å.

R_0 is determined by photophysical properties of the dyes and by solvent properties:

$$R_0^6 = \frac{9000 \ln(10) \kappa^2 Q_D J}{128 \pi^5 n^4 N} \qquad [1.17]$$

where κ^2 is the orientation factor, Q_D is the quantum yield of the donor, J is the overlap integral of the donor emission spectrum and the acceptor absorption spectrum, n is the refractive index of the solvent, and N_A is Avogadro's number. The orientation factor κ^2 describes the relative orientation of the transition dipoles of donor and acceptor. The extreme cases are a static orientational distribution of fluorophore transition dipoles, and fluorophores which are rotating rapidly and isotropically. In the first case, κ^2 can vary between 0 and 4, and R_0 and therefore E can vary accordingly, even though the distance might be constant. This makes it significantly more difficult to obtain the correct distances. In the second case, κ^2 has the average value of 2/3. Here, a single distance corresponds to a single transfer efficiency. For achieving this more convenient situation, flexible linkers are often introduced between the molecule and the fluorescence label. The flexibility of the dyes and the correctness of the 2/3 assumption can be checked by fluorescence anisotropy measurements.

Fluorescence Anisotropy

Fluorescent molecules have absorption and emission dipole moments, which is why light is neither absorbed from nor emitted into all directions isotropically. The probability of excitation depends on the angle between the electric field vector of the incoming light and the vector of the absorption dipole moment of the fluorophore. In an ensemble of randomly orientated dye molecules illuminated by linearly polarized light, the molecules whose absorption dipole moments are orientated nearly parallel to the electric field vector are excited preferentially. Consequently, the emission light is dominated by those selected dyes. In general, the emitted light will also be polarized, and the polarization and intensity of the light will depend on the angle between the excitation light source and the detector. Quantitatively, the effect is described by the fluorescence anisotropy r

$$r = \frac{I_P - I_S}{I_P + 2 I_S} \qquad [1.18]$$

where I_p and I_s are the emission intensities detected with polarization parallel and perpendicular with respect to the excitation light.

Time-resolved anisotropy decays can reveal the timescales of the dye rotation τ_{eff} and of the rotational motion of the molecule the dye is attached to, τ_M (Lipari and Szabo, 1980).

$$r(t) = \left((r_0 - r_\infty) e^{-t/\tau_{eff}} + r_\infty \right) e^{-t/\tau_M} \qquad [1.19]$$

where r_0 is the limiting anisotropy of the fluorophore, which depends on the angle between absorption and emission dipole moments, and r_∞ is the residual anisotropy in the absence of rotational motion of the molecule carrying the fluorophore, which can be used to estimate the angular restriction of the fluorophore.

In the case of FRET, the transfer rate depends on the angle between the emission dipole of the donor and the absorption dipole of the acceptor. The case that κ^2 equals 2/3 is given when the donor dipole orientation randomizes before the photon is emitted. A low anisotropy of the donor fluorophore is often used to justify this assumption.

Biochemical Requirements

In most cases, single molecule fluorescence spectroscopy requires the incorporation of extrinsic fluorophores into the molecule of interest. For the labeling of the molecule, reactive groups are needed for specific derivatization with the fluorophores. Naturally occurring reactive groups in proteins are the sulfhydryl groups of cysteines and the amino groups of lysines and the N-terminal amino acids. Other reactive side chains like azide groups can be introduced if the molecules of interest are produced by solid-phase synthesis or with the use of orthogonal aminoacyl-tRNA/tRNA pairs (Young and Schultz, 2010). A site-specific introduction of the fluorophores is of great advantage for several reasons. First, the fluorophores should be attached in protein segments where they have minimal influence on folding mechanism and stability, and where the fluorophores are not influenced by the protein environment (Marme et al., 2003). Most importantly, they should be in a position where they can probe the distance and distance changes of interest with highest resolution. In order to achieve the site specificity, site directed mutagenesis is used to either introduce amino acids with specific side groups at the according positions and to remove them at other places.

Instrumentation and Data Analysis

The main components of a standard single molecule fluorescence instrument are shown in figure 1.6. A laser beam (either pulsed for lifetime information or continuous wave) is focused with a high numerical aperture objective into the sample volume, resulting in a confocal spot with a size usually of the order of a femtoliter. The concentration of labeled molecules in the sample is very low (on the order of tens of picomolar) to reduce the probability of two molecules being in the confocal volume at the same time to a negligible amount. Molecules that diffuse through the confocal volume will be excited by the laser beam. Fluorescence light collected by the objective passes a dichroic mirror to separate excitation light from fluorescence light, and is focused onto a pinhole that confines the detection volume. A polarizing beam splitter separates the parallel and orthogonal polarized light (with respect to the polarization of the excitation light). Both polarization components are additionally separated by dichroic mirrors into donor and acceptor fluorescence light and focused on single photon avalanche photodiodes (APDs).

Counting electronics record time and detection channel information about all detected photons to a hard disk (Wahl et al., 1998; Wahl, 2004). Different electronics can either record the detection time of each photon with respect to the beginning of the measurement (time tag) with picosecond resolution. Alternatively, the time tag is saved with nanosecond resolution, but in addition the detection time with respect to the last laser pulse with picosecond resolution and accuracy is recorded. This additional time allows the determination of the fluorescence lifetime and fluorescence anisotropy from the measured fluorophores.

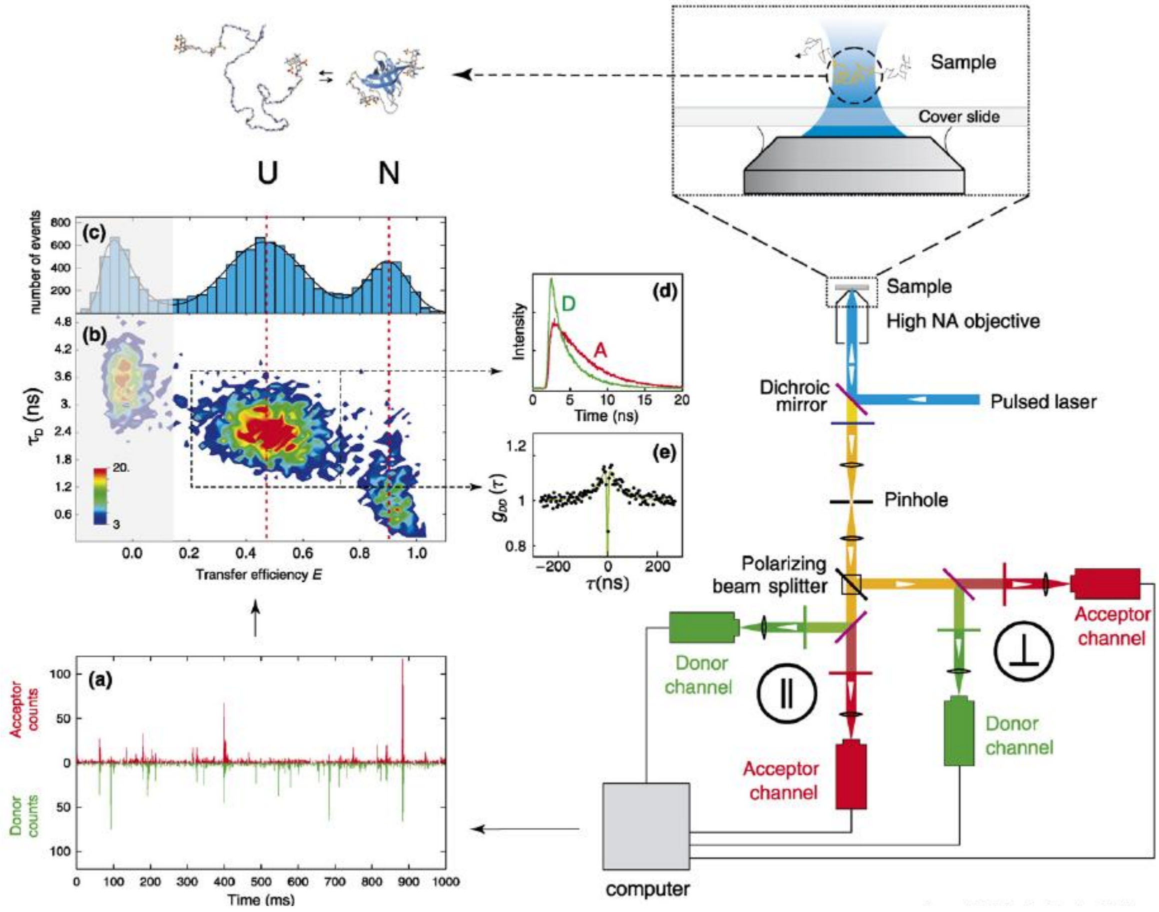

Figure 1.6: Confocal single molecule fluorescence spectroscopy. Scheme showing the main components of the instrument (see text for details) on the right and basic data visualization and analysis on the left, including a photon trajectory (a), a contour plot of donor fluorescence lifetime τ_D versus transfer efficiency E (b), and a transfer efficiency histogram (c). Further analysis based on subpopulations (here unfolded subpopulation selected in (b), marked by dashed squared) include a time-correlated single photon counting histogram (d) to determine accurate lifetimes of acceptor and donor fluorophores, and donor intensity autocorrelation function (e) with nanosecond time resolution. (Adapted from Schuler and Eaton, 2008)

The photon data can be analyzed in different ways. An essential step is the identification of single molecule events in the photon trajectory (figure 1.6 a). Different algorithms have been developed for that purpose. The simplest procedure is to bin the photon trajectory and take bins which have at least a certain number of photons as bursts (Deniz et al., 2001). A second approach is based on the increased photon detection rates in bursts compared to background (Eggeling et al., 2001). First, photons which are separated by a certain maximal interphoton time are combined into bursts. Second, bursts which have at least a certain number of photons are kept for further analysis. This latter approach identifies the start and end points of bursts with higher precision. After their identification, the bursts are corrected for background, different quantum yields of donor and acceptor dyes, cross-talk, direct excitation of the acceptor, and differences in the detection efficiencies for donor and acceptor dye (Schuler, 2006).

The identified photon bursts can be analyzed to obtain the FRET efficiency, the lifetimes of the fluorophores, their anisotropies and number of photons, the length of the photon burst, and the like. The data are usually visualized in histograms like a FRET efficiency histogram (figure 1.6 c) or in contour plots showing two parameters for each burst (e.g. figure 1.6 b). Bursts selected by one or several parameters can be used to extract subpopulation-specific information, e.g. to calculate fluorophore lifetimes (figure 1.6 d) or correlation functions (figure 1.6 e).

1.3.2 KINETIC EXPERIMENTS

Folding and unfolding processes are difficult to study at equilibrium, and only few examples exist where rate constants could be obtained in equilibrium ensemble experiments (Huang and Oas, 1995; Barbar et al., 1998; Teilum et al., 2006). The vast majority of kinetic experiments are done under non-equilibrium conditions. To this end, e.g. stopped-flow instruments are used, in which two solutions are rapidly mixed and the initiated reaction is followed for instance by fluorescence or circular dichroism (Chance, 1951). Although widely used to study protein folding, stopped-flow has two main disadvantages: First, the dead time is about 1 ms, and faster processes can therefore not be resolved. Second, the reaction progress is directly coupled to the measurement time. The amount of signal at a time point of the reaction is therefore limited. This impedes the application of stopped-flow methods to probes that require longer measurement times. Alternatively, kinetic experiments can be triggered by pressure changes (Pryse et al., 1992; Jacob et al., 1999b) or by laser pulses, which either change the temperature (Nölting et al., 1995; Ballew et al., 1996) or manipulate certain groups within the protein (Bredenbeck et al., 2003; Chen et al., 2003). Although these triggering methods allow for much shorter dead times, they are restricted to specialized probes or to pressure or temperature changes as a trigger.

An alternative approach applicable to a broader range of conditions than laser or pressure-induced triggering methods are continuous-flow mixers (Regenfuss et al., 1985; Chan et al., 1997; Shastry and Roder, 1998; Ratner and Sinev, 2000; Lipman et al., 2003; Hertzog et al., 2004). Here, the solutions are continuously transported, mixed and measured, in contrast to stopped-flow mixers. Since the reaction progress and the measurement time are decoupled, extended measurement times are possible, as needed in the case of single molecule fluorescence spectroscopy. Besides the observation of kinetic processes, devices can also be used to investigate populations under unfavorable conditions by populating them transiently, e.g. the unfolded state under native conditions before the refolding reaction starts. The use of microfabrication techniques has lead to numerous advantages such as cheap and rapid production of flexible constructions with small dimensions (Stone et al., 2004). The general requirements for the construction of continuous-flow microfluidic mixers are an optimal design for low dead times, high temporal resolution, a material with appropriate optical properties, minimal interaction with the samples, and sufficient mechanic stability for the pressure build up at the flow rates needed. There are also a couple of disadvantages of continuous-flow mixers, especially compared to stopped-flow instruments that have to be taken into account. The sample consumption is usually higher compared to stopped-flow instruments. However, the low volume rates needed for microfabricated mixers and the low sample concentrations needed for sensitive detection systems like in single molecule spectroscopy can reduce sample needed to a negligible amount. The upper measurement time of a continuous-flow mixer is limited, not only because the observation channel has a finite length, but also because diffusion of the sample molecules parallel to the flow decreases the time resolution for longer observation times. For the analysis of continuous-flow mixing experiments, a thorough understanding of the flow characteristics is required to calculate proper dead times, times after mixing, and the temporal error of a measurement. However, powerful numerical methods, such as finite element calculations are available to simulate flow and diffusion properties of microfluidic mixer designs. Still it is very important to characterize the mixing devices for both their flow and optical properties experimentally.

Continuous-flow mixers have been shown to extend the possibilities for studying fast processes, especially to elucidate the folding mechanisms of proteins. For instance, mixing experiments were used to identify additional folding intermediates of cytochrome c monitored by Trp fluorescence with 50 μs dead time (Shastry and Roder, 1998) and by CD with 400 μs dead time (Akiyama et al., 2000), the fast formation of tertiary structure for cytochrome c, apomyoglobin and lysozyme, monitored by Trp fluorescence with a dead time of 20 μs (Lapidus et al., 2007), and a fast collapse prior to folding for dihydrofolate reductase monitored by SAXS with a dead time of 300 μs (Arai et al., 2007).

1.4 OUTLINE

Further insights in the unfolded state of proteins are essential to understand its impact on protein folding and stability. The analysis of the collapse is an important step towards understanding the properties of unfolded proteins under near-physiological conditions. To gain a more detailed picture of the collapsed unfolded state of Csp*Tm*, several new variants were produced to map different parts of the protein in single molecule FRET measurements. As a complementary approach, a microfluidic mixing system was developed, allowing CD measurements with synchrotron radiation to study the β-sheet content of unfolded Csp*Tm* in non-equilibrium experiments. The performance of the mixer was investigated using the well-studied protein cytochrome C.

In addition to the structural properties, the dynamic properties are crucial for understanding unfolded proteins. An extension of fluorescence correlation spectroscopy to the relevant nanosecond timescale was used to explore the dynamics of the unfolded chain from distance fluctuations monitored by FRET. Interesting questions to study are the dependence of the dynamics on the degree of collapse and on the intramolecular chain separation.

Kinetic experiments are crucial for many problems in protein folding and other biophysical areas. To combine the subpopulation resolution of single molecule fluorescence spectroscopy and the diversity of information available from kinetic experiments, continuous microfluidic mixers were developed that allow single molecule fluorescence experiments.

Single molecule FRET spectroscopy of freely diffusing molecules can reveal many details of heterogeneous systems. Nevertheless, the limited amount of measurement time and thus of signal per molecule constrains both temporal and subpopulation resolution. The potential of using information of molecules which are detected a second time is investigated, and its impact on analyzing single molecule FRET measurements is explored.

II. Structural Properties of Unfolded Csp and Development of SRCD-Mixers

2.1 MAPPING PROTEIN COLLAPSE WITH SINGLE-MOLECULE FLUORESCENCE AND KINETIC SYNCHROTRON RADIATION CIRCULAR DICHROISM SPECTROSCOPY

Mapping protein collapse with single-molecule fluorescence and kinetic synchrotron radiation circular dichroism spectroscopy

Armin Hoffmann[*], Avinash Kane[†‡], Daniel Nettels[*], David E. Hertzog[†], Peter Baumgärtel[§], Jan Lengefeld[§], Gerd Reichardt[¶], David A. Horsley[‖], Robert Seckler[§], Olgica Bakajin[†], and Benjamin Schuler[*,**]**

[*]Biochemisches Institut, Universität Zürich, Winterthurerstrasse 190, 8057 Zürich, Switzerland; [†]BioSecurity and Nanosciences Laboratory, Lawrence Livermore National Laboratory, Livermore, CA 94550; Departments of [‡]Electrical and Computer Engineering and [‖]Mechanical and Aeronautical Engineering, University of California, Davis, CA 95616; [§]Physikalische Biochemie, Universität Potsdam, 14476 Potsdam-Golm, Germany; and [¶]Berliner Elektronenspeicherring-Gesellschaft für Synchrotronstrahlung, 12489 Berlin, Germany

Edited by William A. Eaton, National Institutes of Health, Bethesda, MD, and approved November 6, 2006 (received for review May 26, 2006)

We have used the combination of single-molecule Förster resonance energy transfer and kinetic synchrotron radiation circular dichroism experiments to probe the conformational ensemble of the collapsed unfolded state of the small cold shock protein Csp*Tm* under near-native conditions. This regime is physiologically most relevant but difficult to access experimentally, because the equilibrium signal in ensemble experiments is dominated by folded molecules. Here, we avoid this problem in two ways. One is the use of single-molecule Förster resonance energy transfer, which allows the separation of folded and unfolded subpopulations at equilibrium and provides information on long-range intramolecular distance distributions. From experiments with donor and acceptor chromophores placed at different positions within the chain, we find that the distance distributions in unfolded Csp*Tm* agree surprisingly well with a Gaussian chain not only at high concentrations of denaturant, where the polypeptide chain is expanded, but also at low denaturant concentrations, where the chain is collapsed. The second, complementary approach is synchrotron radiation circular dichroism spectroscopy of collapsed unfolded molecules transiently populated with a microfluidic device that enables rapid mixing. The results indicate a β-structure content of the collapsed unfolded state of ≈20% compared with the folded protein. This suggests that collapse can induce secondary structure in an unfolded state without interfering with long-range distance distributions characteristic of a random coil, which were previously found only for highly expanded unfolded proteins.

Gaussian chain | microfluidic mixing | protein folding | random coil | secondary structure

With the discovery of small proteins that fold in the absence of populated intermediates (1), our quantitative understanding of the elementary properties of protein folding reactions has made significant advances, including the structural characterization of transition states for folding (2) and the prediction of folding rates from native structure (3–5). One of the most severe limitations for the further development of these approaches is our ignorance about the energetic or structural properties of unfolded[††] states of proteins. Because of the structural heterogeneity and complexity of the ensembles of conformations populated by unfolded proteins, their experimental characterization has proven extremely difficult. Traditional methods, such as small-angle scattering techniques (6), provide only global physical properties, e.g., the radius of gyration. In some cases, more detailed structural information can be obtained from NMR (7–10), but these studies usually provide information about the denatured state only under nonnative conditions, typically in the presence of large concentrations of denaturant, or through severe destabilization of the native state induced by covalent modification or mutations. The most interesting and physiologically relevant situation, however, is that of an unfolded state of a stable protein under native conditions. Unfortunately, the great majority of molecules will then be present in their native conformation, thus overwhelming the signal from unfolded molecules.

We avoid this problem by using two complementary optical techniques: single-molecule fluorescence and kinetic synchrotron radiation circular dichroism (SRCD) spectroscopy. Single-molecule spectroscopy has the inherent ability to separate the signals from subpopulations in heterogeneous mixtures and equilibria, which makes it ideally suited to analyze protein folding reactions (11, 12). Specifically, by using single-molecule Förster resonance energy transfer (FRET), intramolecular distances of the unfolded state can be measured even in the presence of a majority of folded molecules (13, 14). Recently, the collapse of unfolded molecules of the small cold shock protein Csp*Tm* at close to native conditions was discovered with this approach (14). This collapsed unfolded form also can be populated kinetically (15, 16) and has by now been found for a range of small proteins (16–20). It is unclear, however, whether this collapse is a nonspecific random heteropolymer collapse (21) or whether it is accompanied by the formation of specific structure. By placing FRET dye pairs in various positions of the protein, we obtain information on distance distributions in different segments of the unfolded polypeptide chain and their dependence on denaturant concentration.

A versatile method to complement such distance constraints with information about the secondary structure content is circular dichroism (CD) spectroscopy. In this case, however, we have to transiently populate the unfolded state under native conditions by using rapid mixing experiments. For this purpose, we use SRCD spectroscopy with a specifically designed microfluidic continuous-flow mixing system with millisecond dead time. In this way, the collapsed unfolded state, which is populated on a microsecond time scale or faster (14, 16), can be studied

---

Author contributions: A.H., A.K., and D.N. contributed equally to this work; O.B. and B.S. designed research; A.H., A.K., D.E.H., P.B., J.L., O.B., and B.S. performed research; A.K., D.N., D.E.H., P.B., G.R., D.A.H., R.S., O.B., and B.S. contributed new reagents/analytic tools; A.H., A.K., D.N., and B.S. analyzed data; and A.H., O.B., and B.S. wrote the paper.

This article is a PNAS direct submission.

Abbreviations: FRET, Förster resonance energy transfer; CD, circular dichroism; SRCD, synchrotron radiation CD.

[**] To whom correspondence may be addressed. E-mail: bakajin1@llnl.gov or schuler@bioc.unizh.ch.

[††] We denote all nonnative conformations as "unfolded" to stress that for true two-state proteins, such as Csp*Tm*, there are no thermodynamically or kinetically distinguishable denatured states.

This article contains supporting information online at www.pnas.org/cgi/content/full/0604353104/DC1.

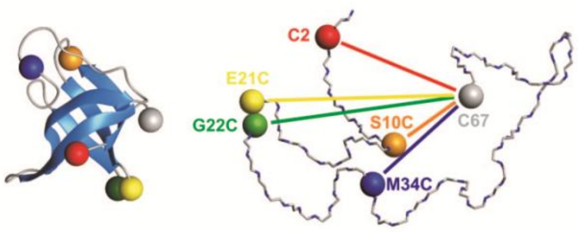

Fig. 1. Schematic of folded (*Left*) and unfolded (*Right*) Csp*Tm* with the sites for dye attachment for FRET indicated by colored spheres. For every variant investigated, one dye was reacted with Cys at position 67, and a second dye was reacted with a Cys at one of the other positions shown.

spectroscopically without interference from the signal of folded molecules, which form on a slower time scale. Importantly, SRCD gives us access to the far-UV wavelength range, where β-structure can be well distinguished from random coil (22, 23) but which is inaccessible with commercial stopped-flow instruments.

Results

Collapse from FRET Efficiency Histograms. For the single-molecule FRET experiments, donor (Alexa Fluor 488) and acceptor (Alexa Fluor 594) dyes were placed specifically at different solvent-exposed positions of Csp*Tm* via pairs of Cys residues introduced by site-directed mutagenesis (Fig. 1). Upon unfolding of the protein, the average distance between the chromophores increases. As a consequence, the rate of energy transfer between them decreases, resulting in a reduced transfer efficiency $E = n_A/(n_A + n_D)$, where n_A and n_D are, respectively, the number of acceptor and donor photons emitted by the molecule [including corrections (24), see *Materials and Methods*]. In confocal single-molecule experiments, transfer efficiencies are determined from photon bursts originating from individual molecules freely diffusing through the focal spot of the laser beam (25). A histogram from a large number of such events shows distinct maxima corresponding to the subpopulations present in the sample (Fig. 2). The peak at high E corresponds to folded molecules, and the peak at intermediate E corresponds to unfolded molecules. The additional peak near $E = 0$ is thought to be caused by molecules lacking an active acceptor chromophore (24, 26) but does not interfere with our analysis.

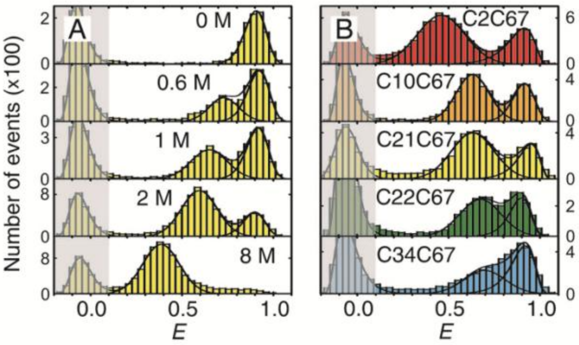

Fig. 2. Energy transfer efficiency (E) histograms from single-molecule FRET measurements. (*A*) Examples from a GdmCl titration of variant C21C67, illustrating unfolded state collapse. See SI Movie 1 for a complete data set of C2C67. (*B*) Histograms of all variants at 1.5 M GdmCl. The peak at $E \approx 0.9$ corresponds to folded molecules, and the peak at intermediate E corresponds to unfolded molecules. The peak at $E \approx 0$ (shaded) originates from molecules with an inactive acceptor (26). To determine mean transfer efficiencies, the unfolded peak was fit to a normal distribution, and the other two peaks were fit to log normal functions (black lines) (14). The colors used correspond to those used in Fig. 1.

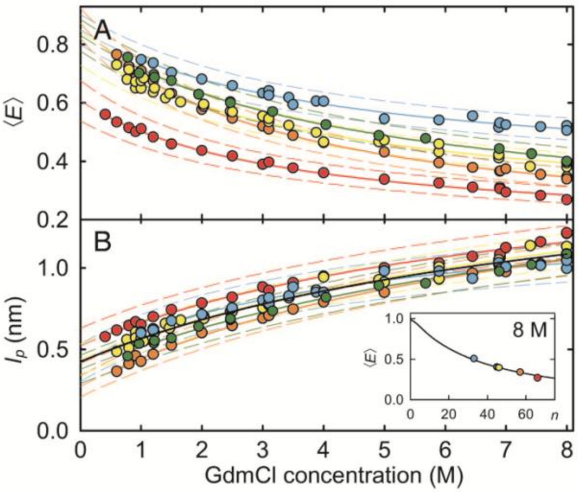

Fig. 3. Denaturant dependence of the mean transfer efficiencies $\langle E \rangle$ and persistence lengths l_p. (*A*) $\langle E \rangle$ of the unfolded state of all variants as a function of GdmCl concentration. (*B*) l_p calculated from $\langle E \rangle$ using Eqs. **1** **4**. (*Inset*) Shows the measured values of $\langle E \rangle$ for all variants at 8 M GdmCl, and as a black line $\langle E \rangle$ for a Gaussian chain calculated from Eqs. **1** **4** for $l_p = 1.1$ nm (the mean value of all variants) as a function of sequence separation n (number of peptide bonds excluding linkers). The solid lines in the GdmCl titrations are fits to the empirical equation $y = y_0\,[1 + \Delta y K x/(1 + Kx)]$ used for interpolation; the solid black line is a fit to all data. Estimated error ranges for $\langle E \rangle$ and l_p are indicated by dashed lines (see *SI Materials and Methods*). The colors used correspond to those used in Fig. 1.

With increasing concentration of the denaturant guanidinium chloride (GdmCl), we observe a change in the relative amplitudes of the signal from native and unfolded molecules, corresponding to the expected redistribution of the two populations (Fig. 2*A*). However, whereas the mean transfer efficiency $\langle E \rangle$ of the folded state is invariant, the peak from unfolded molecules is continuously shifting to higher transfer efficiencies with decreasing GdmCl concentration. By comparison with stiff polyproline peptides, it has previously been shown that this increase in $\langle E \rangle$ corresponds to a collapse of the unfolded state in response to the altered solvent conditions (14). To address the question of whether this collapse is a global process that is evenly distributed across the polypeptide chain or whether it is due to compaction of a specific part of the molecule, we measured single-molecule transfer efficiency histograms of the labeled Csp*Tm* variants at a wide range of denaturant concentrations. At a given GdmCl concentration, $\langle E \rangle$ in the unfolded state shows an overall increase with decreasing sequence separation, as expected (Fig. 2*B*) . Moreover, all variants exhibit the characteristic continuous collapse at low concentrations of denaturant, resulting in an increase in $\langle E \rangle$ [Fig. 3*A* and supporting information (SI) Movie 1].

Distance Distributions from Mean Transfer Efficiencies. To analyze the mean transfer efficiencies in terms of distance distributions in the unfolded state, we use the Gaussian chain model, the simplest realistic model for describing large-scale properties of macromolecules (21), such as highly unfolded peptides and

---

Note that our analysis does not take into account the effect of excluded volume on the length scaling of the end-to-end distance. Such differences become discernible only if unfolded proteins are investigated over a much wider range of chain lengths than here (30).

proteins (6, 27–31). $\langle E\rangle$ of the unfolded state at a given GdmCl concentration can be expressed in terms of the end-to-end distance probability distribution function of a Gaussian chain $P(r)$ and the distance dependence of the transfer efficiency $E(r)$ according to[§§]

$$\langle E\rangle = \int_a^{l_c} E(r)P(r)dr \Big/ \int_a^{l_c} P(r)dr \qquad [1]$$

with

$$E(r) = \frac{1}{1+(r/R_0)^6} \qquad [2]$$

and

$$P(r) = 4\pi r^2\left(\frac{3}{2\pi\langle r^2\rangle}\right)^{3/2}\exp\left(-\frac{3r^2}{2\langle r^2\rangle}\right), \qquad [3]$$

where r is the end-to-end distance, a is the distance of closest approach of the chain ends, l_c is the contour length of the labeled polypeptide segment (with dyes and linkers, see *Materials and Methods*), and R_0 is the Förster radius of the dye pair at the GdmCl concentration of the solution (R_0 = 5.4 nm at 0 M GdmCl; see *SI Materials and Methods* for details). The mean squared end-to-end distance $\langle r^2\rangle$ of a Gaussian chain can be expressed as

$$\langle r^2\rangle = 2l_p\, l_c = 2l_p\, nl, \qquad [4]$$

where n is the number of peptide bonds between the chromophores, l is the projection of the distance between two consecutive α-carbon atoms on the axis of the fully extended chain (0.38 nm), and l_p (the only free parameter in the model) is a measure for the effective chain stiffness, which in our limit of $l_c \gg l_p$ is equivalent to the persistence length commonly used in the worm-like chain model (34). Fig. 3*B Inset* shows the measured $\langle E\rangle$ of our Csp*Tm* variants at 8 M GdmCl. The continuous line shows $\langle E\rangle$ as a function of n calculated according to Eqs. **1–4** with l_p = 1.1 nm. All variants can be described with the same value of l_p, indicative of isotropic distance distributions within unfolded Csp*Tm*, and in agreement with previous results on other proteins unfolded at high denaturant concentrations (27–30).

Fig. 3*B* shows l_p for every variant as a function of GdmCl concentration calculated from $\langle E\rangle$ (Fig. 3*A*) using Eqs. **1–4**. The concomitant renormalization for chain length allows a direct comparison of the variants with different sequence separation of donor and acceptor. The values of l_p averaged over all variants range from 1.1 ± 0.1 nm at 8 M GdmCl, to 0.39 ± 0.07 nm extrapolated to 0 M GdmCl (Fig. 3*B*), close the values found in atomic force microscopy experiments (0.33 to 0.42 nm; summarized in ref. 31) or unstructured peptides [0.64 nm (32)] at 0 M GdmCl. All variants show a similar denaturant dependence of l_p, suggesting isotropic chain collapse. From these data alone we cannot exclude that the more pronounced differences at low denaturant concentrations, especially for variant C10C67, may indicate slight deviations from completely isotropic collapse, but several points suggest otherwise. First, it seems structurally implausible that C2C67 and C21C67, which flank the slightly deviating C10C67, exhibit distance distributions in accord with the remaining variants, whereas a large difference occurs between C2C67 and C10C67. Second, other effects, such as changes in the photophysical properties of the chromophores upon collapse, may play a role; e.g., the two lysine residues directly neighboring Cys-10 may act as fluorescence quenchers (35) whose electrostatic interaction with the negatively charged fluorophores may be shielded at high GdmCl concentrations. In view of the error ranges we estimate for this type of measurement (Fig. 3), we conclude that the data are in agreement with isotropic collapse and do not justify an interpretation beyond this simple model.

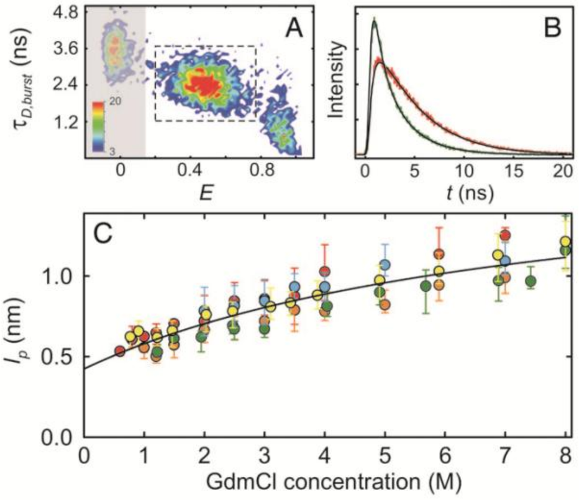

Fig. 4. Fluorescence lifetime distribution analysis. (*A*) All events corresponding to unfolded molecules were selected (dashed box) from a two-dimensional histogram (shown is C2C67 at 1.5 M GdmCl) of the number of bursts (color scale) with transfer efficiency *E* and donor fluorescence lifetime $\tau_{D,burst}$. (*B*) The photons were combined to generate time-correlated single-photon counting histograms for donor (green) and acceptor (red) (see SI Movie 2 for a complete data set of C2C67). (*C*) The rms end-to-end distance was determined and converted to the apparent persistence length l_p (Eq. **4**) by using a global fit assuming the distance distribution of a Gaussian chain (black lines). Error bars indicate the uncertainty in the fits. The solid black line in is a fit to all data as described in Fig. 3. The colors used correspond to those used in Fig. 1.

Subpopulation-Selective Fluorescence Lifetime Distribution Analysis. Mean transfer efficiencies obtained from transfer efficiency histograms do not provide direct information about the shape of the distance distribution, because the dynamics of inter-dye distance fluctuations are fast compared with the millisecond observation time per burst (14, 36). Fluorescence intensity decays, on the other hand, do report directly on the shape of the distance distribution (37, 38), because distance fluctuations for long polypeptides are slow relative to the fluorescence lifetimes of the dyes (32, 33). Conventional approaches to the analysis of distance distributions from fluorescence lifetimes suffer from interference with signal from native molecules; however, in combination with the separation of subpopulations by virtue of single-molecule detection, we can selectively analyze distance distributions in the unfolded state while remaining unaffected by native signal (17). For every individual fluorescence burst, the mean donor fluorescence lifetime is estimated (39) in addition to *E*. From the resulting two-dimensional histograms (Fig. 4*A*), we select the bursts corresponding to the unfolded state and, by combining the photons from all unfolded molecules, obtain high-resolution fluorescence decays (Fig. 4*B*). Donor and acceptor decays are then

---

[§§] For this analysis, we assume intramolecular distance fluctuations to be slow relative to the fluorescence lifetime of the donor chromophore, as expected for long polypeptide chains (32, 33).

analyzed in a global fit[¶¶] that assumes a distribution of transfer rates resulting from the distribution of donor–acceptor distances (see *SI Materials and Methods*), analogous to the established procedures for ensemble data (17, 38, 40). Specifically, we use $P(r)$ of a Gaussian chain (Eq. **3**) with $\langle r^2 \rangle$ as the only free parameter.

The time-correlated single-photon counting histograms from unfolded molecules are fit well, if we assume the distance distribution of a Gaussian chain (Fig. 4*B*; see also SI Movie 2), and again we observe a continuous collapse of the chain for all variants, with the expected increase in $\langle r^2 \rangle$ with n (data not shown). To normalize the data for n and to facilitate direct comparison of lifetime and intensity results, we calculate l_p from $\langle r^2 \rangle$ (Eq. **4**) (Fig. 4*C*). The greater demands on the signal-to-noise ratio for this type of analysis reduces the number of suitable data sets, especially at low GdmCl concentrations, where the overlap between native and unfolded subpopulation increases, but nevertheless we again find a similar GdmCl-dependence of l_p for all variants. The good overall agreement of fluorescence intensity (Fig. 3*B*) and lifetime (Fig. 4*C*) results and the lack of consistent deviations from the averages in Figs. 3*B* and 4*C* provide additional evidence that the remaining differences between variants seen in either analysis are within the errors of the methods. The combined results of single-molecule intensity and lifetime data therefore suggest that the chain dimensions of Csp*Tm* are isotropic and Gaussian chain-like on the length scale we are probing, even for strongly collapsed unfolded molecules. But does this random coil behavior exclude the presence of secondary structure in the collapsed unfolded state?

Secondary Structure Content from SRCD. An ideal method to quantify the secondary structure content of proteins is CD spectroscopy. Collapse of Csp has been shown to occur on a microsecond timescale or faster (12, 14, 16), whereas the folding rate at low GdmCl concentrations is in the tens of milliseconds range (41). In a kinetic mixing experiment with millisecond time resolution, the collapsed unfolded state is therefore formed during the dead time, and only the actual folding process is resolved. The dead time signal amplitude reports on the change in structure during collapse. However, although the formation of α-helical structure is readily observed with stopped-flow CD spectroscopy (typically at 222 nm), formation of β-sheet structure is often not accessible because of the small difference in CD signal between a random coil and β-structure as well as the strong influence of aromatic amino acids at wavelengths of >220 nm (42), the range available in conventional stopped-flow CD. Accordingly, previous attempts to measure secondary structure formation upon collapse of Csp*Tm* with CD spectroscopy have failed (B.S., unpublished results). To solve this problem, we have started to establish a methodology for which SRCD is used with microfabricated rapid mixing devices. SRCD has the advantage of high photon flux in the far UV below 220 nm, where the CD signal differences between random coil and β-structure become very pronounced (43), and the Gaussian beam shape allows focusing into microstructures. Microfluidic mixers (44) permit the implementation of sophisticated mixing strategies, making them the fastest method available for rapid-dilution experiments (45). They can be fabricated in fused silica with path lengths in the micrometer range, thus maximizing transmission in the far UV range. Because of the small feature size, sample consumption is drastically reduced compared with conventional continuous-flow mixing experiments (46), some of which have already led to substantial improvements both in time resolution and accessible wavelength range in kinetic CD experiments (47).

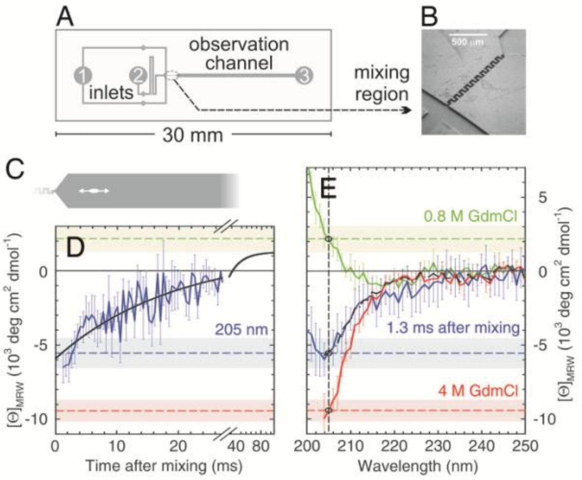

Fig. 5. Secondary structure content of collapsed unfolded Csp*Tm* from SRCD. (*A*) Channel pattern of the microfluidic mixing device. To initiate refolding, unfolded protein injected into inlet 2 is diluted with buffer injected into inlet 1. (*B*) Rapid mixing occurs in the serpentine-shaped channel shown as a scanning electron micrograph. (*C*) The synchrotron radiation beam (white ellipse) is positioned in the observation channel. (*D*) Refolding kinetics of Csp*Tm* at 0.8 M GdmCl measured at 205 nm (blue line; error bars give one standard deviation calculated from eight measurements) and a single-exponential fit to the data (solid black line). (*E*) CD spectrum taken 1.3 ms after mixing (solid blue line), compared with equilibrium spectra under native (solid green line; 0.8 M GdmCl) and unfolding conditions (red line; 4 M GdmCl). The corresponding ellipticities at 205 nm are indicated in the spectra as dashed blue, green, and red lines, respectively. The shaded light blue, green, and red bands indicate one standard deviation from the equilibrium ellipticities of folded and unfolded Csp*Tm*, respectively, at 205 nm. The black dashed dotted curve is a linear combination of the spectra at 0.8 M and 4 M GdmCl used to estimate the secondary structure content of collapsed unfolded Csp*Tm*.

For refolding, Csp*Tm* in 4 M GdmCl was diluted to a final concentration of 0.8 M GdmCl (Fig. 5). The actual mixing region (Fig. 5*B*) consists of a narrow serpentine-shaped channel that performs mixing in the laminar flow regime by virtue of diffusion and chaotic advection (48). CD kinetics were measured by scanning the synchrotron radiation beam along the broader observation channel (Fig. 5*C*). Different positions in the channel thus correspond to different times after mixing, with a dead time of 1.3 ms. A kinetic trace taken at 205 nm (Fig. 5*D*), fit to a single exponential decay, resulted in a time constant of 19 ± 4 ms, in good agreement with the folding rates measured with stopped-flow fluorescence under identical conditions (41). However, the CD signal of -6×10^3 deg·cm^2·dmol^{-1} at 1.3 ms does not coincide with the CD signal of Csp*Tm* unfolded in 4 M GdmCl (Fig. 5 *D* and *E*, dashed red line), indicating the formation of secondary structure before the actual folding reaction.

For spectral information on collapsed unfolded Csp*Tm*, wavelength scans were taken 1.3 ms after mixing (Fig. 5*E*, solid blue line), when the fraction of native molecules calculated from the folding time is only 7%. Steady-state spectra of Csp*Tm* unfolded in 4 M GdmCl (Fig. 5*E*, solid red line), and native Csp*Tm* in 0.8 M GdmCl (Fig. 5*E*, solid green line) were recorded in the same mixing device and corrected for baselines taken without protein under otherwise identical conditions. These spectra illustrate the advantage gained by extending the wavelength range to <220 nm. Fitting the CD spectrum of collapsed unfolded Csp*Tm* to a linear combination of the spectra in 4 M and 0.8 M GdmCl (Fig. 5*E*, black dash–dotted

---

[¶¶] Note that a global analysis is substantially more robust than the individual fits and mitigates the common problems of quantitatively analyzing fluorescence decays deviating from single exponential behavior, especially for the short donor lifetime components, which result in a rise term in the acceptor intensity.

curve) results in a signal change of ≈27% relative to the native structure (excluding the contribution from the 7% folded molecules). Relating this amplitude quantitatively to β-structure content is complicated by the contribution of aromatic amino acids to the native state signal, but from CD reference spectra for β-sheet (43) and the β-structure content from the NMR structure of Csp*Tm* (49), we estimate for the collapsed unfolded protein at 0.8 M GdmCl a β-structure content of ≈20% relative to the native protein (assuming no contribution from aromatic amino acids to the CD of collapsed unfolded Csp*Tm*). A very small population of additional α-helical structure cannot be excluded, but from the signal at 222 nm, the α-helix contribution is not more than approximately -1×10^3 deg·cm^2·dmol^{-1}, corresponding to less than ≈3% α-helix (43).

Discussion

Over the past 40 years, many proteins unfolded at high concentrations of denaturant have been shown to obey Gaussian chain statistics on a global scale (6, 27–30, 50, 51). Csp*Tm* is no exception in this respect. Its radius of gyration in 6 M GdmCl calculated from all labeled variants [using Eq. **4** and $R_g^2 = \langle r^2 \rangle / 6$ (21)] is 2.9 (±0.1) nm excluding dye linkers, in agreement with the 2.4 (+0.4/−0.2) nm calculated from the scaling law given by Kohn *et al.* (30, 51). But how does the collapse of the unfolded state at low GdmCl concentrations affect the intramolecular distance distributions? Surprisingly, even under near-native conditions, the agreement with Gaussian chain behavior is good, and l_p is similar for all intramolecular distance pairs (Figs. 3*B* and 4*B*). At 1 M GdmCl, for instance, the resulting radii of gyration equal 2.2 (±0.2) nm. The small variance suggests that the distance distributions within the unfolded protein are rather isotropic. We thus have no evidence for native state topology in collapsed unfolded Csp*Tm*, in contrast to NMR experiments on staphylococcal nuclease (8) and eglin (52) at high concentrations of urea and in contrast to suggestions from simulations (53). Similarly, there is no obvious relation to the transition state structure (54). Our observation is in contrast to recent measurements on chymotrypsin inhibitor 2 and acyl-CoA-binding protein, where indications were found for a substantial deviation of the collapsed denatured state from Gaussian chain behavior (17) possibly involving folding intermediates (55). In summary, we conclude from the single-molecule fluorescence data that unfolded Csp*Tm* is close to a random coil in terms of polymer physics, even under near-physiological conditions.

It may therefore come as a surprise that the collapsed unfolded state contains a significant amount of β-structure, as was observed in our kinetic SRCD experiments. How can we reconcile these two observations? Clearly, global random coil behavior does not exclude the presence of short structured segments (30, 56–58), even more so if these are only populated transiently. This argument has been used to resolve the seemingly conflicting views of residual structure observed in proteins under highly denaturing conditions on the one hand and the successful description of global properties of unfolded polypeptides with the random coil model on the other (59, 60). Our results suggest that there are cases for which we must extend this notion of a random coil with residual structure even to the collapsed unfolded state, populated under conditions that have so far evaded confrontation with the "reconciliation problem" (6). Compaction of the chain would be expected to contribute to the formation of local structure, because the increase in excluded volume effects will introduce more steric interference with non-nearest-neighbor residues (29, 60). As a result, the backbone will be forced even more into the core regions of the Ramachandran map, corresponding to extended structures that avoid such steric conflicts. The largest one of these regions, and thus entropically the most favorable one, is the extended structure of β-strands. The particular preference of Csp*Tm* for this conformation is reflected by its extremely low propensity for the formation of α-helices [<1% helical content predicted with AGADIR (61)].

Currently, we have no direct evidence for the detailed conformation and average length of β-strand segments populated in collapsed unfolded Csp*Tm*. Because Gaussian-distributed intramolecular distances can only be observed if the segment length is considerably less than the contour length (21), the stretches of β-conformation must be short relative to the sequence separation of our dye pairs. Details about more local distance distributions could be addressed by using FRET pairs with much smaller Förster radii, which are currently inaccessible to single-molecule spectroscopy. In a very recent study, the dead time amplitudes of stopped-flow ensemble FRET experiments were used to probe the first β-hairpin of a closely related cold shock protein for local conformational preferences in the collapsed unfolded state (62). Magg *et al.* (62) observed a stretching of the second β-strand upon collapse, suggesting that the CD signal observed in our experiments could be due to strands of lengths approaching those in the native state. The question of segment length could possibly also be addressed with new methods for the analysis of CD spectra in terms of the number and size of structured segments in proteins (63, 64), but the current quality of our CD spectra for collapsed unfolded Csp*Tm* does not yet warrant such detailed deconvolution. The further development of kinetic SRCD and its combination with single-molecule fluorescence will be an important complementation of NMR methods in clarifying these structural details and the question of whether the behavior of Csp*Tm* is an exception or possibly a more general characteristic of such small all-β proteins.

Materials and Methods

Synthesis and Labeling of Csp*Tm* Variants. Cysteine residues were introduced by site-directed mutagenesis to provide functional groups for the specific attachment of the dyes essentially as described previously (14). Expression and purification of Cys variants and wild-type protein were performed as described by Kremer *et al.* (49) (for details, see *SI Materials and Methods*).

Confocal Fluorescence Spectroscopy. Observations of single-molecule fluorescence were made with a MicroTime 200 confocal microscope (PicoQuant, Berlin, Germany) equipped with a 470-nm pulsed diode laser (LDH 470) operated at 40 MHz (average power, 130 μW) and an Olympus (Tokyo, Japan) UplanApo ×60, 1.20-W objective. Sample fluorescence was separated into donor and acceptor components with a dichroic mirror (Chroma 585DCXR) and two final filters (Chroma HQ525/50 and Omega 600ALP). Each component was focused onto an avalanche photodiode (SPCM-AQR-15; PerkinElmer Optoelectronics, Fremont, CA), and the arrival time of every detected photon was recorded relative to the exciting laser pulse with a time resolution of 38 ps. Samples of labeled protein were diluted to a concentration of ≈20 pM in 50 mM sodium phosphate buffer at the appropriate GdmCl (Pierce, Rockford, IL) concentration and individually adjusted to pH 7. Tween 20 (0.001%; Pierce) was added to prevent surface adhesion of the protein (14). Data were taken for 30–60 min.

Single-Molecule Data Reduction and Analysis. Successive photons detected in either channel separated by <100 μs were combined into one burst. A burst was retained as a significant event if the total number of counts exceeded 50. Identified bursts were corrected for background, differences in quantum yields, the different collection efficiencies of the detection channels, cross-talk, and direct acceptor excitation with the matrix approach (24) (*SI Materials and Methods*). For determining l_p, the length of dyes and linkers were assumed to be equivalent to an additional 9 aa total, comparable with previous estimates (14, 17, 51, 65). Fluorescence lifetime distribution analysis was performed as described by Laurence *et al.* (17), except that the time-correlated single-photon counting histograms obtained from the unfolded state subpopulations were analyzed in terms of donor–acceptor distance distributions of a Gaussian chain (38, 40) (for details, see *SI Materials and Methods*).

Microfluidic Mixing Devices and Synchrotron Radiation Circular Dichroism. Mixers were fabricated by deep reactive ion etching of fused silica substrates (HPFS Standard Grade, Corning code 7980; Corning, Corning, NY) to a depth of 14.5 μm. Mixers were sealed by direct fusion wafer bonding to another fused silica substrate. A serpentine-shaped channel after the T region joining the inlet channels performs mixing in the laminar flow regime by diffusion and chaotic advection (48). Dean vortices in the transverse plane and corner vortices in the longitudinal plane accomplish mixing by stretching and folding the fluid streamlines. The widening of the channel after mixing slows down the flow, resulting in an accessible time window of ≈27 ms before the solution reaches the exit port (labeled "3" in Fig. 5*A*).

Microfluidic devices were mounted in the SRCD sample chamber (see *SI Materials and Methods*) via a custom-designed holder with connections to two syringe pumps (PHD22/2000; Harvard Apparatus, Holliston, MA). Motorized translation stages (M-111.1; PI, Karlsruhe, Germany) allowed reproducible positioning of the mixer relative to the beam. For refolding, a solution of 6.7 mM unfolded Csp*Tm* in 4 M GdmCl/50 mM sodium phosphate buffer (pH 7.0) was injected through inlet 2 (Fig. 5) at a flow rate of 30 μl/min and mixed with buffer solution without GdmCl injected through inlet 1 at a flow rate of 120 μl/min. Complete mixing was assessed via absorbance and CD scans orthogonal to the flow direction across the observation channel. Flow rates ≥150 μl/min [corresponding to flow velocities of 6.9 m/s in the mixing channel (25 μm wide) and 0.43 m/s in the observation channel (400 μm wide)] were found to result in uniform concentrations after the mixing region. The dead time calculated from these flow rates and the position of the synchrotron beam is 1.3 ms.

We thank Jana Kramer for excellent technical assistance. This work has been supported by the Human Frontier Science Program (A.H., D.E.H., O.B., and B.S.), the Schweizerische Nationalfonds (B.S.), and the Deutsche Forschungsgemeinschaft (J.L., B.S., and R.S.). O.B., A.K., and D.E.H. performed work under the auspices of the U.S. Department of Energy at University of California Lawrence Livermore National Laboratory under Contract W-7405-Eng-48, with funding from the Laboratory Research and Development Program and additional support by the National Science Foundation Center for Biophotonics Science and Technology through Cooperative Agreement PHY 0120999 (managed by the University of California, Davis). A.K. also was supported by the Student Employee Graduate Research Fellowship Program at Lawrence Livermore National Laboratory. A.K. and D.E.H.'s travel was supported by the International Institute for Complex Adaptive Matter. R.S., P.B., and the SRCD station at Berliner Elektronenspeicherring-Gesellschaft für Synchrotronstrahlung were supported by German Federal Ministry of Education and Research Contract 05 KS4IP1/2.

1. Jackson SE (1998) *Fold Des* 3:R81–R91.
2. Fersht AR (1998) *Structure and Mechanism in Protein Sci* (Freeman, New York).
3. Galzitskaya OV, Finkelstein AV (1999) *Proc Natl Acad Sci USA* 96:11299–11304.
4. Baker D (2000) *Nature* 405:39–42.
5. Muñoz V, Eaton WA (1999) *Proc Natl Acad Sci USA* 96:11311–11316.
6. Millett IS, Doniach S, Plaxco KW (2002) *Adv Protein Chem* 62:241–262.
7. Shortle DR (1996) *Curr Opin Struct Biol* 6:24–30.
8. Shortle D, Ackerman MS (2001) *Science* 293:487–489.
9. Dyson HJ, Wright PE (2004) *Chem Rev* 104:3607–3622.
10. Religa TL, Markson JS, Mayor U, Freund SM, Fersht AR (2005) *Nature* 437:1053–1056.
11. Jia YW, Talaga DS, Lau WL, Lu HSM, DeGrado WF, Hochstrasser RM (1999) *Chem Phys* 247:69–83.
12. Schuler B (2005) *ChemPhysChem* 6:1206–1220.
13. Deniz AA, Laurence TA, Beligere GS, Dahan M, Martin AB, Chemla DS, Dawson PE, Schultz PG, Weiss S (2000) *Proc Natl Acad Sci USA* 97:5179–5184.
14. Schuler B, Lipman EA, Eaton WA (2002) *Nature* 419:743–747.
15. Lipman EA, Schuler B, Bakajin O, Eaton WA (2003) *Science* 301:1233–1235.
16. Magg C, Schmid FX (2004) *J Mol Biol* 335:1309–1323.
17. Laurence TA, Kong XX, Jager M, Weiss S (2005) *Proc Natl Acad Sci USA* 102:17348–17353.
18. Kuzmenkina EV, Heyes CD, Nienhaus GU (2006) *J Mol Biol* 357:313–324.
19. Sherman E, Haran G (2006) *Proc Natl Acad Sci USA* 103:11539–11543.
20. Qi PX, Sosnick TR, Englander SW (1998) *Nat Struct Biol* 5:882–884.
21. Grosberg AY, Khokhlov AR (1994) *Statistical Physics of Macromolecules* (Am Inst Phys, Woodbury, NY).
22. Sutherland JC (1996) in *Circular Dichroism and the Conformational Analysis of Biomolecules*, ed Fasman GD (Plenum, New York), pp 599–633.
23. Wallace BA, Janes RW (2001) *Curr Opin Chem Biol* 5:567–571.
24. Schuler B (2006) in *Protein Folding Protocols*, eds Bai Y, Nussinov R (Humana, Totowa, NJ), Vol 366.
25. Deniz AA, Laurence TA, Dahan M, Chemla DS, Schultz PG, Weiss S (2001) *Annu Rev Phys Chem* 52:233–253.
26. Schuler B, Lipman EA, Steinbach PJ, Kumke M, Eaton WA (2005) *Proc Natl Acad Sci USA* 102:2754–2759.
27. Tanford C (1968) *Adv Protein Chem* 23:121–282.
28. Damaschun G, Damaschun H, Gast K, Zirwer D (1998) *Biochemistry (Moscow)* 63:259–275.
29. Zhou HX (2002) *J Phys Chem B* 106:5769–5775.
30. Kohn JE, Millett IS, Jacob J, Zagrovic B, Dillon TM, Cingel N, Dothager RS, Seifert S, Thiyagarajan P, Sosnick TR, *et al*. (2004) *Proc Natl Acad Sci USA* 101:12491–12496.
31. Zhou HX (2004) *Biochemistry* 43:2141–2154.
32. Lapidus LJ, Steinbach PJ, Eaton WA, Szabo A, Hofrichter J (2002) *J Phys Chem B* 106:11628–11640.
33. Möglich A, Joder K, Kiefhaber T (2006) *Proc Natl Acad Sci USA* 103:12394–12399.
34. Doi M, Edwards SF (1988) *The Theory of Polymer Dynamics* (Oxford Univ Press, New York).
35. Ratner V, Amir D, Kahana E, Haas E (2005) *J Mol Biol* 352:683–699.
36. Gopich IV, Szabo A (2003) *J Phys Chem B* 107:5058–5063.
37. Haas E, Wilchek M, Katchalskikatzir E, Steinberg IZ (1975) *Proc Natl Acad Sci USA* 72:1807–1811.
38. Van Der Meer BW, Coker, G, III, Chen SYS (1994) *Resonance Energy Transfer: Theory and Data* (VCH, New York).
39. Eggeling C, Berger S, Brand L, Fries JR, Schaffer J, Volkmer A, Seidel CA (2001) *J Biotechnol* 86:163–180.
40. Beechem JM, Haas E (1989) *Biophys J* 55:1225–1236.
41. Perl D, Welker C, Schindler T, Schröder K, Marahiel MA, Jaenicke R, Schmid FX (1998) *Nat Struct Biol* 5:229–235.
42. Woody RW, Dunker AK (1996) in *Circular Dichroism and the Conformational Analysis of Biomolecules*, ed Fasman GD (Plenum, New York), pp 109–158.
43. Greenfield NJ (2004) *Methods Enzymol* 383:282–317.
44. Knight JB, Vishwanath A, Brody JP, Austin RH (1998) *Phys Rev Lett* 80:3863–3866.
45. Hertzog DE, Michalet X, Jager M, Kong XX, Santiago JG, Weiss S, Bakajin O (2004) *Anal Chem* 76:7169–7178.
46. Shastry MG, Luck SD, Roder H (1998) *Biophys J* 74:2714–2721.
47. Kimura T, Uzawa T, Ishimori K, Morishima I, Takahashi S, Konno T, Akiyama S, Fujisawa T (2005) *Proc Natl Acad Sci USA* 102:2748–2753.
48. Chamarthy P, Wereley ST (2004) *2004 Proceedings of the ASME International Mechanical Engineering Congress and Exposition*, 3 Vols (ASME Press, New York), CD-ROM, art no 61902.
49. Kremer W, Schuler B, Harrieder S, Geyer M, Gronwald W, Welker C, Jaenicke R, Kalbitzer HR (2001) *Eur J Biochem* 268:2527–2539.
50. Wilkins DK, Grimshaw SB, Receveur V, Dobson CM, Jones JA, Smith LJ (1999) *Biochemistry* 38:16424–16431.
51. McCarney ER, Werner JH, Bernstein SL, Ruczinski I, Makarov DE, Goodwin PM, Plaxco KW (2005) *J Mol Biol* 352:672–682.
52. Ohnishi S, Lee AL, Edgell MH, Shortle D (2004) *Biochemistry* 43:4064–4070.
53. Zagrovic B, Snow CD, Khaliq S, Shirts MR, Pande VS (2002) *J Mol Biol* 323:153–164.
54. Perl D, Holtermann G, Schmid FX (2001) *Biochemistry* 40:15501–15511.
55. Teilum K, Poulsen FM, Akke M (2006) *Proc Natl Acad Sci USA* 103:6877–6882.
56. Fitzkee NC, Rose GD (2004) *Proc Natl Acad Sci USA* 101:12497–12502.
57. Jha AK, Colubri A, Freed KF, Sosnick TR (2005) *Proc Natl Acad Sci USA* 102:13099–13104.
58. Ding F, Jha RK, Dokholyan NV (2005) *Structure (London)* 13:1047–1054.
59. McCarney ER, Kohn JE, Plaxco KW (2005) *Crit Rev Biochem Mol Biol* 40:181–189.
60. Fitzkee NC, Fleming PJ, Gong HP, Panasik N, Street TO, Rose GD (2005) *Trends Biochem Sci* 30:73–80.
61. Muñoz V, Serrano L (1997) *Biopolymers* 41:495–509.
62. Magg C, Kubelka J, Holtermann G, Haas E, Schmid FX (2006) *J Mol Biol* 360:1067–1080.
63. Pancoska P, Janota V, Keiderling TA (1999) *Anal Biochem* 267:72–83.
64. Sreerama N, Venyaminov SY, Woody RW (1999) *Protein Sci* 8:370–380.
65. Schröder GF, Alexiev U, Grubmüller H (2005) *Biophys J* 89:3757–3770.

Supporting Information, Hoffmann *et al.*

Protein labeling. Labeling was carried out according to the procedures supplied by the manufacturer (Molecular Probes/Invitrogen) under nitrogen atmosphere. First, Alexa Fluor 488 maleimide was reacted with the protein, and singly labeled protein separated from unlabelled and doubly labeled protein by ion exchange chromatography (Mono Q HR 5/5, GE Healthcare). The fractions containing singly labeled Csp*Tm*, as confirmed by electrospray ionization mass spectroscopy, were labeled with Alexa Fluor 594 maleimide after concentration by ultrafiltration. Doubly labeled protein was again separated from singly labeled protein by ion exchange chromatography. The conformational stabilities ΔG_u and unfolding midpoints $c_{1/2}$ of all labeled variants are given in the following table (cooperativity of the transition for all fits: $m = 6.0\,kJ\,mol^{-1}\,M^{-1}$):

	C2C67	**C10C67**	**C21C67**	**C22C67**	**C34C67**
ΔG_u (kJ/mol)	12±1	10±1	14±1	11±1	14±1
$c_{1/2}$ (M)	2.0±0.1	1.7±0.2	2.3±0.1	1.9±0.2	2.4±0.1

Ensemble steady-state polarization measurements of the attached dyes resulted in anisotropies of ~0.1 or less for all samples under unfolding conditions, indicating sufficient rotational averaging during the fluorescence lifetime of the dyes to justify using $\kappa^2 = 2/3$ (1).

Calibration and error analysis of single molecule data. Identified bursts were corrected for background, differences in quantum yields, the different collection efficiencies of the detection channels, cross-talk (acceptor emission detected in the donor channel and donor emission detected in the acceptor channel), and direct excitation of the acceptor with the following matrix approach (2). The relation between the raw photon counts per identified burst $n_{D,0}$ and $n_{A,0,}$ as measured in the two detection channels for acceptor and donor emission, respectively, and the corrected values n'_A and n_D can be expressed by the matrix equation

$$\begin{pmatrix} n_{A,0} \\ n_{D,0} \end{pmatrix} = \begin{pmatrix} a_{11} & a_{12} \\ a_{21} & a_{22} \end{pmatrix} \begin{pmatrix} n'_A \\ n_D \end{pmatrix} + \begin{pmatrix} b_A \\ b_D \end{pmatrix},$$

where the matrix a_{ij} describes the cumulative effect of the differences in quantum yields, the different collection efficiencies of the detection channels, and cross-talk, i.e. acceptor emission detected in the donor channel and donor emission detected in the acceptor channel. b_A and b_D are the background count rates in the acceptor and the donor channel, which can be estimated from a measurement on blank buffer solutions. The elements of matrix a_{ij} were determined for our instrument (except for a scaling factor α) from a measurement of two samples containing protein singly labeled with donor or acceptor dye, respectively, in the micromolar range, with a concentration ratio equal to the ratio of the dyes' extinction coefficients at the excitation wavelength (3) (ensuring that, at identical laser power, the same mean number of excitation events take place per unit time in both samples). By inverting the resulting matrix, the correction matrix $c_{ij} = a_{ij}^{-1}$ is obtained, which transforms the background-corrected raw counts $n_{A,0}$-b_A and $n_{D,0}$-b_D into the corrected values n'_A and n_D. Note that the factor α remains unknown, but cancels if intensity ratios are computed, as in the case of the transfer efficiency. Finally, n'_A has to be corrected for direct excitation of the acceptor according to $n_A = n'_A - (n'_A + n_D)\ \varepsilon_A / (\varepsilon_A + \varepsilon_D)$, where ε_D and ε_A are the extinction coefficients of donor and acceptor, respectively, at the excitation wavelength. These corrections were also taken into account for burst identification. The dependence of the Förster radius R_0 on denaturant concentration was determined by measuring changes in spectral overlap, donor quantum yield, and the refractive index of the solvent, and was found to be dominated by the change in refractive index.

The error ranges given in Fig. 3 are estimates of combined random and systematic errors. Random errors were derived from multiple independent measurements, and range from about $\sigma_{Exp} = 0.02$ at $\langle E \rangle \approx 0.3$ to $\sigma_{Exp} = 0.04$ at $\langle E \rangle \approx 0.8$. The largest sources of systematic error are the changes in extinction coefficients and quantum yields of donor and acceptor upon attachment to different positions in the protein, and especially their change upon collapse. In lack of a method to measure extinction coefficients and quantum yields independently (which contribute differently to the observed value of $\langle E \rangle$), only changes in the emission of samples with identical optical density can be determined. We find standard deviations for this "emissivity" calculated from all singly labeled variants at 8 M GdmCl (normalized to a maximum of 1) of 0.04 and 0.09 for donor and acceptor, respectively, and we assume that changes in extinction coefficients and quantum yields contribute equally. Additional changes in extinction coefficients and quantum yields upon chain collapse are even more difficult to assess. We assume for our error estimates that these changes are less than the average measured differences between the emissivities of singly labeled samples at 8 M and 0 M GdmCl, 0.17 and 0.24 for acceptor and donor, respectively. From these assumptions, we obtain estimates for the uncertainties of E and l_p using error propagation.

Subpopulation-selective fluorescence lifetime distribution analysis. Bursts assigned to the unfolded subpopulation were identified in a plot of $\tau_{D,burst}$ (the donor fluorescence lifetime estimated with a maximum likelihood algorithm (4)) versus $\langle E \rangle$ (Fig. 4a). Photons from these bursts were combined to generate time correlated single photon counting (TCSPC) histograms, $\tilde{I}_D(t)$ and $\tilde{I}_A(t)$, for donor and acceptor, respectively. TCSPC histograms $b_D(t)$ and $b_A(t)$ from all photons not in bursts (5) were used to calculate background-corrected histograms $I_D(t)$ and $I_A(t)$ as

$$I_{D,A}(t) = \tilde{I}_{D,A}(t) - b_{D,A}(t)\,(\text{Total subpopulation burst time})/(\text{Total non-burst time}) . \qquad (1)$$

The resulting decays were fit globally with the coupled equations

$$\begin{aligned} I_D(t) &= IRF_D * h_D\left(t - t_{0,D}\right) \\ I_A(t) &= IRF_A * h_A\left(t - t_{0,A}\right), \end{aligned} \qquad (2)$$

where

$$h_D(t) = a_D \int_0^\infty P(r) e^{-k(r)t} dr \quad \text{and} \qquad (3)$$

$$h_A(t) = a_A \int_0^\infty P(r) \tfrac{k(r)-k_D}{k(r)-k_A} \left(e^{-k_A t} - e^{-k(r)t}\right) dr + \alpha\, h_D(t) + \tfrac{\varepsilon_A}{\varepsilon_A+\varepsilon_D} I_{tot}\, k_A\, e^{-k_A t} \qquad (4)$$

are convolved with the instrument response functions $IRF_{D,A}$ of the donor and acceptor detection channels, respectively. $t_{0,D}$ and $t_{0,A}$ denote the time origins of the decays, and $a_{D,A}$ their amplitudes. The integrands in Eqs. (3) and (4) are the solutions of the rate equations describing donor and acceptor decay including Förster transfer with the chromophores at distance *r*, weighted by the distance distribution $P(r)$ for a Gaussian chain (Eq. 2c of the main text). Distance fluctuations for long polypeptides are expected to be slow relative to the fluorescence lifetime of donor and acceptor (6); we thus assume the inter-dye distance *r* to be constant during the donor fluorescence life time (≤ 4 ns). k_D is the intrinsic decay rate of the donor (without energy transfer), and $k(r) = k_D\left(1 + \left(R_0 / r\right)^6\right)$ is the rate of transfer; k_A is the decay rate of the acceptor. The second term on the right hand side of Eq. (4) corrects for the fraction $\alpha = 0.08$ of donor photons detected in the acceptor channel (cross-talk); the relative amount of acceptor photons observed in the donor channel is negligible. The last term in Eq. (4) accounts for direct excitation of the acceptor; I_{tot} is the total integrated intensity of $I_D(t)$ and $I_A(t)$. Eqs. (2) were fit to the background-corrected TCSPC histograms with $t_{0,D}$, $t_{0,A}$, a_D, a_A, k_A, and $\langle r^2 \rangle$ as free parameters. All remaining parameters were determined independently, and a GdmCl concentration-dependent Förster radius R_0 was used as described above.

k_D was obtained from single exponential fits to background-corrected TCSPC histograms of donor photons in bursts with transfer efficiencies less then 0.2, corresponding to molecules lacking an active acceptor chromophore. The resulting values of k_D increase with denaturant concentration. As the population of the native molecules at low GdmCl concentrations hampers the direct measurement of k_D for the unfolded subpopulation, we estimated k_D by linear extrapolation of the data at denaturant concentrations greater than 3M. In our range of GdmCl concentrations, the resulting k_D varies over a range of 0.27 to 0.33 s^{-1}. Error bars in Fig. 4 were obtained by taking into account both the maximum plausible range of k_D and the uncertainty in R_0. Remaining non-systematic deviations of the TCSPC fits close to t_0 may be due to uncertainties in the background subtraction caused by the count rate-dependence of the detector response functions.

Synchrotron radiation circular dichroism setup. SRCD measurements were implemented essentially as described previously (7). Undulator beam line U125/2-10m NIM at BESSY II (8) was coupled to the sample chamber via a LiF window (Korth Kristalle GmbH, Altenholz, Germany) separating the ultra high vacuum of the beam line from the experimental chamber under atmospheric pressure. As the pressure difference causes strain birefringence in the LiF window, a MgF_2 Rochon polarizer (B. Halle Nachfl. GmbH, Berlin, Germany) follows in the optical path to ensure linear polarization. A photoelastic modulator (Hinds Instruments, Hillsboro, USA; model I/CF50) is used to convert linearly polarized into circularly polarized light. A Suprasil lens (B. Halle Nachfl. GmbH, Berlin, Germany) with a focal length of 10 mm (at $\lambda = 200$ nm) focuses the beam to a spot size of 60 μm and 25 μm (full width at half maximum) parallel and perpendicular to the direction of sample flow, respectively. Transmitted light is detected with a low noise, solar-blind channel photomultiplier (Perkin Elmer, model CPM 1321). The photon flux at the sample is about $5 \cdot 10^{10}$ photons/s at a bandwidth of 0.3 nm. The absolute CD sensitivity was calibrated with (1S)-(+)-camphor-10-sulfonic acid (9). The accessible wavelength range in Fig. 5e is limited by GdmCl absorption.

References

1. Schuler, B., Lipman, E. A., Steinbach, P. J., Kumke, M. & Eaton, W. A. (2005) *Proc. Natl. Acad. Sci. USA* **102,** 2754-2759.
2. Schuler, B. (2006) in *Protein Folding Protocols*, eds. Bai, Y. & Nussinov, R. (Humana Press, Totowa, New Jersey), Vol. 366.
3. Schuler, B., Lipman, E. A. & Eaton, W. A. (2002) *Nature* **419,** 743-747.
4. Eggeling, C., Berger, S., Brand, L., Fries, J. R., Schaffer, J., Volkmer, A. & Seidel, C. A. (2001) *J. Biotechnol.* **86,** 163-80.
5. Laurence, T. A., Kong, X. X., Jager, M. & Weiss, S. (2005) *Proc. Natl. Acad. Sci. USA* **102,** 17348-17353.
6. Lapidus, L. J., Steinbach, P. J., Eaton, W. A., Szabo, A. & Hofrichter, J. (2002) *J. Phys. Chem. B* **106,** 11628-11640.
7. Sutherland, J. C. (1996) in *Circular Dichroism and the Conformational Analysis of Biomolecules*, ed. Fasman, G. D. (Plenum Press, New York and London), pp. 599-633.
8. Reichardt, G., Bahrdt, J., Schmidt, J. S., Gudat, W., Ehresmann, A., Muller-Albrecht, R., Molter, H., Schmoranzer, H., Martins, M., Schwentner, N. & Sasaki, S. (2001) *Nuclear Instruments & Methods in Physics Research Section a-Accelerators Spectrometers Detectors and Associated Equipment* **467,** 462-465.
9. Chen, G. C. & Yang, J. T. (1977) *Anal. Lett.* **10,** 1195-1207.

2.2 MICROFLUIDIC MIXERS FOR THE INVESTIGATION OF RAPID PROTEIN FOLDING KINETICS USING SYNCHROTRON RADIATION CIRCULAR DICHROISM SPECTROSCOPY

Anal. Chem. **2008,** *80,* 9534 9541

Microfluidic Mixers for the Investigation of Rapid Protein Folding Kinetics Using Synchrotron Radiation Circular Dichroism Spectroscopy

Avinash S. Kane,[†,‡] Armin Hoffmann,[§] Peter Baumgärtel,[‖] Robert Seckler,[‖] Gerd Reichardt,[□] David A. Horsley,[‡] Benjamin Schuler,[*,§] and Olgica Bakajin[*,†,‡]

Chemistry, Materials, Life and Earth Sciences Directorate, Lawrence Livermore National Laboratory, 7000 East Avenue, L-233, Livermore, California 94550, University of California, Davis, Davis, California 95817, Biochemisches Institut, Universität Zürich, Winterthurerstrasse 190, 8057 Zürich, Switzerland, Physikalische Biochemie, Universität Potsdam, 14476 Potsdam-Golm, Germany, and Berliner Elektronenspeicherring-Gesellschaft für Synchrotronstrahlung, 12489 Berlin, Germany

We have developed a microfluidic mixer optimized for rapid measurements of protein folding kinetics using synchrotron radiation circular dichroism (SRCD) spectroscopy. The combination of fabrication in fused silica and synchrotron radiation allows measurements at wavelengths below 220 nm, the typical limit of commercial instrumentation. At these wavelengths, the discrimination between the different types of protein secondary structure increases sharply. The device was optimized for rapid mixing at moderate sample consumption by employing a serpentine channel design, resulting in a dead time of less than 200 μs. Here, we discuss the design and fabrication of the mixer and quantify the mixing efficiency using wide-field and confocal epi-fluorescence microscopy. We demonstrate the performance of the device in SRCD measurements of the folding kinetics of cytochrome c, a small, fast-folding protein. Our results show that the combination of SRCD with microfluidic mixing opens new possibilities for investigating rapid conformational changes in biological macromolecules that have previously been inaccessible.

In studies of protein folding kinetics, the folding or unfolding reaction is usually triggered by rapid changes in temperature,[1] pressure,[2] or chemical denaturant concentration.[3] Rapid dilution of chemical denaturants such as guanidinium hydrochloride (GdmCl) or urea is the most commonly used method of starting the folding reaction. The dead time of commercially available stopped-flow mixers that are used to rapidly dilute the denaturant is limited to 0.25 ms under ideal conditions. Typical dead times in commercial instruments using CD spectroscopy are in the range of several milliseconds. Thanks to their rapid mixing time and low sample consumption, microfluidic mixers are being employed increasingly in the studies of folding kinetics. Diffusive mixers with mixing times of 4 μs and femtomole sample consumption have been used to study protein folding using ensemble Förster resonance energy transfer (FRET) spectroscopy.[4] Microfluidic mixers have also been used with single molecule FRET to measure protein folding kinetics and probe the structure of the unfolded state of a protein under folding conditions.[5] Fourier transform-infrared (FT-IR) spectroscopy has been used to probe the α-helix to β-sheet transition in β-lactoglobulin using a diffusive IR mixer.[6] UV fluorescence from tryptophan residues has been used to study the hydrophobic collapse and early folding steps of proteins using a diffusive mixer with a dead time of 20 μs.[7] Small angle X-ray scattering (SAXS) spectroscopy has also been used with mixers to measure the changes in the radius of gyration of cytochrome c.[8,9]

Circular dichroism (CD) is an absorption spectroscopy technique commonly used to identify the secondary structure content of proteins.[10] Protein secondary structures such as α helices and β sheets can be distinguished by their characteristic CD spectra, making CD a powerful method to monitor conformational transitions in biological macromolecules, including protein folding reactions. In contrast to conventional CD sources, synchrotron radiation is a high flux, broadband source of radiation including the far UV (180−250 nm) with high signal-to-noise ratio, permitting measurements below 220 nm, where differences between the CD spectra of the various secondary structure types are often most

---

[*] Corresponding authors. E-mail Bakajin1@llnl.gov, phone (925) 422-0931, fax (925) 422-2041 (O.B.). E-mail schuler@bioc.uzh.ch, phone +41 44 635 5535, fax +41 44 635 5907 (B.S.).

[†] Lawrence Livermore National Laboratory.

[‡] University of California, Davis.

[§] Universität Zürich.

[‖] Universität Potsdam.

[□] Berliner Elektronenspeicherring-Gesellschaft für Synchrotronstrahlung.

(1) Hagen, S. J.; Eaton, W. A. *J. Mol. Biol.* **2000**, *301*, 1019–1027.

(2) Pryse, K. M.; Bruckman, T. G.; Maxfield, B. W.; Elson, E. L. *Biochemistry* **1992**, *31*, 5127–5136.

(3) Chan, C. K.; Hu, Y.; Takahashi, S.; Rousseau, D. L.; Eaton, W. A.; Hofrichter, J. *Proc. Natl. Acad. Sci. U.S.A.* **1997**, *94*, 1779–1784.

(4) Hertzog, D. E.; Ivorra, B.; Mohammadi, B.; Bakajin, O.; Santiago, J. G. *Anal. Chem.* **2006**, *78*, 4299–4306.

(5) Lipman, E. A.; Schuler, B.; Bakajin, O.; Eaton, W. A. *Science* **2003**, *301*, 1233–1235.

(6) Kauffmann, E.; Darnton, N. C.; Austin, R. H.; Batt, C.; Gerwert, K. *Proc. Natl. Acad. Sci. U.S.A.* **2001**, *98*, 6646–6649.

(7) Lapidus, L. J.; Yao, S. H.; McGarrity, K. S.; Hertzog, D. E.; Tubman, E.; Bakajin, O. *Biophys. J.* **2007**, *93*, 218–224.

(8) Pollack, L.; Tate, M. W.; Darnton, N. C.; Knight, J. B.; Gruner, S. M.; Eaton, W. A.; Austin, R. H. *Proc. Natl. Acad. Sci. U.S.A.* **1999**, *96*, 10115–10117.

(9) Akiyama, S.; Takahashi, S.; Kimura, T.; Ishimori, K.; Morishima, I.; Nishikawa, Y.; Fujisawa, T. *Proc. Natl. Acad. Sci. U.S.A.* **2002**, *99*, 1329–1334.

(10) Fasman, G. D. *Circular Dichroism and the Conformational Analysis of Biomolecules*; Plenum Press: New York, 1996.

10.1021/ac801764r CCC: $40.75

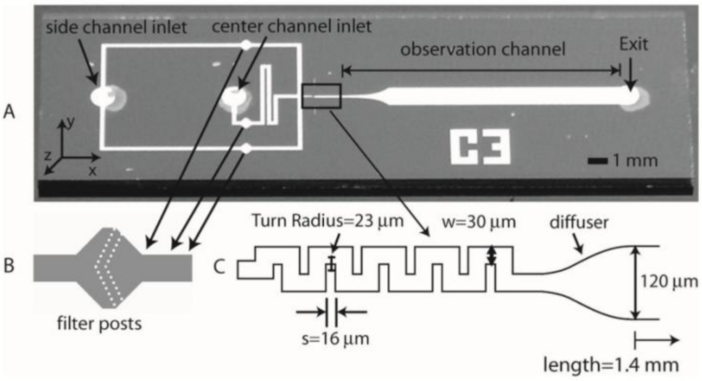

Figure 1. SRCD mixer: (A) photograph of SRCD mixer chip. The aperture is not shown so that details may be easily viewed. (B) Filter posts are designed to minimize clogging of the mixer. (C) Design details of the optimized serpentine mixer showing the channel width, *w*, and turn radius, TR = $^1/_2(w + s)$. The smooth curvature of the diffuser minimizes the creation of any recirculation vortices in the two-section observation channel where kinetics are measured.

pronounced.[11] Akiyama et al.[12] measured kinetics of cytochrome c, a popular model system for rapid protein folding reactions, using a customized conventional CD instrument with a dead time of 0.39 ms and flow rates >20 mL/min.[13] In this study, we describe the development of a new instrument that uses SRCD spectroscopy with a microfluidic mixer, allowing for much lower sample consumption, better dead time, and measurement at 205 nm in the presence of GdmCl. We demonstrate the mixing efficiency of the system using fluorescence microscopy and illustrate its applicability to protein folding in measurements of the microsecond kinetics of secondary structure formation in cytochrome c.

DEVICE DESIGN, MATERIALS, AND FABRICATION

The design of a microfluidic mixer for protein folding is driven by the following figures of merit: dead time, mixing efficiency, and sample consumption. The dead time corresponds to the time difference between the onset of mixing and the first observable point at which experimental data may be measured reliably. The mixing efficiency is a quantitative measure of how well the solutions are mixed. Using SRCD spectroscopy places certain constraints on the design, materials, and fabrication techniques to realize a compatible microfluidic mixer.

Material and Fabrication Constraints. The SRCD mixer needs to be transparent to synchrotron radiation down to 180 nm. Fused silica is a suitable material because it is transparent in the UV and can be micromachined. Since SRCD radiation will be passing directly through the substrate, the etched channel must be sufficiently smooth in order to avoid stray light and to preserve the polarization of the incident light. We determined that deep reactive ion etching (DRIE) provides a suitably smooth channel surface. This technique allows us to create structures with aspect ratios of 3:1 or less.

Mixing Method. A mixer design suitable for our application needs to provide a uniformly mixed solution in the observation region larger than the synchrotron beam. Mixer designs that use turbulence were discarded since this phenomenon occurs only at large Reynolds numbers,[14] implying large channels with high flow rates and excessive sample consumption. Microfluidic devices generally reduce sample consumption but they also exhibit inherently laminar flow, a flow regime which is generally not conducive to fast mixing. Extremely fast mixing times in the laminar flow regime can be achieved using hydrodynamic focusing.[4,15,16] Hydrodynamic focusing has been adapted to wide beams,[5,6] but those designs require high aspect ratio features and multiple etch steps that are difficult to achieve in fused silica. Chaotic advection, where streamlines assume a chaotic trajectory,[17] provides an alternative way to induce mixing. Chaotic advection has been implemented in a variety of microfluidic mixers with periodic perturbations, such as zig-zags,[18] tesla structures,[19] and serpentine shapes.[20−24] We chose to use and optimize the serpentine design because it provides a way to mix solutions in a device whose depth does not change, simplifying the fabrication.

Design and Fabrication of a 2-D Serpentine Mixer for SRCD Spectroscopy. Previously designed serpentine mixers[20−24] are not transparent to synchrotron radiation and do not simultaneously satisfy the requirements of fast dead time (<200 μs) and low sample consumption (<300 μL/min) that we wanted to achieve with our new instrument.

---

(11) Hoffmann, A.; Kane, A.; Nettels, D.; Hertzog, D. E.; Baumgartel, P.; Lengefeld, J.; Reichardt, G.; Horsley, D. A.; Seckler, R.; Bakajin, O.; Schuler, B. *Proc. Natl. Acad. Sci. U.S.A.* **2007**, *104*, 105–110.

(12) Akiyama, S.; Takahashi, S.; Ishimori, K.; Morishima, I. *Nat. Struct. Biol.* **2000**, *7*, 514–520.

(13) Takahashi, S.; Yeh, S. R.; Das, T. K.; Chan, C. K.; Gottfried, D. S.; Rousseau, D. L. *Nat. Struct. Biol.* **1997**, *4*, 44–50.

(14) Brody, J. P.; Yager, P.; Goldstein, R. E.; Austin, R. H. *Biophys. J.* **1996**, *71*, 3430–3441.

(15) Hertzog, D. E.; Michalet, X.; Jager, M.; Kong, X. X.; Santiago, J. G.; Weiss, S.; Bakajin, O. *Anal. Chem.* **2004**, *76*, 7169–7178.

(16) Yao, S.; Bakajin, O. *Anal. Chem.* **2007**, *79*, 5753–5759.

(17) Ottino, J. M. *The Kinematics of Mixing, Stretching, Chaos and Transport* Cambridge University Press: Cambridge, U.K., 1989.

(18) Mengeaud, V.; Josserand, J.; Girault, H. H. *Anal. Chem.* **2002**, *74*, 4279–4286.

(19) Hong, C. C.; Choi, J. W.; Ahn, C. H. *Lab Chip* **2004**, *4*, 109–113.

(20) Liu, R. H.; Stremler, M. A.; Sharp, K. V.; Olsen, M. G.; Santiago, J. G.; Adrian, R. J.; Aref, H.; Beebe, D. J. *J. Microelectromech. Syst.* **2000**, *9*, 190–197.

(21) Kim, D. S.; Lee, S. H.; Kwon, T. H.; Ahn, C. H. *Lab Chip* **2005**, *5*, 739–747.

(22) Vijayendran, R. A.; Motsegood, K. M.; Beebe, D. J.; Leckband, D. E. *Langmuir* **2003**, *19*, 1824–1828.

(23) Chamarthy, P.; Wereley, S. T., ASME/IMECE 2004, Anaheim, CA, November 13−14, 2004, Paper No. 2004-61902.

(24) Chen, H.; Meiners, J. C. *Appl. Phys. Lett.* **2004**, *84*, 2193–2195.

In this study, we chose to optimize the design of a 2-D serpentine mixer. In our device, protein solution with high denaturant concentration is injected into the center channel, while the buffer solution that dilutes the denaturant is injected into the side channels (Figure 1A). The two solutions enter the serpentine channel, in which they are mixed in the laminar flow regime by virtue of diffusion and chaotic advection. Secondary or Dean vortices are created in the cross-sectional plane of the channel as the fluid flows through right-angled bends.[25] These vortices arise when centripetal forces are large relative to the viscous forces on the fluid. In pressure-driven flow, the velocity profile is parabolic and the centripetal force is largest at the center of the channel where the maximum velocity occurs, diminishing to zero at the channel walls. As the centripetal force increases in magnitude, an opposing radial pressure gradient is developed. Fluid near the midplane of the channel is driven toward the outer channel wall where it recirculates to the inner channel wall, resulting in Dean vortices. Fluid flow around sharp bends also leads to the creation of corner vortices in the longitudinal plane. At sufficiently high flow rate, the inertia of the fluid does not allow streamlines to "follow" the sharp bends precisely. This effect leads to the creation of a flow-separation region formed by a stagnation point where the streamline velocity is zero. The flow-separation region is not part of the main flow and consists of streamlines recirculating in a region bounded by the inner channel wall and the main flow. At $Re > 100$, it is the interaction of Dean and corner vortices that stretch, cut, and fold streamlines to produce complete mixing.

After the serpentine channel, the fluid moves through a diffuser (Figure 1C) whose smooth curvature minimizes the creation of any recirculation vortices in the observation channel where kinetics are measured. There are two observation channel sections, which are connected with a logarithmically tapered channel, allowing us to extend the dynamic range of the measurement. Using this design, we can perform both "fast" and "slow" kinetic measurements as the velocity scales with the channel width. The long, wide section also serves to reduce the operating pressure of the device. The variation of the width of the observation channel, although beneficial to increasing the dynamic range of our instrument, also introduced an optical artifact because it changed the amount of collected stray light. Since the stray light affected the SRCD signal, it was necessary to mask off the observation channel with an aperture such that only the CD signal from the inner 100 μm is detected over the entire length of the observation channel (Supporting Information). Filters consisting of arrays of 10 μm × 10 μm posts in each of the side and center channels are designed to minimize clogging of the mixer (Figure 1B).

In this paper, we describe the optimization process of the serpentine mixer geometry in which we considered several design parameters such as the aspect ratio AR (channel depth/width), the number of turns N, and the turn radius $TR = {}^1/_2(w + s)$ (Figure 1C). The parameter w is the channel width and $(w + s)$ is the spacing between turns. The depth of the channel was dictated by the absorption characteristics of the chemical denaturant, GdmCl, which scales linearly with channel depth.[26a] We determined that channel depths from 10−23 μm would provide an SRCD signal that is strong enough, yet not dominated by GdmCl absorption, so we chose the depth of 15 μm for our study. We explored three different aspect ratios values, $AR = 2$, 1, and 0.5 corresponding to widths of 7, 15, and 30 μm. Each design also had $N = 5$ or $N = 10$ for the number of serpentine turns. The turn radius TR was fixed at 23 μm in order to be as short as possible to promote chaotic mixing and to minimize the dead time of the mixer. We characterized the extent of mixing in the different designs first using wide field epi-fluorescence, which gives the top-view distribution of mixing while averaging along the depth of the channel (z-direction). We then use confocal microscopy to determine the degree to which solutions are mixed in the z direction.

Serpentine Channel Design for Optimal Mixing Time and Sample Consumption. The design of the mixer was constrained by the dimensions of the synchrotron beam, device burst pressure, and the signal-to-noise ratio in SRCD measurements. The optimization was a tradeoff between dead time and sample consumption. The flow velocity was ultimately limited by the burst pressure, which itself is limited by the mechanical strength of the 175 μm thick fused silica coverslip. The pressure at which bursting occurred was calculated from flow rates to be approximately 260 psi. At this maximum operating pressure, the serpentine designs with $AR = 2$ and $AR = 1$ resulted in dead times greater than 200 μs. We verified that the design with $AR = 0.5$ and $N = 5$ turns had the best performance by experimentally characterizing the mixing efficiency (see the Results and Discussion). The calculated mixing time, at a point immediately after the diffuser, was $t_{mix} = 140$ μs at a total flow rate of 250 μL/min, corresponding to an operating pressure of 230 psi. At this flow rate, it takes about 8 μs for the fluids to traverse the beam (calculated as the ratio of the synchrotron beam width (20 μm) to the average velocity of 2.36 m/s in the narrow part of the observation channel), indicating that the mixing time ($\gg$8 μs) determines the uncertainty in time for our measurement. A deeper channel with lower impedance would allow for higher flow velocity at the maximum operating pressure, implying a shorter mixing time but at the expense of increased sample consumption and higher GdmCl absorption. A thicker coverslip extends the operating pressure of the mixer but is incompatible with the high numerical aperture, short working distance objectives used in confocal microscopy.

METHODS

Mixer Fabrication Process. Mixers are fabricated in 500 μm thick fused silica wafers (Corning 7980, 0F grade) using a deep reactive ion etching process with nearly vertical sidewalls. In order to bulk micromachine the fused silica substrate, a suitable masking layer must be deposited to accommodate the dry etching process. A 2.0 μm thick undoped polysilicon mask is grown in a low pressure chemical vapor deposition (LPCVD) furnace at a temperature of 625 °C on the fused silica substrate. The process gas is SiH_4 at a flow rate of 250 sccm (standard cubic centimeter per minute), and the chamber pressure is 500 mTorr. A typical deposition rate is 75 Å per min. The first mask containing the mixer pattern is used to perform photolithography on the substrate. The polysilicon layer is etched down to the fused silica

---

(25) Vanka, S. P.; Luo, G.; Winkler, C. M. *AIChE J.* **2004**, *50*, 2359–2368.

(26) (a) Johnson, W. C. in *Circular Dichroism and the Conformational Analysis of Biomolecules*; Fasman, G. D., Ed.; Plenum Press: New York, 1996; pp 635−652. (b) Sutherland, J. C. in *Circular Dichroism and the Conformational Analysis of Biomolecules*; Fasman, G. D., Ed.; Plenum Press: New York, 1996; pp 599−633.

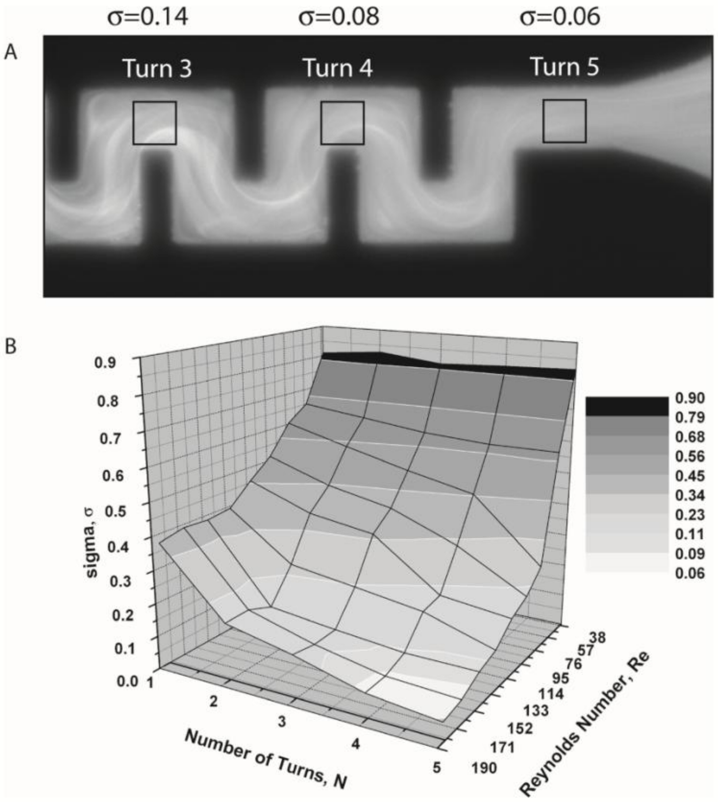

Figure 2. (A) Wide field epi-fluorescence image of a mixer with AR = 0.5 at a total flow rate of 250 μL/min (Re = 185). Pixel data is taken from the 25 μm × 25 μm region of interest (ROI) inside the drawn black square at turns 3, 4, and 5. The calculated σ values are $\sigma = 0.14$ at turn 3, $\sigma = 0.08$ at turn 4, and $\sigma = 0.06$ at turn 5. (B) Surface plot of σ as a function of the number of turns, *N*, and the Reynolds number, Re. This plot allows the designer to determine the number of turns and Reynolds number required for a particular value of σ. σ decreases with both the Reynolds number and number of turns.

using a Surface Technology Systems (STS, Newport, U.K.) deep reactive ion etcher (DRIE). The fused silica substrate is then etched using an STS Advanced Oxide Etcher (AOE) to a depth of 15 μm. The AOE provides an etch selectivity of approximately 17:1 between polysilicon and fused silica. The polysilicon mask is then removed with a XeF_2 etcher. Inlet holes are implemented though the use of micro-sandblasting. Sealing of microfluidic mixers is accomplished by direct fusion wafer bonding to another 175 μm thick fused silica substrate. Both the etched and cover substrates are thoroughly cleaned using piranha solution (sulfuric acid + hydrogen peroxide) and a reverse RCA cleaning procedure. Following the piranha etch, the substrates are cleaned for 20 min in 5:1:1 $H_2O/NH_4OH/H_2O_2$ solution at a temperature of 72 °C. After drying, the substrates are joined together and then annealed at 1100 °C. The aluminum aperture is next implemented by performing photolithography on the bonded wafer stack. A 150 nm thick aluminum aperture with a 100 μm gap has been implemented through a standard liftoff process. The aperture straddles the centerline of the observation channel, leaving a gap of 100 μm to allow for acceptable tolerances during photolithographic alignment to the 120 μm observation channel.

Sample Preparation. Oxidized horse heart cytochrome c (cyt c, from Sigma Aldrich Co., St. Louis, MO) was diluted in unfolding buffer (4 M GdmCl, 100 mM sodium phosphate, pH 7) to a final concentration of 50 g/L. For the reference measurements, this solution was diluted 4-fold either with unfolding or refolding buffer (100 mM sodium phosphate, pH 7). All solutions were filtered (0.22 μm). The reference measurements were performed at the same total flow rate as in the mixing measurements, 250 μL per min. For all measurements, buffer spectra where taken under exactly the same conditions and subtracted from the protein spectra.

Experimental Setup: SRCD. The experimental setup of our synchrotron CD measurements was similar to the one described by Sutherland.[26b] As a synchrotron light source we used the undulator beam line U125/2-10m NIM at BESSY II.[27] A LiF window (Korth Kristalle GmbH, Altenholz, Germany) separates the ultrahigh vacuum of the beam line from the experimental chamber under atmospheric pressure. As the pressure difference introduces stress birefringence in the LiF window, a MgF_2 Rochon polarizer (B. Halle Nachfl. GmbH, Berlin, Germany) followed in the optical path to ensure linear polarization. A photoelastic modulator (PEM) (Hinds Instruments, Hillsboro; model I/CF50) for converting the linearly polarized light into circularly polarized light was used. A Suprasil-lens (B. Halle Nachfl. GmbH, Berlin,

---

(27) Reichardt, G.; Bahrdt, J.; Schmidt, J. S.; Gudat, W.; Ehresmann, A.; Muller-Albrecht, R.; Molter, H.; Schmoranzer, H.; Martins, M.; Schwentner, N.; Sasaki, S. *Nucl. Instrum. Methods Phys. Res., Sect. A* **2001**, *467*, 462–465.

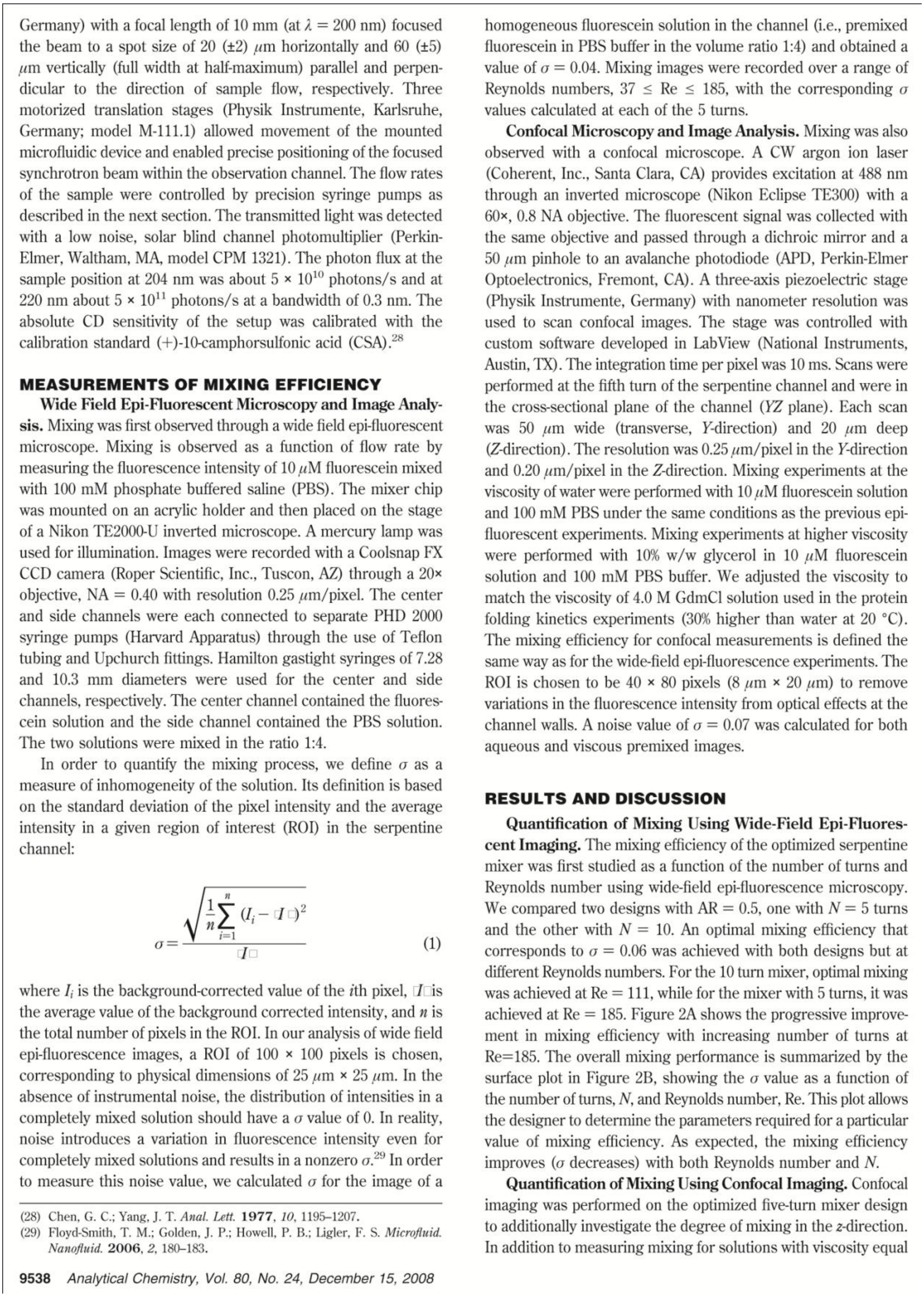

Germany) with a focal length of 10 mm (at $\lambda = 200$ nm) focused the beam to a spot size of 20 (±2) μm horizontally and 60 (±5) μm vertically (full width at half-maximum) parallel and perpendicular to the direction of sample flow, respectively. Three motorized translation stages (Physik Instrumente, Karlsruhe, Germany; model M-111.1) allowed movement of the mounted microfluidic device and enabled precise positioning of the focused synchrotron beam within the observation channel. The flow rates of the sample were controlled by precision syringe pumps as described in the next section. The transmitted light was detected with a low noise, solar blind channel photomultiplier (Perkin-Elmer, Waltham, MA, model CPM 1321). The photon flux at the sample position at 204 nm was about 5×10^{10} photons/s and at 220 nm about 5×10^{11} photons/s at a bandwidth of 0.3 nm. The absolute CD sensitivity of the setup was calibrated with the calibration standard (+)-10-camphorsulfonic acid (CSA).[28]

MEASUREMENTS OF MIXING EFFICIENCY

Wide Field Epi-Fluorescent Microscopy and Image Analysis. Mixing was first observed through a wide field epi-fluorescent microscope. Mixing is observed as a function of flow rate by measuring the fluorescence intensity of 10 μM fluorescein mixed with 100 mM phosphate buffered saline (PBS). The mixer chip was mounted on an acrylic holder and then placed on the stage of a Nikon TE2000-U inverted microscope. A mercury lamp was used for illumination. Images were recorded with a Coolsnap FX CCD camera (Roper Scientific, Inc., Tuscon, AZ) through a 20× objective, NA = 0.40 with resolution 0.25 μm/pixel. The center and side channels were each connected to separate PHD 2000 syringe pumps (Harvard Apparatus) through the use of Teflon tubing and Upchurch fittings. Hamilton gastight syringes of 7.28 and 10.3 mm diameters were used for the center and side channels, respectively. The center channel contained the fluorescein solution and the side channel contained the PBS solution. The two solutions were mixed in the ratio 1:4.

In order to quantify the mixing process, we define σ as a measure of inhomogeneity of the solution. Its definition is based on the standard deviation of the pixel intensity and the average intensity in a given region of interest (ROI) in the serpentine channel:

$$\sigma = \frac{\sqrt{\frac{1}{n}\sum_{i=1}^{n}(I_i - \langle I \rangle)^2}}{\langle I \rangle} \qquad (1)$$

where I_i is the background-corrected value of the ith pixel, $\langle I \rangle$ is the average value of the background corrected intensity, and n is the total number of pixels in the ROI. In our analysis of wide field epi-fluorescence images, a ROI of 100 × 100 pixels is chosen, corresponding to physical dimensions of 25 μm × 25 μm. In the absence of instrumental noise, the distribution of intensities in a completely mixed solution should have a σ value of 0. In reality, noise introduces a variation in fluorescence intensity even for completely mixed solutions and results in a nonzero σ.[29] In order to measure this noise value, we calculated σ for the image of a homogeneous fluorescein solution in the channel (i.e., premixed fluorescein in PBS buffer in the volume ratio 1:4) and obtained a value of $\sigma = 0.04$. Mixing images were recorded over a range of Reynolds numbers, $37 \leq \mathrm{Re} \leq 185$, with the corresponding σ values calculated at each of the 5 turns.

Confocal Microscopy and Image Analysis. Mixing was also observed with a confocal microscope. A CW argon ion laser (Coherent, Inc., Santa Clara, CA) provides excitation at 488 nm through an inverted microscope (Nikon Eclipse TE300) with a 60×, 0.8 NA objective. The fluorescent signal was collected with the same objective and passed through a dichroic mirror and a 50 μm pinhole to an avalanche photodiode (APD, Perkin-Elmer Optoelectronics, Fremont, CA). A three-axis piezoelectric stage (Physik Instrumente, Germany) with nanometer resolution was used to scan confocal images. The stage was controlled with custom software developed in LabView (National Instruments, Austin, TX). The integration time per pixel was 10 ms. Scans were performed at the fifth turn of the serpentine channel and were in the cross-sectional plane of the channel (*YZ* plane). Each scan was 50 μm wide (transverse, *Y*-direction) and 20 μm deep (*Z*-direction). The resolution was 0.25 μm/pixel in the *Y*-direction and 0.20 μm/pixel in the *Z*-direction. Mixing experiments at the viscosity of water were performed with 10 μM fluorescein solution and 100 mM PBS under the same conditions as the previous epi-fluorescent experiments. Mixing experiments at higher viscosity were performed with 10% w/w glycerol in 10 μM fluorescein solution and 100 mM PBS buffer. We adjusted the viscosity to match the viscosity of 4.0 M GdmCl solution used in the protein folding kinetics experiments (30% higher than water at 20 °C). The mixing efficiency for confocal measurements is defined the same way as for the wide-field epi-fluorescence experiments. The ROI is chosen to be 40 × 80 pixels (8 μm × 20 μm) to remove variations in the fluorescence intensity from optical effects at the channel walls. A noise value of $\sigma = 0.07$ was calculated for both aqueous and viscous premixed images.

RESULTS AND DISCUSSION

Quantification of Mixing Using Wide-Field Epi-Fluorescent Imaging. The mixing efficiency of the optimized serpentine mixer was first studied as a function of the number of turns and Reynolds number using wide-field epi-fluorescence microscopy. We compared two designs with AR = 0.5, one with $N = 5$ turns and the other with $N = 10$. An optimal mixing efficiency that corresponds to $\sigma = 0.06$ was achieved with both designs but at different Reynolds numbers. For the 10 turn mixer, optimal mixing was achieved at Re = 111, while for the mixer with 5 turns, it was achieved at Re = 185. Figure 2A shows the progressive improvement in mixing efficiency with increasing number of turns at Re=185. The overall mixing performance is summarized by the surface plot in Figure 2B, showing the σ value as a function of the number of turns, *N*, and Reynolds number, Re. This plot allows the designer to determine the parameters required for a particular value of mixing efficiency. As expected, the mixing efficiency improves (σ decreases) with both Reynolds number and *N*.

Quantification of Mixing Using Confocal Imaging. Confocal imaging was performed on the optimized five-turn mixer design to additionally investigate the degree of mixing in the *z*-direction. In addition to measuring mixing for solutions with viscosity equal

---

(28) Chen, G. C.; Yang, J. T. *Anal. Lett.* **1977**, *10*, 1195–1207.

(29) Floyd-Smith, T. M.; Golden, J. P.; Howell, P. B.; Ligler, F. S. *Microfluid. Nanofluid.* **2006**, *2*, 180–183.

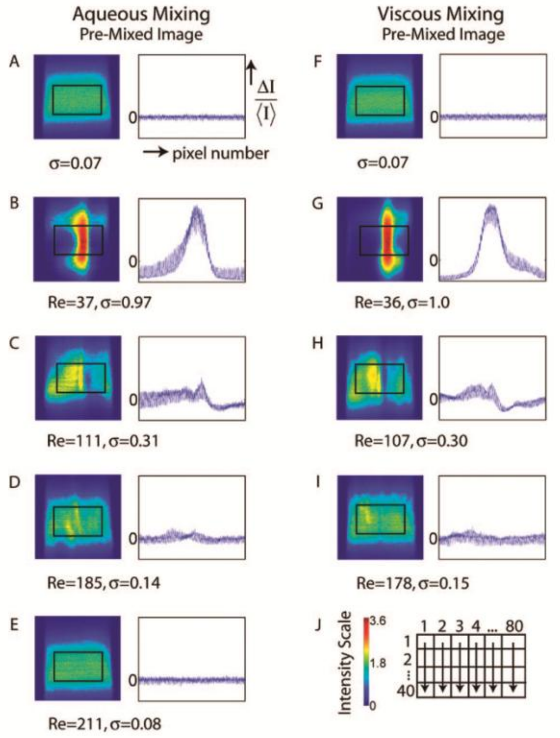

Figure 3. A comparison of confocal images obtained for aqueous and viscous mixing experiments at various Reynolds numbers. The first column corresponds to the aqueous case (A−E) while the second corresponds to the viscous case (F−I). Each panel shows a confocal image with the 40 pixel × 80 pixel (8 μm × 20 μm) ROI indicated by the rectangle. In order to visualize σ and the variation in the pixel intensity across the ROI, the difference between intensity for a given pixel and the average intensity, normalized by the average intensity, is plotted for every pixel. The pixel number value is raster-scanned column by column as illustrated in panel J to cover the entire ROI. The percent difference scale on the y-axis varies from −100% to 300%, and the pixel number on the x-axis ranges from 1 to 3200 for all plots. The premixed images are shown in panels A and F along with the following flow rates (B,G) 50, (C,H) 150, (D,I) 250, and (E) 285 μL/min. The color map (J) indicates fluorescence intensity.

to that of water (aqueous), we also performed measurements on more viscous solutions to mimic the effects of denaturant GdmCl used in protein folding experiments. Figure 3 summarizes the results of confocal imaging at various total flow rates and corresponding Reynolds numbers for both aqueous and viscous cases. The best mixing, which corresponds to $\sigma = 0.08$ (note that $\sigma = 0.07$ is the measured noise level using this imaging method) was achieved at 285 μL/min, Re = 211. The highest mixing efficiency that was measured in the viscous experiment was $\sigma = 0.15$ at a total flow rate of 250 μL/min (Re = 178). Attempts to perform the viscous mixing experiments at higher flow rates caused bursting of the chips due to excessive back-pressure. Figure 4 shows a comparison of measurements by wide-field and confocal epi-fluorescence microscopy. Mixing efficiencies measured over a range of Reynolds number $36 \leq \mathrm{Re} \leq 185$ show that wide field epi-fluorescence results in better σ values. This observation is consistent with the fact that in wide-field measurements, the pixel intensity values are averaged along the depth of the channel (z-direction). However, at flow rates ≥250 μL/min, using the two imaging methods we measure similar differences between the premixed and the mixed σ values indicating that both imaging methods can be used to measure mixing efficiency. Wide-field epi-fluorescence is particularly useful for parametric studies since it is less labor intensive and time-consuming than scanning confocal microscopy. Figure 4 also shows that the 30% increase in viscosity of one of the solutions does not considerably reduce the mixing efficiency. However, increased viscosity does increase the pressure drop in the device and dictates a lower maximum operating flow rate.

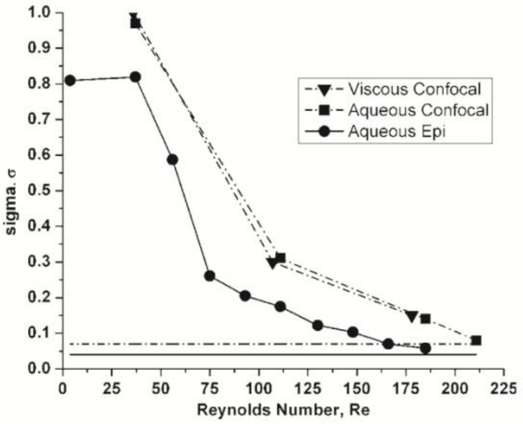

Figure 4. A plot of σ, as a function of Reynolds number, Re, for confocal measurements in the aqueous (■) and viscous case (▼) as well as wide-field epi-fluorescent imaging in the aqueous case (●). Horizontal lines correspond to the values of σ obtained for premixed solutions from confocal (dashed line) and wide field epi-fluorescence (full line) images, showing that the mixer approaches perfect mixing at large Re.

SRCD Spectroscopy of Rapid Protein Folding Kinetics. To demonstrate the performance of the optimized mixer design in monitoring rapid protein folding reactions, we performed SRCD spectroscopy measurements at BESSY II on the small protein cytochrome c. The refolding reaction was initiated by a 4-fold dilution of cyt c in 4 M GdmCl with refolding buffer to a final GdmCl concentration of 0.8 M. The measurement was performed at a total flow rate of 250 μL/min (Re = 178), corresponding to $\sigma = 0.15$ mixing efficiency measured using the confocal setup.

At the first measurement position in the channel, corresponding to $t_{\mathrm{dead}} = 180$ μs after mixing, spectra were taken both for the refolding reaction and under equilibrium start (4 M GdmCl) and end (0.8 M GdmCl) conditions (Figure 5B). The reference spectra at 4 and 0.8 M are typical of an unfolded protein and a folded α-helical protein, respectively.[10] A linear combination of both reference spectra shows that the spectrum acquired 180 μs after the start of refolding corresponds to about 28 ± 6% folded signal. Note that the reference with 4 M GdmCl can be measured down to 205 nm, significantly lower than accessible in conventional stopped-flow CD instrumentation.

We also measured the kinetic progress curve of the refolding reaction at 220 nm along the entire observation channel (up to 30 ms, Figure 5A). The refolding trace was fit with a single exponential with a refolding rate of 190 ± 25 s^{-1}. The accessible time window covers 44 ± 2% of the total signal change. A change

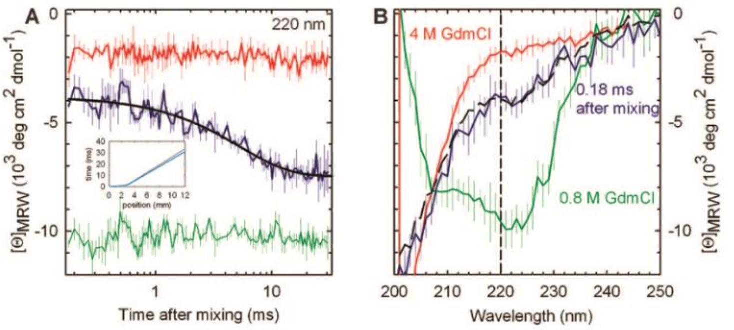

Figure 5. Synchrotron radiation circular dichroism measurements of cyt c in the mixing device. Kinetic measurements under refolding conditions are show in blue, measurements under equilibrium conditions representing the start (4 M GdmCl) and end conditions (0.8 M GdmCl) are shown in red and green, respectively. Error bars show the standard deviation calculated from two kinetic traces (A) or three spectra (B). (A) Refolding kinetics measured at 220 nm and single exponential fit to the data (black). (B) CD spectra measured at 0.18 ms after mixing and linear combination of 28% native and 72% unfolded spectra (black dashed line) The inset in part a shows the time versus position conversion function in the mixer using the average flow rate over the entire channel (gray) and the average flow rate over the calculated spot size (blue), demonstrating that neglecting the shape of the flow profile does not significantly influence the calculation of the time after mixing.

of 22 ± 2% already occurred in the dead time of our instrument, and 33 ± 2% of the signal is still missing after 30 ms. As expected, the reference spectra under equilibrium conditions are invariant along the channel and show the CD signal characteristic of folded and unfolded protein, respectively.

The fast refolding kinetics of cyt c have been studied in great detail,[30−33] which makes cyt c an ideal reference for rapid mixing experiments. The refolding mechanism of cyt c has been shown to exhibit at least three phases: a fast collapse with a rate constant of about 20 ms^{-1} (ref 33) and a change of the CD signal amplitude at 222 nm of about 25%, an increase of the helical secondary structure of about 49% during a second phase with a rate constant of 300 s^{-1}, and a third phase leading to the folded state with a rate constant of about 13 s^{-1}.[12] In the time range accessible with our current instrument design, we can resolve the rate constant of the largest amplitude phase. The good agreement with the rate of the major phase and the amplitudes observed by Akiyama et al.[12] thus provide a stringent test of the capabilities of SRCD in combination with microfluidic devices. The agreement also demonstrates that the effects of flow profile in y and z on the measurement of cytochrome c kinetics at this flow rate are small, as supported by the confocal image from Figure 3I and the very small difference in the time after mixing when averaged over the spotsize vs over the whole channel (inset in Figure 5A). The profile in y and z in the observation region somewhat decreases the time resolution and is captured in the overall uncertainty of our measurement. In summary, the novel combination of SRCD spectroscopy with microfluidic mixing devices opens new opportunities to probe structural changes in biomolecules on previously inaccessible time scales and wavelength ranges. Our device provides an unprecedented dead time for CD experiments in the presence of buffers with high absorption (GdmCl) and clearly demonstrates the potential of the method.

Future improvements in the approach described here are to be expected, especially with the advent of dedicated SRCD beam lines, which are under construction or already in operation at several synchrotrons.[34,35] Higher photon flux will improve the signal-to-noise ratio, accelerate data acquisition, thus reduce sample consumption, enable the use of lower protein concentrations, and possibly allow a further extension of the accessible wavelength range and the use of deeper channels. Of particular importance for the combination with microfluidic mixing is the brilliance of synchrotron sources, allowing the efficient focusing of light into microstructures. Future developments in beam quality and microfabrication are thus expected to enable further improvements in dead time and time resolution. An SRCD beamline optimized specifically for use with microfluidic devices is currently under construction at BESSY. The work presented here presents guidelines for optimizing the mixer geometry for the specific requirements of the synchrotron radiation source and provides an important step toward making kinetic SRCD spectroscopy more broadly available.

ACKNOWLEDGMENT

We thank Shuhuai Yao and David Hertzog for technical assistance and discussions. This work has been supported by the Human Frontier Science Program (A.S.K., O.B., A.H., B.S.), the Schweizerische Nationalfonds (B.S.), and the Deutsche Forschungsgemeinschaft (R.S.). The work of O.B. and A.S.K. was performed at Lawrence Livermore National Laboratory with the support of the LDRD program. Lawrence Livermore National Laboratory is operated by Lawrence Livermore National Security, LLC, for the U.S. Department of Energy, National Nuclear Security Administration under Contract DE-AC52-07NA27344 and partially supported by funding from the Center for Biophotonics, an NSF Science and Technology Center, managed by the University of California, Davis, under

---

(30) Chan, C. K.; Hu, Y.; Takahashi, S.; Rousseau, D. L.; Eaton, W. A.; Hofrichter, J. *Proc. Natl. Acad. Sci. U.S.A.* **1997**, *94*, 1779–1784.

(31) Winkler, J. R. *Curr. Opin. Chem. Biol.* **2004**, *8*, 169–174.

(32) Elove, G. A.; Chaffotte, A. F.; Roder, H.; Goldberg, M. E. *Biochemistry* **1992**, *31*, 6876–6883.

(33) Shastry, M. C.; Roder, H. *Nat. Struct. Biol.* **1998**, *5*, 385–392.

(34) Miles, A. J.; Hoffmann, S. V.; Tao, Y.; Janes, R. W.; Wallace, B. A. *Spectrosc: Int. J.* **2007**, *21*, 245–255.

(35) Miron, S.; Refregiers, M.; Gilles, A. M.; Maurizot, J. C. *Biochim. Biophys. Acta* **2005**, *1724*, 425–431.

Cooperative Agreement No. PHY 0120999. A.S.K. was also supported by the SEGRF Program at LLNL and his trips to Germany were supported by travel awards through U.S. National Science Foundation I2CAM International Materials Institute Award, Grant DMR-0645461. R.S., P.B., and the SRCD station at BESSY are supported by the German Federal Ministry of Education and Research (BMBF), Contract 05 KS4IP1/2.

SUPPORTING INFORMATION AVAILABLE

Additional information as noted in text. This material is available free of charge via the Internet at http://pubs.acs.org.

Received for review August 21, 2008. Accepted October 8, 2008.

AC801764R

Supplementary Information

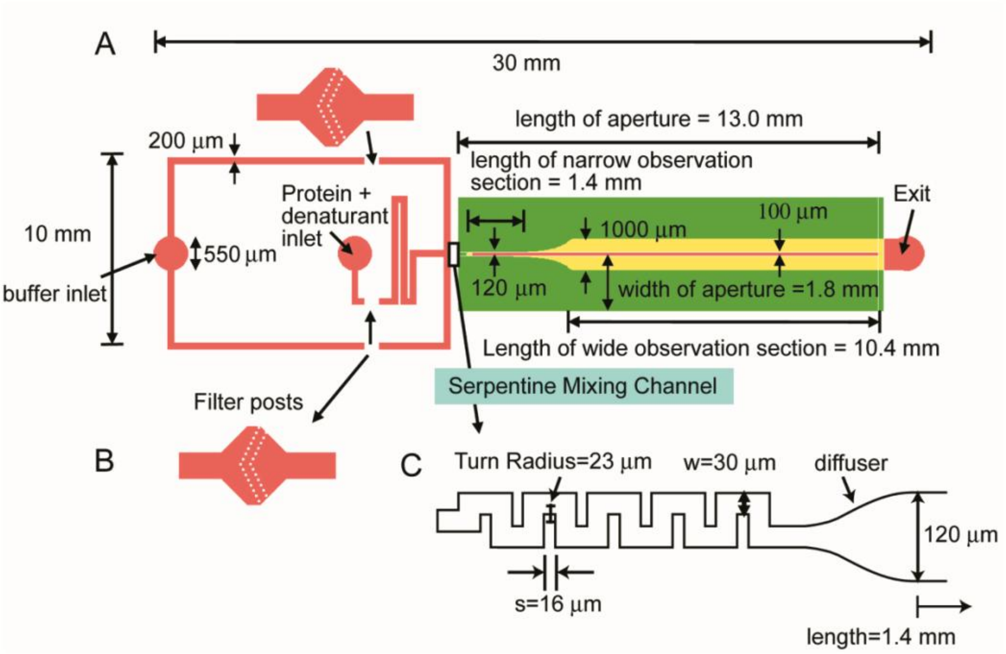

Supplementary Figure 1: SRCD Mixer. (A) Schematic diagram showing design details of the optimized 5-turn mixer. The topside aperture is shown in (green) straddling the two-section observation channel with a gap of 100 µm. The first section of the observation channel is 120 µm wide and is 1.4 mm long. The second section is 1000 µm wide and 10.4 mm long. (B) Filter posts consisting of arrays of 10 µm X 10 µm pillars in each of the buffer and protein channels are designed to minimize clogging of the mixer. (C) Design details of the optimized serpentine channel showing the channel width, w, and turn radius TR=1/2(w+s). The smooth curvature of the diffuser minimizes the creation of any recirculation vortices in the two-section observation channel where kinetics are measured.

Calculation of the time after mixing from the position in the observation channel

The time t after mixing at a point x was calculated as

$$t(x) = \frac{V(x)}{\dot{V}} + t_{dead} \,, \tag{S1}$$

where $V(x)$ is the volume between the starting point of the observation region and $x, \dot{V}$ is the total flow rate, and t_{dead} is the deadtime of the mixer at the chosen flow rate.

We used a laminar flow profile (1) to calculate the position-dependent flow velocity v as

$$v(y,z) = A \times \sum_{i=1,3,5,\ldots}^{\infty} (-1)^{(i-1)/2} \times \left(1 - \frac{\cosh(i\pi z/2a)}{\cosh(i\pi b/2a)}\right) \times \frac{\cos(i\pi y/2a)}{i^3}, \tag{S2}$$

where a denotes the width and b the depth of the channel. y and z originate from the center of the channel cross section and indicate the coordinates in the direction of channel width and depth, respectively. The prefactor A is adjusted to get the known flow rate when v is integrated over the whole channel. Note, however, that in the ratio of the average flowrate in the synchrotron beam v_{beam} and in the whole channel $v_{channel}$, A cancels, and for our geometry we obtain:

$$\frac{v_{beam}}{v_{channel}} = \frac{\int_{y=0}^{30} \int_{z=0}^{7} v(y,z)\, dy\, dz}{\int_{y=0}^{60} \int_{z=0}^{7} v(y,z)\, dy\, dz} = 1.081 \,. \tag{S3}$$

Using this approach, we find a total flow rate of 270 uL/min in the part of the cross section where the beam passes over the channel. Over the range of observation positions, the time versus position conversion function is affected only slightly compared to the average over the entire channel, as shown in the inset to figure 5.

(1) White, F. M. *Viscous Fluid Flow* **1991** (New York: McGraw-Hill)

III. Dynamic Properties of Unfolded Csp

3.1 ULTRAFAST DYNAMICS OF PROTEIN COLLAPSE FROM SINGLE-MOLECULE PHOTON STATISTICS

Ultrafast dynamics of protein collapse from single-molecule photon statistics

Daniel Nettels*, Irina V. Gopich , Armin Hoffmann*, and Benjamin Schuler*[§]

*Biochemisches Institut, Universitat Zurich, Winterthurerstrasse 190, 8057 Zurich, Switzerland; and Laboratory of Chemical Physics, National Institute of Diabetes and Digestive and Kidney Diseases, National Institutes of Health, Bethesda, MD 20892

Communicated by William A. Eaton, National Institutes of Health, Bethesda, MD, December 13, 2006 (received for review November 1, 2006)

We use the statistics of photon emission from single molecules to probe the ultrafast dynamics of an unfolded protein via Forster resonance energy transfer. Global reconfiguration of the chain occurs on a time scale of ≈50 ns and slows down concomitant with chain collapse under folding conditions. These diffusive dynamics provide a missing link between the phenomenological chemical kinetics commonly used in protein folding and a physical description in terms of quantitative free energy surfaces. The experiments demonstrate the potential of single-molecule methods in accessing the biologically important nanosecond time scales even in heterogeneous populations.

correlation | fluorescence | Hanbury Brown and Twiss | photon bunching | protein folding

The discovery of proteins that fold rapidly in the absence of intermediates (1) has substantially advanced our mechanistic understanding of protein folding. The simplicity of their folding behavior allows thermodynamic and kinetic analyses that have led, e.g., to the characterization of transition states for folding (2) and the prediction of folding rates from native structure (3-5). However, because of their limited experimental accessibility, energetic and dynamic differences between the unfolded states of different proteins have usually been ignored. Similarly, the application of rigorous theories of protein folding in terms of statistical mechanics (6-8) has been hampered by our lack of understanding of structure and dynamics in the unfolded state ensemble. The role of unfolded states in determining protein folding mechanisms is thus largely unknown. Although considerable information about the overall dimensions and residual structure of unfolded proteins has been obtained from methods such as small-angle x-ray scattering and NMR, their dynamics in the submicrosecond range have largely eluded experimental determination. The importance of these time scales has become particularly obvious through the identification of proteins that fold in a few microseconds (9). In this regime, the free energy barrier to folding is assumed to be extremely low or even absent, and diffusive chain dynamics become the dominate factor in folding kinetics. Here, we determine these dynamics for an unfolded protein and investigate how they are affected by the collapse of the unfolded chain under near-physiological conditions.

An ideal way to probe the dynamics of the heterogeneous ensemble of unfolded protein conformations is single-molecule spectroscopy (10). The absence of averaging over many molecules allows spontaneous intramolecular distance fluctuations to be observed at equilibrium, without the need for perturbations to synchronize the ensemble. Förster resonance energy transfer (FRET) between two chromophores attached to the polypeptide chain has been suggested as an approach for investigating its submicrosecond dynamics (11, 12), but has eluded experimental implementation. Here, we use this method to directly probe the unfolded state dynamics of the cold shock protein (Csp) from *Thermotoga maritima*, a small, 7.5-kDa β-barrel protein that exhibits two-state thermodynamics and kinetics (13–17). The protein was labeled terminally with a green fluorescent donor and a red fluorescent acceptor dye via amino- and carboxyl-terminal cysteine residues, and freely diffusing molecules were observed in confocal single-molecule experiments (Fig. 1). During the transit of the protein through the observation volume, its donor chromophore is excited by the laser beam. Depending on the distance r to the acceptor, energy transfer results with a rate that determines the relative probabilities of photon emission from donor and acceptor. Correspondingly, distance dynamics within the protein can be measured by fluctuations in the transfer efficiency and thus in the fluorescence emission of the chromophores (Fig. 1).

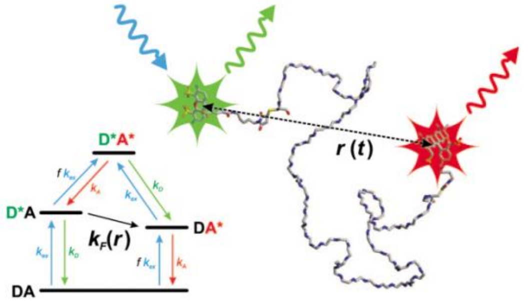

Fig. 1. Principle of measuring distance fluctuations in unfolded proteins with FRET. Energy level diagram (*Left*) of the FRET process between two fluorophores (A and D) attached to the termini of a protein (*Right*) with the relevant transitions between the electronic states. The Forster transfer rate $k_F(r) = k_D(R_0/r)^6$ fluctuates on the same time scale as the distance $r(t)$ between the chain ends and thus allows a direct measurement of chain dynamics. k_{ex} is the excitation rate of the donor D, fk_{ex} is the rate of direct excitation of the acceptor A, and k_D and k_A are the intrinsic decay rates of donor and acceptor, respectively. The possible role of annihilation processes (66 68) in the state D*A* is to the best of our knowledge currently unknown for these chromophores and has thus not been included in our photophysical model. Note, however, that these processes would be expected to occur on a time scale shorter than or similar to the fluorescence lifetime of the dyes and thus would not affect our analysis of the correlation functions on the time scale of protein dynamics.

Results

Measurement of Unfolded State Dynamics. In our experiments, we combine the separation of folded and unfolded subpopulations by single-molecule spectroscopy with the high time resolution available from the photon statistics of a FRET-coupled dye pair. First, a transfer efficiency histogram is created from the photon bursts of individual molecules diffusing through the focus (15,

---

Author contributions: D.N. and B.S. designed research; D.N., I.V.G., A.H., and B.S. performed research; D.N., I.V.G., and B.S. contributed new reagents/analytic tools; D.N. and B.S. analyzed data; and D.N., I.V.G., and B.S. wrote the paper.

The authors declare no conflict of interest.

Abbreviations: FRET, Forster resonance energy transfer; Csp, cold shock protein; GdmCl, guanidinium chloride; APD, avalanche photodiode.

[§]To whom correspondence should be addressed. E-mail: schuler@bioc.unizh.ch.

This article contains supporting information online at www.pnas.org/cgi/content/full/0611093104/DC1.

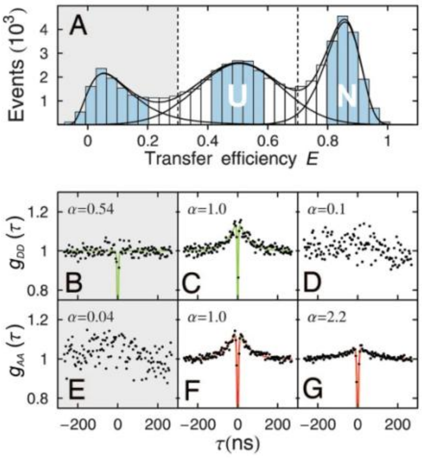

Fig. 2. Intensity autocorrelation functions of the subpopulations identified in single-molecule experiments. (*A*) Transfer efficiency histogram at 1.4 M GdmCl fit with three peaks (black lines) corresponding to the folded or native (N; high E) and unfolded (U; $E \approx 0.5$) subpopulations, and molecules lacking an active acceptor ($E \approx 0$). (*B*–*G*) The ranges of E used for extracting the specific normalized donor and acceptor autocorrelation functions g_{DD} (*B*–*D*) and g_{AA} (*E*–*G*) are shaded in blue. Fits to g_{DD} are shown in green, and fits to g_{AA} are shown in red (for fit functions, see *Materials and Methods*). The normalized signal amplitude α for each correlation function is given relative to the unfolded state ($\alpha = 1$). g_{DD} and g_{AA} were calculated from the corresponding interphoton time distributions by correcting for pile-up and triplet-state components (see *Materials and Methods*).

18). Fig. 2*A* shows an example at a concentration of the denaturant guanidinium chloride (GdmCl) of 1.4 M, where three subpopulations are resolved: folded protein molecules with a transfer efficiency E close to 1, unfolded molecules with $E \approx 0.5$, and molecules lacking an active acceptor chromophore with $E \approx 0$ (15, 19). A second synchronized counting card continuously records the time intervals τ between consecutive detected photons with picosecond time resolution. Dead times of detectors and counting electronics are avoided by using a Hanbury Brown and Twiss detection scheme (20–22). Under our conditions, normalized histograms of the resulting interphoton times are essentially equivalent to the donor or acceptor intensity autocorrelation functions $g_{ii}(\tau)(i = A, D)$ (23), which report directly on the time scales of fluctuations in fluorescence intensity (see *Materials and Methods*). We can obtain $g_{ii}(\tau)$ for each of the subpopulations shown in Fig. 2*A* by using only the interphoton times from molecules assigned to a single subpopulation.

The resulting intensity autocorrelation functions of donor $[g_{DD}(\tau)]$ and acceptor $[g_{AA}(\tau)]$ emission for every subpopulation are shown in Fig. 2 *B–G*. In all cases, $g_{ii}(\tau)$ exhibits a drop in amplitude at $\tau = 0$. This photon antibunching is characteristic of individual quantum systems that cannot emit two photons simultaneously; it decays within a few nanoseconds (22, 24). More interestingly, pronounced photon bunching, i.e., an additional component in $g_{ii}(\tau)$ with positive amplitude, is observed in the 50-ns range. The decay of this bunching signal in the unfolded subpopulation ($E \approx 0.5$) is described by similar time constants for donor and acceptor autocorrelation functions (Fig. 2 *C* and *F*). The behavior of $g_{ii}(\tau)$ agrees with theoretical predictions for a flexible polypeptide chain (11, 12): if, for example, a donor photon is emitted at $\tau = 0$, the chain ends are likely to be far apart at that instant, corresponding to a low rate of energy transfer, k_F. A very short time later, the ends will still be far apart, and the likelihood of emitting another donor photon will still be increased. However, at times much greater than the reconfiguration time τ_r of the chain, the molecule will have lost the "memory" of its initial configuration at $\tau = 0$, and the probability of donor emission will be determined by the average transfer efficiency. In other words, we expect an increased autocorrelation of the emission intensity around $\tau = 0$ that decays approximately on the time scale of chain reconfiguration.[¶]

The acceptor autocorrelation function $g_{AA}(\tau)$ of the native subpopulation also exhibits a small, but significant, relative bunching signal (Fig. 2*G*). This signal may in part be caused by the imperfect separation of subpopulations (Fig. 2*A*), but the slower relaxation compared with the unfolded state could indicate an additional contribution from interactions of the chromophores with the specific environment presented by the native structure. To exclude an influence of native molecules on the determination of unfolded state dynamics, we restrict our measurements and analysis to the donor signal, where only unfolded molecules contribute to bunching (Fig. 2 *B–D*). The optimal signal-to-noise ratio is obtained at a protein concentration of 500 pM, where a separation of subpopulations is no longer possible, but the determination of the correlation times is most accurate. An example for such a measurement is shown in Fig. 3*B*; the pronounced photon bunching yields an intensity autocorrelation time of 44 ± 3 ns. Under identical conditions, this signal is absent in stiff (19) polyproline peptides with the same average transfer efficiency as unfolded Csp (Fig. 2*D*), confirming that photon bunching is indeed caused by chain dynamics in the unfolded protein. The bunching signal is also absent in Csp labeled only with a donor chromophore (data not shown), excluding dye–protein interactions and rotational dynamics of the entire chain as origins of the bunching signal we observe. An additional slower component with a relaxation time of several microseconds was observed in all data sets, as expected from the triplet-state lifetimes of the chromophores (25). Fluorophore reorientation occurs on the time scale of ≈300 ps (19); resulting fluctuations in the energy transfer rate would thus affect the correlation functions only on time scales much shorter than the range relevant for the dynamics investigated here.

Theory and Analysis of Photon Statistics. To analyze our measurements in terms of protein dynamics, we describe the relative motion of the chain ends as a diffusive process on the potential of mean force that corresponds to the end-to-end distance distribution of the unfolded protein. By combining these diffusive chain dynamics with the distance-dependent stochastic photon emission from the coupled dye pair (Fig. 1), the complete photon statistics of the system can be obtained (12). To avoid time-consuming simulations, we use a recently developed theory (26) that allows us to calculate the intensity correlation functions of donor and acceptor emission numerically. Briefly, if we assume for the unfolded protein the end-to-end distance distribution function of a Gaussian chain [which has recently been shown to be a good approximation for Csp (27)], $p_{eq}(r) = 4\pi r^2(2\pi\langle r^2\rangle/3)^{-3/2}\exp(-3r^2/2\langle r^2\rangle)$ (see Fig. 5), protein dynamics can be combined with the photophysics of FRET in the rate matrix:

$$\mathbf{K} = D\partial/\partial r\, p_{eq}(r)\partial/\partial r(p_{eq}(r))^{-1}\mathbf{I} + \mathbf{K}_0(r), \qquad [1]$$

where D is the relative diffusion coefficient of the chain ends, $\mathbf{K}_0(r)$ describes the distance-dependent kinetics of interconversion between the four electronic states illustrated in Fig. 1, and $\mathbf{I}$ is the 4 × 4-identity matrix. The time dependence of all electronic and conformational transitions in the system is then described by the rate equation $d\mathbf{p}/dt = \mathbf{Kp}$, where $\mathbf{p}$ is the vector of the populations of the four electronic states in Fig. 1. By discretizing the diffusion

---

[¶] Because of the nonlinear dependence of the transfer rate k_F on distance, τ_{DD}, τ_{AA}, and τ_r are not strictly identical, but they can be related accurately using our analysis [see *Theory and Analysis of Photon Statistics* and supporting information (SI) *Text*]. In our range of distances and end-to-end diffusion coefficients (Fig. 4), the three time constants differ by <15%.

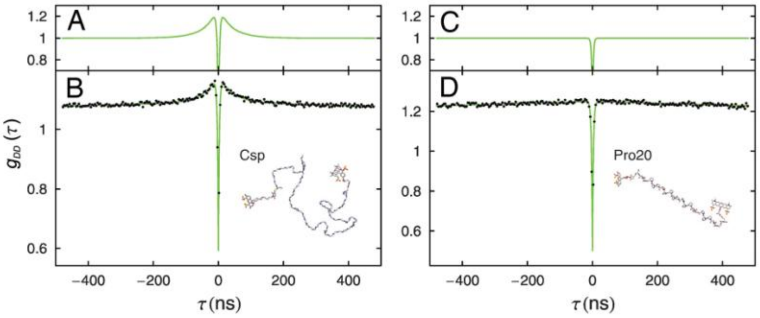

Fig. 3. Calculated (*A* and *C*) and measured (*B* and *D*) donor intensity autocorrelation functions for unfolded Csp (*A* and *B*) and a stiff polyproline peptide (*C* and *D*) at 4 M GdmCl, corroborating that the 44-ns component of g_{DD} is caused by chain dynamics. The curve in *C* was calculated based on the photophysics of the FRET process assuming a fixed distance between the fluorophores, whereas in *A* diffusive end-to-end distance dynamics of a Gaussian chain were included.

operator, the problem is reduced to matrix algebra, and the intensity correlation functions can be calculated to high accuracy with numerical methods (for details, see *Materials and Methods* and *SI Text*). All parameters needed to define the model in terms of our system are known: the photophysical rate constants of the FRET process (Fig. 1) were measured independently, and $p_{eq}(r)$ is defined uniquely by the mean square end-to-end distance $\langle r^2 \rangle$, which can be calculated from the average transfer efficiency of the unfolded subpopulation (15, 27) (see *SI Text*). We can thus determine the only remaining parameter, the effective end-to-end diffusion coefficient D, by adjusting it such that the calculated intensity autocorrelation function fits the experimental result. Finally, the chain reconfiguration time τ_r (the decay time of the end-to-end distance autocorrelation function) for a Gaussian chain is obtained from $\tau_r \simeq \langle r^2 \rangle / 6D$ (see *SI Text*).

In summary, we can thus determine, from the measured intensity correlation function, the dynamics of an unfolded protein in terms of the diffusion coefficient D and the corresponding reconfiguration time τ_r. Examples for calculated intensity correlation functions both with and without chain dynamics are shown in Fig. 3 *A* and *C*, respectively. The excellent agreement between the functional forms of experimental and calculated correlation functions (Fig. 3 *A* and *B*) suggests that our single reaction coordinate is a reasonable approximation for the dynamics of unfolded Csp. It is worth stressing that what we observe here are large-scale chain dynamics along this reaction coordinate, whereas the wide range of subnanosecond dynamics known to occur in polypeptides (28, 29), such as dihedral angle rotations, essentially enter into the diffusion coefficient D (or the energetic roughness of the free energy surface; see *The Free Energy Surface of Collapse and Implications for Protein Folding*).

Effect of Collapse on Unfolded State Dynamics. The unfolded state of Csp has been found to collapse in response to decreasing GdmCl concentrations (15, 17, 27, 30). This collapse precedes the folding reaction in kinetic experiments (17, 30), and single-molecule FRET can be used to quantify the resulting change in chain dimensions under equilibrium conditions by virtue of the separation of folded and unfolded subpopulations (15, 27). Fig. 4*A* shows the corresponding decrease in the rms end-to-end distance $\langle r^2 \rangle^{1/2}$ determined from the mean transfer efficiencies of the unfolded state (27). For an ideal chain, compaction is expected to lead to faster relaxation of intramolecular distances because of the reduced size of the accessible conformational space (Fig. 4*B*). This behavior has indeed been observed for some unstructured peptides (31) (however, also see ref. 52), but what happens in the case of a real protein? To answer this question, we measured the change in the decay time of the donor intensity autocorrelation function τ_{DD} in response to decreasing GdmCl concentrations (Fig. 4*B*). With the above analysis, we find a decrease in the viscosity-corrected diffusion coefficient D_η from $\approx$0.5 nm^2/ns at 8 M GdmCl to $\approx$0.1 nm^2/ns at low GdmCl concentrations [corrected for change in solvent viscosity η_s with increasing denaturant concentration according to $D_\eta = D\eta_s^{-1}$ 1 mPa s(31–35)]. The corresponding chain reconfiguration time τ_r increases from $\approx$20 ns at 8 M GdmCl to $\approx$65 ns under near-native conditions (Fig. 4*B*). In conclusion, we find very fast global chain

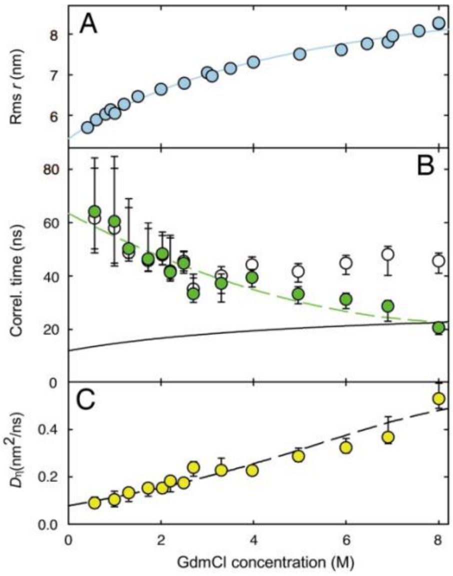

Fig. 4. Denaturant dependence of unfolded state collapse and dynamics. (*A*) rms end-to-end distance r of the unfolded protein as determined from the mean transfer efficiency of the unfolded state in single-molecule fluorescence experiments. The solid line is an empirical fit to the equation rms r = rms r_0 + $Ac/(1 + Bc)$ used to interpolate the values of rms r for further calculations. (*B*) Donor intensity autocorrelation times τ_{DD} (open circles) and viscosity-corrected end-to-end distance autocorrelation times τ_r (green circles) of unfolded molecules determined from measurements as shown in Fig. 3. The dashed green line is an empirical second-order polynomial fit to the distance correlation times. The black line shows the calculated reconfiguration time of an ideal Gaussian chain assuming a constant diffusion coefficient and the rms r values in *A*. (*C*) Effective viscosity-corrected relative diffusion coefficients of the chain ends D_η, illustrating the slowed chain dynamics upon collapse. The dashed line is calculated from the solid and dashed fits in *A* and *B*, respectively, according to $D_\eta = \langle r^2 \rangle / 6\tau_r$. Error bars represent our estimate of the combined experimental errors and the systematic uncertainty in data analysis.

reconfiguration in the unfolded state of Csp, but, concomitant with chain collapse at low denaturant concentrations, we observe a deceleration of these dynamics. This finding is opposite to the behavior expected for an ideal chain with invariant D_η (Fig. 4*B*), suggesting that interactions within the polypeptide chain, or "internal friction" (36), significantly affect unfolded state dynamics upon chain collapse, similar to what has recently been found for unstructured GlySer-repeat peptides (52).

The Free Energy Surface of Collapse and Implications for Protein Folding. With the shape of the end-to-end distance distribution p_{eq} and the effective end-to-end diffusion coefficient D_η as a function of the denaturant concentration, we have obtained the two key parameters for describing the collapse of Csp in terms of a quantitative free energy surface. The change in D_η upon collapse can be expressed in terms of an effective energetic "roughness", i.e., a distribution of small energy barriers caused by intramolecular interactions that slow down diffusion along the reaction coordinate. Possible physical origins of the dependence of D_η on denaturant concentration, as captured by the roughness, are changes in the packing and interaction strength of the polypeptide backbone and side chains in the unfolded state. These interactions may also contribute to the increase in the β-structure content recently observed upon collapse of unfolded Csp (27). Assuming a random amplitude with a Gaussian distribution independent of r, the rms roughness ε is given by $\varepsilon = k_BT\sqrt{ln(D_0/D_\eta)}$ (37, 38), where D_0 is the diffusion coefficient in the absence of intramolecular interactions. For D_0, we choose the viscosity-corrected diffusion coefficient of the unfolded state in 8 M GdmCl. At such high denaturant concentrations, the average chain volume is $\approx$18 times greater than in the folded structure, suggesting complete solvation of the polypeptide chain, and consequently minimal intramolecular interactions. The decrease in D_η we observe upon collapse under native conditions corresponds to an increase in roughness by 1.3 (+0.1/−0.2) k_BT. In Fig. 5, we plot the relative energetic roughness superimposed on the potential of mean force $G(r) = -k_BT\ ln\ p_{eq}(r)$ of unfolded Csp as a function of the denaturant concentration to illustrate the influence of collapse on the energy landscape.

Discussion

The free energy surface in the absence of denaturant (Fig. 5) summarizes the global structure and dynamics of unfolded Csp molecules under folding conditions. The rate of folding is determined both by the effective free energy barrier $G^{\ddagger}$ separating folded and unfolded states, and the "attempt frequency" for crossing the barrier from the unfolded state. In generalized transition state expressions for the folding time τ_f of type $\tau_f = \tau_0 \exp(\ G^{\ddagger}/k_BT)$, the reconfiguration time τ_r of the chain within the unfolded state potential is directly related to the inverse attempt frequency, or the preexponential factor τ_0. In a simplified Kramers description (39–41), where the curvature of the free energy surface and the effective diffusion coefficient are assumed to be similar in the unfolded well and on the top of the barrier, the preexponential factor is given by $\tau_0 \approx 2\pi\tau_r$. In the absence of a barrier, τ_0 remains as an approximation to the "speed limit" (42), i.e., the minimum time scale of folding. With our value of 65 ns for τ_r of unfolded Csp under native conditions, large-scale chain diffusion thus sets a lower limit of $\tau_0 \approx 0.4\ \mu$s to the folding time for a protein the size of Csp[‖], remarkably similar to estimates based on the length scaling of folding rates (9, 43). It remains to be clarified whether the decrease in the

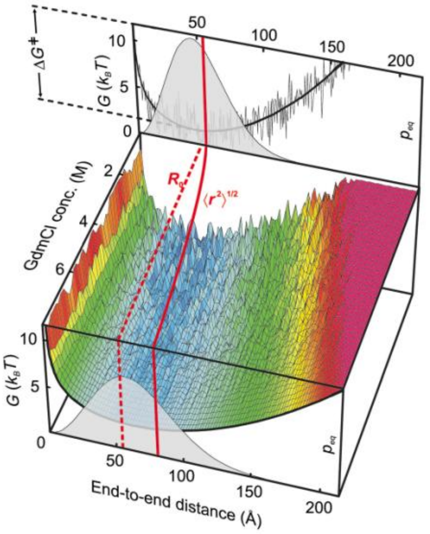

Fig. 5. Schematic free energy surface of Csp collapse. End-to-end distance distribution functions p_{eq} (gray filled functions) and the corresponding potentials of mean force G (thick black lines) of unfolded Csp at 8 M GdmCl (*Lower*) and 0 M GdmCl (*Upper*) are shown, assuming a Gaussian chain model (27). A 3D plot of the potential of mean force in the range of 8 to 0 M GdmCl illustrates the collapse and increasing roughness calculated from the data in Fig. 4. The Forster radius R_0 (dashed red line) and the rms end-to-end distance (rms r, red line) are indicated. The thin line superimposed on the average free energy surface (thick line) in *Upper* (0 M GdmCl) shows one representative distribution of energies compatible with the model for the roughness used (37). Note, however, that the discretization of the end-to-end distance is arbitrary and was introduced only for the purpose of illustration. G is given in units of k_BT and scaled to a maximum value of 10 k_BT relative to the minimum of the average potential at 0 M GdmCl, where 10 k_BT is the height of the free energy barrier for folding.

intramolecular diffusion coefficient we observe upon collapse (Fig. 4) continues toward the transition state region, as suggested from theory (44–47). The rapid folding observed for some proteins [folding times ranging from 0.7 μs for a variant of villin headpiece (48) to several microseconds (9)] suggests that this effect might not be large. This issue could be addressed with a combination of single-molecule experiments of the type described here, and laser temperature-jump experiments, which have been used to determine the molecular time scale of $\approx 2\ \mu$s for the relaxation from the transition state region to the unfolded state in variants of the five-helix bundle protein λ_{6-85} (49, 50).

Note, however, that the preexponential factor for Csp folding as approximated above is virtually invariant compared with the nine orders of magnitude decrease in its folding time τ_f from 8 to 0 M GdmCl (13). The large change in τ_f is thus almost entirely caused by a change in $G^{\ddagger}$, supporting the assumption of a linear dependence of $G^{\ddagger}$ on denaturant concentration frequently made in the analysis of protein folding kinetics (2, 13).

Comparison to Peptide Dynamics. Short unstructured peptides have been investigated intensively as model systems for the chain dynamics of real proteins, using ensemble lifetime fluorometry (51, 52) and quenching methods (32–35, 53, 69, 70). Extrapolating the rates of contact formation observed in quenching experiments of peptides to the length of the Csp chain yields values between $\approx 0.5 \times 10^6\ s^{-1}$ and $5 \times 10^6\ s^{-1}$. For a direct comparison to our results, we estimate the end-to-end contact formation rate for unfolded Csp assuming a Gaussian chain as $k_c = 4\pi Da/(2\pi\langle r^2\rangle/3)^{3/2}$ (54), where a is the contact distance. With our values for D and $\langle r^2\rangle$ (Fig. 4), and

---

[‖] The folding time of 12 ms for labeled Csp*Tm* (15) results in a free energy barrier for folding of 10 kT at 0 M GdmCl (Fig. 5).

$a = 0.4$ nm (34, 52), we calculate contact rates of $(0.8 \pm 0.1) \times 10^6$ s^{-1}, within the extrapolated values from peptide dynamics. Similarly, the end-to-end diffusion coefficients between 0.04 and 0.2 nm^2/ns, obtained for peptides under a variety of denaturant concentrations (34, 52), are close to the values we find for unfolded Csp**. The similarity of the dynamic time scales observed in unfolded Csp and unstructured peptides, and the single exponential decay of our measured intensity correlation functions (Fig. 3*C*), indicate the absence of specific interactions and corresponding large energy barriers (55), even in collapsed unfolded Csp under native conditions.

Rate of Collapse. Finally, we point out that, according to Onsager's regression hypothesis, or, more generally, the fluctuation dissipation theorem, small fluctuations decay on the average in exactly the same way as macroscopic deviations from equilibrium (56). In other words, the time correlation functions of the spontaneous end-to-end distance fluctuations we observe in single molecules (Figs. 2 and 3) decay with the same time constants as the macroscopic signal would in ensemble perturbation experiments, such as rapid changes in solution conditions or laser-induced temperature jumps. The reconfiguration times measured in our experiments are thus equivalent to the collapse time of unfolded Csp. The similarity in time scale to the dynamics of unstructured peptides shows that the collapse of Csp is a purely diffusive, "downhill" process. Conversely, previous observations of denatured state dynamics in the microsecond range (57, 58) thus probably involve the crossing of substantial barriers.

Our measurement of the reconfiguration time of ≈50 ns is in good agreement with the relaxation time expected for an ideal chain (59–61) and theoretical estimates of the collapse times for proteins (43, 62). Additional evidence for the connection between reconfiguration dynamics and the collapse time comes from laser-induced temperature jump experiments on the 40-residue protein BBL; the collapse of its acid-denatured state occurs on a time scale of ≈60 ns (63), remarkably similar to the reconfiguration time of Csp. Future experiments will have to address in more detail issues such as the dependence of collapse times on chain length, temperature, and other parameters (43). For BBL, the enthalpy change involved in collapse evidently is large enough to allow temperature-induced perturbations of chain compactness. For a closely related Csp, laser-induced temperature jump experiments have not resulted in an observable signal (64), raising the possibility that its collapse does not involve a sufficient enthalpy change. Other perturbation methods, such as pressure jump and even the fastest mixing methods, are currently limited to time scales in the tens of microsecond range and above. Spontaneous fluctuations of individual molecules at equilibrium, however, are a universal property of sufficiently thermalized systems. Single-molecule photon statistics thus provide a versatile approach for investigating the dynamics of macromolecules on the biologically important nanosecond time scales.

Materials and Methods

Samples and Instrumentation. Labeled Csp and polyproline peptides were produced as described (15, 19, 27). All experiments were performed in 50 mM sodium phosphate buffer adjusted to pH 7, containing 0.001% Tween 20 to prevent surface adhesion of the polypeptides. High-purity GdmCl solutions (Pierce, Rockford, IL) were used for denaturation experiments. Single-molecule fluorescence was observed by using a PicoQuant MicroTime 200 confocal microscope equipped with a continuous wave solid-state diode-pumped laser (Sapphire 488-200; Coherent, Santa Clara, CA) operating at 488 nm (average radiant power at the sample: 100 μW), a 1.2 NA, ×60 microscope objective (UplanApo ×60/1.20W; Olympus, Melville, NY), and a 100-μm confocal pinhole. A dichroic mirror (585DCXR; Chroma, Rockingham, VT) separated donor and acceptor fluorescence. Subsequently, each fluorescence component was divided randomly by a 50/50 beam splitter between a pair of two avalanche photodiodes (APDs; Optoelectronics SPCM-AQR-15; PerkinElmer, Wellesley, MA). Additional interference filters [HQ525/50 (Chroma) and 525AF45 (Omega Optical, Brattleboro, VT) for the donor APDs, 600HQLP (Chroma) and HQ640/100 (Chroma) for the acceptor APDs] completed spectral separation of the sample fluorescence and served to suppress the mutual detection of APD breakdown flashes in the infrared (65). Each of the two APD pairs was connected to a photon counter: the donor detectors to a PicoHarp 300 and the acceptor detectors to a TimeHarp 200 (both PicoQuant, Berlin, Germany). In their histogram mode, which we used for the measurements at 500 pM Csp and Pro20, the two input channels of these cards operate as start and stop channels. The measured time intervals $\ t$ between start and stop were histogrammed in 256-ps (PicoHarp) or 304-ps (TimeHarp) bins. To avoid cross-talk between the two channels at short time intervals and simplify data analysis, an electronic time delay $\ t_0$ was imposed onto the stop channel (SI Fig. 6). Mean transfer efficiency data for calculating rms end-to-end distances (Fig. 4*A*) were taken from ref. 27. The dependence of the Förster radius R_0 on denaturant concentration was determined by measuring changes in spectral overlap, donor quantum yield, and the refractive index of the solvent and was found to be dominated by the change in refractive index. For more details on data acquisition and analysis and the measurement of subpopulation-specific correlation functions (Fig. 2), see *SI Text*.

Analysis of Interphoton Time Distributions. The histograms shown in Fig. 3 *B* and *C* (integration time 10 h) represent interphoton time distributions $\tilde{\phi}_{ii}(\ t)$ $(i = A, D)$, which are, in the limit of very low mean photon detection rates τ_i^{-1}, proportional to the intensity autocorrelation function $g_{ii}(\tau)$ with the lag time $\tau = \ t - \ t_0$. At higher count rates, shorter interphoton times are detected more frequently than longer ones. To correct for this pile-up effect, we fitted the data to:

$$\tilde{\phi}_{ii}(\ t) = A\,e^{-\ t/\tau_i}\,g_{ii}(\ t \qquad t_0), \qquad [2]$$

where $g_{ii}(\tau)$ was approximated by

$$\begin{aligned} g_{ii}(\tau) &= g_{AB}(\tau)\cdot g_{CD}(\tau)\cdot g_T(\tau) \\ &= (1 \quad c_{AB}\,e^{-|\tau|/\tau_{AB}})(1 + c_{CD}\,e^{-|\tau|/\tau_{ii}})(1 + c_T\,e^{-|\tau|/\tau_T}), \end{aligned} \qquad [3]$$

assuming separation of time scales. A is an overall amplitude, $\exp(-\ t/\tau_i)$ accounts for the pile-up effect (compare Eq. **8**), g_{AB}, g_{CD}, and g_T correspond to the contributions of photon antibunching, chain dynamics, and triplet-state dynamics, respectively, to the overall autocorrelation function $g_{ii}(\tau)$. For each sample, we determined the triplet-state correlation time τ_T from independent conventional fluorescence correlation spectroscopy measurements. Typical values were in the range of 1–4 μs. All remaining parameters of $\tilde{\phi}_{ii}(\ t)$ were determined by least-square fitting to the histogram data. The values obtained for τ_i^{-1} ($\approx 10^5$ s^{-1}) are in good agreement with the mean photon count rates during a photon burst, i.e., during the passage of a molecule through the observation volume. The pile-up-corrected correlation data shown in Fig. 3 were obtained by dividing each histogram value by $A\exp(-\ t/\tau_i)$.

Calculation of Intensity Correlation Functions and Interphoton Time Distributions. The intensity autocorrelation functions of fluorescence from donor and acceptor are defined as:

**The somewhat lower intramolecular diffusion coefficients compared to Csp reported recently for GlySer-repeat peptides (52) may be caused by the strong intramolecular hydrogen bonding that has been suggested to occur within these very compact peptides.

$$g_{ii}(\tau) = \frac{\langle n_i(0) n_i(\tau)\rangle}{\langle n_i\rangle^2}, \quad i = A, D, \qquad [4]$$

where $n_i(\tau)$ is the fluorescence count rate (photon counts per unit time), which fluctuates because of the stochastic processes of photophysics and protein dynamics. The correlation functions are normalized such that $g_{ii}(\tau) \rightarrow 1$ as $\tau \rightarrow \infty$. The distribution of the times between donor or between acceptor photons are denoted by $\phi_{DD}(\tau)$ and $\phi_{AA}(\tau)$ and are normalized according to $\int_0^\infty \phi_{ii}(\tau) d\tau = 1$, $i = A, D$.

Recently, a general theory of these quantities has been developed (26). In this theory, the rate matrix **K** describes all electronic and conformational transitions in the system, and the matrix elements of the off-diagonal matrices $\mathbf{V}_A$ and $\mathbf{V}_D$ specify those transitions that result in the emission of acceptor or donor photons. Let $\mathbf{p}_{ss}$ be the vector of normalized steady-state probabilities obtained by solving $\mathbf{K}\mathbf{p}_{ss} = 0$ $(\mathbf{1}^\top \mathbf{p}_{ss} = \Sigma_i \mathbf{p}_{ss}(i) = 1$, where **1** is the unit vector). The mean time between detected acceptor (donor) photons, τ_i, and the mean fluorescence count rate $\langle n_i\rangle$ $(i = A, D)$ are then given by:

$$\tau_i^{-1} = \langle n_i\rangle = \mathbf{1}^\top \mathbf{V}_i \mathbf{p}_{ss} \qquad [5]$$

(see equation **2.16** of ref. 26). The intensity correlations are:

$$g_{ii}(\tau) = \tau_i^2 \mathbf{1}^\top \mathbf{V}_i \, e^{\mathbf{K}\tau} \, \mathbf{V}_i \mathbf{p}_{ss} \qquad [6]$$

(see equation **2.18** of ref. 26). The interphoton time distributions are:

$$\phi_{ii}(\tau) = \tau_i \mathbf{1}^\top \mathbf{V}_i \, e^{(\mathbf{K}-\mathbf{V}_i)\tau} \, \mathbf{V}_i \mathbf{p}_{ss} \qquad [7]$$

(see equation **2.25** of ref. 26). The interphoton time distributions can be related to the corresponding intensity correlation functions if the mean time between photons τ_i is much longer (in our case on the microsecond time scale) than the relaxation time of the correlation function (in our case on the nanosecond time scale). Then, using the separation of time scales, the interphoton time distribution can be approximated as:

$$\phi_{ii}(\tau) \simeq \tau_i^{-1} g_{ii}(\tau) \, e^{-\tau/\tau_i}. \qquad [8]$$

We confirmed numerically that this approximation holds very well under the conditions of our experiments. Thus, the intensity correlation function can be obtained by multiplying the interphoton time distribution by an exponential (pile-up effect correction; compare Eq. **2**).[††] Details of the theoretical model used for calculating $g_{ii}(\tau)$ and the procedures for comparing measured and calculated correlation functions are given in *SI Text*.

Note Added in Proof. Two papers (71, 72) published since submission of this manuscript are closely related to the present work.

We thank Attila Szabo for guidance on theoretical issues, and William Eaton, Peter Hamm, Christian Hübner, Gerhard Hummer, and Rudolf Rigler for discussion and helpful comments on the manuscript. This work was supported by the Swiss National Science Foundation and the Human Frontier Science Program. I.V.G. was supported by the Intramural Research Program of the National Institutes of Health, National Institute of Diabetes and Digestive and Kidney Diseases.

Note that the experimentally determined ϕ_{ii} of Eq. **2** and the calculated ϕ_{ii} of Eq. **8** are related according to $\tilde{\phi}_{ii}(t) = Ae^{-t_0/\tau_i}\tau_i^{-1}\phi_{ii}(t - t_0)$.

1. Jackson SE (1998) *Fold Des* 3:R81–R91.
2. Fersht AR (1998) *Structure and Mechanism in Protein Science* (Freeman, New York).
3. Muñoz V, Eaton WA (1999) *Proc Natl Acad Sci USA* 96:11311–11316.
4. Galzitskaya OV, Finkelstein AV (1999) *Proc Natl Acad Sci USA* 96:11299–11304.
5. Baker D (2000) *Nature* 405:39–42.
6. Bryngelson JD, Onuchic JN, Socci ND, Wolynes PG (1995) *Proteins* 21:167–195.
7. Dill KA, Chan HS (1997) *Nat Struct Biol* 4:10–19.
8. Dobson CM, Sali A, Karplus M (1998) *Angew Chem Int Ed Engl* 37:868–893.
9. Kubelka J, Hofrichter J, Eaton WA (2004) *Curr Opin Struct Biol* 14:76–88.
10. Talaga DS, Lau WL, Roder H, Tang J, Jia Y, DeGrado WF, Hochstrasser RM (2000) *Proc Natl Acad Sci USA* 97:13021–13026.
11. Haas E, Steinberg IZ (1984) *Biophys J* 46:429–437.
12. Wang ZS, Makarov DE (2003) *J Phys Chem B* 107:5617–5622.
13. Perl D, Welker C, Schindler T, Schröder K, Marahiel MA, Jaenicke R, Schmid FX (1998) *Nat Struct Biol* 5:229–235.
14. Wassenberg D, Welker C, Jaenicke R (1999) *J Mol Biol* 289:187–193.
15. Schuler B, Lipman EA, Eaton WA (2002) *Nature* 419:743–747.
16. Schuler B, Kremer W, Kalbitzer HR, Jaenicke R (2002) *Biochemistry* 41:11670–11680.
17. Lipman EA, Schuler B, Bakajin O, Eaton WA (2003) *Science* 301:1233–1235.
18. Deniz AA, Laurence TA, Dahan M, Chemla DS, Schultz PG, Weiss S (2001) *Annu Rev Phys Chem* 52:233–253.
19. Schuler B, Lipman EA, Steinbach PJ, Kumke M, Eaton WA (2005) *Proc Natl Acad Sci USA* 102:2754–2759.
20. Hanbury Brown R, Twiss RQ (1956) *Nature* 177:27–29.
21. Berglund AJ, Doherty AC, Mabuchi H (2002) *Phys Rev Lett* 89:068101.
22. Mets Ü (2001) in *Fluorescence Correlation Spectroscopy*, eds Elson ES, Rigler R (Springer, Berlin), pp 346–359.
23. Reynaud S (1983) *Ann Phys* 8:315–370.
24. Ehrenberg M, Rigler R (1974) *Chem Phys* 4:390–401.
25. Widengren J, Mets Ü, Rigler R (1995) *J Phys Chem* 99:13368–13379.
26. Gopich IV, Szabo A (2006) *J Chem Phys* 124:154712.
27. Hoffmann A, Kane A, Nettels D, Hertzog D, Baumgärtel P, Lengefeld J, Reichardt G, Horsley DA, Seckler R, Bakajin O, Schuler B (2007) *Proc Natl Acad Sci USA* 104:105–110.
28. Karplus M, McCammon JA (1983) *Annu Rev Biochem* 52:263–300.
29. Palmer AG (2001) *Annu Rev Biophys Biomol Struct* 30:129–155.
30. Magg C, Schmid FX (2004) *J Mol Biol* 335:1309–1323.
31. Buscaglia M, Lapidus LJ, Eaton WA, Hofrichter J (2006) *Biophys J* 91:276–288.
32. Bieri O, Wirz J, Hellrung B, Schutkowski M, Drewello M, Kiefhaber T (1999) *Proc Natl Acad Sci USA* 96:9597–9601.
33. Lapidus LJ, Eaton WA, Hofrichter J (2000) *Proc Natl Acad Sci USA* 97:7220–7225.
34. Lapidus LJ, Steinbach PJ, Eaton WA, Szabo A, Hofrichter J (2002) *J Phys Chem B* 106:11628–11640.
35. Krieger F, Fierz B, Bieri O, Drewello M, Kiefhaber T (2003) *J Mol Biol* 332:265–274.
36. Hagen SJ, Qiu LL, Pabit SA (2005) *J Phys Cond Mat* 17:S1503–S1514.
37. Zwanzig R (1988) *Proc Natl Acad Sci USA* 85:2029–2030.
38. Bryngelson JD, Wolynes PG (1989) *J Phys Chem* 93:6902–6915.
39. Kramers HA (1940) *Physica* 7:284–304.
40. Socci ND, Onuchic JN, Wolynes PG (1996) *J Chem Phys* 104:5860–5868.
41. Klimov DK, Thirumalai D (1997) *Phys Rev Lett* 79:317–320.
42. Hagen SJ, Hofrichter J, Szabo A, Eaton WA (1996) *Proc Natl Acad Sci USA* 93:11615–11617.
43. Li MS, Klimov DK, Thirumalai D (2004) *Polymer* 45:573–579.
44. Camacho CJ, Thirumalai D (1993) *Proc Natl Acad Sci USA* 90:6369–6372.
45. Portman JJ, Takada S, Wolynes PG (2001) *J Chem Phys* 114:5082–5096.
46. Shea JE, Brooks CL (2001) *Annu Rev Phys Chem* 52:499–535.
47. Best RB, Hummer G (2006) *Phys Rev Lett* 96:228104.
48. Kubelka J, Chiu TK, Davies DR, Eaton WA, Hofrichter J (2006) *J Mol Biol* 359:546–553.
49. Yang WY, Gruebele M (2003) *Nature* 423:193–197.
50. Yang WY, Gruebele M (2004) *Biophys J* 87:596–608.
51. Haas E, Katchalskikatzir E, Steinberg IZ (1978) *Biopolymers* 17:11–31.
52. Möglich A, Joder K, Kiefhaber T (2006) *Proc Natl Acad Sci USA* 103:12394–12399.
53. Hudgins RR, Huang F, Gramlich G, Nau WM (2002) *J Am Chem Soc* 124:556–564.
54. Szabo A, Schulten K, Schulten Z (1980) *J Chem Phys* 72:4350–4357.
55. Hagen SJ (2003) *Proteins* 50:1–4.
56. Chandler D (1987) *Introduction to Modern Statistical Mechanics* (Oxford Univ Press, New York).
57. Kuzmenkina EV, Heyes CD, Nienhaus GU (2005) *Proc Natl Acad Sci USA* 102:15471–15476.
58. Chattopadhyay K, Elson EL, Frieden C (2005) *Proc Natl Acad Sci USA* 102:2385–2389.
59. Zimm BH (1956) *J Chem Phys* 24:269–278.
60. de Gennes PG (1985) *J Phys Lett* 46:L639–L642.
61. Doi M, Edwards SF (1988) *The Theory of Polymer Dynamics* (Oxford Univ Press, New York).
62. Thirumalai D (1995) *J Phys I* 5:1457–1467.
63. Sadqi M, Lapidus LJ, Munoz V (2003) *Proc Natl Acad Sci USA* 100:12117–12122.
64. Magg C, Kubelka J, Holtermann G, Haas E, Schmid FX (2006) *J Mol Biol* 360:1067–1080.
65. Kurtsiefer C, Zarda P, Mayer S, Weinfurter H (2001) *J Mod Optic* 48:2039–2047.
66. Bradforth SE, Jinenez R, Vanmourik F, Vangrondelle R, Fleming GR (1995) *J Phys Chem* 99:16179–16191.
67. De Schryver FC, Vosch T, Cotlet M, Van der Auweraer M, Müllen K, Hofkens J (2005) *Acc Chem Res* 38:514–522.
68. Hübner CG, Zumofen G, Renn A, Herrmann A, Müllen K, Basché T (2003) *Phys Rev Lett* 91:093903.
69. Neuweiler M, Doose S, Sauer M (2005) *Proc Natl Acad Sci USA* 102:16650–16655.
70. Neuweiler M, Löllmann M, Doose S, Sauer M (2007) *J Mol Biol* 365:856–869.
71. Merchant KA, Best RB, Louis JM, Gopich IV, Eaton WA (2007) *Proc Natl Acad Sci USA* 104:1528–1533.
72. Xu Y, Purkayastha P, Gai F (2006) *J Am Chem Soc* 128:15836–15842.

SI Text

Subpopulation-Specific Correlation Functions

For resolving folded and unfolded subpopulations (Fig. 2), measurements at 50 pM Csp were performed by using the time-tagged mode of the counters, where the detection time T of the start photon of each start-stop pair was recorded, and stored together with the interphoton time Δt on hard drive if $\Delta t < 1{,}200$ ns. The time resolution of the tags T was 100 ns in the case of the TimeHarp 200 and 4 ps for the PicoHarp 300; the time resolution of the time intervals Δt between start and stop was 256 ps (PicoHarp) or 304 ps (TimeHarp). The acquisition time of the data shown in Fig. 2 was 50 h. The solution was replaced every 10 h to avoid sample deterioration.

For identifying photon bursts from individual molecules, photon counts were combined in one 1-ms bins. While for the PicoHarp 300 binning is possible in parallel to the recording of the interphoton times, the TimeHarp 200 lacks this functionality. For binning the acceptor photons, we thus used a third counting card (National Instruments, NI-6602), which also served as a master clock for synchronizing the three counters. After subtracting the background signal, sequences of adjacent bins with at least 40 donor or acceptor photons and a combined total of at least 80 photons were identified as significant bursts. To account for the different quantum yields of the fluorophores and the different efficiencies of donor and acceptor photon detection, the donor counts per bin were multiplied by $\gamma = 1.25$ before burst identification.

An energy transfer efficiency, $E = \tilde{n}_A / (\tilde{n}_A + \gamma\, \tilde{n}_D)$, was assigned to each identified burst, where $\tilde{n}_D$ and $\tilde{n}_A$ are the background-corrected donor and acceptor photon counts, respectively. Transfer efficiency histograms as shown in Fig. 2A were generated from the E values of all identified bursts. Finally, we reduced the start-stop data by keeping only those interphoton intervals that coincide with bursts within a given range of E in the transfer efficiency histogram. From the Δt values of the respective subsets, the subpopulation-specific correlation functions of Fig. 2 were calculated and corrected for the pile-up effect and triplet-state dynamics. This correction was done by fitting the Δt histograms in the same way as described above and subsequently dividing the data by $A \exp(-\Delta t / \tau_i)\, g_T(\Delta t - \Delta t_0)$. The values of α in Fig. 2 were calculated as $A\,(1 + c_T)$.

Theoretical Model for $g_{ii}(\tau)$

We apply this formalism to a model that includes excited donor and acceptor states coupled with conformational dynamics as proposed by Wang and Makarov (1). The kinetic scheme is given in Fig. 1. The donor is excited with the rate k_{ex}. The acceptor can also be excited with a rate $f\,k_{ex}$, where $f = \varepsilon_A/(\varepsilon_A + \varepsilon_D) \ll 1$, and ε_D and ε_A are the extinction coefficients of donor and acceptor, respectively, at the excitation wavelength. The excited state of the donor decays with the rate k_D, which includes both radiative and nonradiative decay, or its energy can be transferred to the acceptor with the rate $k_F(r)$, which depends on the distance between the fluorophores r as $k_F(r) = k_D\left(R_0/r\right)^6$, where R_0 is the Förster radius. While the acceptor is in the excited state, the donor can be re-excited, which is taken into account by introducing the state D^*A^*. The rate of acceptor decay is k_A. The chain dynamics of the protein are described as diffusion in a potential of mean force. Wang and Makarov (1) calculated intensity correlation functions by performing combined Brownian dynamics and Monte Carlo simulations of this model. Here we obtain these directly by using Eq. **6**.

For this model, the rate matrix $\mathbf{K}$ is

$$\mathbf{K} = D\,\partial/\partial r\; p_{eq}(r)\,\partial/\partial r\left(p_{eq}(r)\right)^{-1}\mathbf{I} + \mathbf{K}_0(r) \qquad \textbf{[9]}$$

where $\mathbf{K}_0(r)$ describes transitions in the four-state system in Fig. 1 and is given by (in the basis (DA, D^*A, D^*A^*, DA^*))

$$\mathbf{K}_0(r) = \begin{pmatrix} -k_{ex}(1+f) & k_D & 0 & k_A \\ k_{ex} & -k_D - fk_{ex} - k_F(r) & k_A & 0 \\ 0 & fk_{ex} & -k_A - k_D & k_{ex} \\ fk_{ex} & k_F(r) & k_D & -k_A - k_{ex} \end{pmatrix}. \qquad \textbf{[10]}$$

The first term in Eq. **9** describes diffusion in the potential of mean force. Here $\mathbf{I}$ is the 4×4 unit matrix and D is the diffusion coefficient. The equilibrium interdye distance distribution $p_{eq}(r)$ is assumed to be that of a Gaussian chain,

$$p_{eq}(r) \;=\; 4\pi r^2\left(\frac{3}{2\pi\left\langle r^2\right\rangle}\right)^{3/2}\exp\left(-\frac{3r^2}{2\left\langle r^2\right\rangle}\right). \qquad \textbf{[11]}$$

The matrix corresponding to the acceptor photons, $\mathbf{V}_A$, is obtained by first setting all the elements of $\mathbf{K}$ to zero except for those off-diagonal ones that correspond to the transitions $D^*A^* \to D^*A$ and $DA^* \to DA$, and then multiplying by the quantum yield Φ_A and the detection efficiency η_A for acceptor photons (2):

$$\mathbf{V_A} = \Phi_A \eta_A \begin{pmatrix} 0 & 0 & 0 & k_A \\ 0 & 0 & k_A & 0 \\ 0 & 0 & 0 & 0 \\ 0 & 0 & 0 & 0 \end{pmatrix}. \qquad \textbf{[12]}$$

The corresponding matrix for the donor photons, $\mathbf{V_D}$, is

$$\mathbf{V_D} = \Phi_D \eta_D \begin{pmatrix} 0 & k_D & 0 & 0 \\ 0 & 0 & 0 & 0 \\ 0 & 0 & 0 & 0 \\ 0 & 0 & k_D & 0 \end{pmatrix}. \qquad \textbf{[13]}$$

where Φ_D and η_D are the quantum yield and the detection efficiency for donor photons, respectively.

To calculate the correlation functions, the diffusion operator is discretized, i.e., replaced by an $N \times N$ tridiagonal matrix $\mathbf{L}$ with the nonzero elements $L_{ii} = -(l_i^+ + l_i^-)$, $L_{i\pm1i} = l_i^\pm$, $L_{11} = -l_1^+$, $L_{NN} = -l_N^-$ where $l_i^\pm = D\, p_{eq}(r_{i\pm1/2})/(s^2 p_{eq}(r_i))$, s is the step size ($s = 3\left\langle r^2 \right\rangle/N$), $r_i = r_c + s(i-1/2)$, and r_c is a cutoff value for r near zero. $N = 100$ proved to be suitable for the calculations. The matrix exponentials in Eqs. [6] are obtained by diagonalizing $\mathbf{K} = \mathbf{T\Lambda T}^{-1}$, where $\mathbf{\Lambda}$ is a diagonal matrix of eigenvalues. The vector of the steady-state probabilities $\mathbf{p}_{ss}$ corresponds to the zeroth eigenvalue of $\mathbf{K}$. Numerical values for the correlation functions were calculated from

$$g_{ii}(\tau) = \tau_i \tau_i \mathbf{1}^\top \mathbf{V}_i\, \mathbf{T} \exp(\mathbf{\Lambda}\tau) \mathbf{T}^{-1} \mathbf{V}_i \mathbf{p}_{ss} \qquad \textbf{[14]}$$

by using Mathematica (Wolfram Research, Champaign, IL). For a single set of parameters, the calculation of the entire time course of the correlation function takes a few seconds on a personal computer.

Comparison of Calculated and Measured Correlation Functions and Determination of *D*

For determining $g_{DD}(\tau)$ according to Eq. **14**, the relevant photophysical parameters were determined independently. k_D was obtained from fluorescence lifetime measurements of donor-only labeled Csp, resulting in values between $k_D = 0.27\,\text{ns}^{-1}$ at 0 M GdmCl and $0.33\,\text{ns}^{-1}$ at 8 M GdmCl. k_A, as derived from lifetime measurements on doubly labeled protein, was $0.24\,\text{ns}^{-1}$, without any significant dependence on denaturant concentration. For determining k_{ex}, we measured $g_{DD}(\tau)$ of a 100 pM sample of donor-only labeled polyproline. In the absence of energy transfer, only antibunching and triplet dynamics are observed. The antibunching correlation time can then be approximated by $\tau_{AB} = (k_D + k_{ex})^{-1}$ (3), which allows us to calculate k_{ex} from the measured values of k_D and τ_{AB} as $k_{ex} = 0.02\,\text{ns}^{-1}$. The fraction of direct acceptor excitation was $f = 0.05$. We used $r_c = 0.1$ nm for the contact distance unless stated otherwise. The only free parameter is the diffusion constant D (note that Φ_D and η_D cancel in Eq. **14**, which was determined by calculating $g_{DD}(\tau)$ in a range up to $\tau = 500$ ns, fitting to it Eq. **3** (with c_T set to zero) to obtain a value for τ_{DD}, and comparing it with τ_{DD} from the experimental data fit to Eq. **2**. Systematic variation of parameters in calculations of the end-to-end distance autocorrelation function show that the reconfiguration time τ_r can be computed very accurately as $\tau_r \simeq \langle r^2 \rangle / 6D$ over the entire range of $\langle r^2 \rangle$ and D relevant for our analysis.

Our theoretical model can obviously be extended to the analysis of the intensity crosscorrelation functions $g_{DA}(\tau)$ and $g_{AD}(\tau)$. In this case, the dynamics of the protein's end-to-end distance result in an antibunching component in the correlation function (i.e. $c_{CD} < 0$ in $g_{CD}(\tau)$, Eq. **3**) instead of the bunching component in $g_{DD}(\tau)$ and $g_{AA}(\tau)$. Although this hampers the separation of photophysics and protein dynamics, the measured relaxation times of this antibunching component are comparable to τ_{DD} and τ_{AA} (data not shown). However, in measurements with a protein concentration of 500 pM, the acceptor contribution to the crosscorrelation may contain signal from folded molecules, as described for the acceptor autocorrelation function (Fig. 2), and the complicated and asymmetric functional form of the crosscorrelation data at shorter times ($|\tau| < 10$ ns) limits an accurate quantitative analysis (see ref. 4 for a more detailed discussion). We thus restrict our study to the autocorrelation data, where photon antibunching and bunching components can be clearly separated. Future studies of the type described here may also help to clarify the role of annihilation processes in Förster transfer.

Determination of Mean Transfer Efficiencies from FRET Histograms

The arrival time of every detected photon was recorded relative to the exciting laser pulse with a time resolution of 38 ps. Protein concentrations of ~20 pM were used. Successive photons detected in either channel separated by <100 µs were combined into one burst. A burst was retained as a significant event if the total number of counts was >50. Identified bursts were corrected for background, differences in quantum yields, the different collection efficiencies of the detection channels, cross-talk (acceptor emission detected in the donor channel and donor emission detected in the acceptor channel), and direct excitation of the acceptor with the following approach (5). The relation between the raw photon counts per identified burst $n_{D,0}$ and $n_{A,0}$, as measured in the two detection channels for acceptor and donor emission, respectively, and the corrected values n'_A and n_D can be expressed by the matrix equation

$$\begin{pmatrix} n_{A,0} \\ n_{D,0} \end{pmatrix} = \begin{pmatrix} a_{11} & a_{12} \\ a_{21} & a_{22} \end{pmatrix} \begin{pmatrix} n'_A \\ n_D \end{pmatrix} + \begin{pmatrix} b_A \\ b_D \end{pmatrix}, \qquad \textbf{[15]}$$

where the matrix a_{ij} describes the cumulative effect of the differences in quantum yields, the different collection efficiencies of the detection channels, and cross-talk. b_A and b_D are the background count rates in the acceptor and the donor channel, which can be estimated from a measurement on blank buffer solutions. The elements of matrix a_{ij} were determined for our instrument (except for a scaling factor α) from a measurement of two samples containing protein singly labeled with donor or acceptor dye, respectively, in the micromolar range, with a concentration ratio equal to the ratio of the dyes' extinction coefficients at the excitation wavelength (6) (ensuring that, at identical laser power, the same mean number of excitation events take place per unit time in both samples). By inverting the resulting matrix, the correction matrix $c_{ij} = a_{ij}^{-1}$ is obtained, which transforms the background-corrected raw counts $n_{A,0}$-b_A and $n_{D,0}$-b_D into the corrected values n'_A and n_D. Note that the factor α remains unknown, but cancels if intensity ratios are computed, as in the case of the transfer efficiency. Finally, n'_A has to be corrected for direct excitation of the acceptor according to $n_A = n'_A - f\ (n'_A + n_D)$. These corrections were also taken into account for burst identification.

Distance Distributions from Mean Transfer Efficiencies

Mean transfer efficiencies $\langle E \rangle$ of the unfolded subpopulation were obtained from transfer efficiency histograms essentially as described (6). To analyze $\langle E \rangle$ in terms of distance distributions in the unfolded state, we use the Gaussian chain model, the simplest realistic model for describing large-scale properties of macromolecules (7), such as highly unfolded peptides and proteins (8-13). $\langle E \rangle$ of the unfolded state at a given GdmCl concentration can be expressed in terms of the radial end-to-end distance probability distribution function of a Gaussian chain $p_{eq}(r)$ (Eq. **11**) and the distance dependence of the transfer efficiency $E(r)$ according to

$$\langle E \rangle = \frac{\int_a^{l_c} E(r)\, p_{eq}(r)\, dr}{\int_a^{l_c} p_{eq}(r)\, dr} \quad \text{with} \quad E(r) = \frac{1}{1 + (r/R_0)^6}\ , \qquad \textbf{[16]}$$

where r is the end-to-end distance, a is the distance of closest approach of the chain ends, l_c is the contour length of the polypeptide, and R_0 is the characteristic Förster radius of the dye pair, 5.4 nm at 0 M GdmCl (6, 14).

References

1. Wang ZS, Makarov DE (2003) *J Phys Chem B* 107: 5617-5622.
2. Gopich I, Szabo A (2005) *J Chem Phys* 122: 014707.
3. Mets Ü (2001) in *Fluorescence Correlation Spectroscopy*, eds Elson ES, Rigler R (Springer, Berlin, Germany), pp 346-359.
4. Berglund AJ, Doherty AC, Mabuchi H (2002) *Phys Rev Lett* 89: 068101.
5. Schuler B (2006) in *Protein Folding Protocols*, eds Bai Y, Nussinov R (Human, Totowa, NJ), vol 366, pp 115-138.
6. Schuler B, Lipman EA, Eaton WA (2002) *Nature* 419: 743-747.
7. Grosberg AY, Khokhlov AR (1994) *Statistical Physics of Macromolecules* (AIP, Woodbury, NY).
8. Tanford C (1968) *Adv Protein Chem* 23: 121-282.
9. Flory PJ (1969) *Statistical Mechanics of Chain Molecules* (Wiley, New York).
10. Millett IS, Doniach S, Plaxco KW (2002) *Adv Protein Chem* 62: 241-262.
11. Kohn JE, Millett IS, Jacob J, Zagrovic B, Dillon TM, Cingel N, Dothager RS, Seifert S, Thiyagarajan P, Sosnick TR, *et al*. (2004) *Proc Natl Acad Sci USA* 101: 12491-12496.
12. Zhou HX (2002) *J Phys Chem B* 106: 5769-5775.
13. Zhou HX (2004) *Biochemistry* 43: 2141-2154.
14. Hoffmann A, Kane A, Nettels D, Hertzog DH, Baumgärtel P, Lengefeld J, Reichardt G, Horsley DA, Seckler R, Bakajin O, Schuler B (2007) *Proc Natl Acad Sci USA* 104: 105-110.

3.2 UNFOLDED PROTEIN AND PEPTIDE DYNAMICS INVESTIGATED WITH SINGLE-MOLECULE FRET AND CORRELATION SPECTROSCOPY FROM PICOSECONDS TO SECONDS

J. Phys. Chem. B 2008, *112,* 6137−6146

Unfolded Protein and Peptide Dynamics Investigated with Single-Molecule FRET and Correlation Spectroscopy from Picoseconds to Seconds†

Daniel Nettels, Armin Hoffmann, and Benjamin Schuler*

Biochemisches Institut, Universität Zürich, Winterthurerstrasse 190, 8057 Zürich, Switzerland

Received: August 30, 2007; In Final Form: February 8, 2008

Single-molecule fluorescence spectroscopy and correlation methods are finding increasing applications in the investigation of biomolecular dynamics, especially together with Förster resonance energy transfer (FRET). Here, we use the combination of start−stop experiments and classical fluorescence correlation spectroscopy (FCS) to obtain complete intensity auto- and cross-correlation functions from picoseconds to seconds for investigating the dynamics of unfolded proteins and peptides. In combination with distance information from single-molecule transfer efficiency histograms, we can analyze the data in terms of a diffusive process on a potential of mean force to obtain intramolecular diffusion coefficients. This allows us to extend our previous analysis of the time scales of chain dynamics into the low nanosecond range for peptides and into the microsecond range for a small cold shock protein (Csp). Dynamics in short unstructured peptides can be detected down to a time scale of about 10 ns, placing a lower limit on the time scales accessible with correlation methods and currently used dye pairs. We find no evidence for microsecond fluctuations in unfolded Csp, suggesting that its global chain dynamics occur predominantly in the tens of nanosecond range. We further investigate the position dependence of these dynamics by placing donor and acceptor dyes at different positions within the chain and find a decrease in the intramolecular diffusion coefficient by a factor of 3 upon moving one of the dyes toward the center of the polypeptide. Obtaining dynamic information on a wide range of time scales from single-molecule photon statistics will be of increasing importance for the study of unfolded proteins and for biomolecules in general.

Introduction

Elucidating the structure and dynamics of proteins in their denatured states, the starting point for the folding reaction, is a key prerequisite for a mechanistic understanding of protein folding. Correspondingly, there have been increasing recent efforts to address this question. Considerable information about the overall dimensions and residual structure of unfolded proteins has been obtained, especially from methods such as small-angle X-ray scattering[1,2] and NMR,[3−6] and a large number of studies have investigated the dynamics of unstructured peptides as models for segments of unfolded proteins.[7−10] A limitation of these methods is the averaging over a large ensemble of molecules, which complicates the analysis of distances and dynamics in heterogeneous systems, such as proteins under conditions where both unfolded and folded molecules are populated at the same time. Recently, single-molecule spectroscopy has emerged as a complementary method[11−15] that allows the separation of subpopulations in heterogeneous mixtures. In combination with Förster resonance energy transfer (FRET), it enables the measurement of intramolecular distances,[16,17] distance distributions,[17−19] and conformational dynamics down to the nanosecond time scale,[19,20] even for individual subpopulations of molecules.[21] The absence of averaging over many molecules allows spontaneous intramolecular distance fluctuations to be observed at equilibrium, without the need for perturbations to synchronize the ensemble. For this approach, the protein or peptide is labeled with fluorescent donor and acceptor dyes via amino groups or cysteine residues at specific positions of the chain. In the simplest type of experiment, freely diffusing molecules are observed during their transit through a confocal observation volume, where the donor chromophore is excited by the laser beam. Depending on the distance r to the acceptor, energy transfer results, with a rate that determines the relative probabilities of photon emission from donor and acceptor. Correspondingly, both distances and distance dynamics within the protein can be measured from the detected donor and acceptor photons via the transfer efficiency and its fluctuations. The Förster radii of currently available dye pairs suitable for single-molecule experiments in the range of about 5 nm allow measurements on relatively large distances, making this approach highly complementary to NMR, from which, typically, distance information and dynamics on shorter length scales have become available.

Here, we extend our analysis of conformational dynamics from single-molecule FRET experiments to the entire range of time scales available from confocal experiments on freely diffusing molecules. By combining conventional fluorescence correlation spectroscopy (FCS) with start−stop experiments, we obtain correlation data from picoseconds to seconds. We use this approach to identify the time scales on which conformational dynamics occur in the unfolded state of the cold shock protein (Csp) from *Thermotoga maritima*, a small (7.5 kDa) β-barrel protein that exhibits two-state thermodynamics and kinetics,[22−26] and to investigate the dependence of chain dynamics on the position of the chromophores within the polypeptide. Moreover, we test the limits of the method for detecting dynamics in the

---

† Part of the "Attila Szabo Festschrift".

* To whom correspondence should be addressed. E-mail: schuler@bioc.uzh.ch.

10.1021/jp076971j CCC: $40.75

short distance regime with unstructured and stiff peptides and compare them to calculated correlation functions using a model that describes the distance dynamics as a diffusive process on a free-energy surface.

Materials and Methods

Samples. Labeled Csp and polyproline peptides were prepared as described previously.[17,18,24] The unstructured peptide with sequence G(AGQ)$_6$AGC was purchased from GL Biochem (Shanghai, China) and labeled analogous to the polyproline peptides by reacting it sequentially via its amino and sulfhydryl groups, respectively, with Alexa 488 succinimidyl ester and Alexa 594 maleimide (Molecular Probes/Invitrogen, Eugene, Oregon), followed by size-exclusion chromatography (Superdex Peptide HR 10/30, Amersham GE Biosciences, Piscataway, NJ) to separate the product from unreacted dye. All measurements were performed in 50 mM sodium phosphate buffer adjusted to pH 7, containing 0.001% Tween 20 to prevent surface adhesion of the polypeptides. High-purity GdmCl solutions (Pierce, Rockford, IL) were used for denaturation experiments. Transfer efficiency histograms were recorded at peptide concentrations of 50 pM. Correlation experiments were performed at a 500 pM protein/peptide concentration to optimize signal contrast.

Single-Molecule Instrumentation. Single-molecule fluorescence was observed using a PicoQuant MicroTime 200 confocal microscope equipped with a cw solid-state diode-pumped laser (Coherent Sapphire 488-200) operating at 488 nm (average radiant power at the sample: 150μW), a 1.2 NA, 60× microscope objective (Olympus UplanApo 60×/1.20W), and a 100 μm confocal pinhole. A dichroic mirror (Chroma 585DCXR) separated donor and acceptor fluorescence. For donor−acceptor cross-correlation measurements, the donor and acceptor fluorescence is detected by a pair of two avalanche photodiodes (APDs, Perkin-Elmer Optoelectronics SPCM-AQR-15). For autocorrelation measurements, each fluorescence component was divided further randomly by a 50/50 beam splitter between a pair of APDs. In both configurations, additional interference filters (Chroma HQ525/50 and Omega 525AF45 for the donor APDs, Chroma 600HQLP and HQ640/100 for the acceptor APDs) completed spectral separation of the sample fluorescence and served to suppress the mutual detection of APD breakdown flashes in the infrared.[27] Each of the two APD pairs was connected to a photon counter (two PicoHarp 300, PicoQuant). In their histogram mode, which we used for the measurements at 500 pM Csp, the two input channels of these counters operate as start and stop channels. The measured time intervals between start and stop were histogrammed in 256 ps bins. To avoid cross-talk between the two channels at short time intervals and to simplify data analysis (see below), an electronic time delay $t_0 \approx 500$ ns was imposed onto the stop channel. For conventional FCS measurements, the photon events on the four detectors were recorded by a TimeHarp 200 or a PicoHarp 300 counting card (PicoQuant) equipped with a four channel router. FCS diagrams were recorded by the data acquisition software SymphoTime (PicoQuant) with 2−30 min of integration time.

Processing of the Start−Stop Raw Data. The histograms recorded in start−stop measurements represent unnormalized interphoton time distributions $\tilde{\phi}_{ij}(t)$ (i,j = A,D), which, in the limit of low mean photon rates, can be related to the fluorescence correlation function $g_{ij}(\tau)$ by[21]

$$\tilde{\phi}_{ij}(t) = A\mathrm{e}^{-t/\tau_{ij}} g_{ij}(t - t_0) \qquad (1)$$

This approximation is valid as long as $t \ll \tau_{ij}$, where τ_{ij} denotes the mean interphoton time. When the correlation function $g_{ij}(\tau)$ is symmetric with respect to $\tau = 0$, τ_{ij} can be obtained from the measured histogram (interpolated by the function $\phi_m(t)$) by numerically minimizing the integral

$$\int_0^{t_0} (\phi_m(t)\mathrm{e}^{t/\tau_{ij}} - \phi_m(2t_0 - t)\mathrm{e}^{(2t_0 - t)/\tau_{ij}})^2 \mathrm{d}t$$

Here, the delay t_0 is, to a first approximation, taken from the histogram bin with the minimum number of counts. The resulting τ_{ij} are typically in a range of 10−20 μs, in good agreement with the mean interphoton time during the passage of a labeled polypeptide through the confocal volume. Multiplication of the raw data by $\mathrm{e}^{t/\tau_{ij}}$ then yields the correlation function, except for a scaling factor A that is obtained from a combined global fit to the start−stop data and the FCS data as described in the following section. The cross-correlation $g_{AD}(\tau)$ is, in general, not perfectly symmetric with respect to $\tau = 0$ (see refs 28 and 29). The procedure described above can nevertheless be applied since the asymmetry arising in the systems studied here occurs mainly on the time scales of singlet-state photophysics, that is, in the nanosecond range.

Global Analysis of Start−Stop Data and FCS Data. The start−stop data (corrected according to eq 1) and the FCS data represent the fluorescence correlation functions on different time scales and have only a small overlap in the microsecond range. For combining and interpreting the two data sets, we globally fit them with a model function, $g_{ij}(t - t_0^{(ij)})$, (i,j = A,D), where, in the case of the start−stop data, the function has an additional amplitude A_{ij} as a prefactor. The $g_{ij}(\tau)$ is of the form

$$g_{ij}(\tau) = 1 + \frac{(1 - c_{ab}^{(ij)}\mathrm{e}^{-|\tau|/\tau_{ab(ij)}})(1 + c_{cd}^{(ij)}\mathrm{e}^{-|\tau|/\tau_{cd}})(1 + c_{T}^{(ij)}\mathrm{e}^{-|\tau|/\tau_{T(ij)}})}{n_{ij}\left(1 + \frac{|\tau|}{\tau_D}\right)\left(1 + \frac{|\tau|}{s^2\tau_D}\right)^{1/2}} \qquad (2)$$

where the three terms in the numerator describe photon antibunching (ab), conformational peptide dynamics (cd), and triplet blinking (T). The denominator describes the effect of diffusion of the peptides through the confocal volume,[30] which is assumed to be of Gaussian shape with a ratio of axial over lateral radii of $s = \omega_2/\omega_1$; n_{ij} is the average effective number of peptides in the confocal volume contributing to $g_{ij}(\tau)$, and τ_D is given by $\tau_D = \omega_1^2/4D_t$, where D_t is the translational diffusion coefficient. All parameters in eq 2 lacking the indices ij are assumed to be the same in $g_{DD}(\tau)$, $g_{AA}(\tau)$, and $g_{AD}(\tau)$. These parameters are the common fit parameters of the global analysis of the 3 × 2 data sets presented in Figure 1. For the autocorrelations $g_{ii}(\tau)$, the amplitudes $c_{ab}^{(ii)}$ are set to unity ($c_{ab}^{(ii)} = 1$), that is, the autocorrelation is $g_{ii}(\tau{=}0) = 1$ at time zero, as two coincidently emitted photons must originate from two different fluorophores and are hence uncorrelated. The amplitudes $c_{cd}^{(ij)}$, associated with conformational dynamics, are positive (correlated) in the case of the autocorrelation functions and negative (anticorrelated) in the case of the cross-correlation functions. For the fitting of the cross-correlation in Figure 1, we set $c_T^{(AD)}$ in eq 2 equal to zero since the fluorescence cross-correlation is (to good approximation) not influenced by triplet blinking at low excitation rates (see Results section). Further, we note that, as indicated in the last section, the cross-correlation $g_{AD}(\tau)$ is asymmetric with respect to $\tau = 0$ on the nanosecond time scale relevant for photophysical processes.[28,29,31−33] This

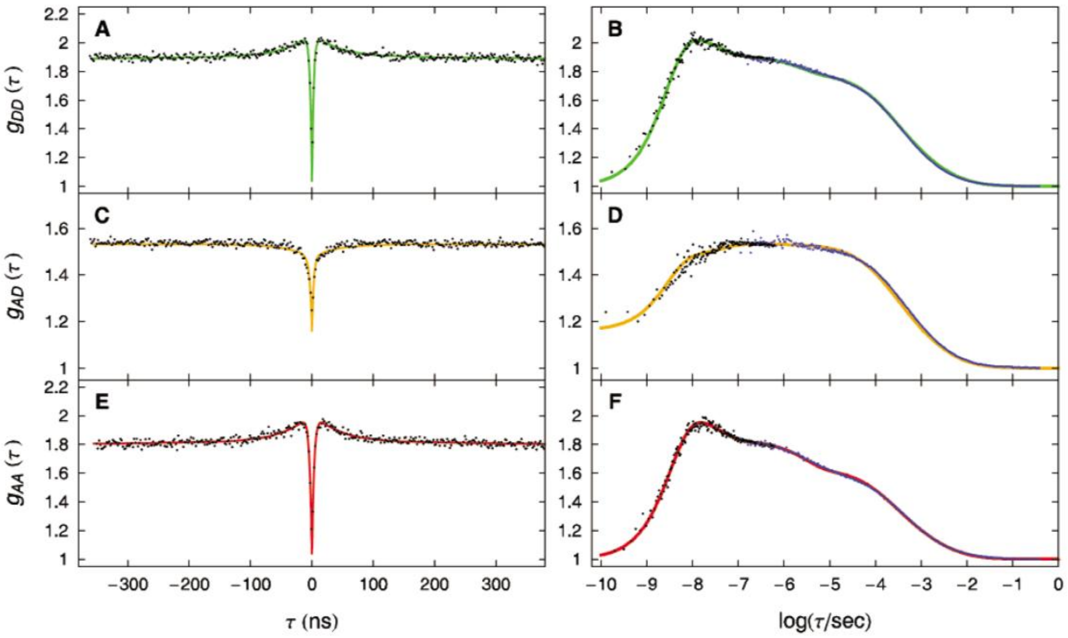

Figure 1. Measured intensity correlation functions for unfolded Csp in 4 M GdmCl. The left panels (A,C,E) show the results from start−stop experiments (black data points), the right panels (B,D,F) the complete correlation functions from picoseconds to 1 s, obtained by combining the start−stop experiments with conventional FCS measurements (blue data points). The result of the global fit is shown as a solid line in green for the donor intensity autocorrelation (A,B), in red for the acceptor intensity autocorrelation (E,F), and in yellow for the cross-correlation (C,D).

asymmetry can be approximated by setting $\tau_{ab}^{AD} = \tau_{ab}^{DD}$ for $\tau > 0$ and $\tau_{ab}^{AD} = \tau_{ab}^{AA}$ for $\tau < 0$, as we did in the fit of $g_{AD}(\tau)$ in Figure 1. Deviations from this approximation may contribute to the slight imperfections in the fit of the cross-correlation functions (Figure 1c,d).

Time-Resolved Anisotropy. Anisotropy decay data were recorded with a custom-built fluorescence lifetime spectrometer. The samples were 1 μM donor-only-labeled Csp under native and unfolding conditions (4 M GdmCl), both with 50 mM sodium phosphate buffer adjusted to pH 7.0 and 0.001% Tween 20. The fluorophores were excited at 470 nm by vertically polarized laser pulses from a LDH 470 diode laser (PicoQuant). A high degree of linear polarization was achieved by using a Glan-Thompson polarizer (extinction ratio > 100 000:1). The laser beam diameter was confined by a 1 mm circular aperture centered at the laser entrance opening of the cuvette holder (TLC 50F, Quantum NorthWest). A narrow cone of fluorescence light, emitted in the perpendicular direction with respect to the laser beam, was collimated by a planoconvex lens ($f = 40$ mm). The opening angle of the cone was defined by a circular 2 mm aperture positioned at a distance of 16 mm from the center of the cuvette. The collimated light passed an analyzing polarizer (of Glan-Thompson type) and a band-pass filter (Chroma, z 582/15) before it was focused onto a microchannel plate PMT (R3809U-50, Hamamatsu). The output pulses of the PMT were preamplified (by a PAM 102-M, PicoQuant) and recorded by a photon counting module (PicoHarp 300, PicoQuant), which measures the times between laser pulses (as provided from the synchronization signal of the laser driver) and the fluorescence photon arrival times at the PMT, from which fluorescence decay histograms with 8 ps bin width were formed. The overall instrument response function (IRF) of the system was measured to have a fwhm of $\Delta_{IRF} = 80$ ps. The repetition period of the laser pulses was 50 ns, whereas the fluorescence lifetime of the donor dye was about 4 ns. Overlap between adjacent excitation−emission cycles is hence negligible.

Two fluorescence decays, $I_V(t)$ and $I_H(t)$, were measured for each sample with the analyzing polarizer in the vertical and in horizontal orientation, respectively. From these decays, the anisotropy as a function of time was determined as[34,35]

$$r(t) = \frac{I_V(t) - GI_H(t)}{I_V(t) + 2GI_H(t)} \tag{3}$$

where G is a correction factor compensating for the slightly different instrumental detection sensitivity for vertically and horizontally polarized photons. We measured $G = 1.02$ for our instrument following standard procedures.[34,35] To the resulting anisotropy decay data, we fit the function[36]

$$r(t) = ((r_0 - r_{¥})e^{-(t-t_0)/\tau_{eff}} + r_{¥})e^{-(t-t_0)/\tau_M} \tag{4}$$

which models the decay as the combined effect of restricted dye rotation near the protein surface (decay constant τ_{eff}) and the rotational motion of the entire molecule, that is, the protein−dye complex (decay constant τ_M). t_0 is the time delay between the registration of the sync signal of the laser driver and the actual fluorophore excitation at the sample site, and r_0 is the fundamental anisotropy of the dye molecule. We measured $r_0 = 0.38$ for Alexa 488 in a matrix of 99% glycerol at −10 °C, where rotational motion is negligible. $r_{¥}$ in eq 4 is the residual anisotropy measured at long times in the absence of rotation of the protein carrying the dye. For the fit, we considered only data with times t that approximately satisfy $t > t_0 + 2\Delta_{IRF}$ and used t_0, $r_{¥}$, τ_{eff}, and τ_M as fit parameters. Using this procedure, we avoid the error-prone deconvolution of the fluorescence decays, $I_V(t)$ and $I_H(t)$, before calculating eq 3.

Results

Analysis of Fluctuations from Picoseconds to Seconds. Distance dynamics within a FRET-labeled protein lead to fluctuations of the transfer rate between the dyes, and thus of the instantaneous photon emission rates of the donor and acceptor, on the time scale of the dynamics. Consequently, chain dynamics can be obtained from the corresponding photon statistics using correlation methods.[30] In practice, classical FCS is typically limited to time scales above about 1 μs because of the dead time of detectors and counting electronics in the >100 ns range. Shorter times become accessible with experiments where two separate detectors are used to record consecutive photons.[28,31,37−43] From such Hanbury Brown and Twiss experiments, interphoton times can be determined with a time resolution limited only by the timing accuracy of the counting electronics (several picoseconds for latest-generation time-correlated single-photon counting (TCSPC) cards[44,45]) and the jitter of the detectors (several hundred picoseconds for the Perkin-Elmer SPCM-AQR avalanche photodiodes[44] typically used in single-molecule experiments). The resulting interphoton time distributions can be related directly to the intensity correlation function.[21,39,46] The combination of these two methods thus enables access to time scales from picoseconds up to the order of the length of the observation time.[44,45] In practice, the photon antibunching signature in the correlation function[38,47] on the time scale of the fluorescence lifetime of the chromophores (typically a few nanoseconds) constitutes the lower end of the time window usable for extracting distance dynamics. (Dynamics on the time scale of the fluorescence lifetime of the dyes can be investigated by analyzing fluorescence lifetime decays with a model including diffusive distance dynamics.[19,48,49]) The upper limit of the exploitable time range is about 1 ms, the maximum observation time for protein molecules freely diffusing through a diffraction-limited confocal volume. (Longer times can be accessed by slowing down diffusion or by observation of immobilized molecules.)

A complete and robust way of analyzing such correlation data is to combine the results from start−stop experiments and FCS and to utilize both donor and acceptor autocorrelation and acceptor−donor cross-correlation measurements. The resulting three complete correlation functions ranging from picoseconds to seconds can then be interpreted in terms of a global fit with a model including all relevant processes[50] (Figure 1). The processes almost universally observed are singlet-state photophysics, resulting in pronounced photon antibunching in the range of a few nanoseconds, triplet-state photophysics in the microsecond range, and fluctuations originating from the diffusion of molecules through the focus in the millisecond range. Rotational dynamics can also contribute to the correlation functions,[38,47] but for the cases investigated here, the free rotation of the chromophores dominates, with rotational correlation times of a few hundred picoseconds (Figure 2). Especially important for our application of the method here is that in the presence of intramolecular distance fluctuations, an additional component is expected in the correlation functions of a FRET-labeled sample, which has been used to measure long-range dynamics in unfolded proteins.[21] Figure 1 shows the three complete correlation functions for terminally labeled Csp unfolded in 4 M guanidinium chloride (GdmCl), fit globally with eq 2, which takes into account all of these components (see Materials and Methods). Rapid conformational dynamics of the unfolded chain[21] result in a positive amplitude component in the autocorrelations and a negative amplitude component in the cross-correlation with $\tau_{cd} = 40$ ns. The dynamics of all processes that can be detected in our system with single-molecule FRET are thus captured in the entire range of accessible times from picoseconds to milliseconds.

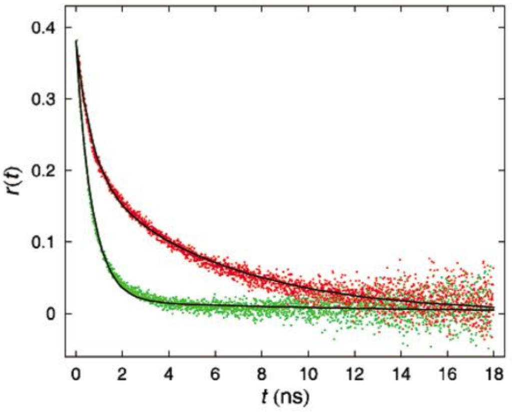

Figure 2. Time-resolved fluorescence anisotropy decay $r(t)$ of folded (red) and unfolded (green) Csp labeled only with a donor dye. While the fluorescence emission for folded Csp indicates significant residual anisotropy ($r_\infty = 0.20$, $\tau_M = 5.7$ ns), the anisotropy of Csp unfolded in 4 M GdmCl can be well approximated by a single exponential decay with a time constant of 0.74 ns, indicating rapid reorientation of the fluorophore. Fits to eq 4 are shown as black lines.

Time Scales of Unfolded State Dynamics in Csp. In the analysis of start−stop experiments, we have identified fast Brownian dynamics of the polypeptide chain ends relative to each other in terminally labeled unfolded Csp on the time scale of ∼50 ns (see ref 21). The time scale of these dynamics is of fundamental interest to a quantitative understanding of the folding process because it is closely related to the effective diffusion coefficient underlying a description of protein folding as a diffusive process on a free-energy surface, which is frequently used in statistical mechanical models.[51,52] The determination of such elementary time scales has gained even more relevance in view of the discovery of proteins folding in microseconds[53] and faster,[54] close to the expected "speed limit"[7,53,55,56] of folding. A comparison with the time scales of chain dynamics found in unstructured model peptides[7−9,49,57] and the observation of dynamics on a similar time scale for a series of other unfolded proteins (Nettels, Hillger, Wuttke, and Schuler, unpublished observations) suggest that long-range chain dynamics in the nanosecond range are a universal feature of unfolded proteins. The question remains, however, whether dynamics on longer time scales also contribute, especially in view of the microsecond phases frequently observed in protein folding kinetics.[58,59]

The availability of the complete correlation functions now allows us to address this question for Csp (Figure 1). Of particular value for analyzing distance dynamics is the fact that even though the component corresponding to distance dynamics must show up in all three correlation functions, it results in an amplitude of opposite sign for auto- and cross-correlations.[29,60] This difference allows us to distinguish distance dynamics from other processes, most importantly triplet blinking, which typically occurs in the microsecond range.[61] Figure 1 shows this characteristic signature for chain dynamics with a relaxation time of 40 ns; both donor (Figure 1a,b) and acceptor (Figure 1e,f) autocorrelations exhibit a component with positive amplitude, while the cross-correlation (Figure 1c,d) contains a component with negative amplitude that can be described with the same time constant. In contrast, however, the autocorrela-

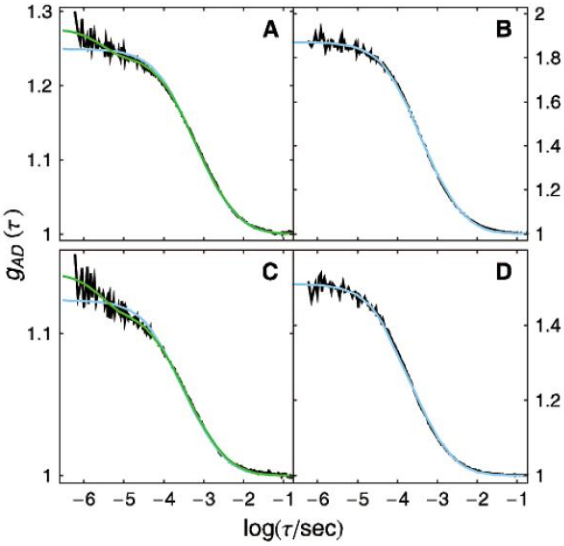

Figure 3. Cross-correlation functions for unfolded Csp (A,B) and for Pro20 (C,D) at different excitation rates. Whereas a residual triplet component is clearly visible at high laser power (A,C, 350 μW), it is absent at low power (B,D, 8 μW). Fits including only translational diffusion are shown in blue, and fits including an additional triplet component are shown in green.

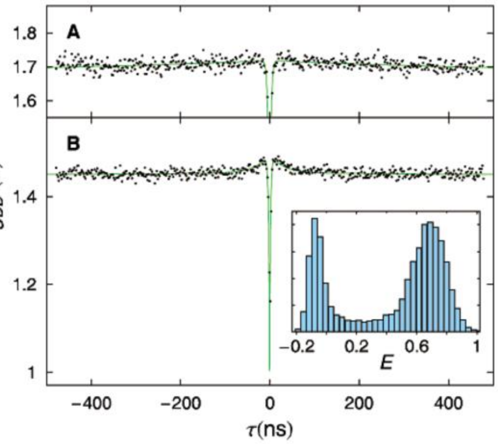

Figure 4. Donor intensity autocorrelation functions measured for Pro20 (A) and the labeled unstructured peptide G(AGQ)$_6$AGC in 8 M GdmCl (B). The unstructured peptide shows rapid end-to-end distance dynamics with a characteristic time of τ_{cd} = 15 ns; the dynamics in Pro20 are too rapid to be detected, as expected from simulations. The inset in (B) shows the transfer efficiency histogram of G(AGQ)$_6$AGC with á*E*ñ = 0.69 used for calculating the mean-squared end-to-end distance. The peak at $E \approx 0$ is due to molecules with an inactive acceptor.[17]

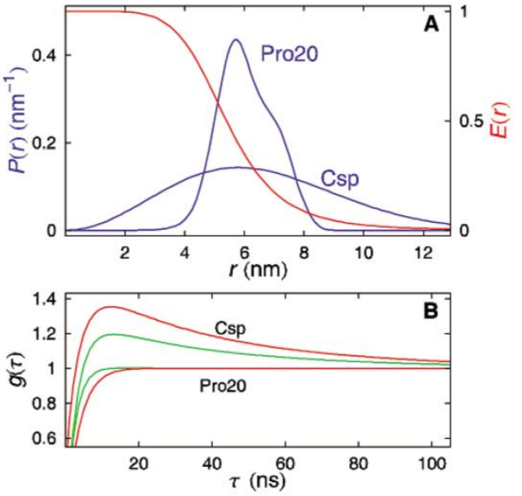

Figure 5. (A) End-to-end distance probability density function $P(r)$ and (B) the resulting calculated acceptor (red) and donor (green) intensity autocorrelation functions for Csp and Pro20. $P(r)$ for Csp is derived from experimental data[18] and $P(r)$ for Pro20 from simulations.[62] The distance dependence of the transfer efficiency E is shown in (A).

tions exhibit a large change in amplitude in the microsecond range (Figure 1b,f), but not the cross-correlation (Figure 1d). This is the typical signature found for triplet dynamics,[50,60] and already indicates the absence of a strong contribution of distance fluctuations on that time scale. However, a slight influence of triplet dynamics on the cross-correlation cannot be excluded, first because of the slight overlap of the donor emission spectrum with the wavelength range for acceptor detection (effectively resulting in a small contribution of the donor autocorrelation to the observed cross-correlation) and second because the effect of populating the triplet state in one dye on the emission of the other dye is currently unknown for the chromophores used here. In general, however, triplet states are increasingly populated at high excitation rates.[61] To further investigate the presence of a microsecond component originating from distance fluctuations, and in particular the possibility of accidental cancellation of triplet and distance dynamics in the cross-correlation function, we thus performed FCS measurements at different excitation rates and compared them to measurements on Pro20, for which microsecond distance fluctuations are not expected (Figure 3; note that start−stop experiments are not feasible at low excitation rates because of the resulting low count rates). While at high laser power (350 μW) a residual triplet component is visible, at the lowest laser power (8 μW), the cross-correlations both for unfolded Csp and Pro20 show no evidence for a change in the correlation amplitude in the microsecond range (and clearly no component with negative amplitude, as would be expected in the case of distance dynamics) and are well fit by a correlation function taking into account only translational diffusion. Within the accuracy of the method, we thus find no evidence for microsecond distance fluctuations in Csp at 4 M GdmCl, suggesting that the dynamics in the unfolded state of this two-state protein are dominated by diffusive chain reconfiguration in the tens of nanosecond range.

Exploring the Limits of the Method in the Nanosecond Range. To further investigate the sensitivity of the method in the nanosecond range, we present two examples of measurements on peptides with previously characterized dynamic properties. The first example (Figure 4a) is a polyproline peptide (20 residues, Pro$_{20}$), which we used earlier as a reference for a polypeptide with negligible intramolecular distance dynamics above the nanosecond range.[21,24] Molecular dynamics simulations have shown significant flexibility of polyproline peptides,[17,62] and very recent simulations including the fluorophores[62] give an even more detailed picture of the dynamics involved. Despite the significant width of the distance distribution (Figure 5), the dynamics of the system remain undetected in start−stop experiments (Figure 4a) because their characteristic time scale is too close to the fluorescence lifetime of the fluorophores (~2−4 ns) and thus coincides with the photon antibunching phase in the correlation function (Figure 5b). This observation is in agreement with molecular dynamics simulations, which place the end-to-end dynamics of the peptide in the 2 ns range.[17,62] A better characterization of all fast photophysical processes involved might allow the deconvolution of dynamic information even in this time range, but our lack of quantitative understanding of processes such as singlet−singlet annihilation for the chromophores currently prevents a more complete analysis. However, polyproline peptides remain a valuable reference for correlation experiments because of their large stiffness and their lack of dynamics on longer time scales than a few nanoseconds.

The second example is the unstructured peptide ($G(AGQ)_6AGC$) of the kind previously investigated in much detail in experiments employing the contact quenching of tryptophan triplet states by cysteine[8,57,63] to quantify the kinetics of elementary loop formation in polypeptides. While we were not able to detect chain dynamics for this peptide in the absence of denaturants (because of the narrow distance distribution with a small mean distance located in the plateau region of the Förster curve), we were able to observe peptide dynamics in the presence of 8 M GdmCl, where the chain is sufficiently expanded (Figure 4b). To obtain an effective end-to-end diffusion coefficient, we describe the relative motion of the chain ends as a diffusive process on the potential of mean force that corresponds to the end-to-end distance distribution of the labeled peptide. By combining these conformational dynamics with the distance-dependent stochastic photon emission from the coupled dye pair, the complete photon statistics of the system can be obtained.[29] We use a recently developed theory[46] that allows us to calculate the intensity correlation functions of donor and acceptor emission numerically.[21] Briefly, if we assume for the unfolded protein the end-to-end distance distribution of a Gaussian chain[8,57,63]

$$p_{\mathrm{eq}}(r) = 4\pi r^2 (2\pi\langle r^2\rangle/3)^{-3/2} \exp(-3r^2/2\langle r^2\rangle) \qquad (5)$$

protein dynamics can be combined with the photophysics of FRET in the rate matrix

$$\mathrm{K} = D\partial/\partial r\, p_{\mathrm{eq}}(r)\, \partial/\partial r\, (p_{\mathrm{eq}}(r))^{-1}\mathrm{I} + \mathrm{K}_0(r) \qquad (6)$$

where D is the relative diffusion coefficient of the chain ends, $\mathrm{K}_0(r)$ describes the distance-dependent kinetics of interconversion between the electronic states involved, and I is the 4 × 4 identity matrix. The time dependence of all electronic and conformational transitions in the system is then described by the rate equation $\mathrm{d}p/\mathrm{d}t = \mathrm{K}p$, where p is the vector of the populations of the electronic states. By discretizing the diffusion operator, the problem is reduced to matrix algebra, and the intensity correlation functions can be calculated to high accuracy with numerical methods.[21] All parameters needed to define the model in terms of our system are known; the photophysical rate constants of the FRET process were measured independently,[21] and $p_{\mathrm{eq}}(r)$ is defined uniquely by the mean-squared end-to-end distance $\langle r^2\rangle$, which we calculate[18,21,24] from the corresponding mean transfer efficiency of $\langle E\rangle \approx 0.69$ (Figure 4b, inset) as 4.8 nm. We can thus determine the only remaining parameter, the effective end-to-end diffusion coefficient D, by adjusting it such that the calculated intensity correlation function fits the experimental result.

From the decay time of the intensity correlation function of 15 ns (Figure 4b), we obtain an intramolecular end-to-end diffusion coefficient of 0.27 nm^2/ns. Assuming that the diffusion coefficient is inversely proportional to the viscosity of the solvent,[49,57,64] we get a viscosity-corrected diffusion coefficient of 0.64 nm^2/ns. This result is close to the value of 0.53 nm^2/ns for Csp in 8 M GdmCl,[21] suggesting that the chains' dynamics are very similar at these high concentrations of denaturant. The value found here is somewhat larger than the diffusion coefficients determined from viscosity-dependent tryptophan triplet quenching experiments for the same AGQ-repeat sequence[57,63] (between 0.08 and 0.17 nm^2/ns). Even though a direct comparison is difficult because those measurements were not performed at 8 M GdmCl, part of the difference could be caused by relatively small deviations from the distance distributions assumed in the analysis and the fact that the two methods probe different parts of the equilibrium distribution.

Overall, our measurements on this short unstructured peptide show the accuracy of correlation methods down to ~10 ns. At shorter distances and smaller time scales, fluorophores with smaller Förster radii and shorter fluorescence lifetimes would become necessary to use this approach. On the time scale of a few nanoseconds, dynamic information is available from the analysis of fluorescence lifetime decays;[48,49] even faster dynamics require methods such as pump−probe laser spectroscopy or NMR.

Position Dependence of Intramolecular Dynamics. Previously, we have investigated the intramolecular dynamics of unfolded Csp for a variant with the fluorescent labels at the termini (residue 2 and 67) of the polypeptide chain.[21] Here, we extend our analysis to variants where one of the chromophores is located at the carboxy terminus (residue 67), the other at position 2, 10, 21, 22, or 34 (Figure 6a), to probe the dependence of intramolecular diffusion on the position within the chain. Start−stop and correlation experiments were performed and analyzed as described above for the unstructured peptide. The resulting fluorescence intensity correlation times τ_{cd} corresponding to chain dynamics in these variants are shown in Figure 6b as a function of the sequence separation of the labeled residues. We observe a steady increase of τ_{cd} upon moving the second fluorophore from the terminus toward the middle of the polypeptide chain, from 40 to 67 ns. This increase is reminiscent of recent triplet−triplet energy-transfer experiments on unstructured Gly-Ser peptides, where a continuous decrease of the contact rate was found with increasing length of the tail segment.[65]

An advantage of investigating intramolecular dynamics with FRET is that both the distance distributions[18] (via measurements of the transfer efficiency) and dynamic information (via correlation functions[21] or fluorescence lifetime decay analysis[48,49]) can be obtained. The use of single-molecule spectroscopy additionally allows the separation of subpopulations[18,21,24,43,66] necessary for performing such an analysis even under conditions where folded and unfolded molecules coexist. As explained above, the fluorescence intensity correlation time τ_{cd} in combination with the shape of the end-to-end distance distribution can be used to extract intramolecular diffusion coefficients. As for the unstructured peptide, we use the end-to-end distance distribution of a Gaussian chain, which has been shown to be a good approximation for unfolded Csp.[18] By adjusting the intramolecular diffusion coefficient D such that calculation and experiment agree, D can be determined. The chain reconfiguration time τ_{r} (the decay time of the end-to-end distance autocorrelation function) is then obtained from $\tau_r \simeq \langle r^2\rangle/6.2D$ (see ref 21).

Figure 6b also shows the root-mean-square distance (rms r) between the fluorophores in the unfolded Csp variants,[18] and Figure 6c shows the intramolecular diffusion coefficient as a

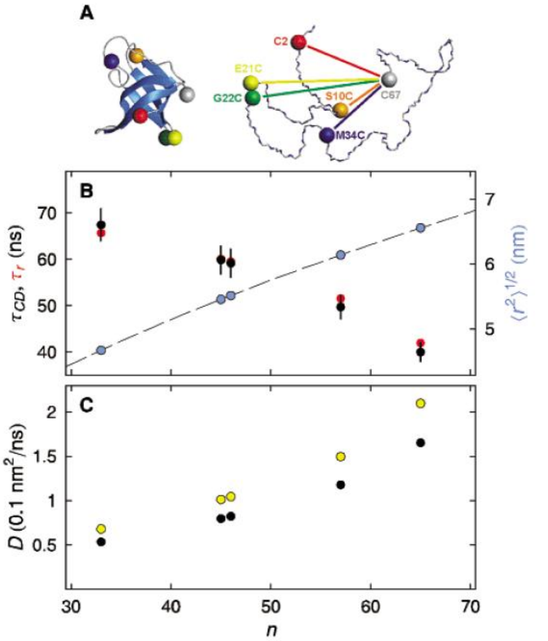

Figure 6. Position dependence of intramolecular dynamics in unfolded Csp (4 M GdmCl). (A) Schematic of folded (left) and unfolded (right) Csp with the sites for dye attachment for Förster resonance energy transfer indicated by colored spheres. For every variant, one dye was reacted with Cys at position 67 and the second dye with a Cys at one of the other positions shown. (B) Decay time τ_{cd} of the intensity correlation function, decay time τ_{r} of the intramolecular distance correlation function (the reconfiguration time), and root-mean-square distance $\langle r^2\rangle^{1/2}$ between the probes as a function of their separation within the polypeptide chain *n*. The $\langle r^2\rangle^{1/2}$ as a function of *n* was calculated from the apparent persistence length of 0.87 nm determined previously for unfolded Csp in 4 M GdmCl.[18] (C) Relative intramolecular diffusion coefficient *D* as a function of sequence separation calculated from the values in (B) both with (yellow) and without (black) viscosity correction, indicating slowed dynamics when one of the dyes is moved toward the middle of the chain. The error bars in (B) are our estimates of the experimental error.

function of sequence separation. As expected, the mean distance between the dyes decreases as they are moved closer together in sequence. For a diffusion coefficient independent of the probe position, smaller sequence separation would be expected to result in faster chain reconfiguration, and thus to a decrease in τ_{cd}, because of the smaller configuration space available. By contrast, upon moving one of the dyes toward the middle of the chain, we observe an increase in τ_{cd} from 40 to 67 ns, corresponding to a decrease in *D* by a factor of 3 (Figure 6c). This suggests that the faster relaxation expected from the narrowing of the distance distribution within the chain must be overcompensated by slower chain dynamics. Note that Figure 6c contains both the diffusion coefficients in 4 M GdmCl (black) and the viscosity-corrected values[49,57,64] (yellow) for direct comparison with experiments at other denaturant concentrations.

One expected contribution to this decrease in *D* is the increase in length of the chain segments that need to move in order to allow translational diffusion of one probed position with respect to the other. The relative intramolecular distance diffusion coefficient *D* can formally be regarded as the sum of two diffusion coefficients D_1 and D_2, which describe the relative diffusion of two positions in the chain, assuming that one or the other was fixed in space. If we further assume that $D_1 = D_2$ for the relative diffusion of the chain ends and that D_1 and D_2 were mutually independent, *D* could never decrease by more then a factor of 2, even if one residue was effectively immobilized. Our observation of a decrease of *D* by a factor of 3 suggests that D_1 and D_2 are not independent and that both the internal and the terminal residues are affected in their motion within the unfolded chain. One possibility is that the internal residue is effectively shielded by the tail segment, resulting in additional internal friction also for the terminal residue. Note, however, that the reconfiguration time, which is the parameter proportional to the preexponential factor in Kramers-like models of protein folding[52,67,68] and thus most relevant for the fast formation of contacts within an unfolded protein, varies by only about 50% for the different segments (Figure 6b). This suggests that the position dependence of chain reconfiguration has only a moderate effect on the overall time scales of protein folding, at least for all but the fastest folding proteins.

Discussion

Correlation methods are a versatile tool for analyzing dynamic processes and have recently gained increasing popularity especially in combination with fluorescence detection.[30] Depending on the experimental setup, processes from picoseconds to many hours are accessible, if the molecules are suitably immobilized. Here, we focus on measurements on freely diffusing molecules, a common approach that has the advantages that surface interactions that could interfere with the dynamics can largely be excluded and that reliable photon statistics become available simply by waiting for a sufficient number of molecules to cross the confocal volume. Of course, the accessible time scales are then limited by the diffusion time of a molecule through the confocal volume, but many biomolecular processes occur in the submillisecond range and can thus be studied relatively easily over several orders of magnitude in time.

Taking our previous observations of unfolded state dynamics[21] with a Hanbury Brown and Twiss-type instrument[43] in the tens of nanosecond range as a starting point, we are now extending the time scales used in our analysis to both shorter and longer times. To probe the accessibility of shorter times, we investigated two small peptides, a stiff polyproline peptide and an unstructured peptide with the properties of a random coil. While the polyproline dynamics expected on the ~2 ns time scale from simulations[17,62] remain undetected, the dynamics of the unstructured peptide can be detected, at least in high concentrations of GdmCl, with a correlation time of 15 ns and a resulting intramolecular diffusion coefficient that is in approximate agreement with tryptophan triplet quenching studies.[57,63] This time scale places an approximate lower bound on the dynamics accessible from correlation analyses with the Förster radii and fluorescence lifetimes of the typical dye pairs currently available for single-molecule FRET. On shorter time scales, the analysis of fluorescence lifetime decays[19,48,49] on the same type of samples can be used to extract information on dynamics down to times of about 50 ps. Time scales above the typical dead times of detectors and counting electronics are easily accessible with classical FCS measurements. By combining them with the start−stop experiments, fluctuations from picoseconds to milliseconds become available and can be analyzed with a global fit using a model that contains all dynamic processes in this time window. Here, we used this information to investigate the existence of slow unfolded state dynamics of the small two-state protein Csp.

The existence of submillisecond components in Csp folding dynamics has been difficult to clarify. Previous pressure-[70] and temperature-jump[71] experiments both on closely related cold shock proteins and the FRET-labeled Csp used here (Kubelka, J.; Schuler, B.; Eaton, W. A. Unpublished observation) with a time resolution in the microsecond range and below have not lead to an identification of any kinetic components in the submillisecond range. However, such kinetic ensemble experiments require a change in volume or enthalpy connected to the conformational change involved to allow a perturbation of the system. By contrast, single-molecule experiments monitor spontaneous fluctuations at equilibrium and thus lack this requirement. This advantage has allowed us to identify the previously elusive unfolded state dynamics of Csp on the tens of nanosecond time scale.[21] With the extended time scale available through the combination of start−stop experiments with FCS, we were now able to extend our analysis into the microsecond range and find no indication for distance fluctuations in unfolded Csp on time scales above the tens of nanosecond range.

The absence of microsecond components in the unfolded state dynamics and the folding kinetics of Csp is indicative of a lack of specific interactions within the polypeptide before it crosses the main transition state for folding, in contrast to observations on a wide range of larger proteins or proteins with cofactors,[59] where microsecond phases are frequently observed. While the results presented here cannot exclude short-range interactions in specific segments of the polypeptide leading to slow low-amplitude dynamics in the unfolded state, the observation of a rather isotropic, random coil-like collapse of unfolded Csp[18] at low GdmCl concentrations suggests that such interactions might indeed be absent. In principle, conformational dynamics in denatured states of proteins can apparently occur on a very broad range of time scales and might be highly specific for every protein—even extremely slow dynamics cannot be excluded, such as those on the 100 s time scale inferred from single-molecule experiments on RNase H[72]—but their structural basis is often unclear. On the other hand, the nanosecond dynamics that are dominant in the unfolded state of Csp are most probably a universal characteristic of unfolded proteins, as suggested by comparison with the time scales of chain dynamics found in unstructured model peptides[7−9,49,57] and the observation of dynamics on a similar time scale for a series of other unfolded proteins[73] (Nettels, Hillger, Wuttke, and Schuler, unpublished observations). The corresponding process of elementary chain reconfiguration thus provides a reasonable value for the diffusion of a polypeptide chain on its conformational energy landscape, or the "speed limit" for protein folding reactions. The current "record holders" in terms of fast protein folding, which probably approach the "speed limit"[53] expected for a "downhill" process, are in the range of several hundred nanoseconds[54] to a few microseconds,[53,56,74] similar to the preexponential factor of 0.4 μs estimated from the reconfiguration time of unfolded Csp.[21]

While our previous experiments were done on terminally labeled Csp, an important question for protein folding is how the relative position of residues within the polypeptide sequence affects the time scale of intramolecular distance fluctuations between them. This issue of "external" versus "internal" loop formation has been addressed in a range of theoretical[75−80] and experimental work,[63,65,81] especially in polymer physics, and more recently also for unstructured polypeptides. In general, two effects would be expected to influence the position dependence of loop formation kinetics. First, the additional residues of the "tail" segment will contribute excluded volume in the vicinity of the residues probed, thus changing the underlying equilibrium distance distribution between them and reducing their probability of approaching each other. Second, there could be dynamic effects resulting from additional viscous drag of the tail segment or altered interactions within the chain.

In our experiments, we change the distance distribution between the probed residues both by moving the dyes closer within the chain and by concurrently increasing the tail segment length. However, as we can obtain the resulting change in the equilibrium distance distribution between the donor and acceptor from measurements of the transfer efficiency and the fluorescence lifetime decay in the unfolded subpopulation,[18] we can obtain direct information about the change in polypeptide dynamics, that is, the relative diffusion coefficient D between the two points in the chain. We observe a decrease in D with decreasing separation within the sequence (Figure 6c). D depends both on the change in viscous drag, which would be expected to increase with tail length, and on the details of the interactions within the chain, that is, between the backbone and side chains of the polypeptide. As previous experiments have indicated a rather uniform collapse of the chain,[18] suggesting a uniform distribution of interactions within the unfolded protein, the increase in viscous drag appears to dominate the change in D. It would of course be interesting to know whether there is a turnover of the position dependence of D for even shorter sequence separations, as expected from theory and as possibly suggested by the nonlinearity of the dependence of D on sequence separation in our data (Figure 6c), but shorter distances cannot be probed reliably with our current dye pair because of its large Förster radius.

A method that can be used for probing shorter distance dynamics is triplet state quenching, and it has previously been used to investigate the effect of tail segment length on loop formation in unstructured peptides.[63,65] Experiments using tryptophan triplet state quenching by cysteine indicated a very strong effect already from adding a single amino acid to the terminus, with not much change when the tail segment was lengthened further.[63] This result was interpreted in terms of the dominance of the first residue in shielding the quencher, which is reasonable in view of the fact that the cysteine side chain must essentially make van der Waals contact with tryptophan to quench its triplet state,[82] and especially considering the small size of the thiol group. In a different study, where the larger groups xanthone and napthylalanine were incorporated into peptides to investigate the formation of interior loops by triplet quenching, the contact rate was found to decrease continuously with tail length up to more than 20 residues.[65] While this result exhibits a qualitatively similar trend as we observe in unfolded Csp, a quantitative comparison to the intramolecular diffusion coefficients determined here is complicated by the lack of information on the interprobe distance distribution in these experiments.

Conclusions

The analysis of single-molecule photon statistics has become an increasingly valuable tool for our understanding of biomolecular dynamics on a wide range of time scales. For molecules freely diffusing in solution, the accessible time scales range from nanoseconds to the diffusion time through the confocal volume, typically in the range of several hundred microseconds. Using complete correlation functions from picoseconds to seconds, we showed that the dynamics of unstructured peptides labeled with a FRET pair can be analyzed down to the low nanosecond range and found no evidence for dynamics slower than in the tens of nanoseconds range for unfolded Csp. Upon moving one of the fluorophores from the terminus of Csp toward the center of the sequence, we observed a substantial decrease of the intramolecular diffusion coefficient, presumably resulting from the viscous drag of the tail segment. The methodology used here should be applicable to a large number of questions, especially for processes with heterogeneous kinetics, in complex environments, or in cases where a synchronization of the ensemble by perturbation methods is difficult. Developments such as the gentle immobilization of proteins[72,83,84] or the use of ratios of correlation functions to eliminate the diffusive component[85,86] will help to extend the accessible time scales even further.

Acknowledgment. We thank Attila Szabo for many insightful and delectable discussions over the years. We thank Irina Gopich for advice on photon statistics and diffusive processes and for providing the algorithms to calculate correlation functions numerically. This work was supported by the Swiss National Science Foundation, the Human Frontier Science Program, the Swiss National Center of Competence in Research for Structural Biology, and the VolkswagenStiftung.

References and Notes

(1) Millett, I. S.; Doniach, S.; Plaxco, K. W. *Adv. Protein Chem.* 2002, *62*, 241.

(2) Kohn, J. E.; Millett, I. S.; Jacob, J.; Zagrovic, B.; Dillon, T. M.; Cingel, N.; Dothager, R. S.; Seifert, S.; Thiyagarajan, P.; Sosnick, T. R.; Hasan, M. Z.; Pande, V. S.; Ruczinski, I.; Doniach, S.; Plaxco, K. W. *Proc. Natl. Acad. Sci. U.S.A.* 2004, *101*, 12491.

(3) Vendruscolo, M. *Curr. Opin. Struct. Biol.* 2007, *17*, 15.

(4) Mittag, T.; Forman-Kay, J. D. *Curr. Opin. Struct. Biol.* 2007, *17*, 3.

(5) Shortle, D. R. *Curr. Opin. Struct. Biol.* 1996, *6*, 24.

(6) Dyson, H. J.; Wright, P. E. *Chem. Rev.* 2004, *104*, 3607.

(7) Bieri, O.; Wirz, J.; Hellrung, B.; Schutkowski, M.; Drewello, M.; Kiefhaber, T. *Proc. Natl. Acad. Sci. U.S.A.* 1999, *96*, 9597.

(8) Lapidus, L. J.; Eaton, W. A.; Hofrichter, J. *Proc. Natl. Acad. Sci. U.S.A.* 2000, *97*, 7220.

(9) Hudgins, R. R.; Huang, F.; Gramlich, G.; Nau, W. M. *J. Am. Chem. Soc.* 2002, *124*, 556.

(10) Neuweiler, H.; Schulz, A.; Böhmer, M.; Enderlein, J.; Sauer, M. *J. Am. Chem. Soc.* 2003, *125*, 5324.

(11) Jia, Y. W.; Talaga, D. S.; Lau, W. L.; Lu, H. S. M.; DeGrado, W. F.; Hochstrasser, R. M. *Chem. Phys.* 1999, *247*, 69.

(12) Haran, G. *J. Phy.: Condens. Matter* 2003, *15*, R1291.

(13) Schuler, B. *ChemPhysChem* 2005, *6*, 1206.

(14) Michalet, X.; Weiss, S.; Jager, M. *Chem. Rev.* 2006, *106*, 1785.

(15) Schuler, B.; Eaton, W. A. *Curr. Opin. Struct. Biol.* 2008, *18*, 16.

(16) Ha, T.; Enderle, T.; Ogletree, D. F.; Chemla, D. S.; Selvin, P. R.; Weiss, S. *Proc. Natl. Acad. Sci. U.S.A.* 1996, *93*, 6264.

(17) Schuler, B.; Lipman, E. A.; Steinbach, P. J.; Kumke, M.; Eaton, W. A. *Proc. Natl. Acad. Sci. U.S.A.* 2005, *102*, 2754.

(18) Hoffmann, A.; Kane, A.; Nettels, D.; Hertzog, D. E.; Baumgärtel, P.; Lengefeld, J.; Reichardt, G.; Horsley, D. A.; Seckler, R.; Bakajin, O.; Schuler, B. *Proc. Natl. Acad. Sci. U.S.A.* 2007, *104*, 105.

(19) Laurence, T. A.; Kong, X. X.; Jäger, M.; Weiss, S. *Proc. Natl. Acad. Sci. U.S.A.* 2005, *102*, 17348.

(20) Neuweiler, H.; Doose, S.; Sauer, M. *Proc. Natl. Acad. Sci. U.S.A.* 2005, *102*, 16650.

(21) Nettels, D.; Gopich, I. V.; Hoffmann, A.; Schuler, B. *Proc. Natl. Acad. Sci. U.S.A.* 2007, *104*, 2655.

(22) Perl, D.; Welker, C.; Schindler, T.; Schröder, K.; Marahiel, M. A.; Jaenicke, R.; Schmid, F. X. *Nat. Struct. Biol.* 1998, *5*, 229.

(23) Wassenberg, D.; Welker, C.; Jaenicke, R. *J. Mol. Biol.* 1999, *289*, 187.

(24) Schuler, B.; Lipman, E. A.; Eaton, W. A. *Nature* 2002, *419*, 743.

(25) Schuler, B.; Kremer, W.; Kalbitzer, H. R.; Jaenicke, R. *Biochemistry* 2002, *41*, 11670.

(26) Lipman, E. A.; Schuler, B.; Bakajin, O.; Eaton, W. A. *Science* 2003, *301*, 1233.

(27) Kurtsiefer, C.; Zarda, P.; Mayer, S.; Weinfurter, H. *J. Mod. Opt.* 2001, *48*, 2039.

(28) Berglund, A. J.; Doherty, A. C.; Mabuchi, H. *Phys. Rev. Lett.* 2002, *89*, 068101.

(29) Wang, Z. S.; Makarov, D. E. *J. Phys. Chem. B* 2003, *107*, 5617.

(30) Rigler, R.; Elson, E. S. *Flourescence Correlation Spectroscopy: Theory and Applications*; Springer: Berlin, Germany, 2001.

(31) Hübner, C. G.; Zumofen, G.; Renn, A.; Herrmann, A.; Müllen, K.; Basché, T. *Phys. Rev. Lett.* 2003, *91*.

(32) De Schryver, F. C.; Vosch, T.; Cotlet, M.; Van, der Auweraer, M.; Müllen, K.; Hofkens, J. *Acc. Chem. Res.* 2005, *38*, 514.

(33) Bradforth, S. E.; Jinenez, R.; Vanmourik, F.; Vangrondelle, R.; Fleming, G. R. *J. Phys. Chem.* 1995, *99*, 16179.

(34) Kapusta, P.; Erdmann, R.; Ortmann, U.; Wahl, M. *J. Fluoresc.* 2003, *13*, 179.

(35) Lakowicz, J. R. *Principles of Fluorescence Spectroscopy*, 2nd ed.; Kluwer Academic/Plenum Publishers: New York, 1999.

(36) Lipari, G.; Szabo, A. *Biophys. J.* 1980, *30*, 489.

(37) Hanbury Brown, R.; Twiss, R. Q. *Nature* 1956, *177*, 27.

(38) Ehrenberg, M.; Rigler, R. *Chem. Phys.* 1974, *4*, 390.

(39) Fleury, L.; Segura, J. M.; Zumofen, G.; Hecht, B.; Wild, U. P. *Phys. Rev. Lett.* 2000, *84*, 1148.

(40) Tinnefeld, P.; Müller, C.; Sauer, M. *Chem. Phys. Lett.* 2001, *345*, 252.

(41) Weston, K. D.; Dyck, M.; Tinnefeld, P.; Müller, C.; Herten, D. P.; Sauer, M. *Anal. Chem.* 2002, *74*, 5342.

(42) Hofkens, J.; Cotlet, M.; Vosch, T.; Tinnefeld, P.; Weston, K. D.; Ego, C.; Grimsdale, A.; Mullen, K.; Beljonne, D.; Bredas, J. L.; Jordens, S.; Schweitzer, G.; Sauer, M.; De Schryver, F. *Proc. Natl. Acad. Sci. U.S.A.* 2003, *100*, 13146.

(43) Nettels, D.; Schuler, B. *IEEE J. Sel. Top. Quant. Electron.* 2007, *13*, 990.

(44) Felekyan, S.; Kühnemut, R.; Kudryavtsev, V.; Sandhagen, C.; Becker, W.; Seidel, C. A. M. *Rev. Sci. Instrum.* 2005, *76*, 083104.

(45) Wahl, M.; Rahn, H. J.; Gregor, I.; Erdmann, R.; Enderlein, J. *Rev. Sci. Instrum.* 2007, *78*, 033106.

(46) Gopich, I. V.; Szabo, A. *J. Chem. Phys.* 2006, *124*, 154712.

(47) Mets, Ü. Antibunching and Rotational Diffusion in FCS. In *Fluorescence Correlation Spectroscopy*; Elson, E. S., Rigler, R., Eds.; Springer-Verlag: Berlin, Germany, 2001.

(48) Haas, E.; Katchalskikatzir, E.; Steinberg, I. Z. *Biopolymers* 1978, *17*, 11.

(49) Möglich, A.; Joder, K.; Kiefhaber, T. *Proc. Natl. Acad. Sci. U.S.A.* 2006, *103*, 12394.

(50) Eggeling, C.; Kask, P.; Winkler, D.; Jäger, S. *Biophys. J.* 2005, *89*, 605.

(51) Bryngelson, J. D.; Onuchic, J. N.; Socci, N. D.; Wolynes, P. G. *Proteins* 1995, *21*, 167.

(52) Socci, N. D.; Onuchic, J. N.; Wolynes, P. G. *J. Chem. Phys.* 1996, *104*, 5860.

(53) Kubelka, J.; Hofrichter, J.; Eaton, W. A. *Curr. Opin. Struct. Biol.* 2004, *14*, 76.

(54) Kubelka, J.; Chiu, T. K.; Davies, D. R.; Eaton, W. A.; Hofrichter, J. *J. Mol. Biol.* 2006, *359*, 546.

(55) Hagen, S. J.; Hofrichter, J.; Szabo, A.; Eaton, W. A. *Proc. Natl. Acad. Sci. U.S.A.* 1996, *93*, 11615.

(56) Yang, W. Y.; Gruebele, M. *Nature* 2003, *423*, 193.

(57) Lapidus, L. J.; Steinbach, P. J.; Eaton, W. A.; Szabo, A.; Hofrichter, J. *J. Phys. Chem. B* 2002, *106*, 11628.

(58) Roder, H.; Shastry, M. R. *Curr. Opin. Struct. Biol.* 1999, *9*, 620.

(59) Bilsel, O.; Matthews, C. R. *Curr. Opin. Struct. Biol.* 2006, *16*, 86.

(60) Schwille, P. Cross-Correlation Analysis in FCS. In *Fluorescence Correlation Spectroscopy*; Elson, E. S., Rigler, R., Eds.; Springer-Verlag: Berlin, Germany, 2001.

(61) Widengren, J.; Mets, Ü.; Rigler, R. *J. Phys. Chem.* 1995, *99*, 13368.

(62) Best, R.; Merchant, K.; Gopich, I. V.; Schuler, B.; Bax, A.; Eaton, W. A. *Proc. Natl. Acad. Sci. U.S.A.* 2007, *104*, 18964.

(63) Buscaglia, M.; Lapidus, L. J.; Eaton, W. A.; Hofrichter, J. *Biophys. J.* 2006, *91*, 276.

(64) Krieger, F.; Fierz, B.; Bieri, O.; Drewello, M.; Kiefhaber, T. *J. Mol. Biol.* 2003, *332*, 265.

(65) Fierz, B.; Kiefhaber, T. *J. Am. Chem. Soc.* 2007, *129*, 672.

(66) Deniz, A. A.; Laurence, T. A.; Beligere, G. S.; Dahan, M.; Martin, A. B.; Chemla, D. S.; Dawson, P. E.; Schultz, P. G.; Weiss, S. *Proc. Natl. Acad. Sci. U.S.A.* 2000, *97*, 5179.

(67) Kramers, H. A. *Physica* 1940, *7*, 284.

(68) Klimov, D. K.; Thirumalai, D. *Phys. Rev. Lett.* 1997, *79*, 317.

(69) Reference deleted in proof.

(70) Jacob, M.; Holtermann, G.; Perl, D.; Reinstein, J.; Schindler, T.; Geeves, M. A.; Schmid, F. X. *Biochemistry* 1999, *38*, 2882.

(71) Magg, C.; Kubelka, J.; Holtermann, G.; Haas, E.; Schmid, F. X. *J. Mol. Biol.* 2006, *360*, 1067.

(72) Kuzmenkina, E. V.; Heyes, C. D.; Nienhaus, G. U. *Proc. Natl. Acad. Sci. U.S.A.* 2005, *102*, 15471.

(73) Sadqi, M.; Lapidus, L. J.; Munoz, V. *Proc. Natl. Acad. Sci. U.S.A.* 2003, *100*, 12117.

(74) Naganathan, A. N.; Doshi, U.; Munoz, V. *J. Am. Chem. Soc.* 2007, *129*, 5673.

(75) Friedman, B.; Oshaughnessy, B. *Macromolecules* 1993, *26*, 4888.

(76) Chan, H. S.; Dill, K. A. *J. Chem. Phys.* 1989, *90*, 492.

(77) Sheng, Y. J.; Hsu, P. H.; Chen, J. Z. Y.; Tsao, H. K. *Macromolecules* 2004, *37*, 9257.

(78) Zhou, H. X. *Biochemistry* 2004, *43*, 2141.

(79) Pastor, R. W.; Zwanzig, R.; Szabo, A. *J. Chem. Phys.* 1996, *105*, 3878.

(80) Wang, Z. S.; Makarov, D. E. *J. Chem. Phys.* 2002, *117*, 4591.

(81) Doucet, D.; Roitberg, A.; Hagen, S. J. *Biophys. J.* 2007, *92*, 2281.

(82) Lapidus, L. J.; Eaton, W. A.; Hofrichter, J. *Phys. Rev. Lett.* 2001, *8725*, 8101.

(83) Rhoades, E.; Gussakovsky, E.; Haran, G. *Proc. Natl. Acad. Sci. U.S.A.* 2003, *100*, 3197.

(84) Rhoades, E.; Cohen, M.; Schuler, B.; Haran, G. *J. Am. Chem. Soc.* 2004, *126*, 14686.

(85) Li, G.; Levitus, M.; Bustamante, C.; Widom, J. *Nat. Struct. Mol. Biol.* 2005, *12*, 46.

(86) Torres, T.; Levitus, M. *J. Phys. Chem. B* 2007, *111*, 7392.

IV. Non-Equilibrium Single-Molecule Experiments

4.1 A MICROFLUIDIC MIXING SYSTEM FOR SINGLE-MOLECULE MEASUREMENTS

REVIEW OF SCIENTIFIC INSTRUMENTS **80**, 055105 (2009)

A microfluidic mixing system for single-molecule measurements

Shawn H. Pfeil,[1] Charles E. Wickersham,[1] Armin Hoffmann,[2] and Everett A. Lipman[1]
[1]*Department of Physics, University of California, Santa Barbara, California 93106, USA*
[2]*Biochemisches Institut, Universität Zürich, Winterthurerstrasse 190, 8057 Zürich, Switzerland*

(Received 23 December 2008; accepted 7 April 2009; published online 14 May 2009)

This article describes the design and fabrication of a microfluidic mixing system optimized for ultrasensitive optical measurements. Channels are replica-molded in polydimethylsiloxane elastomer and sealed with fused-silica coverglass. The resulting devices have broad chemical compatibility and extremely low fluorescence background, enabling measurements of individual molecules under well-characterized nonequilibrium conditions. Fluid delivery and pressure connections are made using an interface that allows for rapid assembly, rapid sample exchange, and modular device replacement while providing access for high numerical aperture optics. © *2009 American Institute of Physics.* [DOI: 10.1063/1.3125643]

I. INTRODUCTION

Since their introduction by Austin and co-workers[1,2] in the late 1990s, microfabricated diffusive mixers have found application in a large and growing number of chemical and biochemical kinetics measurements.[3–7] Compared with stopped flow[8] and turbulent mixers,[9,10] these laminar-flow devices provide greater uniformity of, and control over, mixing conditions, and require only microscopic sample volumes.

During the same period, the inception and development of single-molecule fluorescence measurements[11–15] have made possible the observation of macromolecular properties and behavior formerly cloaked by ensemble averaging. Combination of these techniques[16–21] enables measurements under nonequilibrium conditions with single-molecule resolution. For example, transiently inhabited subpopulations can be identified, examined, and tracked in protein folding experiments.[16,19,20] This ability to extract new information from biochemical kinetics experiments using only microliters of sample is promising, but the application of single-molecule diffusive mixers has remained limited.

In this article, we describe a system designed to overcome many of the difficulties commonly encountered in single-molecule microfluidic measurements.

Mixing devices are replica-molded[22–24] from poly(dimethylsiloxane) elastomer, so that cleanroom processing is unnecessary after mold fabrication. The channel pattern is designed to provide complete mixing with minimal dead time prior to observation, subject to constraints imposed by the optical system. Channel impedances have been selected to allow a wide range of precisely controllable flow rates and mixing ratios with a simple pressure regulation system.

Once contact-bonded to fused-silica windows, devices with cast feedthroughs are mounted in a spring-loaded chip carrier containing integrated sample wells, eliminating the need for adhesives, punching, and needle insertion to attach pressure and fluid feeds. The chip carrier can be rapidly loaded into a pressure manifold that mounts directly onto a microscope. All connections to the chip carrier are made using face-type static O-ring seals, so pressure delivery fittings can remain in place while devices are exchanged. Sample wells in the chip carrier are accessible with the carrier mounted, and can be emptied or refilled without moving the device or undoing any connections.

Although this system is optimized for single-molecule measurements, these devices can, if a suitable window-bonding technique is used, be run at least an order of magnitude faster for ensemble measurements.

II. DEVICE REQUIREMENTS AND DESIGN

A. Mixer materials

A microfluidic device intended for use with single-molecule detection is subject to a number of inescapable requirements, chief among which is the need for extremely low background fluorescence. In earlier work,[16] channel patterns were fabricated directly in silicon, and anodic bonding[25] was used to seal a window over the channels. This method takes advantage of mature silicon fabrication technology and the strong seal formed in the bonding process. Unfortunately, it requires that the window be made of Pyrex (or a similar glass), which produces significant fluorescence background. Further disadvantages are that these devices must be fabricated in a cleanroom, and are permanently sealed, making cleaning and reuse impractical.

Among available transparent materials, fused silica stands out as the best choice for the device window. It is transparent from 180–2100 nm,[26–28] has broad chemical compatibility, does not affect polarization, is readily available in the appropriate thickness, has an index of refraction compatible with high numerical aperture water-immersion optics, and produces approximately one-tenth the fluorescence background of Pyrex.

In typical fluorescence measurements of untethered single molecules,[13–16,29,30] photons are collected as the sample molecule drifts (by diffusion, flow, or both) through a laser focus coincident with a confocal detection volume having dimensions on the order of 1 μm. A meaningful measurement, for example of a Förster resonance energy transfer

0034-6748/2009/80(5)/055105/9/$25.00

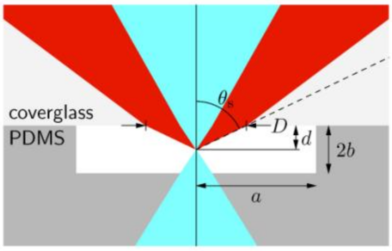

FIG. 1. (Color online) Laser beam and sample fluorescence in microfluidic channel. With the laser focus at depth d, the collected light cone will have diameter D at the top of the channel. $D=2Ad/\sqrt{n_s^2-A^2}$, where n_s is the index of refraction in the channel, and $A=n_s \sin\theta_s$ is the numerical aperture of the optical system used to collect the light. For $n_s=1.33$ and $A=1.2$, $D=4.18d$. Optimal measurements at the full depth $d=2b=10$ μm therefore require a channel width $2a \geq 41.8$ μm. In the present mixer design, $2a=50$ μm.

efficiency,[15] usually requires the detection of tens to hundreds of photons, corresponding to a dwell time in the focus on the order of 1 ms. For this reason, the flow velocity in the mixer's observation channel should not be significantly higher than 1 μm/ms (=1 mm/s). As a result of optical constraints (described below), the cross-sectional area of the observation channel is such that this maximum flow velocity is easily achieved with a driving pressure differential of less than 15 kPa.

This relatively low pressure requirement enables the use of poly(dimethylsiloxane) (PDMS) as the device substrate. With the exception of several narrow absorption bands in the near-infrared, PDMS is transparent from 240 to 2100 nm.[31,32] It is compatible with a wide range of laboratory chemicals,[33] suitable for biological samples,[34] and inexpensive. It also allows device fabrication using replica-molding methods introduced by Duffy, *et al.*[22] and developed by Whitesides and co-workers[23,31,33,34] and Quake and co-workers.[24,35] PDMS undergoes reversible conformal contact bonding with fused silica, forming a seal that is usable up to approximately 30 kPa.[36] Higher pressures, useful for ensemble experiments employing rapid flow, can be withstood by irreversible device-window seals formed using plasma, ultraviolet light, or additional PDMS.[22,37–39]

B. Observation channel

A microscope objective with numerical aperture $A \equiv n \sin\theta$ can collect a cone of light with half-angle θ, where n is the index of refraction of the medium in which θ is measured (see Fig. 1). Since typical fluorescence lifetimes are 10–100 times longer than rotational correlation times for freely diffusing molecules in aqueous solution, emission is expected to be isotropic. The cone will therefore contain a fraction

$$f_c = \tfrac{1}{2}(1-\cos\theta_s) = \tfrac{1}{2}[1-\sqrt{1-(A/n_s)^2}] \qquad (1)$$

of the light emitted by a sample molecule, where θ_s is the cone half-angle at the sample, and n_s is the index of refraction in the observation channel (Although θ changes as the light cone propagates from one medium to another, A is invariant). For typical values $n_s=1.33$ and $A=1.2$, $\theta_s=64.5°$, and the collection efficiency $f_c=0.28$.

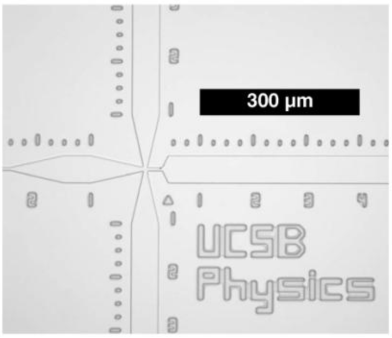

FIG. 2. Microfluidic device mixing region. Etched reference marks facilitate precise positioning of the confocal measurement volume. 50 μm wide areas are used for measurements in the inlet channels at top, left, and bottom. The first position where a measurement can be made using the entire collection cone of an objective with numerical aperture $A=1.2$ is indicated by a small triangle below the observation channel.

To prevent further loss of the already scarce signal from a single-molecule sample, microfluidic channels must be wide enough to accommodate the entire light cone originating at observation depth d (Fig. 1). At the level of the PDMS-coverglass interface, the cone diameter $D=2Ad/\sqrt{n_s^2-A^2}$. For the parameters given above, $D=4.18d$. If measurements are to be made down to the bottom center of an observation channel with depth $2b$ and width $2a$, the maximum numerical aperture that can be fully accommodated is $A_c=n_s/\sqrt{1+4(b/a)^2}$.

Single-molecule kinetic measurements made possible by this type of microfluidic mixer rely on the conversion between channel position and time using the flow rate in the device. To minimize measurement uncertainty, it is necessary to have a uniform flow profile throughout the confocal volume from which signal is being collected. The confocal volume has a vertical extent on the order of 1 μm, so the channel depth must be significantly greater than this to assure the desired flow uniformity.

A channel depth of 10 μm was chosen for the present mixer design. This is sufficient to ensure a velocity variation of no more than 1% over the 1×1 μm square area at the center of the channel cross section in fully developed flow.[40] Observations at the full depth with an $A=1.2$ water-immersion microscope objective (UPLSAPO 60XW, Olympus) then require that the channel be at least 41.8 μm wide (Fig. 1). Accordingly, the observation channel width was chosen to be 50 μm. Figure 2 shows the observation channel and 50 μm wide areas used for control measurements of sample and buffer prior to mixing.

C. Mixing performance and dead time

A perfect mixer would combine reactants completely and instantaneously, allowing observation of the sample from the moment of mixing onward. In realizable devices, departures from this ideal are described by a mixing delay and a measurement dead time. How one defines these two quantities is somewhat arbitrary. For example, the driving pressure can always be increased, resulting in a higher flow rate and correspondingly lower dead time. For single-molecule experiments, however, the amount of signal collected is reduced when the sample spends less time in the confocal volume, and at some point claims of extremely short dead times will become meaningless as the signal-to-noise ratio approaches zero. Likewise, measurements made prior to complete mixing of reactants are difficult or impossible to interpret.

1. Mixing delay

The dimensions of the channels in our microfluidic mixers are on the order of tens of microns, and the flow velocities (see Sec. II A above) are on the order of millimeters per second. Accordingly, for aqueous samples the Reynolds number[40,41]

$$R_e \equiv \frac{\rho U L}{\eta} \approx 10^{-2}, \tag{2}$$

where $\rho \approx 1000\ \mathrm{kg/m^3}$ is the density of water, U is the flow velocity, L is the channel dimension, and $\eta \approx 0.001$ Pa s is the viscosity of water. The transition to turbulent flow is not expected below $R_e \approx 2000$, so it is clear that flow in these mixers will be completely laminar, and mixing will be by diffusion alone.

In the experiment described in Ref. 16, protein molecules in a relatively high concentration of a denaturant, guanidinium chloride (GdmCl), were made to refold upon dilution of the denaturant. Dilution is complete once the denaturant molecules have had time to diffuse throughout the entire available post-mixing solution volume. In a symmetric planar mixer (Fig. 3) delivering a relatively large amount of buffer (side inlets), the sample solution (central inlet) is initially confined by hydrodynamic focusing[2] to a region near the horizontal center of the channel. Denaturant molecules with diffusion constant $\mathcal{D}$ will reach the sides of the channel in a time $\tau_m \approx a^2/2\mathcal{D}$, where a is the channel half-width (Fig. 1).

The present mixer (Fig. 3) was designed with a 5 μm wide neck following the mixing intersection, minimizing τ_m while keeping feature sizes well above the resolution limit (about 1 μm) of the fabrication process. For small molecules with $\mathcal{D} \approx 1\ \mu\mathrm{m^2/ms}$, we then have $\tau_m \approx 3$ ms. The average flow velocity U_m in the mixing neck will be ten times that in the 50 μm wide observation channel (the depth of all device features is 10 μm). The neck must therefore have a length $U_m \tau_m \approx 30\ \mu$m for complete mixing.

Mixer parameters were tested and refined using numerical fluid flow calculations coupled with a Newtonian transport model for diffusion (OpenFOAM software, www.opencfd.co.uk). Figure 3(a) shows the result of a calculation with aqueous ($\eta = 1$ mPa s) solutions in all three inlets and a small-molecule ($\mathcal{D} = 1\ \mu\mathrm{m^2/ms}$) solute in the center inlet. For this calculation and the corresponding ink-mixing experiment [Fig. 3(b)], pressures at all three inlets were set to 12.4 kPa above that at the outlet. Under these conditions, the average flow velocity in the outlet channel is approximately 1.1 μm/ms. At the first observation point (see Fig. 2 caption), the velocity u_c of the central streamline is 4.3 μm/ms. Further down the observation channel, u_c approaches its asymptotic value of 1.8 μm/ms. In Fig. 3(a), contour lines are drawn at 90% of the initial and 110% of the final solute concentrations. If we regard these lines as indicating the onset and completion of mixing (These choices are arbitrary, and the kinetics of a given sample may suggest different definitions for τ_m and dead time τ_d.), then we find a mixing delay $\tau_m = 1.5$ ms. Evidently this definition of τ_m makes the estimate $\tau_m \approx a^2/2\mathcal{D}$ rather conservative, as 110% of the final solute concentration is reached well before the mean-squared diffusion distance is half the channel width.

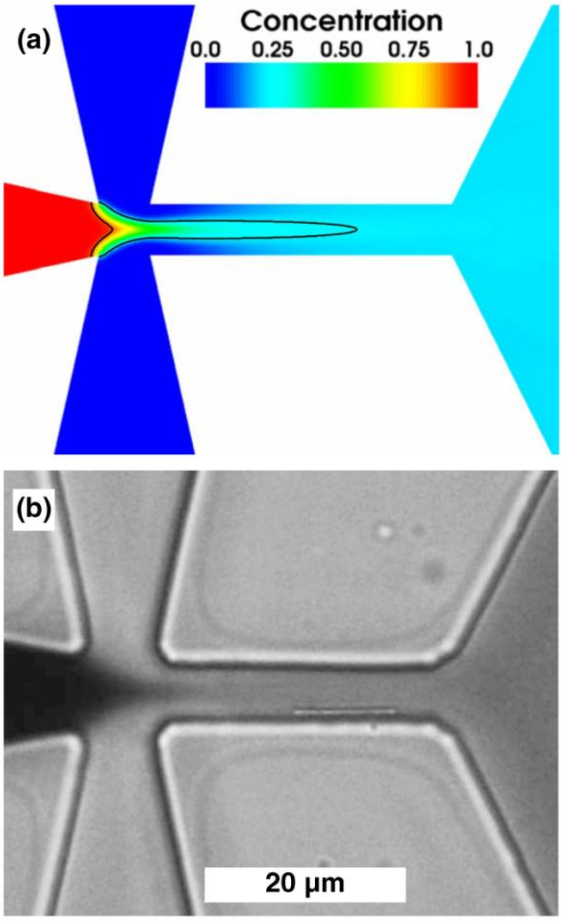

FIG. 3. (Color online) Numerical calculation of flow pattern and photograph of mixing region. Inlet channels narrow from observation areas (see Fig. 2) to an intersection followed by a 5 μm wide mixing channel. The mixing channel widens into the observation channel. (a) Calculation of ink concentration in the mixing pattern. Black lines are contours at 90% of the initial concentration and 110% of the final concentration. (b) Photograph of ink (Quink, Parker) mixing with water in the microfluidic device.

An average outflow velocity of 1 μm/ms results in a value of u_c too high for optimal single-molecule measurements, especially when, to minimize dead-time, observations must be made in a region where the central streamline is still decelerating. If the inlet pressures are reduced to 6.9 kPa, $\tau_m = 2.2$ ms, and at the first observation point $u_c = 2.4\ \mu$m/ms. Single-molecule measurements shown in Fig. 9 were made under these conditions at a point in the observation channel 100 μm downstream from the mixing inter-

TABLE I. Results of numerical mixing calculations (see text). Pressure P_i (relative to the outlet) is applied to the mixer inlets, resulting in mixing delay τ_m, dead time τ_d, and central streamline velocities u_{ci} at the first observation point and u_{cf} in the asymptotic fully developed flow. τ_m and τ_d are defined as the transit times from the 90% contour [see Fig. 3(a)] to the 110% contour and the first observation point (Fig. 2), respectively.

P_i (kPa)	τ_m (ms)	τ_d (ms)	u_{ci} (μm/ms)	u_{cf} (μm/ms)
20.2	1.8	1.8	7.0	3.0
12.4	1.5	3.1	4.3	1.8
6.9	2.2	6.3	2.4	1.0
4.0	4.4	11.7	1.4	0.61
3.0	8.0	18.9	1.0	0.44

section, where u_c had reached its asymptotic value of 1.0 μm/ms. Results from mixer calculations with various inlet pressures are summarized in Table I.

2. Dead time

In a planar mixing device optimized for optical single-molecule measurements, the confocal volume must be located at least half the channel-top light cone diameter ($D/2$ in Fig. 1) from any device wall in order to prevent occlusion of the fluorescence collected by the optical system. Since sample components must be separated by the device prior to mixing, $D/2$ is the minimum distance a mixed sample must travel before optimal observations can be made. The measurement dead time τ_d between the onset of mixing and the first observation is therefore constrained by this distance and the need to reduce u_c to a value on the order of 1 μm/ms (see Sec. II A) at the confocal volume.

With constant u_c, we would have $\tau_d \geq D/2u_c$, and typical values $u_c=1$ μm/ms, $d=5$ μm (Fig. 1), and $A=1.2$ would yield $D=20.9$ μm and $\tau_d \geq 10.5$ ms. In the present mixer design, the first measurement point (Fig. 2) is located well within the hydrodynamic entrance length[40] of the observation channel, so the fluid on the central streamline is decelerating as it passes through the confocal volume. If we define τ_d as the transit time from the 90% contour [see Fig. 3(a)] to the first measurement point, the calculation shown in Fig. 3(a) gives $\tau_d=3.1$ ms (see the second line in Table I). When the inlet pressures are reduced to 6.9 kPa, $\tau_d=6.3$ ms.

To set $u_c=1$ μm/ms at the first measurement point, the inlet pressures must be 3.0 kPa, and $\tau_d=18.9$ ms. Because of deceleration within the entrance length, the minimum dead time for an observation velocity $u_c=1$ μm/ms is obtained with the parameters shown on the fourth line of Table I. In this case, the optimal observation point is actually 4.9 μm beyond the first observation point, and the sample arrives there 16.1 ms after crossing the 90% contour [Note that we have defined τ_d as the time from the 90% contour to the first observation point (11.7 ms). The sample arrives at the first point where $u_c=1.0$ μm/ms in 16.1 ms.].

In ensemble experiments, or if one is willing to suffer loss of signal from single-molecule samples, τ_d can be reduced further by increasing the flow rate. It remains necessary to ensure that $\tau_d \geq \tau_m$. In the present mixer, the 110% contour coincides with the first measurement point ($\tau_d=\tau_m$) under the conditions shown in the first line of Table I.

The dead time limitation resulting from the optical configuration could possibly be overcome in multilayer devices by delivering the mixed sample to the confocal volume vertically.

D. Controllability

Flow in the microfluidic mixer is driven by a compressed air system (see Sec. II E), the resolution of which is limited to approximately 70 Pa (=0.01 PSI). So that the mixing pattern can be balanced, and the volume ratio of mixed fluids will be repeatable, it is necessary to have precise control over inlet flow rates. This can be achieved only if the mixer impedance is sufficient to prevent pressure changes on the order of the system resolution from having significant effects.

The combination of small dimensions and low fluid velocities ensures that flow in the mixer will be laminar (see Sec. II C 1). For channels with constant rectangular cross section, there will be a linear relationship between the driving pressure gradient dp/dx and the volume flow rate Q:[40]

$$Q=\left(-\frac{dp}{dx}\right)\frac{4ba^3}{3\eta}\left[1-\frac{192a}{\pi^5 b}\sum_{k=1,3,5,\ldots}^{\infty}\frac{\tanh(k\pi b/2a)}{k^5}\right], \tag{3}$$

where flow is positive in the $+x$ direction, η is the fluid viscosity, a is the channel half-width, and b is the channel half-height (see Fig. 1). This equation can be recast in a form analogous to Ohm's law,[2]

$$Q=\Delta p/Z, \tag{4}$$

where Δp is the pressure drop along the length L of the channel ($dp/dx=-\Delta p/L$), and the flow impedance Z depends on L,a,b, and η.

For the observation channel (see Sec. II B) in the present mixer, $a=25$ μm, $b=5$ μm, and $L=11$ mm. With $\eta=1$ mPa s (water), the impedance $Z=3.0$ kPa s/nL. The average observation channel flow velocity $\bar{u}=Q/4ab$, so from Eq. (4), $\bar{u}=\Delta p/4abZ$. If we express Δp in kilopascals and Z in kPa s/nL, we have $\bar{u}=2.0\Delta p/Z=0.67\Delta p$ μm/ms. A fluctuation of 70 Pa in Δp would therefore change $\bar{u}$ by $0.67\times 0.07=0.05$ μm/ms, approximately 5% of the nominal observation channel velocity. Precise control over the fluid mixing ratio and outflow velocity clearly requires inlet channel impedances significantly larger than that resulting from the natural dimensions of the observation channel.

The present mixer was designed using the four-terminal lumped impedance model of Knight, *et al.*[2] [Fig. 4(a)]. Parameters were chosen to produce the conditions for a reference experiment in which a solution of protein in 7 M GdmCl denaturant ($\eta=1.92$ mPa s) is mixed with buffer ($\eta=1.0$ mPa s) at a ratio $Q_1/Q_4=0.1$ to initiate folding [It should be noted that in this experiment, rapid dilution, rather than mixing with a triggering reagent, is the goal. This is fundamentally different from the experiments of Knight, *et al.*[2] and similar subsequent work. Complete dilution requires that denaturant from the central inlet be distributed

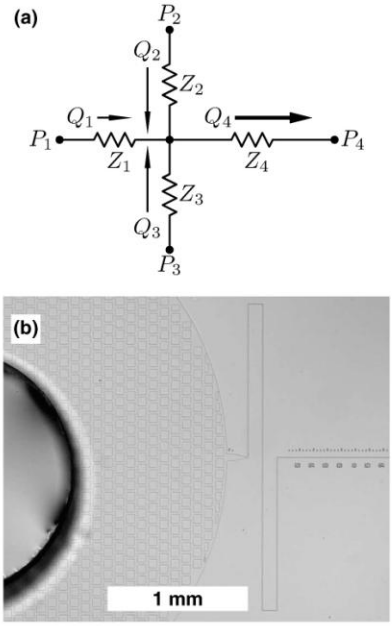

FIG. 4. (a) Four-terminal lumped impedance model used for device design (Ref. 2). Volume flow rates Q_i are proportional to pressure drops and inversely proportional to impedances Z_i, which for uniform rectangular channels are completely determined by fluid viscosity and channel dimensions. (b) Photograph of central inlet region. The fluid inlet, extending through the thickness of the device, is formed by casting to prevent rough edges and damage to the channel pattern. The PTFE post used for this purpose is centered within a large waffle-patterned pad (see text). The 5 μm wide central inlet channel is made to follow a serpentine path, increasing impedance and enabling precise control over flow rates and mixing.

uniformly throughout the entire post-mixing volume, and this must occur within the mixing neck, prior to observations. As shown in Fig. 3, denaturant concentration will have no significant variation across the channel width by the time sample solution enters the observation region (typical denaturant diffusion coefficients are similar to that of the ink seen in the figure).]. The observation channel average velocity is set to 1.0 μm/ms, and the nominal inlet pressures were chosen to be 12.4 kPa. The necessary impedances and resulting channel dimensions are shown in Table II. Tapered junctions and widened observation regions add on the order of 1% to the impedances shown, and have been neglected in the device design. Small pressure adjustments can be made if the design and/or fabrication do not provide sufficient precision for a particular experiment.

TABLE II. Channel dimensions and flow impedances. Values listed are for major segments of the mixer channels. Unlisted segments (tapers and premixing observation regions) add on the order of 1% to the tabulated inlet channel impedances. Impedances vary linearly with viscosity. Those shown here are calculated using η=1.0 mPa s (water). Dimensions a and b are shown in Fig. 1.

Channel	Z (kPa s/nL)	a (μm)	b (μm)	L (mm)
Central inlet	112	2.5	5	8.0
Side inlets	47	3	5	5.3
Mixing neck	0.42	2.5	5	0.030
Observation	3.0	25	5	11.0

Figure 4(b) shows extra length added to an inlet channel for increased impedance. Under the conditions of the design reference experiment, inlet flow rates can be controlled with a precision of approximately 0.6%.

Given a mixer with a predefined set of channel impedances, one can adjust the flow pattern by varying the inlet and outlet pressures. In this manner, a range of values can be chosen for the mixing ratio $m \equiv Q_1/Q_4$ [Fig. 4(a)] and the asymptotic central streamline velocity u_{cf} in the observation channel. Following Knight, *et al.*,[2] we consider a symmetric mixer for which the side inlet pressures $P_2=P_3=P_s$ and impedances $Z_2=Z_3=Z_s$. Analysis of the model yields

$$\frac{P_s - P_4}{P_1 - P_4} = \frac{1 + 2\sigma - m}{2(\sigma + \gamma m)}, \qquad (5)$$

where $\sigma=Z_4/Z_s$ and $\gamma=Z_1/Z_s$. If the inlet pressures are made equal ($P_s=P_1$), Eq. (5) gives the natural mixing ratio for the device,

$$m_0 = \frac{1}{1 + 2\gamma}. \qquad (6)$$

For the present mixer, $m_0=0.17$ for aqueous solutions (η =1.0 mPa s).

The selected value of m fixes the ratio of inlet pressures, leaving one degree of freedom by which u_{cf} may be adjusted,

$$P_1 - P_4 = \quad Z_s(\sigma + m\gamma)u_{\mathrm{cf}}. \qquad (7)$$

Here is a geometry-dependent conversion factor between u_{cf} and the volume flow rate in the observation channel. For the observation channel described in Sec. II B, =0.294 (nL/s)$\times$(μm/ms)$^{-1}$.

For a given set of channel impedances, pressures must be chosen so that flow is not reversed in the inlets or outlet.[2] Setting $m=0$ and $m=1$ in Eq. (5) gives

$$\frac{\sigma}{\sigma + \gamma} < \frac{P_s - P_4}{P_1 - P_4} < \frac{1 + 2\sigma}{2\sigma}. \qquad (8)$$

Because of relatively low overall flow rates in single-molecule measurements, care must be taken to prevent premature mixing by diffusion into the inlet channels. This effect determines the usable lower bound on m in the present mixer, and is partly responsible for the increased values of τ_m and τ_d seen in the last line of Table I.

It should also be noted that diffusion will eventually erode the correspondence, initially provided by u_c, between position along the observation channel and time since mixing. Sample molecules will diffuse along the flow axis, and will arrive in the confocal volume after having explored slower off-axis streamlines. In the observation channel of the present mixer (Figs. 1 and 2), the sample distribution passes through a number of qualitatively different stages. Molecules in the central mixing jet first diffuse across the vertical extent of the channel ($t \approx b^2/2\mathcal{D}_s$, on the order of hundreds of milliseconds, where $\mathcal{D}_s$ is the sample diffusion constant), and later fill the entire channel ($t \approx a^2/2\mathcal{D}_s$, on the order of seconds). Eventually the solution reaches an asymptotic limit of uniform sample concentration across the observation channel

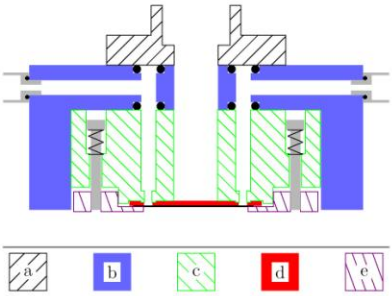

FIG. 5. (Color online) Interface cross section. (a) Removable pressure cap with optical port. (b) Aluminum pressure manifold. (c) PTFE chip carrier with sample wells. (d) PDMS microfluidic device bonded to coverglass. (e) Spring-loaded aluminum clamping plate. Screws holding the chip carrier in the manifold are not visible in this section.

cross section, and the arrival time distribution in any confocal volume will be very broad. If precise knowledge of this distribution is required, a careful analysis of the relationship between diffusion and the laminar flow profile must be carried out.[42]

E. Interface

The interface for the microfluidic mixer was developed with goals of precise flow control, access for high numerical aperture optics, broad chemical compatibility, and rapid exchange of both sample solutions and mounted mixing devices.

Fluid flow is driven by compressed air, which enables precise control over a wide range of flow rates on the order of nanoliters per second. The building compressed air supply (>1000 kPa) is passed through an in-line filter and reduced to 140 kPa using a general-purpose step-down regulator (Marsh-Bellofram Type 40, #960 065 000). The output of the step-down regulator supplies four precision mechanical regulators (Marsh-Bellofram Type 10LR, #960 053 000, 3.45 172 kPa range, 0.1% accuracy), each equipped with a digital pressure gauge (Cecomp Electronics DPG1000B5PSIG). Within the range from 3.5 to 34 kPa, the four pressure outputs can be adjusted with a precision of approximately 70 Pa, and an absolute accuracy, constrained by the gauges, of approximately 150 Pa.

The PDMS microfluidic mixer, bonded to a fused-silica coverglass, is clamped to a polytetrafluoroethylene (PTFE) chip carrier with integral sample wells (Figs. 5 and 6). Clamping force is provided by an adjustable spring-loaded anodized aluminum plate containing a window large enough to allow access by high numerical aperture microscope objectives. Raised circular bosses at the sample well outlets seal against the back side of the PDMS device, forming pressure-tight connections to the fluid inlet holes [Fig. 4(b)].

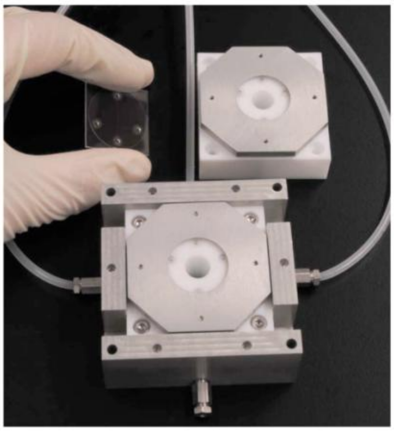

FIG. 6. (Color online) Assembled microfluidic mixing system (compare to Fig. 5). A microfabricated PDMS device, bonded to a fused-silica coverslip, is held against the PTFE chip carrier by a spring-loaded clamping plate. A large window in the clamping plate allows access for a microscope objective with high numerical aperture. Raised bosses around the chip carrier sample well outlets form seals with the inlets on the back side of the mixing device. Face-type static O-ring seals (Fig. 5) allow chip carriers with mounted devices to be rapidly swapped into and out of the aluminum pressure manifold.

The chip carrier is mounted in an anodized aluminum pressure manifold, and connected using face-type static O-ring seals. Once the mixer and interface are in place on a microscope (Fig. 7), the removable pressure cap allows fluids to be placed directly in the sample wells using gel-loading pipette tips. With the cap in place, pressure from the regulators, delivered via tubing connectors on the sides of the manifold (Figs. 5 and 7), can be applied to the sample wells.

A port, extending through the pressure cap, manifold, and chip carrier, enables illumination and observation of the back side of the mixer. Chip carriers, manifolds, pressure caps, and clamping plates were fabricated using a numerically controlled milling machine.

III. DEVICE FABRICATION

Device fabrication consists of four steps: generation of the mixer pattern, creation of a microfabricated mold in silicon, replica molding of PDMS devices, and final assembly.

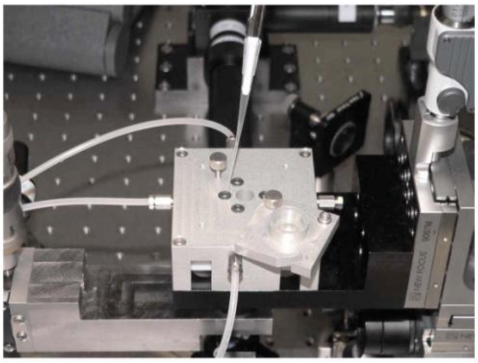

FIG. 7. (Color online) Mixing system mounted on single-molecule instrument. The removable pressure cap enables sample exchange using gel-loading pipette tips. Tubing connected to the aluminum manifold delivers precision-regulated compressed air for driving flow in the microfluidic mixer. The microscope objective (not visible) screws into the stainless steel beam below and to the left of the mixing system.

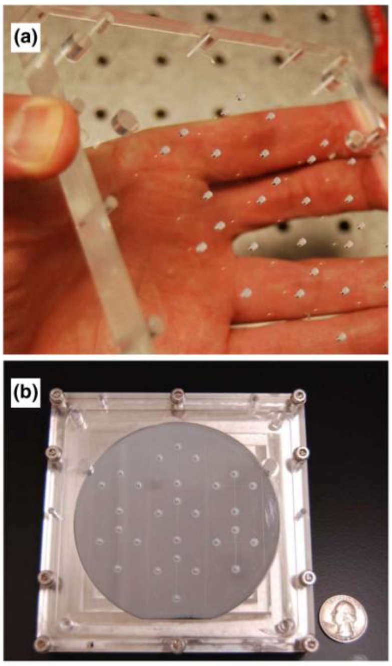

FIG. 8. (Color online) Composite casting dish. (a) PTFE posts embedded in the lid are used to cast smooth fluid inlets through the PDMS devices. (b) Complete casting assembly. When the lid is screwed down, inlet posts make firm contact with the silicon wafer. PDMS flows into the mold through holes near lid corners. The current design fits seven 27×27 mm^2 devices on a 100 mm diameter silicon wafer.

A. Mask generation

The channel pattern is drawn using computer-aided design software (DesignCAD, IMSI Design), and exported to a mask writer (DWL 66, Heidelberg Instruments) in DXF format. The pattern is written in AZ1518 (AZ Electronic Materials, Branchburg, NJ) photoresist on a chrome-plated soda-lime glass blank (Nanofilm Inc., Westlake Village, CA). Exposed photoresist is selectively removed with a 1:4 dilution of AZ400K developer in de-ionized water, and the remaining photoresist is used as a chemical etch mask for the chrome coating.

B. Silicon master creation

Masters for replica-molding must have their channel patterns aligned with the casting dish and lid (Fig. 8) in order to ensure proper placement of fluid inlets. Prior to photolithography, silicon wafers are screwed down into a form-fitting indentation in the casting dish, and reference marks are diamond-scribed on the wafers using a guide that is mechanically aligned with the dish.

After they are scribed, the wafers are immersed in piranha solution (1:5 v/v 30% hydrogen peroxide in concentrated sulfuric acid at 120 °C) for 20 min, thoroughly rinsed with de-ionized water, blown dry with nitrogen, and baked at 200 °C for 10 min to remove residual water.

Scribed and cleaned wafers are spin-coated with AZ5214-IR photoresist at 4000 RPM for 30 s, then soft-baked on a 95 °C hot plate for 60 s. A mask aligner (MA6, Karl Suss) is used to match scribed reference marks with corresponding marks in the chrome mask pattern, and the photoresist is exposed through the mask with 75 mJ/cm^2 of mercury I-line UV light.

Wafers and resist are given a post-exposure bake at 110 °C for 60 s, followed by a 450 mJ/cm^2 flood exposure. The photoresist is developed in a 1:4 dilution of AZ400K in de-ionized water for 45 s. Remaining photoresist, corresponding to the initial UV exposure pattern, is hardened at 200 °C for 10 min, removing any residual solvents in the process.

Bosch-process[43] deep reactive-ion etching was performed with an inductively coupled plasma system (Plasma-Therm 770) until the pattern depth reached 10 μm (approximately 8 min). Side-wall scalloping was negligible compared with channel dimensions. Feature heights were verified using a profilometry system (Dektak IIA, Veeco) prior to casting.

C. Device casting

In order to prevent PDMS adhesion, the silicon master must be chemically treated. The etched wafer is cleaned in piranha solution (see above) to remove residual photoresist, rinsed in distilled water, blown dry, and dehydrated at 200 °C for 10 min. Prior to each casting, the wafer is placed in a sealed Petri dish with a drop of trimethyl chlorosilane (TMCS) for 1 h. Because of its high vapor pressure, TMCS fills the reaction container. It reacts with the native silicon oxide layer on the wafer, coating the exposed surface with methyl groups that do not bond to PDMS as the oxide layer would.[44] This and all subsequent casting and assembly procedures can be performed outside of a cleanroom environment.

Following TMCS treatment, the patterned wafer is placed into a form-fitting cutout in the stainless steel casting dish [Fig. 8(b)], and held down with nylon screws. The depth of the cutout is such that after assembly, a 1 mm gap, defining the device thickness, is left between the top of the wafer and the bottom of the lid.

The casting assembly lid [Fig. 8(a)] is machined from clear acrylic. PTFE posts, cut from 1.6 mm diameter cord stock (McMaster-Carr Supply Co.), are embedded in milled holes that match fluid inlet positions on the wafer. When screwed down to the dish, the lid forces the posts into conformal contact with the wafer. Resulting smooth-edged fluid feeds in the cast devices eliminate the need for punching, which could damage or block the relatively shallow channels in the mixing devices. To minimize alignment problems, the silicon mold is designed with waffle-pattern inlet pads several millimeters in diameter [Fig. 4(b)]. The channels in the pattern have a relatively small width-to-height aspect ratio, which prevents collapse of the elastomeric device onto the coverglass. In addition, large particles in the incoming fluid are trapped, and a low-impedance path from the fluid inlet to the channel is ensured.

For casting, ten parts by weight of PDMS (RTV615, General Electric) are mixed with one part of crosslinking agent. The mixture is stirred for 5 min, then degassed in a vacuum desiccator for 40 min. Air is frequently bled into the desiccator to break bubbles. Degassed PDMS is slowly poured through a 4 mm diameter funnel into a hole near the corner of the casting assembly lid [Fig. 8(b)], allowing most remaining air bubbles to float to the surface rather than entering the assembly. Once the mold is filled, the assembly is placed on an 80 °C hot plate to cure for 5 h.

After curing is completed, the lid is removed and individual devices are diced in place using a scalpel guided by etched borders on the wafer. Devices are left on the mold until they are mounted in order to minimize exposure of channel surfaces to airborne dust. For repeatable damage-free removal, a spatula-tipped tweezer is used to lift a few millimeters of the device around its entire perimeter, after which it is slowly peeled away from the wafer. Tweezer contact with patterned areas of the device must be avoided to prevent contamination.

D. Device assembly

The fourth wall of the cast microfluidic channels is provided by a fused-silica coverglass (see Sec. II A). Untreated PDMS is hydrophobic, which can make micron-scale channels difficult to fill with aqueous solutions. Pretreatment of the coverglass with piranha solution (see Sec. III B) or air plasma will remove fluorescent contaminants and make a sufficient fraction of the channel surface hydrophilic to enable low-pressure device loading.

For conformal contact bonding (Sec. II A), the coverglass (e.g., R425000, www.escoproducts.com) is cleaned with piranha solution as described in Sec. III B, rinsed in distilled water, and blown dry. It is then immediately brought into contact with the PDMS portion of the device. After use, the PDMS can be peeled off and discarded, allowing reuse of the relatively expensive fused-silica coverglass.

If high driving pressures (High-speed ensemble measurements in the microfluidic mixer can be compared with, for example, data from a commercial stopped-flow system.) or sample solutions that disrupt noncovalent contact bonding are to be used, a permanent PDMS-coverglass bond can be made using an air or oxygen plasma.[22] In this case, the coverglass is mechanically cleaned sequentially with detergent, acetone, isopropanol, and distilled water, blown dry, and exposed to plasma for 10 min (18 W at 10 MHz as produced in 40 Pa of air by a Harrick PDC-32G plasma cleaner). The coverglass is then mechanically cleaned with methanol to remove any remaining residue, and stored under distilled water to prevent contamination. Prior to bonding, the coverglass is blown dry and returned to the plasma cleaner along with a PDMS device placed so that the channels are exposed. The cleaner is then run with 40 Pa air at 7 W for 20 s. The plasma-treated sides of the coverglass and PDMS device are immediately brought into contact, and air bubbles are removed by applying light pressure with a cleanroom swab. Bonded devices can typically be used 1 h after assembly.

IV. SINGLE-MOLECULE DETECTION

Single-molecule measurements in the microfluidic mixer were performed using a custom-designed modular confocal microscope[29,30] (Fig. 7). A 488 nm continuous-wave laser (Coherent Sapphire) was reduced to 145 μW using absorptive neutral density filters, and focused in the observation channel using a water immersion microscope objective (Olympus UPLSAPO 60XW, 60×, $A=1.2$). The focal volume was placed at the center of the observation channel (as shown in Fig. 1) using reflections from the coverglass-water and water-PDMS interfaces.

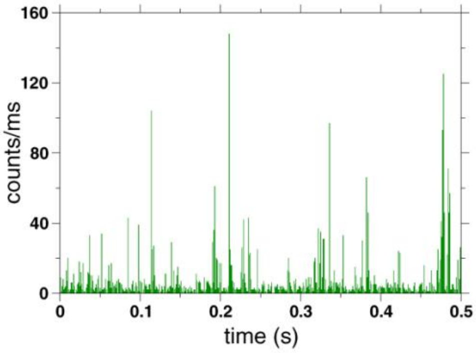

FIG. 9. (Color online) Fluorescence measurement in the microfluidic mixer. Single-molecule bursts are seen as a 15 pM solution of Alexa Fluor 488 hydrazide dye in distilled water flows through the confocal detection volume at the center of the observation channel. The solution is fed into all three inlets at a pressure of 6.9 kPa with respect to the outlet. Under these conditions, the flow velocity at the confocal volume, located 100 μm downstream from the mixing intersection, is 1.0 mm/s (=1.0 μm/ms). The measured background level is 1.1 ms^{-1}.

A 15 pM solution of Alexa Fluor 488 hydrazide dye (Invitrogen-Molecular Probes) in distilled water was delivered at 6.9 kPa to all three mixer inlets. The resulting asymptotic central streamline velocity in the observation channel was 1.0 μm/ms. The focal volume was placed in the fully developed flow 100 μm downstream from the mixing region.

Fluorescence from individual molecules passing through the focal volume was collected by the same objective used for excitation, and passed through an excitation beamsplitter (Omega 505DRLP, XF2010), tube lens, long-pass filter (Omega 493AELP, XR3000), and 100 μm confocal pinhole. The remaining signal was then reflected from a second dichroic beamsplitter (Omega 560DCLP, XF2016), filtered one last time (Chroma D525/50m), and focused on a photon-counting avalanche photodiode detector (PerkinElmer SPCM-AQR-16). Pulses from the detector module were collected by a 100 ps time digitizer (Ortec 9353), and photon arrival times were stored on a computer.

Data gathered into 1 ms bins are shown in Fig. 9. Single-molecule events are clearly visible, and the fluorescence background level (Background levels were determined by using parabolic fits to the peaks of the binned-signal histograms.) is 1.1 ms^{-1}. For the largest events, the signal-to-noise ratio exceeds 100 in 1 ms. Background levels in previous experiments[16] were 3–10 times higher, depending on the detection wavelength.

V. OUTLOOK

Although designed with protein folding experiments in mind, the microfluidic mixing system we have described is flexible, and well-suited to a wide variety of measurements requiring rapid mixing and ultrasensitive light detection. In some applications, this technology will be able to replace conventional methods requiring sample volumes many orders of magnitude larger. For example, measurements of the firefly luciferin-luciferase reaction and its kinetics (to be published elsewhere) can be made with approximately one thousandth the sample volume used in a typical luminometer.

The device fabrication method and interface presented here will readily accommodate new mixer designs. Incorporation of sophisticated fluid handling[24,45] and three-dimensional fabrication can be expected to enhance the performance and utility of high-sensitivity optical measurements in future microfluidic mixers.

ACKNOWLEDGMENTS

We thank Benjamin Schuler for extensive testing of the microfluidic system and many valuable suggestions. We thank David Wood, Andrew Cleland, Stephen Quake, and Todd Squires for enlightening discussions and suggestions. Support for this work was provided by the Human Frontier Science Program and the DMEA Center for Nanoscience Innovation for Defense. A portion of this work was done in the UCSB nanofabrication facility, part of the NSF-funded NNIN network. E.A.L. is an Alfred P. Sloan research fellow.

[1] J. P. Brody, P. Yager, R. E. Goldstein, and R. H. Austin, Biophys. J. **71**, 3430 (1996).
[2] J. B. Knight, A. Vishwanath, J. P. Brody, and R. H. Austin, Phys. Rev. Lett. **80**, 3863 (1998).
[3] S. A. Pabit and S. J. Hagen, Biophys. J. **83**, 2872 (2002).
[4] D. E. Hertzog, X. Michalet, M. Jager, X. X. Kong, J. G. Santiago, S. Weiss, and O. Bakajin, Anal. Chem. **76**, 7169 (2004).
[5] M. B. Kerby, J. Lee, J. Ziperstein, and A. Tripathi, Biotechnol. Prog. **22**, 1416 (2006).
[6] D. J. Bornhop, J. C. Latham, A. Kussrow, D. A. Markov, R. D. Jones, and H. S. Sorensen, Science **317**, 1732 (2007).
[7] H. Y. Park, S. A. Kim, J. Korlach, E. Rhoades, L. W. Kwok, W. R. Zipfell, M. N. Waxham, W. W. Webb, and L. Pollack, Proc. Natl. Acad. Sci. U.S.A. **105**, 542 (2008).
[8] B. Chance, Rev. Sci. Instrum. **22**, 619 (1951).
[9] P. Davidovits and S. C. Chao, Anal. Chem. **52**, 2435 (1980).
[10] P. Regenfuss, R. M. Clegg, M. J. Fulwyler, F. J. Barrantes, and T. M. Jovin, Rev. Sci. Instrum. **56**, 283 (1985).
[11] E. B. Shera, N. K. Seitzinger, L. M. Davis, R. A. Keller, and S. A. Soper, Chem. Phys. Lett. **174**, 553 (1990).
[12] T. Ha, T. Enderle, D. F. Ogletree, D. S. Chemla, P. R. Selvin, and S. Weiss, Proc. Natl. Acad. Sci. U.S.A. **93**, 6264 (1996).
[13] S. Weiss, Science **283**, 1676 (1999).
[14] C. Zander, J. Enderlein, and R. A. Keller, *Single Molecule Detection in Solution* (Wiley, Berlin, 2002).
[15] C. Gell, D. Brockwell, and A. Smith, *Handbook of Single Molecule Fluorescence Spectroscopy* (Oxford University, Oxford, 2006).
[16] E. A. Lipman, B. Schuler, O. Bakajin, and W. A. Eaton, Science **301**, 1233 (2003).
[17] P. S. Dittrich, B. Muller, and P. Schwille, Phys. Chem. Chem. Phys. **6**, 4416 (2004).
[18] P. S. Dittrich and A. Manz, Anal. Bioanal. Chem. **382**, 1771 (2005).
[19] S. S. White, S. Balasubramanian, D. Klenerman, and L. M. Ying, Angew. Chem., Int. Ed. **45**, 7540 (2006).
[20] K. M. Hamadani and S. Weiss, Biophys. J. **95**, 352 (2008).
[21] D. Liao, P. Galajda, R. Riehn, R. Ilic, J. L. Puchalla, H. G. Yu, H. G. Craighead, and R. H. Austin, Opt. Express **16**, 10077 (2008).
[22] D. C. Duffy, J. C. McDonald, O. J. A. Schueller, and G. M. Whitesides, Anal. Chem. **70**, 4974 (1998).
[23] Y. N. Xia and G. M. Whitesides, Angew. Chem., Int. Ed. **37**, 550 (1998).
[24] M. A. Unger, H. P. Chou, T. Thorsen, A. Scherer, and S. R. Quake, Science **288**, 113 (2000).
[25] M. Elwenspoek and H. Jansen, *Silicon Micromachining* (Cambridge University, Cambridge, 1998).
[26] P. S. Shaw, K. R. Lykke, R. Gupta, T. R. O Brian, U. Arp, H. H. White, T. B. Lucatorto, J. L. Dehmer, and A. C. Parr, Appl. Opt. **38**, 18 (1999).
[27] N. Neuroth, in *The Properties of Optical Glass*, edited by H. Bach and N. Neuroth (Springer, Berlin, 1995), Chap. 2, pp. 82 96.
[28] S. G. Kaplan, L. M. Hanssen, E. A. Early, M. E. Nadal, and D. Allen, Metrologia **39**, 157 (2002).
[29] B. Schuler, E. A. Lipman, and W. A. Eaton, Nature (London) **419**, 743 (2002).
[30] B. Schuler, E. A. Lipman, P. J. Steinbach, M. Kumke, and W. A. Eaton, Proc. Natl. Acad. Sci. U.S.A. **102**, 2754 (2005).
[31] J. C. McDonald and G. M. Whitesides, Acc. Chem. Res. **35**, 491 (2002).
[32] D. K. Cai, A. Neyer, R. Kuckuk, and H. M. Heise, Opt. Mater. (Amsterdam, Neth.) **30**, 1157 (2008).
[33] J. N. Lee, C. Park, and G. M. Whitesides, Anal. Chem. **75**, 6544 (2003).
[34] S. K. Sia and G. M. Whitesides, Electrophoresis **24**, 3563 (2003).
[35] H. P. Chou, C. Spence, A. Scherer, and S. Quake, Proc. Natl. Acad. Sci. U.S.A. **96**, 11 (1999).
[36] J. C. McDonald, D. C. Duffy, J. R. Anderson, D. T. Chiu, H. K. Wu, O. J. A. Schueller, and G. M. Whitesides, Electrophoresis **21**, 27 (2000).
[37] K. Haubert, T. Drier, and D. Beebe, Lab Chip **6**, 1548 (2006).
[38] L. Chen, J. C. Ren, R. Bi, and D. Chen, Electrophoresis **25**, 914 (2004).
[39] S. Satyanarayana, R. N. Karnik, and A. Majumdar, J. Microelectromech. Syst. **14**, 392 (2005).
[40] F. White, *Viscous Fluid Flow*, 2nd ed. (McGraw Hill, Boston, Massachusetts, 1991).
[41] T. M. Squires and S. R. Quake, Rev. Mod. Phys. **77**, 977 (2005).
[42] R. Mauri and S. Haber, SIAM J. Appl. Math. **51**, 1538 (1991).
[43] F. Laermer and A. Schlip, *Method of Anisotropically Etching Silicon*, U.S. Patent No. 5501893 (1996).
[44] S. Biggs and F. Grieser, J. Colloid Interface Sci. **165**, 425 (1994).
[45] J. Melin and S. R. Quake, Annu. Rev. Biophys. Biomol. Struct. **36**, 213 (2007).

4.2 MEASURING SINGLE-MOLECULE KINETICS IN MILLISECONDS

(Manuscript in preparation)

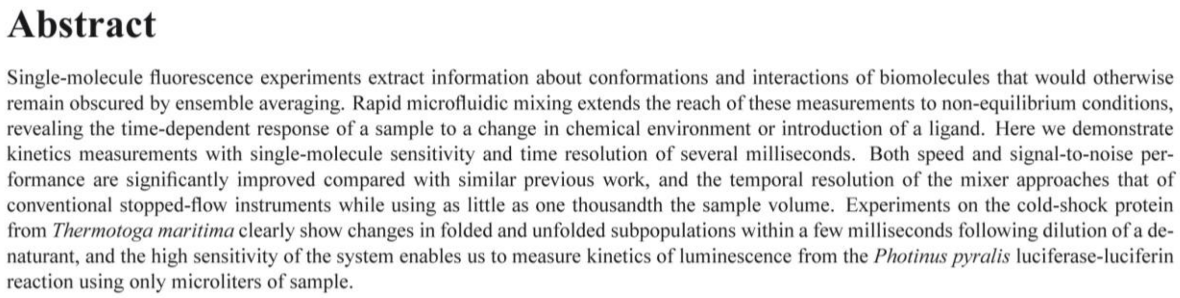

Abstract

Single-molecule fluorescence experiments extract information about conformations and interactions of biomolecules that would otherwise remain obscured by ensemble averaging. Rapid microfluidic mixing extends the reach of these measurements to non-equilibrium conditions, revealing the time-dependent response of a sample to a change in chemical environment or introduction of a ligand. Here we demonstrate kinetics measurements with single-molecule sensitivity and time resolution of several milliseconds. Both speed and signal-to-noise performance are significantly improved compared with similar previous work, and the temporal resolution of the mixer approaches that of conventional stopped-flow instruments while using as little as one thousandth the sample volume. Experiments on the cold-shock protein from *Thermotoga maritima* clearly show changes in folded and unfolded subpopulations within a few milliseconds following dilution of a denaturant, and the high sensitivity of the system enables us to measure kinetics of luminescence from the *Photinus pyralis* luciferase-luciferin reaction using only microliters of sample.

Measuring Single-Molecule Kinetics in Milliseconds

Shawn H. Pfeil,[†,§] Armin Hoffmann,[‡] Charles E. Wickersham,[†] Benjamin Schuler,[‡] and Everett A. Lipman[*,†,¶]

Department of Physics, University of California, Santa Barbara, California 93106, Biochemisches Institut, Universität Zürich, Winterthurerstrasse 190, 8057 Zürich, Switzerland, and Program in Biomolecular Science and Engineering, University of California, Santa Barbara, California 93106, USA

Macromolecular folding and binding are the essence of life at the smallest scales. In order to study the kinetics of these processes, it is necessary to prepare samples out of equilibrium, and to then make measurements with minimal delay and sufficient time resolution to observe changes as new conformations or states are adopted. Non-equilibrium conditions can be produced using a variety of methods, for example pressure and temperature jumps, however the versatility of rapid solvent exchange is unmatched. Conventional ensemble experiments employ fluorescence, circular dichroism, and other spectroscopic techniques in turbulent stopped-flow mixers,[1–4] which typically provide millisecond resolution using milliliters of sample. Microfluidic mixers[5–12] enable ensemble measurements with dead times from a few microseconds to several milliseconds,[13–15] consuming only microliters of solution. These continuous-flow devices decouple measurement duration from reaction progress, allowing extended signal averaging at a point in the mixer outlet corresponding to a fixed time after mixing.

The combination of microfluidic mixers with single-molecule fluorescence detection[16–22] can reveal properties of transient subpopulations, such as unfolded protein under native conditions, that would be obscured by ensemble averaging in traditional experiments. In the first measurement of this type,[16] cold shock protein (Csp) from *Thermotoga maritima* in 4 M guanidinium hydrochloride (GdmCl) denaturant was refolded by dilution to 1 M GdmCl. Csp is a 7.5 kDa β-barrel protein exhibiting two-state folding thermodynamics and millisecond kinetics.[23,24] End-to-end distance measurements using single-molecule Förster resonance energy transfer[25] (FRET) enabled unambiguous observation of an initial unfolded state collapse followed by a slower shift of population to the distinct folded state. Because of the relatively high residual denaturant concentration, folding proceeded far more slowly than it would under native conditions, and the design of the mixer precluded reliable measurements at times less than 100 ms. Background noise significantly broadened the observed FRET efficiency peaks corresponding to the folded and unfolded states.

Subsequently, capillary-based single-molecule mixers were developed by White et al.[18] and Hamadani and Weiss,[19] the latter employing 3-dimensional flow focusing and achieving substantially improved time resolution, with a 90% reduction in denaturant concentration as early as 19 ms. A mixer recently described by Lemke et al.[21] introduced a mechanism for sample deoxygenation by diffusion through the device walls. Though not optimized for high time resolution, this mixer is a significant advance, since deoxygenation greatly improves the photostability of fluorescent dyes, and the use of enzymatic oxygen scavenging systems in conjunction with denaturants is difficult or impossible.

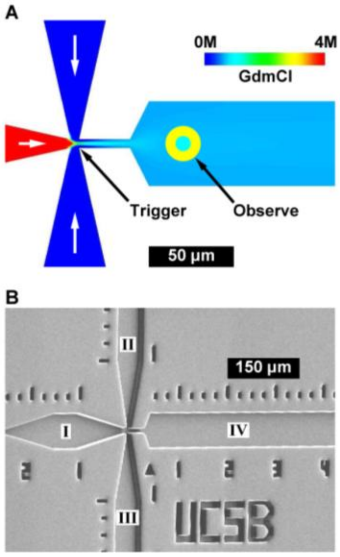

Figure 1. Microfluidic mixer. (A) Numerical calculation of the denaturant concentration resulting from flow and diffusion in a protein refolding experiment. The laser beam (inner circle) and cone of collected fluorescence (outer circle) are drawn to scale intersecting the channel-coverglass interface at a typical observation point. (B) Scanning electron micrograph showing central inlet (I), side inlets (II,III), and observation channel (IV). A small triangle below the observation channel marks the position of earliest observation.

Until now, the greatly increased information content of these measurements has come at the cost of poor time resolution and/or low signal quality relative to what can be obtained in ensemble experiments. Here we demonstrate the capabilities of a microfluidic mixing system, recently used to collect sub-100 ms data in a study of chaperone-mediated protein folding,[22] enabling single-molecule measurements with time resolution approaching that of stopped flow. The mixing device (Figure 1) is replica-molded in polydimethylsiloxane and bonded to a fused-silica coverglass, which minimizes background fluorescence. Observation regions are designed to allow unobstructed collection of a 1.2 numerical aperture light cone down to the full depth of the channels along their central axes. Detailed descriptions of the design, fabrication, interfacing, and modeling of this mixer are given in Ref. 20. The rapid mixing and high dilution ratios provided by this device enable single-molecule FRET measurements of Csp folding under near-native conditions with dead times of several milliseconds. Low noise

---

[†] Department of Physics, University of California, Santa Barbara, California 93106

[‡] Biochemisches Institut, Universität Zürich, Winterthurerstrasse 190, 8057 Zürich, Switzerland

[¶] Program in Biomolecular Science and Engineering, University of California, Santa Barbara, California 93106, USA

[§] Current address: Pennsylvania Muscle Institute, University of Pennsylvania, Philadelphia, Pennsylvania 19104

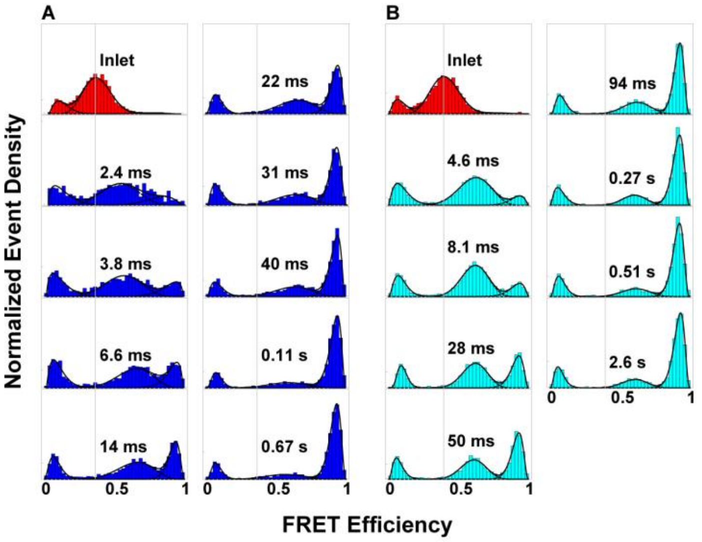

Figure 2. Single-molecule refolding kinetics of cold-shock protein from *Thermotoga maritima*. Histograms of FRET efficiency E display changes in unfolded ($E \approx 0.35$–0.65) and folded ($E \approx 1$) populations. Peaks seen near $E = 0$ are caused by sample molecules with inactive acceptor dyes. Fit curves are generalized beta distributions. (A) Dilution from 4 M to 0.2 M guanidinium chloride (GdmCl) denaturant. Mixing is 95% complete by 2.4 ms, and 98% complete by 6.6 ms. (B) Dilution from 4 M to 0.4 M GdmCl. Mixing is 97% complete by 4.6 ms. See Supporting Information for experimental parameters and data analysis.

ensures clear separation of signal peaks corresponding to folded and unfolded states. Measurements of chemiluminescence from the *Photinus pyralis* luciferase-luciferin reaction using only microliters of sample demonstrate high optical collection efficiency and the potential for diagnostic use of microfluidic mixers with single-molecule sensitivity.

For protein refolding kinetics measurements, Csp labeled with donor and acceptor dyes (Alexa Fluor 488 and Alexa Fluor 594 as described by Schuler et al.[24]) was denatured in 4 M GdmCl and placed in the central mixer inlet (Figure 1). Side inlets were filled with refolding buffer, and flow through the mixer was driven by precision-regulated compressed air. Mixing ratios and flow speeds were selected by adjusting the pressures applied to the mixer inlets (see Supporting Information for buffer compositions and experimental parameters). A confocal detection volume illuminated with a 488 nm laser was placed in the observation channel at a position corresponding to the desired delay after mixing. For individual labeled protein molecules passing through the detection volume, donor and acceptor fluorescence were measured by photon counting, and a FRET efficiency was calculated. Histograms of the resulting efficiency values are shown in Figure 2.

Figure 2A shows data from dilution of GdmCl by a factor of 20. Mixing is 98% complete by 6.6 ms, and under these near-native conditions folding proceeds rapidly. As described previously,[20] there is a tradeoff between time resolution and signal quality. The confocal volume must be placed sufficiently far from mixer walls to prevent obstruction of the collected light cone (Figure 1), while high flow speeds, which carry the sample quickly to the observation point, limit the duration of diffusive mixing and reduce observation time, increasing the effect of shot noise. The earliest observation, at 2.4 ms, has lower signal quality than subsequent measurements, but clearly shows population in the folded state, as well as a significant change in the average size of the unfolded state. Reconfiguration of Csp on distance scales comparable to the size of the unfolded protein has been shown to take approximately 50 ns.[26] If unfolded state collapse[16,24] requires a similar time, its onset is far too fast to observe in these experiments. The progress of the unfolded peak shift seen at 2.4 ms is consistent with calculations[20] that show mixing to be 95% complete at this point, and with observations of Hamadani and Weiss[19] made prior to the completion of mixing. No significant unfolded state collapse is observed after 6.6 ms.

Figure 2B shows the effect of denaturant dilution by a factor of 10, where higher asymptotic concentration results in slower folding. Mixing is 97% complete by 4.6 ms, and no significant collapse is seen after this time.

The folded state of Csp is expected to produce a single consistent value of the FRET efficiency, so the width of the corresponding peak serves as an indication of the measurement uncertainty. Folded-state peak widths shown in Figure 2 exceed the shot noise limit by an average of only **XX**%. This substantial improvement over previous similar experiments is necessary for precise determination of populations, and will enable measurements of transient states in future studies of proteins with complex folding behavior.

While the diffusion of small denaturant molecules is rapid, the relatively large Csp molecules take far longer to mix, and the slight unfolded state expansions in the final histograms of each series may indicate a bias for diffusion of more compact sample molecules out of the central streamline where observations take place.

As shown in Figure 3, predictions of a two-state kinetic model fit the folded population fractions determined from single-molecule FRET histograms (see Supporting Information). The observed rate constants ($42 \pm 1\ \mathrm{s}^{-1}$ and $21 \pm 1\ \mathrm{s}^{-1}$ for 0.2 M and 0.4 M final GdmCl concentrations, respectively) are consistent with previously reported ensemble folding measurements.[16]

Many of the benefits of the present mixer, including ultrasensitive light detection and low sample consumption, are applicable to chemiluminescent detection. Unlike single-molecule fluorescence, chemiluminescence can be detected in complex, autofluorescent samples,[27] and is therefore promising for clinical applications. If luminescence kinetics can be measured, multiplexed detection becomes possible.[28] We have used the microfluidic mixer to observe the luciferase-luciferin reaction from *Photinus pyralis*, monitoring

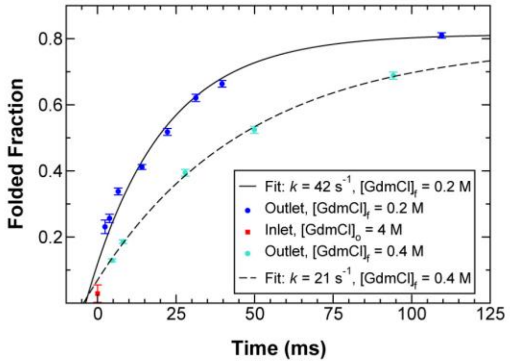

Figure 3. Protein folding rate constant determination. Unfolded and folded populations were determined from fits to histograms in Figure 2, and two-state kinetic models were fit to the resulting folded-fraction data.

reaction kinetics and detecting minute quantities of ATP.

For kinetics measurements, luciferase is incubated in a saturating concentration of luciferin, and this combination is then rapidly mixed with an excess of ATP. Following an initial lag in light production lasting approximately 25 ms, there is a rapid increase in output, peaking near 300 ms, and finally a non-exponential decay caused by product inhibition.[29,30] Figure 4 shows data from both microfluidic mixer and conventional stopped flow measurements, using identical final solution conditions (see Supporting Information). Though it uses approximately one thousandth the sample consumed by the stopped flow instrument, the mixer produces a reliable measurement of the reaction kinetics. Mixer data yield an intensity peak at 310 ± 30 ms, corresponding to the peak at 312 ms obtained with stopped-flow.

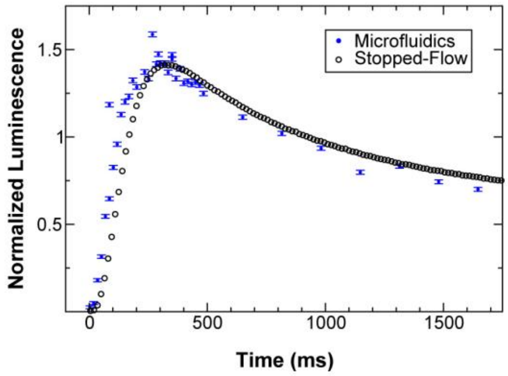

Figure 4. Kinetics of firefly luciferase/luciferin reaction. Microfluidic mixer data were acquired using microliters of sample. Measured luminescence is shown normalized by the area under the curve during the first 1.5 s.

Because of the linear relationship between the height of the luminescence intensity peak and the concentration of ATP, the luciferase-luciferin reaction can be used to measure this concentration.[29] We performed a series of measurements in the mixer to quantify our sensitivity to ATP with other reagents in excess. Under typical flow conditions, concentrations as low as 10 nM could be detected using only 3.6 femtomoles per data point (see Supporting Information), roughly the amount contained in a single human cell. To adequately sample chemiluminescence kinetics, approximately ten data points are needed, requiring 40 femtomoles of ATP. This compares favorably with stopped-flow measurements consuming picomoles.[31]

Measurements of the type we have demonstrated could readily be adapted to make possible single-molecule versions of microfluidic quench-flow experiments.[32] With multiple confocal detection volumes[33] along the mixer observation channel, it should be possible with ultra-low sample concentrations to follow the progress of individual folding proteins. The resulting data would provide conditional probabilities of state-to-state transitions[34] at selected times after the initiation of folding, and would be equivalent to a "trail map" through the free energy landscape. Such information would enable direct comparison with numerical simulations.

References

(1) Chance, B. *Rev. Sci. Instrum.* **1951**, *22*, 619–627.
(2) Chance, B.; Legallais, V. *Rev. Sci. Instrum.* **1951**, *22*, 627–634.
(3) Magg, C.; Schmid, F. X. *J. Mol. Biol.* **2004**, *335*, 1309–1323.
(4) Magg, C.; Kubelka, J.; Holtermann, G.; Haas, E.; Schmid, F. X. *J. Mol. Biol.* **2006**, *360*, 1067–1080.
(5) Miyake, R.; Ohki, H.; Yamazaki, I.; Yabe, R. A Development of Micro Sheath Flow Chamber. *Proc. IEEE MEMS 91*, New York, 1991; pp 265–270.
(6) Miyake, R.; Lammerink, T.; Elwenspoek, M.; Fluitman, J. Micro Mixer with Fast Diffusion. *Proc. IEEE MEMS 93*, New York, 1993; pp 248–253.
(7) Elwenspoek, M.; Lammerink, T. S. J.; Miyake, R.; Fluitman, J. H. J. *J. Micromech. Microeng.* **1994**, *4*, 227–245.
(8) Knight, J. B.; Vishwanath, A.; Brody, J. P.; Austin, R. H. *Phys. Rev. Lett.* **1998**, *80*, 3863–3866.
(9) Pabit, S. A.; Hagen, S. J. *Biophys. J.* **2002**, *83*, 2872–2878.
(10) Uzawa, T.; Akiyama, S.; Kimura, T.; Takahashi, S.; Ishimori, K.; Morishima, I.; Fujisawa, T. *Proc. Natl. Acad. Sci. U. S. A.* **2004**, *101*, 1171–1176.
(11) Hertzog, D. E.; Michalet, X.; Jager, M.; Kong, X. X.; Santiago, J. G.; Weiss, S.; Bakajin, O. *Anal. Chem.* **2004**, *76*, 7169–7178.
(12) Kane, A. S.; Hoffmann, A.; Baumgartel, P.; Seckler, R.; Reichardt, G.; Horsley, D. A.; Schuler, B.; Bakajin, O. *Anal. Chem.* **2008**, *80*, 9534–9541.
(13) Hertzog, D. E.; Ivorra, B.; Mohammadi, B.; Bakajin, O.; Santiago, J. G. *Anal. Chem.* **2006**, *78*, 4299–4306.
(14) Hoffmann, A.; Kane, A.; Nettels, D.; Hertzog, D. E.; Baumgartel, P.; Lengefeld, J.; Reichardt, G.; Horsley, D. A.; Seckler, R.; Bakajin, O.; Schuler, B. *Proc. Natl. Acad. Sci. U. S. A.* **2007**, *104*, 105–110.
(15) Yao, S.; Bakajin, O. *Anal. Chem.* **2007**, *79*, 5753–5759.
(16) Lipman, E. A.; Schuler, B.; Bakajin, O.; Eaton, W. A. *Science* **2003**, *301*, 1233–1235.
(17) Dittrich, P. S.; Manz, A. *Anal. Bioanal. Chem.* **2005**, *382*, 1771–1782.
(18) White, S. S.; Balasubramanian, S.; Klenerman, D.; Ying, L. M. *Angew. Chem.-Int. Edit.* **2006**, *45*, 7540–7543.
(19) Hamadani, K. M.; Weiss, S. *Biophys. J.* **2008**, *95*, 352–365.
(20) Pfeil, S. H.; Wickersham, C. E.; Hoffmann, A.; Lipman, E. A. *Rev. Sci. Instrum.* **2009**, *80*, 055105.
(21) Lemke, E. A.; Gambin, Y.; Vandelinder, V.; Brustad, E. M.; Liu, H. W.; Schultz, P. G.; Groisman, A.; Deniz, A. A. *J. Am. Chem. Soc.* **2009**, *131*, 13610–13612.
(22) Hofmann, H.; Hillger, F.; Pfeil, S. H.; Hoffmann, A.; Streich, D.; Haenni, D.; Nettels, D.; Lipman, E. A.; Schuler, B. *Proc. Natl. Acad. Sci. U. S. A.* **2010**, In press.
(23) Perl, D.; Welker, C.; Schindler, T.; Schroder, K.; Marahiel, M. A.; Jaenicke, R.; Schmid, F. X. *Nat. Struct. Biol.* **1998**, *5*, 229–235.
(24) Schuler, B.; Lipman, E. A.; Eaton, W. A. *Nature* **2002**, *419*, 743–747.
(25) Gell, C.; Brockwell, D.; Smith, A. *Handbook of Single Molecule Fluorescence Spectroscopy*; Oxford University Press: Oxford, 2006.
(26) Nettels, D.; Gopich, I. V.; Hoffmann, A.; Schuler, B. *Proc. Natl. Acad. Sci. U. S. A.* **2007**, *104*, 2655–2660.
(27) Roda, A.; Guardigli, M.; Pasini, P.; Mirasoli, M.; Michelini, E.; Musiani, M. *Anal. Chim. Acta* **2005**, *541*, 25–36.
(28) Pulgarin, J. A. M.; Bermejo, L. F. G.; Gallego, J. M. L.; Garcia, M. N. S. *Talanta* **2008**, *74*, 1539–1546.
(29) Deluca, M.; Mcelroy, W. D. *Biochemistry* **1974**, *13*, 921–925.
(30) Ribeiro, C.; da Silva, J. C. G. E. *Photochem. Photobiol. Sci.* **2008**, *7*, 1085–1090.
(31) Rhee, S. G.; Greifner, M. I.; Chock, P. B. *Anal. Biochem.* **1975**, *66*, 259–264.
(32) Bokenkamp, D.; Desai, A.; Yang, X.; Tai, Y. C.; Marzluff, E. M.; Mayo, S. L. *Anal. Chem.* **1998**, *70*, 232–236.
(33) Brinkmeier, M.; Dorre, K.; Stephan, J.; Eigen, M. *Anal. Chem.* **1999**, *71*, 609–616.
(34) Pfeil, S. H. Ph.D. thesis, University of California, Santa Barbara, 2009.

Acknowledgement The authors thank Alexis Vallée-Bélisle and Kevin Plaxco for assistance with stopped-flow measurements. Support for this work was provided by the Human Frontier Science Program and the DMEA Center for Nanoscience Innovation for Defense. E.A.L. is an Alfred P. Sloan research fellow.

Supporting Information Available: Methods, mixer linearity measurement, and data analysis. This material is available free of charge via the Internet at `http://pubs.acs.org/`.

V. Recurrence Analysis of Single Particles

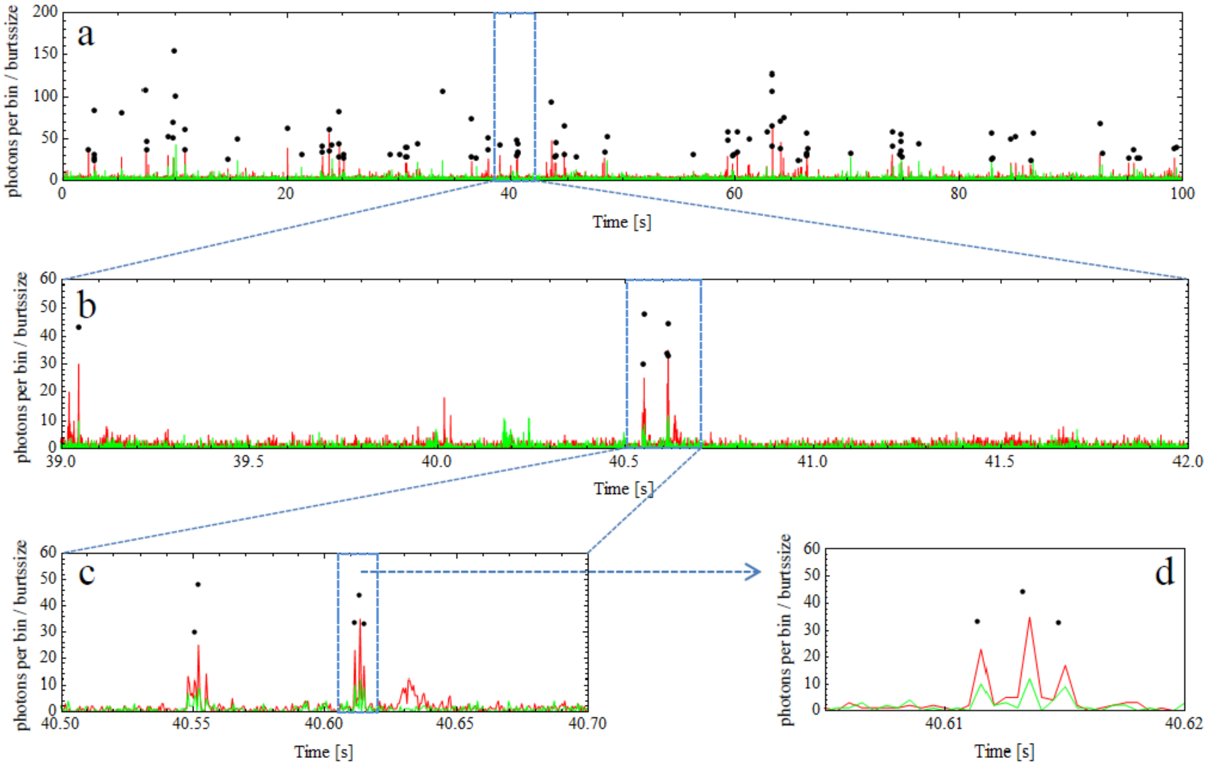

Figure 5.1: Single Molecule Time Trajectories with donor (green) and acceptor (red) photon counts. Points mark the size and positions of identified bursts. Already in the overview (a) clustering of bursts can be recognized. This effect gets visible better when zooming into a cluster (b), revealing two smaller clusters which are separated from other bursts by more than a second. The smaller clusters are separated by approximately 70 ms (c). The final zoom shows a time separation of the single bursts of a few milliseconds (d). [Measurement of Csp*Tm* in 1.1 M GdmCl]

5.1 INTRODUCTION

Single-molecule fluorescence spectroscopy has been shown to give unique insights into heterogeneous molecular systems (see chapter 1.3.1). The sample is either freely diffusing in solution or immobilized on a surface. Immobilized molecules can be observed for extended times, which is beneficial e.g. for monitoring kinetic processes, but might be perturbed by interactions with the surface. In addition, measurements with molecules in diffusion are much easier to perform. However, the observation time in single molecule diffusion experiments is typically only about one millisecond, which has two consequences. First, the amount of signal per molecule is limited, resulting in stochastic broadening (i.e. shot noise) of the subpopulation representing transfer efficiency peaks. Second, the limited observation time for each molecule restricts the time range in which dynamical processes can be studied.

In diffusion experiments, the single molecules which transverse the confocal volume are detected as a significant increase of the photon rate above the fluorescence background level (see chapter 1.3.1). Standard analysis methods treat the emitted bursts of photons as independent events, i.e. as originating from independent molecules. However, due to the low concentrations of molecules in single-molecule experiments (typically tens of picomolar), two bursts detected within a short time interval are likely to originate from the same molecule. This recurrence effect has to our knowledge been ignored for the analysis of standard single-molecule data, although its importance was pointed out in theoretical papers (Földes-Papp, 2007) and it was also accounted for the interpretation of correlation times of single quantum dots (Zumofen et al., 2004) and cells (Edel et al., 2001). The recurrence effect can be easily seen in photon trajectories, as shown in figure 5.1. A closer look at these trajectories suggests that the bursts are not uniformly distributed in time, but are clustered, which cannot be explained by a stochastically independent appearance of molecules. A second hint of recurrence comes from standard fluorescence correlation functions, which typically indicate a correlation at times higher than 10 ms, i.e. at significant longer times than the burst duration which is about 1 ms.

In this chapter, the benefits of using this recurrence information are explored. To this end, two complementary methods were developed. First, it will be shown that the analysis of transfer efficiency histograms can be significantly improved. In a simple and basically model free way, peak shapes and positions of separate subpopulations can be extracted. Peak broadening due to shot noise can be easily distinguished from broadening due to non-stochastic effects such as an underlying distance distribution. Second, burst time correlation analysis will be introduced as a powerful method to extract the probability that two bursts originate from the same molecule and to estimate interconversion rates between subpopulations. Finally, to use the temporal information of recurrence analysis, a procedure will be described to obtain protein folding relaxation rates from single molecule diffusion experiments at equilibrium.

5.2 RECURRENCE TRANSFER EFFICIENCY DISTRIBUTIONS

The clustering of bursts in photon trajectories (figure 5.1) strongly suggests the recurrence of single molecules, but how can we show that these clustered bursts belong to the same molecule? If we consider that a molecule retains its mean transfer efficiency for a certain amount of time, then two bursts separated by a short time interval are very likely to have the same transfer efficiency. We can visualize this by constructing histograms of bursts selected by two criteria. First, the burst must be detected in a defined time interval after a previous burst, e.g. where it is likely that it is a recurring molecule. Second, this previously detected burst has to have a certain transfer efficiency, e.g. it belongs to a certain subpopulation. We call the distribution of bursts selected by those criteria 'recurrence transfer efficiency (E) distribution' and the corresponding histogram 'recurrence transfer efficiency (E) histogram'.

Recurrence Transfer Efficiency Histograms

Examples of recurrence E histograms are shown in figure 5.2, which were obtained from a measurement from Csp*Tm* (labeled at positions 2 and 67, see chapter II) in 1.1 M GdmCl[III]. For comparison, the histogram of all detected bursts (the 'full histogram') is shown as a dashed line. The E range of the previous detected bursts (the 'initial' E range) is shown as a gray box. Figure 5.2 a-g illustrate the dependence of the recurrence histogram on the initial E range for a fixed recurrence time interval of τ=25 ms. Notably, all histograms resemble only the subpopulations which are present in the initial E range chosen. This is only expected if the bursts originate from the same molecules. In addition, the rate of interconversion between the subpopulations has to be significant slower than the recurrence time (25 ms), because otherwise peaks of the other subpopulations would appear as well.

The recurrence peaks show not only transfer efficiencies in the initial range, but they resemble the whole, isolated peaks of the respective subpopulation(s) seen in the full transfer efficiency histogram. This is expected for purely shot-noise broadened peaks as the bursts of the recurring molecules show the same photon statistics as the initial ones. Therefore, recurrence analysis can be used as a simple method to obtain isolated subpopulation peaks, for the case that the subpopulation is static in the recurrence time interval. It should be emphasized that the subpopulation peak isolation can be obtained in a basically model-free way. In addition, more complicated scenarios might be distinguished:

1. The subpopulation is not represented by a single distance, but by a static distance distribution. In this case, also the recurrence histogram will always contain a distribution of distances, which will result in a position dependence of the final recurrence peak on the initial transfer efficiency window. By this, heterogeneity of a subpopulation can be identified (see chapter "Peak Width Analysis", page 106).

[III] Note that all sample concentrations are in the range between 5 pM and 25 pM, thus improving the recurrence analysis. However, the analysis can also be applied to measurements with higher sample concentrations.

2. The subpopulation represents a single distance, but overlaps with another subpopulation. In this case, the initial transfer efficiency window can be chosen such that only one subpopulation dominates the recurrence histogram.

3. The subpopulation represents a single distance, but interconverts with another subpopulation on the recurrence time scale (e.g. due to bleaching, folding, or unfolding). In this case, a sufficiently short recurrence time window will yield the pure peak of the initial subpopulation. By constructing time dependent recurrence histograms, the interconversion rate might be obtained (see chapter 5.4).

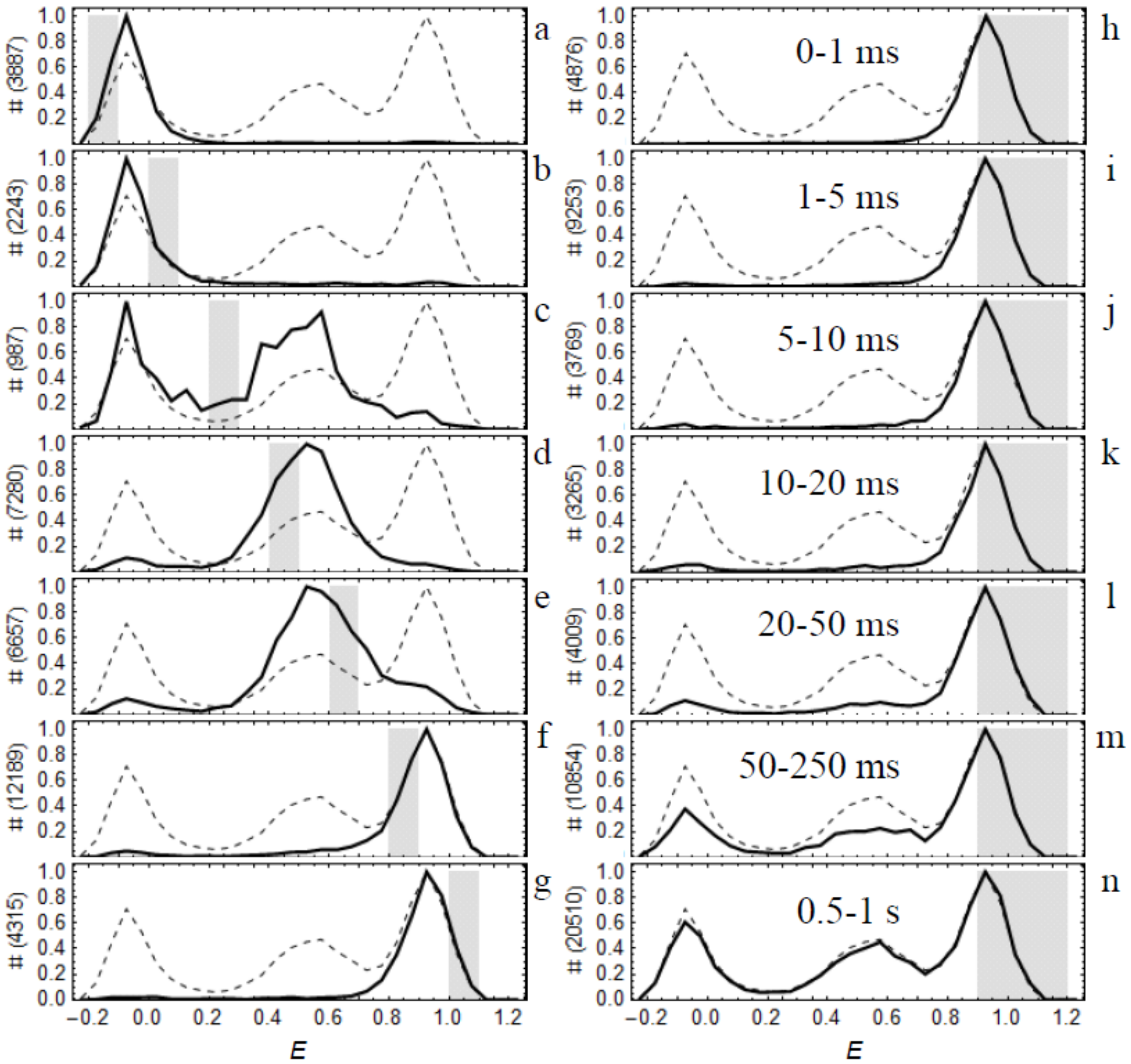

Figure 5.2: Normalized recurrence E histograms of Csp*Tm* in 1.1 M GdmCl (solid lines) compared to the full histogram (dashed line). Plots a-g show the start *E* dependence (gray box) for bursts detected within 25 ms after another one. The recurrence peaks resemble the whole width of the subpopulations present in the start *E* range. Plots h-n show the recurrence time dependence of bursts detected after a bursts from the folded subpopulation. With increasing time (> 50 ms), the probability of bursts being from recurred molecules decreases relative to the amount of bursts from different molecules. As the different molecules show the distribution of the overall ensemble, the histograms approach the full histograms.

The recurrence E histograms for different recurrence times in plots h-n (figure 5.2) illustrate the difference between recurring molecules and different molecules. In the absence of interconversion, recurring molecules will only resemble the subpopulation they originate from, while different molecules will be distributed corresponding to their overall distribution in the sample. With increasing recurrence time, the probability of detecting new molecules increases, and for very long times, the recurrence histogram will have the same subpopulation distribution as the full histogram. Between 20 and 50 ms the majority of detected molecules still are recurring molecules. That means that the recurrence analysis allows the observation time to be expanded from about 1 ms for a single burst by a factor of 20 to 50.

Recurrence Transfer Efficiency Contour Plots

An alternative visualization of the recurrence E distribution is a ‘recurrence E contour plot’, as shown in figure 5.3. The contour plots are obtained from a two-dimensional binning of burst pairs, where the initial burst and the burst from the recurring molecule have a transfer efficiency in range E_A and E_B, respectively. Each plot is constructed for a certain recurrence time interval.

Recurrence transfer efficiency contour plots give a detailed picture of all subpopulations present in a measured sample and also of the extent of their interconversion on the recurrence time scale. The recurrence histograms of figure 5.2 a-g can be seen as vertical slices of distinct E_{A} ranges in a contour plot. Figure 5.3 shows the contour plot of the same sample as in figure 5.2 for two recurrence time intervals. The contour plots can be interpreted in the following way. Each subpopulation which is static on the recurrence time scale will appear on the identity line, as the transfer efficiencies of the initial burst and the recurring bursts (i.e. E_A and E_B) are the same. As shot noise affects both bursts to the same extend, the transfer efficiencies will be broadened equally on both x and y axis, thus forming a circular peak[IV]. In both plots in figure 5.3, the three expected subpopulations of folded and unfolded molecules and molecules with inactive acceptor can be clearly distinguished. Notably, the unfolded peak is not circular, but slightly elliptically shaped. This can be taken as a hint for heterogeneity in the unfolded state population. A non-circular shape means that molecules detected with for instance a low transfer efficiency within the unfolded state are also likely to still have a lower E at the second time detected. In other words, the molecules have a memory of their transfer efficiency within the peak of the unfolded state, which it is not expected for a peak broadened by shot noise only. The unfolded state seems to consist of at least two subspecies with quite similar transfer efficiencies which do not interconvert within 5 ms.

Another important feature of transfer efficiency contour plots is the appearance of cross-peaks. There are two possible sources of cross-peaks. The first one is interconversion between subpopulations: If a molecule changes its conformation on the recurrence timescale, it will have first a transfer efficiency (E_A) representing state 1 and a second transfer efficiency (E_B) of state 2. If the system is in equilibrium, two cross-peaks (for state 1 to state 2 and vice versa) are expected. In the supplement it is shown that both cross-peaks should have the same

---

[IV] For peaks at the extremes of the transfer efficiency range, i.e. higher than 0.9 or lower than 0.1, the shape does not appear exactly circular, but the edges towards 1.2 and -0.2 are compressed. It can be better modeled by a two dimensional log normal function.

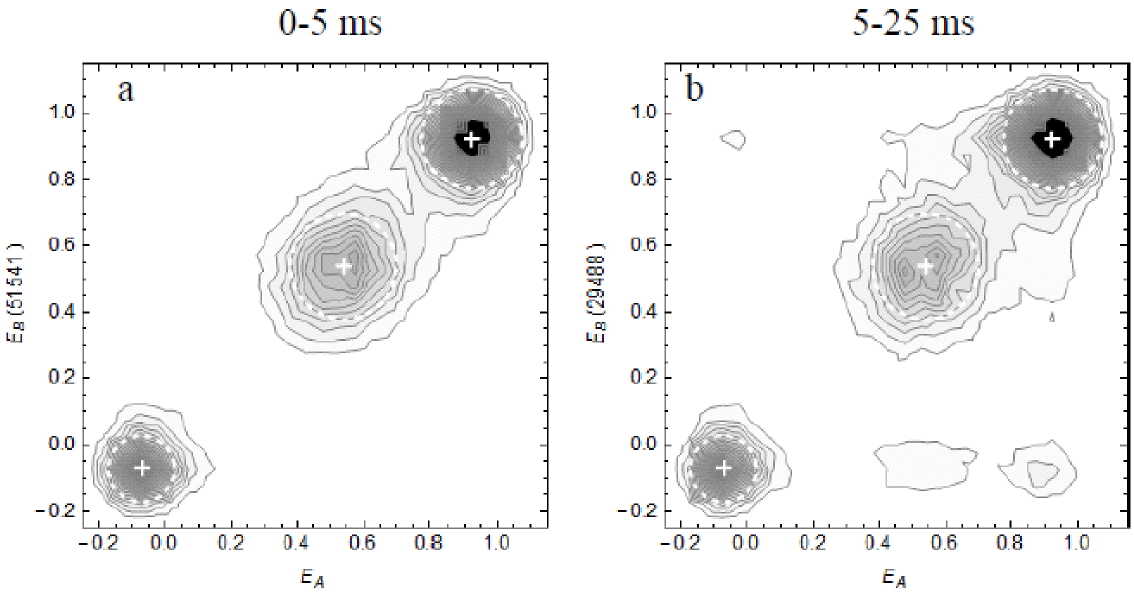

Figure 5.3: Recurrence *E* contour plot of Csp*Tm* in 1.1 M GdmCl. Each bin corresponds to bursts which have a transfer efficiency of E_B and are detected between 0 and 5 ms (a) or between 5 and 25 ms (b) after a burst with transfer efficiency E_A was detected. Molecules which have the same E for the first and second burst will appear on the identity line, shot-noise broadening creates circular peaks. For short recurrence time intervals (a), the three subpopulations i.e. unfolded, folded and acceptor inactive molecules are clearly visible. For longer recurrence time intervals (b), cross-peaks appear, which can originate either from interconversion of subpopulations or from the appearance of new molecules. As the amount of new molecules increases from 1% in a to 10% in b, the cross-peaks originate most likely not from conformational changes.

size, regardless of the population ratio between the two states. In the case of acceptor photobleaching, cross-peaks are only expected for one direction, i.e. the first transfer efficiency of an acceptor active state and the second transfer efficiency of the acceptor inactive state. Another photophysical effect to be considered is blinking, which is often observed for immobilized single molecules. Blinking of the donor dye does not influence the analysis as it is not distinguishable from a molecule leaving or entering the confocal volume. Blinking of the acceptor dye, however, would result in a molecule with a transfer efficiency varying between zero and a value corresponding to its mean inter-dye distance. Therefore, cross-peaks are expected at the corresponding areas in the contour plot. However, an approach introduced in the next chapter (5.3) to quantify blinking shows that acceptor blinking can be neglected for all measurements presented here.

The second possible origin of cross-peaks is the appearance of different molecules. The probability of this different molecule to belong to a certain subpopulation is given by the equilibrium distribution within the sample. Obviously the ability to distinguish between these two sources for cross-peaks is a prerequisite for analyzing inter-subpopulation kinetics. For that purpose, two methods have been developed to estimate the probability of a burst to originate from a recurring molecule rather than from a different molecule. They will be introduced in detail in chapters 5.3 and 5.4.

In figure 5.3 a, no significant interconversion between the states is observed. This is expected at least for the interconversion between folded and unfolded subpopulations, as the folding relaxation rate for the labeled Csp*Tm* at this condition is known to be about 4 s^{-1} (Schuler et al., 2002). During 5 ms, less than 1% of the proteins are expected to interconvert from the folded to the unfolded state and vice versa. In contrast to this, the contour plot for longer times (figure 5.3 b) shows significantly higher cross-peaks between folded and unfolded subpopulations. Also between acceptor-active and acceptor-inactive subpopulations, cross-peaks are faintly visible. From correlation analysis (see chapter 5.3), it was determined that the fraction of burst pairs not originating from the same molecule is about 1% integrated over the first 5 ms and 10% integrated from 5 ms to 25 ms. For the longer recurrence time interval, the expected fraction of folded molecules detected after unfolded ones can be calculated to be 3% of the initially unfolded molecules[V]. This is indeed in approximation the case and one can conclude that between 5 and 25 ms, no significant folding or unfolding events can be detected. A precise quantitative analysis is given in chapter 5.4.

As a second example, Polyproline 20 was measured in 3.5 M GdmCl (figure 5.4). The recurrence E contour plots show in addition to the acceptor-inactive subpopulation a second wide-stretched peak. The corresponding peak in the full FRET histogram can be well fitted with two Gaussians. However, the recurrence E contour plot clearly reveals that at least three species are needed to describe the population. The slight broadening of the distribution at later times (figure 5.4 b) can be fully attributed to bursts from new molecules (i.e. 7%). In conclusion, the interconversion must be slower than 10 ms.

[V] The fraction of cross-peaks expected from new molecules are calculated as follows: If 10% of the molecules detected after an unfolded molecule are different ones, then 90% of the bursts have an E_B corresponding to an unfolded molecule and the E_B of the other 10% are distributed as in the full histogram. As the amount of folded molecules in the full histogram is about 33%, the cross-peak corresponding to an unfolded to folded transition will be 33% times 10% i.e. about 3% of the unfolded peak.

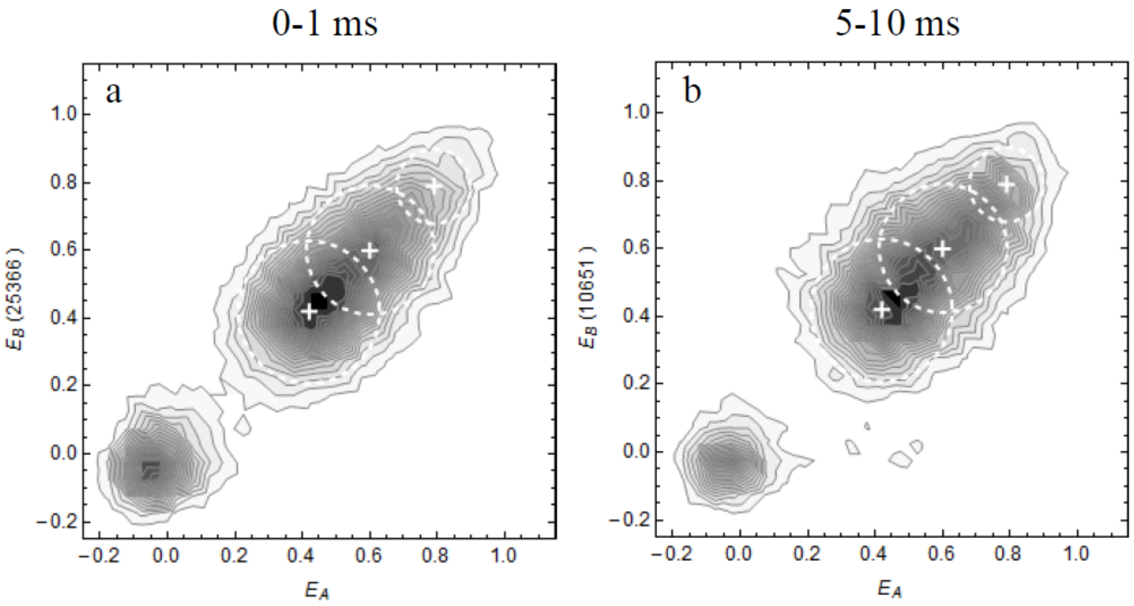

Figure 5.4: Recurrence *E* contour plot of Polyproline 20 in 3.5 M GdmCl for the first 1 ms (a) and within 5 and 10 ms after a burst. The acceptor-active subpopulation exhibits a very distorted peak, which needs to be modeled by more than three subpopulations, as the indicated shot-noise broadened peaks cannot describe the peak. For longer times, the peak gets broader compared to the identity line. Again, as the fraction of new molecules increases from 1% to 7%, the broadening can be attributed to the new molecules rather than interconversion.

As a third example, Csp*Tm* was measured in 50% ethylene glycol and 3.5 M GdmCl (figure 5.5). The unfolded state peak in the standard transfer efficiency histogram shows an unusual asymmetry with a shoulder towards higher transfer efficiencies. The recurrence analysis again reveals more details. At least four subpopulations are distinguishable: The acceptor-inactive molecules with a circular peak shape at transfer efficiencies around 0, the unfolded main peak at about 0.4, which continuously merges into a smaller, more elliptically shaped subpopulation centered around 0.65, and finally a small, but significant population with a transfer efficiency at 0.9, where the peak from the folded state is expected. Note that the latter population contains only about one percent of the total distribution and is hardly visible in the standard FRET histogram.

For longer times, significant cross-peaks appear both from the main unfolded peak to the acceptor-inactive subpopulation and between the lower and higher *E* parts of the unfolded subpopulation. As the diffusion slows down significantly in the presence of ethylene glycol, the recurrence time window can be extended to 20 ms without increasing the fraction of new molecules a lot. The expected increase of the cross-peaks from new molecules is about 3% between the two contour plots. Clearly, the observed increase of the cross-peaks is much more pronounced (figure 5.5 b). Therefore the recurrence analysis suggests that the subpopulations of the unfolded state interconvert on a timescale of about 10 ms.

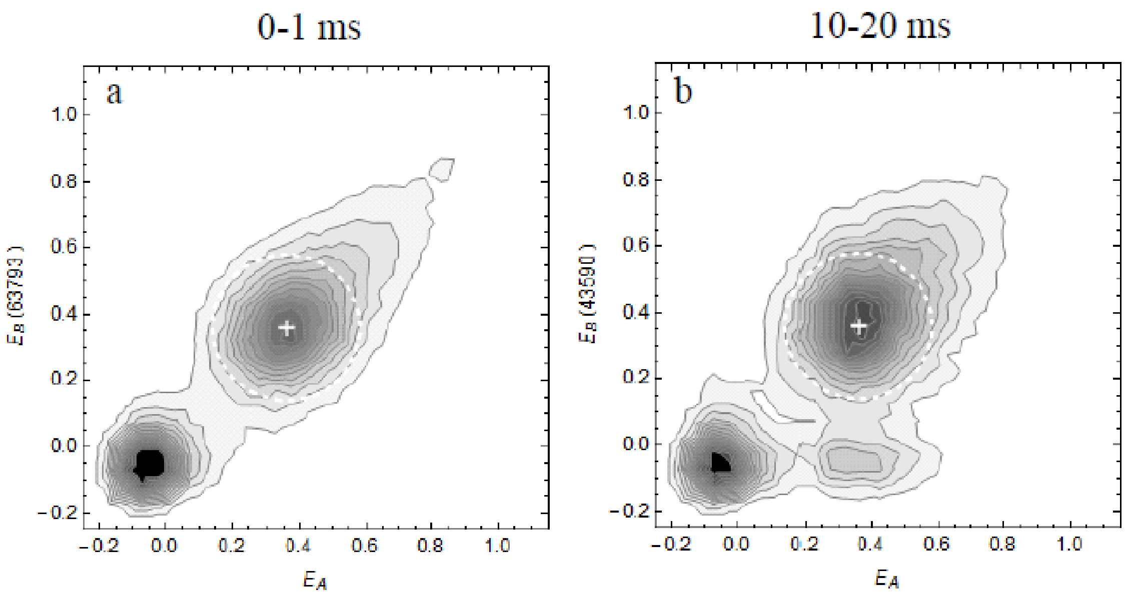

Figure 5.5: Recurrence *E* contour plots of Csp in 3.5 M GdmCl and 50% ethylene glycol. The unfolded peak appears very heterogeneous, in addition to a small peak at a transfer efficiency of about 0.9. Transfer efficiency distributions of the unfolded subpopulation appear in non-circular shape, suggesting a structurally diverse subset of molecules. Although only a small fraction of different molecules is expected within 10 to 20 ms (i.e. 3% from correlation analysis), significant cross-peaks appear, which indicate interconversion within the non-native ensemble.

Peak Width Analysis

The plots a-g in figure 5.6 show recurrence histograms of the same Csp*Tm* data as presented in figure 5.2, but with a much narrower initial transfer efficiency range which is shifted in small steps over the unfolded state peak. Again, as shot-noise is the main reason for peak broadening, the recurrence peak widths are similar to the unfolded peak width visible in the full histogram. However, there is a slight position dependence of the recurrence peak on the initial *E* range. This suggests that heterogeneous broadening contributes to some extent to the width of the unfolded peak, as already mentioned in the discussion of the corresponding contour plot.

An analogous analysis of the polyproline 20 data (figure 5.6 h-l) shows an even stronger position dependence of the recurrence peak on the initial *E* range. The recurrence peak shifts continuously between 0.4 and 0.7. No discrete subpopulations are resolved (The latter should result in an increase and decrease of peaks at distinct positions.) This means that polyproline 20 has a rather heterogeneous and slowly interconverting distribution of end-to-end distances. The absence of interconversion can be demonstrated with histograms for different recurrence times (figure 5.6 m, n). The lower transfer efficiency half of the peak does not interconvert to the other half within 10 to 20 ms. The slight broadening of the peaks can again be explained with the appearance of new molecules, as the fraction of bursts in the shoulder is similar to the fraction of acceptor-active molecules detected after the acceptor-inactive state in this time range.

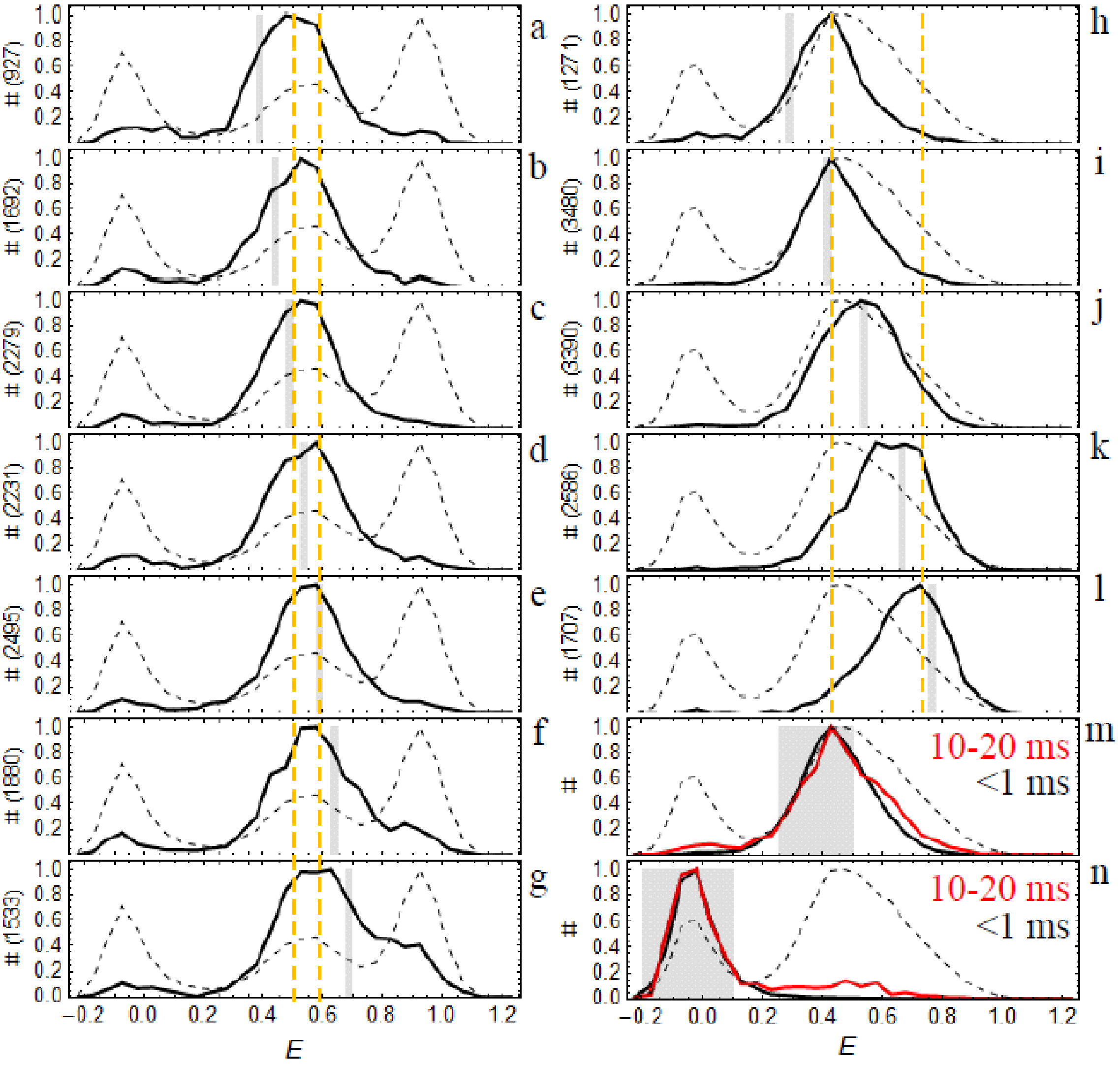

Figure 5.6: Recurrence *E* histograms with narrow initial *E* ranges. Plots a-g show the dependence of the unfolded peak on the initial *E* range in a measurement of Csp*Tm* in 1.1 M GdmCl for bursts detected within 25 ms after a previous burst. The orange dashed lines mark the average peak positions of the first and last histogram, showing a slight dependence of the peak position on the start *E* range. Plots h-n show results from a measurement of Polyproline 20 in 3.5 M GdmCl. The peak position dependence (plots h-l, indicated with orange dashed line) is much more pronounced than for Csp. Time-dependent histograms show no interconversion between the low and high transfer efficiency halves of the peak for shorter than 20 ms (m), as about 10 % new molecules are expected in this time window. This can be illustrated by the appearance of a similar fraction of acceptor active molecules after acceptor inactive bursts in the same time (n).

Fitting transfer efficiency histograms

By choosing short recurrence times and initial transfer efficiency ranges representing only a single subpopulation, as shown in figure 5.2, we can obtain the peak shape and position of the respective subpopulation. The shape and position of the peaks should not change, irrespective of whether the full histogram or a recurrence histogram is constructed. We can therefore improve the fitting of histograms in the following way: First we construct a recurrence histogram consisting only of a single subpopulation. Than we fit this subpopulation with either a Gaussian or Lognormal distribution. Now we can use the position and the shape of the fit results to constrain the fits of histograms which have more than one subpopulation. By fitting only the amplitudes, we can accurately fit also histograms which have very little bursts or which have subpopulation peaks that strongly overlap or are low populated.

5.3 BURST TIME CORRELATIONS

A second way to analyze the recurrence behavior is correlation analysis. For independent bursts, no correlation of bursts is expected. If bursts result from the same molecule, they should be correlated. In analogy to photon time correlation functions used in fluorescence correlation spectroscopy (FCS), the 'burst time' correlation function is defined as:

$$g_{AB}(\tau)=\frac{p\left(\{b_A,t\},\{b_B,t+\tau\}\right)}{p\left(\{b_A,t\}\right)p\left(\{b_B,t\}\right)} \qquad [5.1]$$

where $p\left(\{b_A,t\},\{b_B,t+\tau\}\right)$ denotes the joint probability of measuring two bursts b_A and b_B at times t and $t+\tau$, respectively, and $p\left(\{b_A,t\}\right)$ and $p\left(\{b_B,t\}\right)$ are the probability of detecting bursts b_A and b_B, respectively. It is assumed that all three probabilities do not explicitly depend on the arbitrary time point t. A and B denote any subsets of bursts, for example defined by ranges of transfer efficiencies. As a time range is needed to calculate the correlation values, τ corresponds to the mean value of the interval $[\tau-\Delta\tau,\ \tau+\Delta\tau]$, where the size of the window (i.e. $2\ \Delta\tau$) is the size of the bins used for burst identification (see supplement).

Using burst time correlation analysis has two advantages compared to standard FCS: First, the recurrence effect can be monitored directly, as it is not masked by the strong signal from the diffusion of the molecules. Second, it is very easy to correlate different subsets of molecules with each other, as bursts can be chosen by certain criteria representing the different subpopulations, for example. Therefore we can use burst time correlation to calculate the probability of two bursts to be emitted by the same molecule and to analyze the interconversion between subpopulations.

Same Molecule Probability

For a quantitative recurrence analysis it is of elementary interest to determine the probability $p_s(\tau)$ that two photon bursts measured at times t_1 and t_2 (with $t_2-t_1=\tau$) were emitted by the same molecule. We show in the supplement that the 'same molecule' probability $p_s(\tau)$ is given by:

$$p_S(\tau)=1-\frac{1}{g(\tau)} \qquad [5.2]$$

where $g(\tau)$ is the autocorrelation function of all detected bursts. Figure 5.7 shows the $g(\tau)$ and $p_s(\tau)$ of the Csp*Tm* measurement at 1.1 M GdmCl. For further analyzing the data, it is practical to approximate $p_s(\tau)$ for short lag times τ by a quadratic polynomial (see figure 5.7 b):

$$p_S(\tau)=a+b\tau+c\tau^2 \qquad [5.3]$$

For a given recurrence histogram, we can now determine the relative fraction of bursts coming from recurring molecules by calculating $p_s(\tau)$ for each burst and taking the average over all bursts in the histogram.

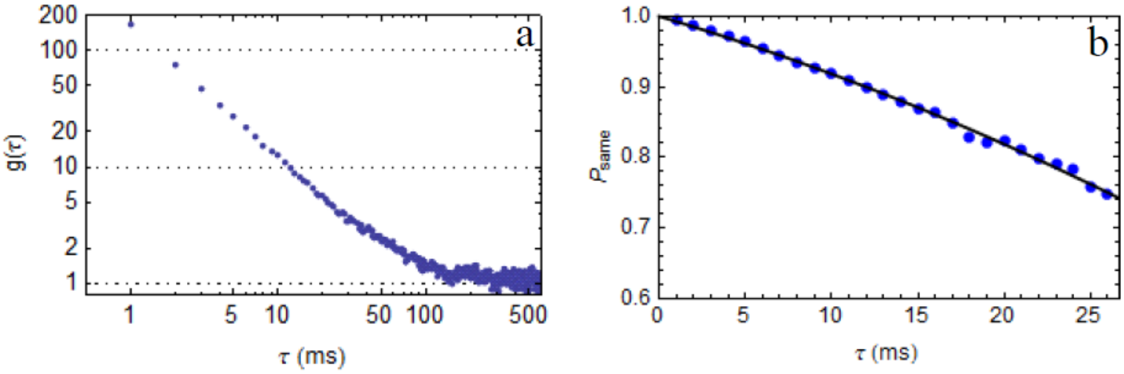

Figure 5.7: Same Molecule Probability. (a) The burst time autocorrelation curve of Csp*Tm* in 1.1 M GdmCl exhibits a large amplitude showing a strongly increased probability to detect bursts after another burst has been detected shortly before. (b) The correlation $g(\tau)$ can be transferred to the probability of a burst to be from the same molecule as a burst detected a time τ before. An empirical fit (black line) to this probability is used for further analysis. See text for details.

Subpopulation-Specific Burst Time Correlation

A and B in the definition of $g_{AB}(\tau)$ can represent burst classes which correspond to different subpopulations present in the sample. In subpopulation-specific correlations two processes are convoluted: Like the autocorrelation of all bursts, the subpopulation correlations decrease with time to unity as the recurrence probability decreases. In addition, cross-correlation between subpopulations can reveal interconversion dynamics.

As an example, subpopulations can be chosen by selecting transfer efficiency ranges, as shown in figure 5.8 a for the folded, unfolded and acceptor inactive molecules at high, intermediate and close to zero transfer efficiencies, respectively. The subpopulation autocorrelations (figure 5.8 b) obtained from these burst subsets have higher amplitudes than the autocorrelation function of all bursts. This is expected for subpopulations with a low degree of interconversion, as the concentration of each subpopulation of molecules is smaller than the total concentration and therefore the probability of a different molecule to appear lower. In addition, the decay is very similar for each subpopulation, showing that the recurrence behavior is very similar for all of them. Even more interesting are the cross-correlations. Both cross-correlations from molecules with an inactive acceptor to an active one (unfolded or folded) are completely flat (figure 5.8 c). That means that the amount of molecules which recover their acceptor fluorescence (e.g. due to blinking) on the recurrence timescale is negligible. We can conclude that all burst pairs with an inactive acceptor at first and an active one at second must be emitted by two different molecules. The opposite cross-correlations, i.e. a burst from a folded or unfolded molecule first and from a molecule with inactive acceptor second, show small but significant amplitudes (figure 5.8 d). This effect can be explained by bleaching of the acceptor dye before the recurrence of the molecule[VI]. The third pair of cross-correlations is between the folded and unfolded state (figure 5.3e), which also show small amplitudes for both directions. This might reflect the small folding rate of 4 s^{-1}.

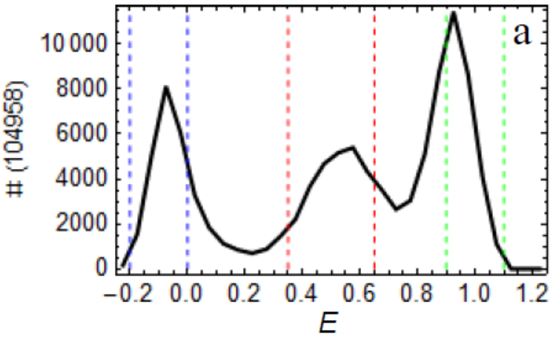

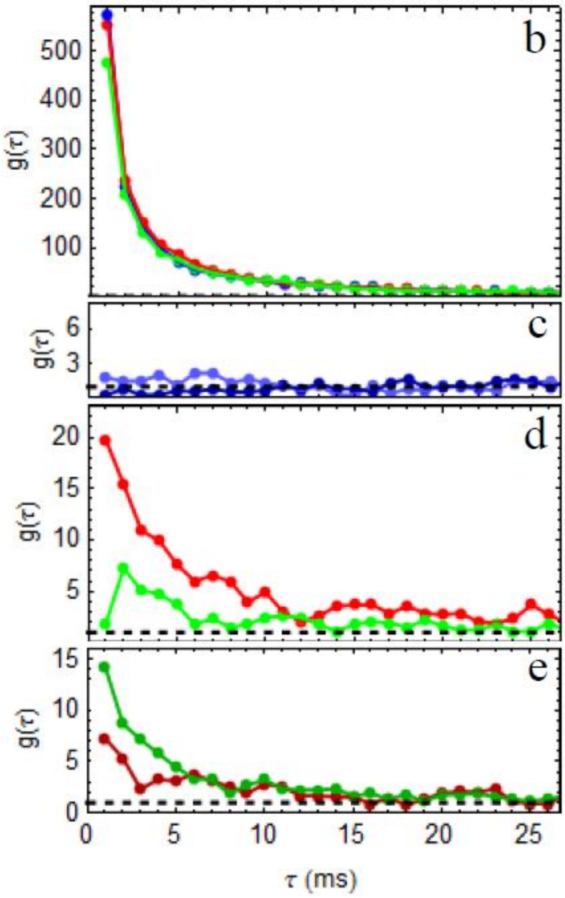

Figure 5.8: Subpopulation-specific burst time correlations. Bursts were selected for transfer efficiency ranges reflecting the unfolded (red lines), folded (green lines) or acceptor-inactive (blue lines) subpopulations, like shown in the FRET histogram (a). Curve colors in b-e correspond to the start burst region. (b) Subpopulation-specific autocorrelations show high amplitudes reflecting the high probability to remain in the same subpopulation. (c) No cross-correlations from acceptor inactive to active subpopulations can be observed, showing that blinking processes can be neglected for recurrence analysis. The opposite direction (d) exhibits significant amplitudes, showing that acceptor photo bleaching is a significant process on the recurrence timescale. The cross-correlations between folded and unfolded subpopulations show smaller but still significant amplitudes. Importantly, cross-correlations are convolutions of the recurrence probability, which decreases with time, and subpopulation interconversion, which increases with time.

It should be pointed out that by using this rather crude subpopulation selection, it is difficult to collect a whole subpopulation without also getting some false positives from neighboring subpopulations. In case of shot-noise limited peaks, a molecule being at the edge of the distribution during its first detection is very likely to be more around the centre of the peak during its second detection. That means that false positives lead to a false cross-correlation signal. On the other hand, with a more restricted choice, molecules with a transfer efficiency in the chosen range during the first detection might be still in the same subpopulation, but just with a transfer efficiency outside the range, thus reducing the autocorrelation amplitude.

[VI] A bleaching of the donor dye is undistinguishable from ultimately leaving the confocal volume, except in experiments where a second laser is used to directly excite the acceptor .

These considerations complicate the quantitative analysis of subpopulation-specific burst time correlations, and one has to be careful with the interpretation, as the choice of transfer efficiency ranges is crucial. Nevertheless, by choosing more restricted ranges, one gets a qualitative picture of which subpopulations interconvert and which do not. It might be possible to get quantitative information by looking at the dependence of the correlation signal on the transfer efficiency ranges.

5.4 FOLDING KINETICS FROM RECURRENCE ANALYSIS

Recurrence analysis can also be used to obtain kinetic information on the timescale of the recurrence. In this chapter, we introduce a method to extract folding relaxation times from time dependent recurrence histograms. The main idea is to choose transfer efficiency ranges which are selective for one subpopulation, construct histograms for different recurrence times, fit the histograms, and extract the fractions of one subpopulation versus time. The following procedure is for the simple case of a two-state systems (i.e. only an unfolded and a folded state are present), but it can be easily extended for more complicated systems.

In order to get the correct rates, we have to convert the fractions of bursts from unfolded molecules in a recurrence histogram to the fraction of unfolded molecules which have recurred. The bursts in a recurrence histogram originate from recurring molecules and from different molecules. Hence, the fraction of unfolded bursts[VII] in a recurrence histogram $f^{b}_{U,RH}(\tau, \Delta E_A)$ is the sum of the fraction of unfolded bursts from recurring molecules $f^{b}_{U,R}(\tau, \Delta E_A)$ and different molecules $f^{b}_{U,D}$, weighted by $p_S(\tau)$

$$f^{b}_{U,RH}(\tau, \Delta E_A) = p_S(\tau)\ f^{b}_{U,R}(\tau, \Delta E_A) + (1 - p_S(\tau))\ f^{b}_{U,D} \qquad [5.4]$$

The fraction of bursts from unfolded molecules for the different molecules is the same as for the full histogram. Hence, for longer times, when p_S approaches zero, the fraction of bursts from unfolded molecules in the recurrence histogram will approach the value of the full histogram. This effect is shown in figure 5.2, plots h-n.

We also have to consider that the fraction of bursts might be different from the fraction of molecules, as the detection efficiency might differ for folded and unfolded subpopulations. The fraction of unfolded bursts from different molecules $f^{b}_{U,D}$ is

$$f^{b}_{U,D} = \frac{1}{1 + DE\left(\frac{1}{f_U} - 1\right)} \qquad [5.5]$$

where DE is the ratio of the detection efficiencies of unfolded and folded molecules (see supplement for derivation), and f_U is the fraction of unfolded molecules in the sample. The fraction of unfolded bursts from recurring molecules might be also affected by the detection efficiency difference. In addition, the recurrence probability might also be different, for instance when one subpopulation bleaches with a higher probability than the other. Similar to equation 5.5, we can express $f^{b}_{U,R}(\tau, \Delta E_A)$ as

---

[VII] Here, the fraction of unfolded bursts is defined as the area of the unfolded peak divided by the sum of the areas of unfolded and folded peaks.

$$f_{U,R}^{b}(\tau,\Delta E_A)=\frac{1}{1+RP(\tau)\left(\dfrac{1}{f_{U,R}(\tau,\Delta E_A)}-1\right)} \tag{5.6}$$

where $f_{U,R}(\tau,\Delta E_A)$ is the fraction of recurring molecules corrected for differences of detection efficiency and recurrence probability of folded and unfolded molecules, and $RP(\tau)$ is the ratio of the recurrence probabilities of unfolded and folded proteins (see supplement for derivation).

The fraction of recurred, unfolded molecules relaxes from the initial value $f_{U,0}$ to the equilibrium fraction f_U as described by:

$$f_{U,R}(\tau,\Delta E_A)=f_{U,0}(\Delta E_A)+\left(f_U-f_{U,0}(\Delta E_A)\right)e^{-\lambda\tau} \tag{5.7}$$

Note that the time τ used for constructing the recurrence histograms and estimating $p_s(\tau)$ and $RP(\tau)$ corresponds to a the mean value of the time interval $[\,\tau-\Delta\tau/2,\ \tau+\Delta\tau/2\,]$.

For the fit of the unfolded fraction as function of time, only λ is unknown. The recurrence probabilities are obtained independently as described in chapter 5.3. The initial and end fractions of the unfolded state are known from the full transfer efficiency histogram. As described at the end of chapter 5.2, the fitting of the recurrence histograms can be improved considerably, as the shape and positions of all peaks can be extracted independently and constraint for fits of histograms having more than one subpopulation. In total, there are three factors influencing the time dependence of recurrence histograms:

(i) The appearance of new molecules, described by $p_s(\tau)$, which can be calculated by two independent methods (see chapter 5.3 and next paragraph)

(ii) Subpopulation interconversion, e.g. folding/unfolding, as described by equation 5.7

(iii) Different recurrence behavior of subpopulations, described by $RP(\tau)$, which can also be calculated independently (see supplement)

Folding Time Examples: CspTm

As a first example, we apply the method to the single molecule data obtained from Csp in 1.1 M GdmCl. In ensemble stop-flow measurements, the folding-unfolding relaxation rate under this conditions was shown to be 4 s^{-1} (Schuler et al., 2002). Obviously, on the recurrence time scale, which is in the range of 10 milliseconds, the number folding and unfolding events per protein is negligible. Therefore, this example serves as a negative control to see how good the model can compensate for those factors, which will also cause the fraction of bursts from unfolded molecules to decay to the equilibrium value. We selected three different initial transfer efficiency intervals, which represent the acceptor inactive, the unfolded and the folded subpopulations. The recurrence histograms for different values of τ were constructed and fitted. The first histograms for τ =1 ms show mostly the corresponding initial subpopulations (plots a, e, and i in figure 5.9). At longer τ, the other subpopulations

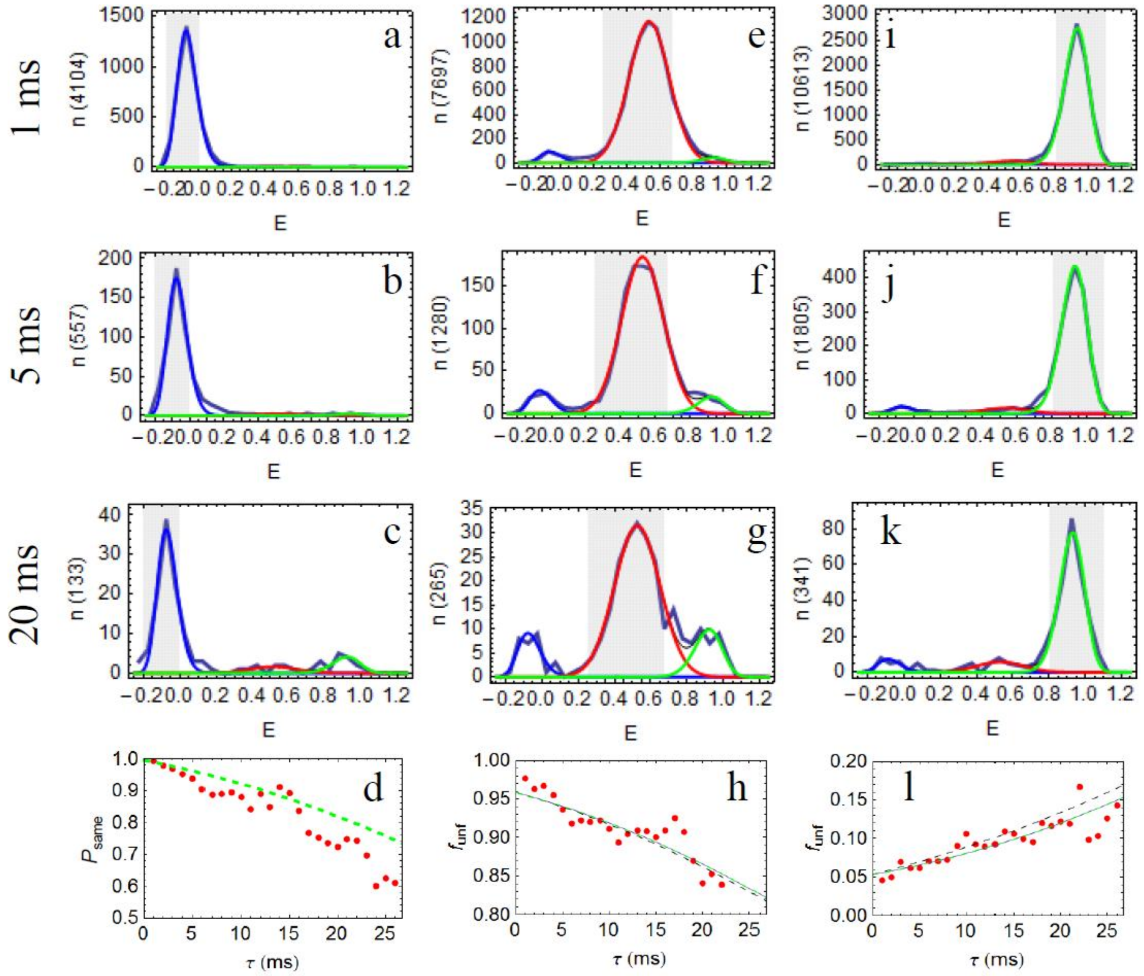

Figure 5.9: Representative recurrence *E* histograms of Csp*Tm* in 1.1 M GdmCl for different recurrence time ranges and subpopulation specific E_A ranges (acceptor inactive, unfolded and folded in a-c, e-g and i-k, respectively and time ranges indicated at the left of each row, i.e. 1 ms ± 0.5 ms, 5 ms ± 0.5 ms, and 20 ms ± 0.5 ms). For all three E_A ranges, the two other populations slightly increase over time. The acceptor-active population in a-c can be directly translated into the recurrence probability (d, red discs) and is compared to the recurrence probability calculated from the burst autocorrelation (green dashed line), showing the good agreement between both methods. The unfolded fractions for recurrence *E* histograms starting from unfolded and folded molecules (red discs in h and l, respectively) were globally fitted with the model including both folding of recurred molecules and occurrence of new molecules (blue lines). The black dashed lines shows the fit result with the relaxation rate constrained to the ensemble value.

appear, which is expected both from folding and unfolding, and from the occurrence of different molecules. The time dependencies of the unfolded fraction obtained from recurrence histograms with initial transfer efficiency ranges representing the folded and the unfolded populations were fitted globally both without constraints and with the folding-unfolding relaxation time set to the value known from the stop-flow measurement (plots h and l in figure 5.9). Although the initial unfolded fractions are already known from the full transfer efficiency histogram, we did not constrain them, as they are fitted very well (0.82 and 0 from the fit compared to 0.83 and 0 from the overall histogram for the start *E* ranges representing mostly unfolded and folded molecules, respectively). The free fit gives a folding-unfolding relaxation rate of 10^{-6} s^{-1}. The fit with the constrained rate looks very similar, showing that the real rate is too slow to be obtained from recurrence analysis. Hence, this example shows that our procedure can clearly separate the appearance of different molecules from folding or unfolding events.

An alternative procedure to obtain $p_s(\tau)$

In the absence of interconversion, the example of Csp in 1.1 M GdmCl shows that the present decay rates can be solely described by the appearance of different molecules. We know from burst time analysis that the subpopulation of molecules without an active acceptor does not interconvert to the other subpopulations. Hence, the only effect which decreases the fraction of bursts from molecules with an inactive acceptor[VIII] (AI) over time ($f_{AI,RH}^{b}(\tau,\Delta E_A)$) is the appearance of different molecules. In analogy to equation 5.4 we can write

$$f_{AI,RH}^{b}(\tau,\Delta E_A) = p_S(\tau)\; f_{AI,R}^{b}(\Delta E_A) + (1 - p_S(\tau))\; f_{AI,D}^{b} \qquad [5.8]$$

where the fraction of bursts from acceptor inactive molecules from the initial transfer efficiency range ($f_{AI,R}^{b}(\Delta E_A)$) and from the full histogram ($f_{AI,D}^{b}$) can be extracted from the full histogram. Note that the fraction of bursts from recurring molecules with an inactive acceptor is not time dependent. Simple rearrangement of equation 5.8 yields

$$p_S(\tau) = \frac{f_{AI,RH}^{b}(\tau,\Delta E_A) - f_{AI,D}^{b}}{f_{AI,R}^{b}(\Delta E_A) - f_{AI,D}^{b}} \qquad [5.9]$$

Thus, we can calculate the time-dependent same molecule probability in a second way independent from burst correlation analysis. As shown in figure 5.9 d, both methods agree very well. We expect a minor error for this procedure from the fact that the fractions extracted from the full histogram are apparently to high, as they contain also bursts from molecules which bleached during the detection. This explains why the same molecule probabilities obtained with equation 5.9 are lower than the values obtained from burst correlation analysis. In addition, the values can be more easily obtained from burst correlation analysis, as no fitting is required. However, equation 5.9 can be used for a quick estimation of $p_s(\tau)$ for recurrence histograms or contour plots, as all required values can be easily estimated as well.

[VIII] Note that unlike for the fraction of unfolded bursts, we define the fraction of bursts from molecules with an inactive acceptor as the area of the peak representing these bursts divided by all bursts in the histogram.

Folding Time Examples: Spectrin R15

To show that this method can give reasonable folding-unfolding relaxation times, we measured the spectrin R15. R15 is the 15th domain of the chicken brain α-spectrin. This extensively studied protein folds into a coiled coil and is well described as a two-state folder (Scott et al., 2004; Wensley et al., 2010). A variant of R15 labeled with Alexa 488 and Alexa 594 at positions 39 and 99 was measured in 1.1 M GdmCl. Ensemble measurements showed that the relaxation rate is about 30 s^{-1} under these conditions, and is therefore in a time range appropriate for recurrence analysis. Figure 5.10 shows a selection of time dependent recurrence *E* histograms starting from folded, unfolded, and acceptor inactive molecules.

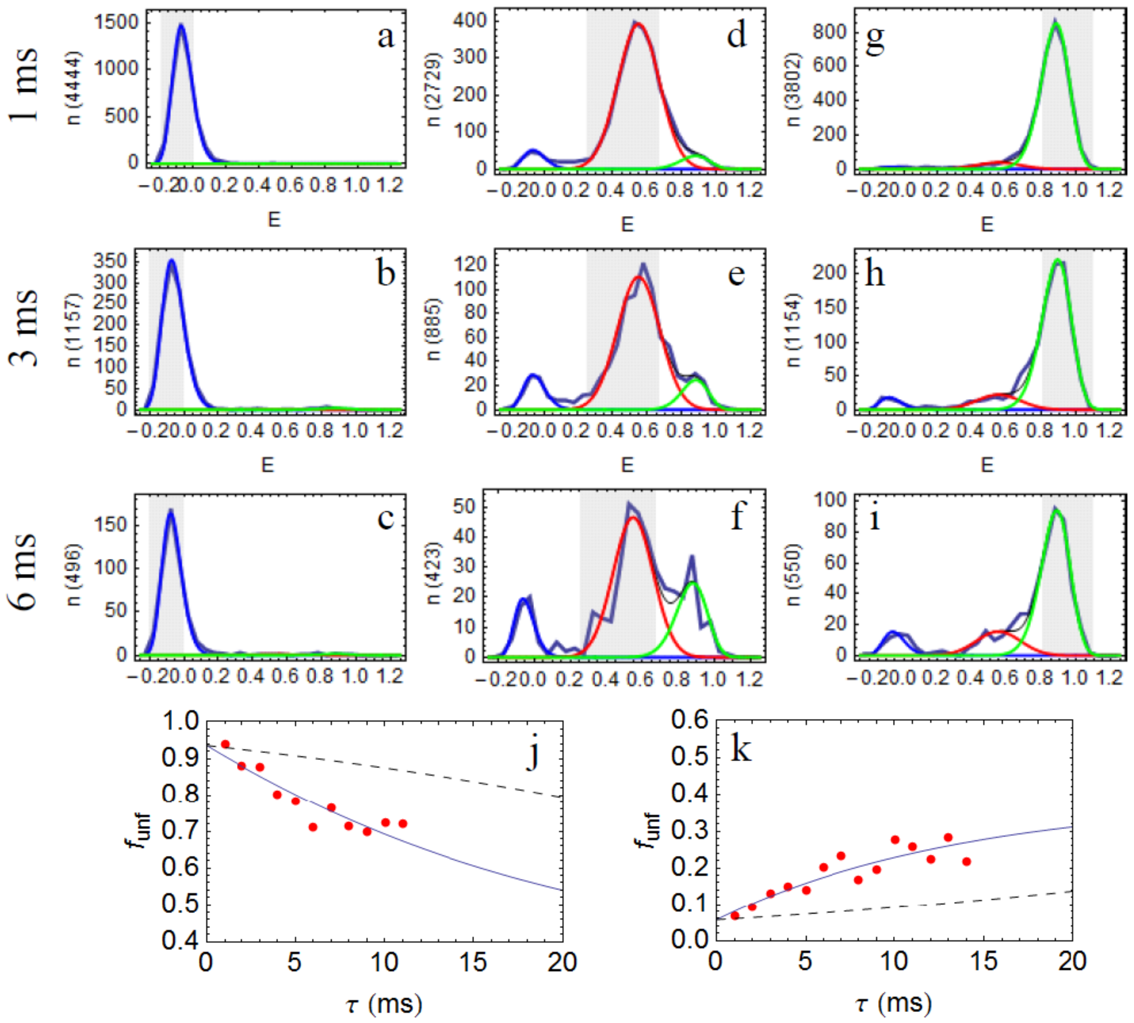

Figure 5.10: Kinetic Analysis of R15 in 1 M GdmCl analogous to figure 5.9. Starting from mostly unfolded molecules, the appearance of folded molecules and vice versa is faster than expected from the appearance from different molecules (d-i), showing the contribution from recurred molecules which change their conformation. The control of molecules with inactive acceptor confirms the slower appearance of different molecules (a-c). The globally fitted relaxation time (j,k) reveals a rate of 58 s^{-1}, which is in good agreement with the ensemble value of 30 s^{-1}. The curve in the absence of a relaxation rate (i.e. appearance of different molecules only) is shown as a dashed line.

The histograms at τ=1 ms exhibit mostly the subpopulations corresponding to the initial transfer efficiency range. The recurrence histograms with ΔE_A corresponding to molecules with inactive acceptor (figure 5.10 a-c) show no significant appearance of acceptor active molecules as expected from burst time correlation analysis which shows that more than 94% of the secondary bursts originate from the recurring molecules after 6±1 ms. For the recurrence histograms starting from unfolded (figure 5.10 d-f) and folded (figure 5.10 g-i) molecules, there are significant fractions of other subpopulations appearing over time. For longer times, the amount of detected molecules per time reduces, resulting in worse quality of the histograms. However, the only free parameters for the histogram fits are the amplitudes of the three subpopulations, allowing reasonable fitting of histograms with only a few hundreds of bursts. The unfolded fractions were fitted with a relaxation rate of 58 s^{-1} and a final unfolded fraction of 0.27 and agree well with the ensemble values of 30 s^{-1} and 0.32, respectively (plots j and k in figure 5.10).

Folding Time Examples: B Domain of Protein A

As a third example, the B domain of protein A (BdpA) from *Staphylococcus aureus* was measured in 2.5 M GdmCl at 37°C. BdpA belongs to the group of fast folding proteins and adopts a three helix bundle fold (Myers and Oas, 2001; Dimitriadis et al., 2004). The variant used has a number of mutations which facilitate characterization (F13W), speed up folding (G29A), and allow the specific incorporation of fluorescence dyes (Y14C P57C). The folding relaxation time is around 3 ms^{-1} at the conditions measured (Clark, 2008). As the protein is expected to fold already during its diffusion time, the photon rate was increased by using higher laser powers (300 μW) and the binning time was decreased to 50 μs. Although this small bin sizes increases the shot noise broadening, the quality of the fits is not significantly reduced, as the position and width of all subpopulations can be determined in the absence of other subpopulations and were fixed for fitting the time dependent recurrence histograms.

Figure 5.11 shows the results of the recurrence analysis. Within 50 μs, the proteins do only marginally interconvert to other subpopulations, thus it is possible to determine the shapes of the corresponding peaks (plots a,d,g). After 500 μs, a significant fraction of folded molecules has unfolded (plot h), whereas a smaller amount of the unfolded proteins has folded (plot e). After 5 ms, more than half of the folded molecules have unfolded (plot i), but still the fraction of molecules remaining unfolded starting from a nearly purely unfolded subset is still higher. This indicates that the system is still not at equilibrium. The appearance of different molecules is still relatively unlikely at this time, as only a very low fraction of acceptor active molecules is observed in the recurrence histograms starting from acceptor inactive molecules (plots a-c). Plot j shows again the good agreement between the two methods introduced to obtain the same-molecule probability. Plot k summarizes the folding relaxation of both folded and unfolded molecules. In this case, both traces were fitted independently for the following reasons: BdpA has three prolines and we therefore only observe the folding of the protein fraction where all prolines are in the trans (i.e. folding competent) conformation. The unfolding reaction is not affected by the proline isomerization state and we consequently get the final equilibrium fraction only for the unfolding reaction, but not for the folding reaction. The rates for folding and unfolding differ slightly as well. We assume that this is caused by an increased acceptor bleaching rate for the unfolded molecules compared to the folded molecules. This effect is more prominent in this measurement as a higher laser intensity was used. Consequently, the relaxation rate will be apparently higher for the folding reaction and apparently lower for the unfolding reaction compared to the real rate. The rates were fitted with 2 ms^{-1} for starting from unfolded molecules and 0.8 ms^{-1} starting from folded molecules, which are in good agreement with the results from temperature jump measurements, revealing a relaxation rate of 3 ms^{-1} (Clark, 2008).

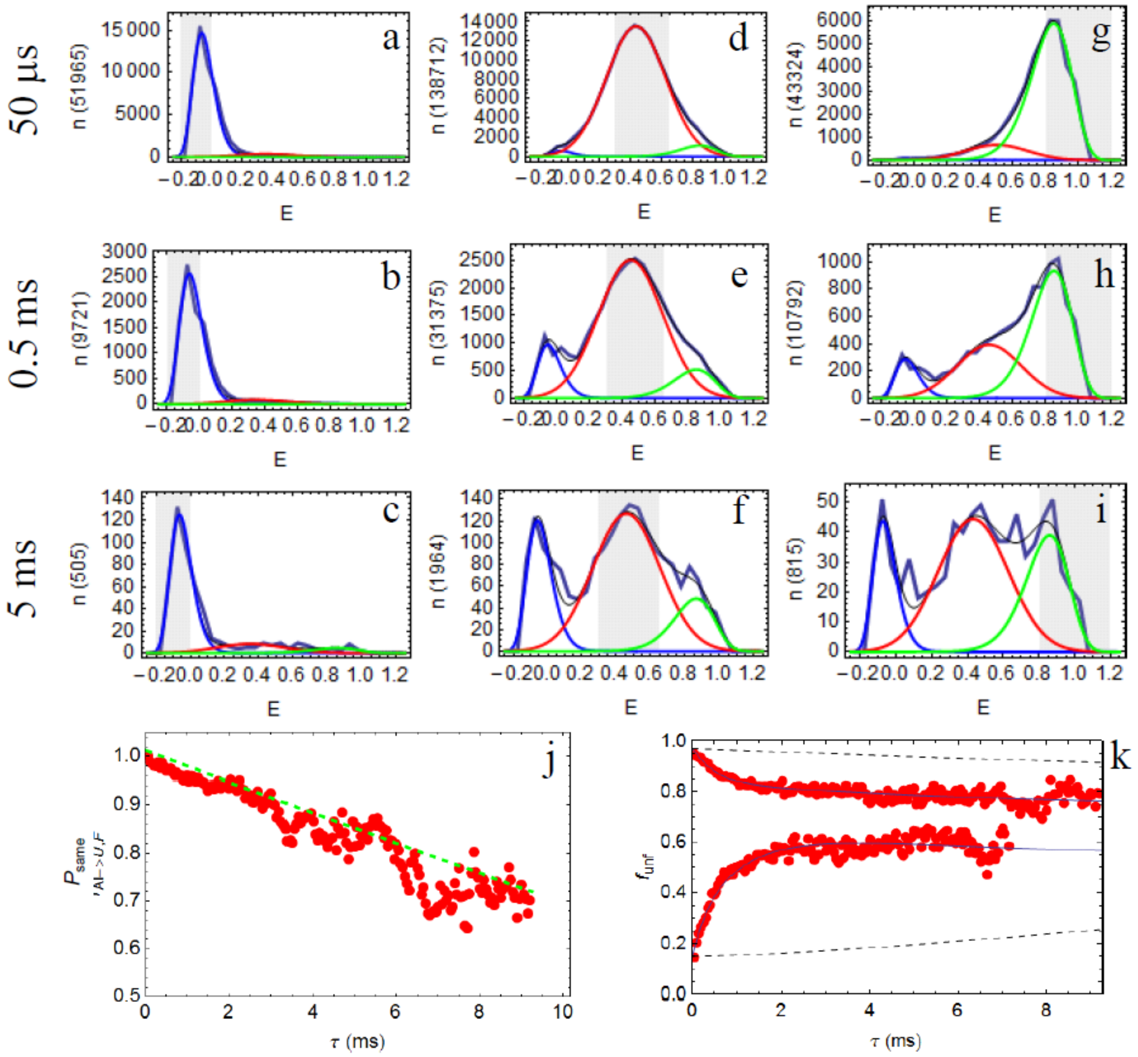

Figure 5.11: Kinetic Analysis of BdpA in 3.5 M GdmCl at 37 °C analogous to figure 5.9. Figures a-c show the appearance of acceptor-active molecules from acceptor-inactive molecules as a complementary method to estimate same molecule probability. Times shown in histograms titles are the recurrence time intervals (50 ms ±25 ms, 500 ms ± 25 ms, and 5 ms ± 25 ms). Figure j shows the very good agreement between the histogram-based approach (red circles) and the correlation approach (green dashed line, see text for details). Figures d-f and g-i show recurrence histograms for initial *E* ranges with mostly unfolded or folded fractions, respectively. The resulting unfolded fractions as function of recurrence time are shown in figure k, showing folding relaxation on the millisecond timescale. Because BdpA has a second folding rate due to proline isomerization, the fractions after 3 ms are not the same.

5.5 DISCUSSION

For the analysis of single molecule FRET experiments of freely diffusing molecules, an important step is to identify bursts, i.e. the bursts of photons which correspond to molecules traversing the confocal volume. To our knowledge, all methods to analyze bursts have treated them as independent events. In contrast, the models used in fluorescence correlation spectroscopy (FCS) include the recurrence of molecules to describe molecular diffusion (Zander et al., 2002 p. 69 ff.). The recurrence effect is also apparent from the photon trajectory of single molecule experiments. A possibility to use this information would be to just add the photons from all bursts originating from the same single molecule, which would result in a decrease of the peak width caused by shot noise in transfer efficiency histograms. The same effect could be achieved by simply increasing the photon rates with higher laser power. Here, we do not add the bursts, but compare their properties (i.e. their transfer efficiencies), which has three advantages. Firstly, we keep the temporal information, which can be used to analyze kinetic processes. Secondly, we can include the probabilities that two bursts detected within a certain time range belong to the same or two different molecules very easily. Thirdly, we can differentiate between different processes causing the broadening of transfer efficiency peaks, i.e. shot noise from other, intrinsic factors.

The potential of recurrence analysis has been exemplified with several measurements. The recurrence transfer efficiency histograms for short times show that we can extract the peaks of single subpopulations with their position and shot noise width as in the full histogram (figures 5.2 and 5.9-11). This single subpopulation peaks can in principle be used to fit the full histogram by simply adjusting the amplitudes. Alternatively (and as done in the kinetic analysis in chapter 5.3), we can fit the subpopulation peaks with model distributions (i.e. a Gaussian or a lognormal peak) and use the results to constrain the peak shapes and positions for fits where more than one subpopulation is present.

By comparing the recurrence peaks with the full histogram, we can also identify heterogeneities within the subpopulations as shown for the unfolded peak of Csp*Tm* or polyproline 20 in figure 5.6. For Csp*Tm*, it was shown that the peak width of the unfolded subpopulation is broader than expected from shot-noise broadening only and that the bursts from different parts of the peak have slightly different donor lifetimes, suggesting that they represent subsets of unfolded molecules with slightly different mean transfer efficiencies (Merchant et al., 2007). With recurrence analysis, a small but significant heterogeneity of the unfolded state of Csp can be directly demonstrated. The contour plot (figure 5.3) reveals an elliptical peak, and the position of the unfolded peak in the recurrence histogram depends on the initial transfer efficiency range (figure 5.6), which cannot be explained by shot noise.

As a well-studied example for heterogeneity, polyproline 20 was measured and analyzed. Polyproline has been used as a spectroscopic ruler for FRET (Stryer and Haugland, 1967; Schuler et al., 2005) and its heterogeneous distance distribution has been analyzed both experimentally and by MD simulation (Watkins et al., 2006; Doose et al., 2007; Best et al., 2007). The recurrence analysis of polyproline 20 allows visualizing the structural origin of the peak broadening without any introduction of models or additional measurements. Figure 5.6 (h-l) reveals that the position of the recurrence peak depends strongly on the choice of the initial transfer efficiency region as expected for a static distance distribution. Although the standard transfer efficiency histogram can be fitted with two Gaussian functions, the recurrence histograms clearly reveal a much more heterogeneous origin of the peak. The similarity between the peak widths in the recurrence histograms for times within 1 ms (figure 5.6 m) and between 10 and 20 ms (figure 5.6 n) shows that the interconversion between the different species within the peak is expected to be slower than tens of milliseconds.

As a third example, Csp is measured in the presence of viscogens, i.e. 40% (w/v) ethylene glycol. Studying the effect of viscogens on the folding and stability of proteins is of fundamental interest, as the presence of viscogens can mimic important aspects of the protein’s environment inside the cell (Rösgen et al., 2005). An interesting effect of ethylene glycol on Csp can be seen in figure 5.5. Next to the pronounced unfolded peak, a second subpopulation appears with transfer efficiencies higher than the main unfolded peak, but lower than the expected folded subpopulation. Its distorted shape suggests that this second subspecies has not only one single, shot noise broadened transfer efficiency, and a comparison for different recurrence times reveals that it interconverts with the main unfolded peak on the order of milliseconds. These findings identify a third subpopulation in Csp, a classical example of a two-state folder so far. However, to exclude a photophysical origin of the additional population, additional investigations are important.

Recurrence analysis can also be used to obtain kinetic information. Depending on the measurement conditions, the recurrence time window (i.e. the time after an initial burst where the amount of bursts originating from recurring molecules is sufficient to calculate accurate subpopulation fractions) can be on the order of 20 to 50 ms. By constructing recurrence histograms or contour plots for different τ, it can be tested whether subpopulations interconvert on the recurrence time scale or not. Although still restricted to a narrow time window, numerous interesting dynamical processes can be monitored.

From a more technical point of view, an important example for dynamical processes are photo-physical effects of the fluorescence dyes, which can directly infer with the measurement and its analysis. Photo bleaching of dyes limits both the length of measurements with immobilized samples as well as the upper limit of laser intensities and therefore photon rates in diffusion experiments. A detailed understanding of photo-bleaching is therefore of interest, especially to develop strategies to improve the photo stabilities of the dyes for example by using buffer additives to remove oxygen (Rasnik et al., 2006; Vogelsang et al., 2008) or to quench the triplet states of the dyes (Widengren et al., 2007). Recurrence analysis offers a simple approach to test the effects of such additives by monitoring the bleaching behavior in diffusion experiments. The other photo-physical effect that is especially prominent in single molecule experiments with immobilized samples is photo-blinking, i.e. the recovery of photo emission capability of a dye after a short time where it is unable to emit. In the standard analysis of diffusion experiments, blinking is difficult to identify, as the time windows are too short. Burst time correlation can directly show that blinking is not relevant on the recurrence time scale, as there is no significant cross-correlation signal between acceptor-inactive and acceptor-active states both for Csp in 1.1 M GdmCl (figure 5.8 c) and in all other samples analyzed.

More interesting than photophysical effects are dynamical structural processes of the sample molecules. Protein folding is the most prominent example, and analyses of spectrin R15 and BdpA were shown to give reasonable folding relaxation times. As the signal used can be directly transferred to the fraction of unfolded molecules, the fit directly reveals whether a single relaxation rate is sufficient to obtain the same final equilibrium fraction starting from folded or unfolded molecules (as for spectrin, figure 5.10), or whether an additional phase is needed (as for BdpA, figure 5.11). The determination of sub-milliseconds relaxation times is not possible with conventional stopped flow instruments, therefore the presented analysis offers a new complimentary approach besides techniques such as laser temperature jump (Dimitriadis et al., 2004) or NMR lineshape analysis (Myers and Oas, 2001). Next to protein folding, dynamical processes within subpopulations can be studied as well, as shown for Csp in 40% (w/v) ethylene glycol.

The methods introduced to obtain kinetic processes and to distinguish between different origins for peak broadening are not restricted to the comparison of different bursts from the same molecule. The methods can also be applied to different parts of a burst, but the time range and the amount of photons will be reduced. Notably, although in the presented examples only the transfer efficiency has been used, the method can be extended to any parameter which can be obtained from a burst, such as burst size, lifetimes, or anisotropies. Time dependent changes of these parameters might allow additional insights into the system.

A convenient feature of recurrence analysis is that the additional information is available in any state in most single molecule diffusion experiment setups. No adjustments have to be made for the instrument, no more information is needed about the system, and no models have to be assumed. That also means that the analysis can be applied also to measurements already taken to obtain new information about them. In case a better subpopulation separation is required, the measurement can be extended, as done for the measurements presented. As the usable recurrence time range is coupled to the same-molecule probability, the concentration of the sample can be decreased for extending the recurrence time window.

Taken together, recurrence analysis was shown to have the potential to significantly improve the analysis of single molecule measurements, to extend the amount of information that can be extracted, and with that to give new interesting insights into biochemical processes on the single molecule level.

5.6 MATERIAL AND METHODS

Purification and labelling of Csp*Tm* (labelled at positions 2 and 67, chapter II), R15 (Scott et al., 2004), and BdpA (Clark, 2008) were performed as described previously. All experiments were performed in buffer containing 0.001% Tween 20 to prevent surface adhesion of the polypeptides, and 20 mM cysteamine, and 150 mM β-mercaptoethanol to reduce photo damage. Additional buffer conditions are listed in table 5.1. Protein concentrations are in the range between 5 and 25 pM and were adjusted to obtain appropriate burst rates (see table 5.1).

	Csp	**Polyproline**	**Csp**	**R15**	**BdpA**
buffer	1.1 M GdmCl, 50 mM NaP, pH 7	3.5 M GdmCl, 50 mM NaP, pH 7	3.5 M GdmCl, 50% EG, 50 mM NaP, pH 7	1.1 M GdmCl, 50 mM NaP, pH 7	2.5 M GdmCl, 20 mM NaAc, 100 mM NaCl, pH 5, 37°C[IX]
laser power (μW)	100	100	100	100	300
1st min. number	25	50	60	25	80
2nd min. number	25	20	20	20	15
bin size (ms)	1	1	0.5	1	0.05
bursts per s	1	2	2	2	8
measurement time (h)	20	15	8	14	14

Table 5.1: Measurement conditions and analysis parameters. ‘1st min number’ refers to the first burst identification step, ‘2nd min number’ and the bin size to the second step (see supplement for details). Bursts per second were calculated after the first burst identification step. Temperature was 22° C is not noted otherwise.

The single-molecule fluorescence experiments were performed with a MicroTime 200 confocal microscope (PicoQuant, Berlin, Germany) equipped with a 488 nm diode laser (Sapphire 488-100 CDRH, Coherent, Santa Clara, CA) and an Olympus UplanApo 60x/1.20W objective. After passing through a 100 μm pinhole, sample fluorescence was separated into donor and acceptor components using a dichroic mirror (585DCXR, Chroma, Rockingham, VT). After passing two filters (Chroma ET525/50M, HQ650/100), each component was focused onto avalanche photodiodes (SPCM-AQR-15, PerkinElmer Optoelectronics, Vaudreuil, QC, Canada), and the arrival time of every detected photon was recorded using time resolved counting electronics (Hydra Harp, PicoQuant, Berlin, Germany). Measurements were performed with laser powers as indicated in table 5.1.

The burst detection was performed in two steps. First, photons were combined into one burst which were detected in either channel and separated by less than 100 μs. A burst was retained as a significant event if the total number of counts exceeded values between 25 and 80, depending o the measurement (see table 5.1, ‘1st min number’). In a second step, all photons not belonging to bursts were discarded. The trajectory of the remaining photons were binned in different sizes between 50 ms and 1 ms (see table 5.1, ‘bin size’) and bins with

---

[IX] Temperature was adjusted and calibrated as described previously (Nettels et al., 2009).

more than 15 to 25 photons (see table 5.1 ‘2nd min number’) were retained for further analysis. Identified bursts were corrected for background, differences in quantum yields of donor and acceptor, the different collection efficiencies in the detection channels, cross-talk, and direct acceptor excitation as described previously (Schuler, 2006).

5.7 SUPPLEMENT

Optimized Burst Detection Algorithms for RASP

As a standard approach to obtain bursts from a single molecule trajectory, photons are first grouped into bursts where adjacent photons are separated by less than a certain time (e.g. 100 μs). As a second criterion, bursts are rejected which have less photons than a certain threshold (e.g. 50 photons). An alternative burst identification approach is to bin the trajectory (e.g. with 1 ms bin size), retain bins of certain sizes, combine adjacent retained bins into bursts, and retain bursts of certain size.

Both approaches have advantages and disadvantages when performing RASP. The binning approach detects the beginning and ending of bursts less accurate, but it can simplify and improve certain aspects of RASP. For that, we use a slightly modified version of the binning approach: Instead of combing adjacent bins, we analyze them separately. That means that we are no longer differentiating whether two bins belong to the same burst (e.g. the molecule was continuously in the confocal volume between the bins), or to two different bursts (e.g. the molecule left the confocal volume and recurred). We found that when plotting the resulting burst correlations (which actually is a “bin time correlation”) in a double logarithmic way (e.g. in figure 5.7), we get perfectly linear relationship for the first few milliseconds, which include bins belonging to the same burst and to bursts from recurred molecules. This illustrates also one of the advantages of using this modified binning approach: The analysis of burst time correlations is much easier, as other approaches, for instance the interphoton time based one, result in “anti-bunching” behavior. I.e. we get a lower correlation amplitude for times on the time scale of the burst duration, simply because a recurred molecule can only be detected after it has left the confocal volume. The second advantage of the adjusted binning approach is that the bin size can be reduced to get a higher temporal resolution, like it was done for the analysis of the BdpA data.

To benefit from both approaches, we use a two step bursts analysis. First, we identify bursts after the interphoton time criterion (with 100 μs and 1st min. number in table 5.1) and discard all photons not belonging to a burst, i.e. the background photons. In the second step we use the binning approach on the remaining photons (with bin size and 2nd min. number as in table 5.1).

Cross-peaks from conformational transitions have the same amount of bursts

In a recurrence contour plot which exhibits dynamic changes between two conformations, four peaks will appear. One for the molecules of each subpopulation (i.e. state A and B) which have not changed between the two time points, and two peaks for molecules which either interconverted from state A to B or vice versa. The relative fraction of state A (f_A) at time points t_1 (initial detection) and t_2 (second detection) can be written as:

$$f_A(t_1) = \frac{[A_1]}{[A_1]+[B_1]} = \frac{[A_1A_2]+[A_1B_2]}{[A_1A_2]+[A_1B_2]+[B_1A_2]+[B_1B_2]} \qquad [5.10]$$

$$f_A(t_2) = \frac{[A_2]}{[A_2]+[B_2]} = \frac{[A_1A_2]+[B_1A_2]}{[A_1A_2]+[B_1A_2]+[B_1B_2]+[A_1B_2]} \qquad [5.11]$$

where $[X_n]$ is the concentration of state X (either A or B) at time point n (either 1 or 2) and $[X_1Y_2]$ is the concentration of molecules which have been in state X at time 1 and Y at time 2. As the samples are measured under equilibrium conditions, the fraction of one state is constant in time, i.e. $f_A(t_1) = f_A(t_2)$. As the denominator is the same in both cases, it follows that the size of the crosspeaks is identical, i.e. $[A_1B_2]$ is equal to $[B_1A_2]$, independent of the fraction f_A.

Derivation of Same Molecule Probability

The probability that two molecules (i and j) measured at time t and $t+\tau$ are identical ("the same", i.e. i=j) can be written as:

$$p_S(\tau) = p\left(i = j \,|\, \{j,t+\tau\} \cap \{i,t\}\right) \qquad [5.12a]$$

$$= \frac{p\left(i = j \cap \{j,t+\tau\} \,|\, \{i,t\}\right)}{p\left(\{j,t+\tau\} \,|\, \{i,t\}\right)} \qquad [5.12b]$$

$$= \frac{p\left(\{j,t+\tau\} \,|\, \{i,t\}\right) - p\left(i \neq j \,| \cap \{i,t+\tau\} \,|\, \{i,t\}\right)}{p\left(\{j,t+\tau\} \,|\, \{i,t\}\right)} \qquad [5.12c]$$

$$= 1 - \frac{p\left(i \neq j \cap \{j,t+\tau\} \,|\, \{i,t\}\right)}{p\left(\{j,t+\tau\} \,|\, \{i,t\}\right)} \qquad [5.12d]$$

$$= 1 - \frac{p\left(\{j,t+\tau\} \,|\, i \neq j \cap \{i,t\}\right) p\left(i \neq j \,| \cap \{i,t\}\right)}{p\left(\{j,t+\tau\} \,|\, \{i,t\}\right)} \qquad [5.12e]$$

$$= 1 - \frac{p\left(\{j,t+\tau\}\right) p\left(i \neq j\right)}{p\left(\{j,t+\tau\} \,|\, \{i,t\}\right)} \quad \text{(using temporal independence of molecules)} \qquad [5.12f]$$

$$= 1 - \frac{p\left(i \neq j\right)}{g(\tau)} = 1 - \frac{1 - 1/N}{g(\tau)} \qquad [5.12g]$$

$$\overset{N\to\infty}{=} 1 - \frac{1}{g(\tau)} \qquad [5.12h]$$

using for 5.12a to 5.12b and 5.12d to 5.12e

$$p\left(A \cap B \,|\, C\right) = p\left(A \,|\, B \cap C\right) p\left(B \,|\, C\right) \qquad [5.13]$$

N is the total number of molecules in the sample.

Detection efficiency ratio

The detection efficiency DE_X of one subpopulation X we define as

$$DE_X = \frac{n_{X,D}}{[X]} \tag{5.14}$$

Here $[X]$ is the concentration and $n_{X,D}$ is the rate with which bursts are emitted from molecules of subpopulation X. We can then define the detection efficiency ratio as:

$$DE = \frac{DE_F}{DE_U} \tag{5.15}$$

Equations 5.14 and 5.15 result in

$$DE = \frac{[U]}{[F]}\frac{n_{F,D}}{n_{U,D}} = \frac{\frac{1}{f_{U,D}^{b}}-1}{\frac{1}{f_U}-1} \tag{5.16}$$

which is equivalent to equation 5.5, with the fraction of unfolded molecules in the sample f_U and detected $f_{U,D}^{b}$.

Recurrence probability ratio

For a quantitative description of conformational changes within the recurrence time we have to consider that the recurrence probabilities for the subpopulations might be different. Possible reasons are differences in diffusion times or bleaching probabilities. In case that the recurrence probabilities for all subpopulations are the same, their fractions in recurrence histograms constructed for the whole transfer efficiency range $f_{U,RH}^{b}(\tau)$ should be the same for all recurrence times τ as well.

Analogous to the detection efficiency, we define the recurrence probability of subpopulation X, $RP_X(\tau)$ as

$$RP_X(\tau) = \frac{n_X(\tau)}{[X]} \tag{5.17}$$

Here $n_X(\tau)$ is the rate with which recurred bursts are detected from molecules of subpopulation X at time τ after they were initially detected. For simplicity reasons, this parameter therefore includes both the correction for the probability to be detected after being detected before (i.e. recurrence probability) and the probability to be detected the first time compared to the occurrence in the sample (i.e. detection efficiency).

Accordingly, the recurrence probability ratio is the ratio between the recurrence probabilities of folded (F) and unfolded (U) subpopulations:

$$RP(\tau) = \frac{RP_F(\tau)}{RP_U(\tau)} \qquad [5.18]$$

Equations 5.17 and 5.18 result in

$$RP(\tau) = \frac{n_F(\tau)}{n_U(\tau)} \frac{[U]}{[F]} = \frac{\frac{1}{f^b_{U,RH}(\tau)} - 1}{\frac{1}{f_U} - 1} \qquad [5.19]$$

with the fractions of unfolded molecules in detected in the recurrence histograms $f^b_{U,RH}(\tau)$ and in the sample f_U.

We can obtain *RP* as a function of τ by first constructing time dependent recurrence histograms starting from all transfer efficiencies, fitting the histograms, and calculating the fraction of unfolded molecules. These steps are identical to the procedure to produce fractions of unfolded molecules for restricted transfer efficiencies as done in chapter 5.4. We can fit RP versus τ by an empirical function and use this function in equation 5.6.

VI. Appendix

6.1 ABBREVIATIONS AND SYMBOLS

a	contact distance
Å	Ångström (0.1 nm)
APD	avalanche photodiode
ATP	adenosine triphosphate
BdpA	B domain of protein A
b_X	burst with characteristic X
C_∞	characteristic ratio in limit $n \rightarrow \infty$
CD	circular dichroism
c_F	concentration of folded subpopulation
C_n	characteristic ratio
Csp	cold shock protein
Csp*Bc*	cold shock protein from *Bacillus caldolyticus*
Csp*Bs*	cold shock protein from *Bacillus subtilis*
Csp*Tm*	cold shock protein from *Thermotoga maritima*
c_U	concentration of unfolded subpopulation
D	diffusion coefficient
Da	Dalton
DE	detection efficiency ratio
DLS	dynamic light scattering
DNA	desoxyribo nucleic acid
E	transfer efficiency
E_0	potential free energy height
EG	ethylene glycol
$f^{x}_{U,D}$	fraction of unfolded molecules for different molecules, not corrected for different detection efficiency
$f^{x}_{U,R}$	fraction of unfolded molecules for recurred molecules, not corrected for different recurrence probability
$f^{x}_{U,RH}$	fraction of unfolded molecules, not corrected for different recurrence probability or detection efficiency
f_{AI}	fraction of molecules with inactive acceptor
FCS	fluorescence correlation spectroscopy
ff.	following pages
FRET	Förster resonance energy transfer
f_U	fraction of unfolded molecules
$f_{U,0}$	initial fraction of unfolded molecules
$f_{U,D}$	fraction of unfolded molecules for different molecules
$f_{U,RH}$	fraction of unfolded molecules for recurred molecules
g_{AB}	crosscorrelation function between event A and B
GdmCl	guanidinium chloride
I_P	intensity of parallel polarized light
I_S	intensity of perpendicular polarized light
J	overlap integral
k	contact formation rate
$k_{A'}$	radiative acceptor decay rate
k_B	Boltzmann constant
k_D	donor decay rate
$k_{D'}$	radiative donor decay rate
k_f	radiative fluorescence decay rate
k_{nA}	non-radiative acceptor decay rate
k_{nD}	non-radiative donor decay rate
k_{nf}	non-radiative fluorescence decay rate
l	contour length
l_p	persistence length
M	molar
MFD	multi-parameter fluorescence detection
n	refractive index
n	number of monomers
N_A	Avogadro’s number
NaAc	sodium acetate
NaP	sodium phosphate
n_C	total number of contacts
nm	nanometer
NMR	nuclear magnetic resonance
ns	nanosecond
p.	page
PEG400	polyethylene glycol with 400 Da
pp.	pages
ps	picoseconds

p_S	‘same molecule’ probability
Q	quantum yield
Q	number of native contacts
Q_A	quantum yield of acceptor dye
Q_D	quantum yield of donor dye
r	fluorescence anisotropy
R	inter-dye distance
R	ideal gas constant
r_0	fundamental anisotropy
R_0	Förster distance
r_∞	residual anisotropy
RASP	recurrence analysis of single particles
RCM	route correction matrix
R_G	radius of gyration
RP	recurrence probability ratio
RP_X	recurrence probability of subpopulation X
SAXS	small angle X-ray scattering
SRCD	synchrotron radiation circular dichroism
T	temperature
t	time
Trp	Tryptophan
v	exponential scaling factor
ΔG	free energy difference
E_A	transfer efficiency of initial burst
E_B	transfer efficiency of second burst
η	dynamic viscosity
κ^2	orientation factor
μs	microsecond
σ	internal friction
τ	fluorescence lifetime
τ	time between two bursts
τ_D	lifetime of donor dye in absence of acceptor dye
τ_{DA}	lifetime of donor dye in presence of acceptor dye
τ_{eff}	decay rate of dye rotation
τ_M	decay rate of molecule rotation

6.2 REFERENCES

Abbondanzieri, E.A., G. Bokinsky, J.W. Rausch, J.X. Zhang, S.F.J. Le Grice, and X. Zhuang. 2008. Dynamic binding orientations direct activity of HIV reverse transcriptase. Nature. 453(7192): 184-189.

Agashe, V.R., M.C. Shastry, and J.B. Udgaonkar. 1995. Initial hydrophobic collapse in the folding of barstar. Nature. 377(6551): 754-757.

Akiyama, S., S. Takahashi, K. Ishimori, and I. Morishima. 2000. Stepwise formation of alpha-helices during cytochrome c folding. Nat Struct Biol. 7(6): 514-520.

Ansari, A., C.M. Jones, E.R. Henry, J. Hofrichter, and W.A. Eaton. 1992. The role of solvent viscosity in the dynamics of protein conformational changes. Science. 256(5065): 1796-1798.

Arai, M., E. Kondrashkina, C. Kayatekin, C.R. Matthews, M. Iwakura, and O. Bilsel. 2007. Microsecond hydrophobic collapse in the folding of Escherichia coli dihydrofolate reductase, an alpha/beta-type protein. J Mol Biol. (1): 219-229.

Baldwin, R.L. 1995. The nature of protein folding pathways: the classical versus the new view. J. Biomol. NMR. 5(2): 103-109.

Ballew, R.M., J. Sabelko, and M. Gruebele. 1996. Direct observation of fast protein folding: the initial collapse of apomyoglobin. Proc. Natl. Acad. Sci. U.S.A. 93(12): 5759-5764.

Barbar, E., M. Hare, V. Daragan, G. Barany, and C. Woodward. 1998. Dynamics of the conformational ensemble of partially folded bovine pancreatic trypsin inhibitor. Biochemistry. 37(21): 7822-7833.

Best, R.B., K.A. Merchant, I.V. Gopich, B. Schuler, A. Bax, and W.A. Eaton. 2007. Effect of flexibility and cis residues in single-molecule FRET studies of polyproline. Proc. Natl. Acad. Sci. U.S.A. 104(48): 18964-18969.

Bieri, O., J. Wirz, B. Hellrung, M. Schutkowski, M. Drewello, and T. Kiefhaber. 1999. The speed limit for protein folding measured by triplet-triplet energy transfer. Proc. Natl. Acad. Sci. U.S.A. 96(17): 9597-9601.

Blanchard, S.C., H.D. Kim, R.L. Gonzalez, J.D. Puglisi, and S. Chu. 2004. tRNA dynamics on the ribosome during translation. Proc. Natl. Acad. Sci. U.S.A. 101(35): 12893-12898.

Bokinsky, G., and X. Zhuang. 2005. Single-molecule RNA folding. Acc Chem Res. 38(7): 566-573.

Bredenbeck, J., J. Helbing, A. Sieg, T. Schrader, W. Zinth, C. Renner, R. Behrendt, L. Moroder, J. Wachtveitl, and P. Hamm. 2003. Picosecond conformational transition and equilibration of a cyclic peptide. Proc. Natl. Acad. Sci. U.S.A. 100(11): 6452-6457.

Bryngelson, J.D., and P.G. Wolynes. 1987. Spin glasses and the statistical mechanics of protein folding. Proc. Natl. Acad. Sci. U.S.A. 84(21): 7524-7528.

Buscaglia, M., B. Schuler, L.J. Lapidus, W.A. Eaton, and J. Hofrichter. 2003. Kinetics of intramolecular contact formation in a denatured protein. J. Mol. Biol. 332(1): 9-12.

Cantor, C.R., and P.R. Schimmel. 1980. The behavior of biological macromolecules. W. H. Freeman.

Chakrabartty, A., and R.L. Baldwin. 1995. Stability of [alpha]-Helices. p. 141-176. *In* Advances in Protein Chemistry. Academic Press.

Chan, C.K., Y. Hu, S. Takahashi, D.L. Rousseau, W.A. Eaton, and J. Hofrichter. 1997. Submillisecond protein folding kinetics studied by ultrarapid mixing. Proc. Natl. Acad. Sci. U.S.A. 94(5): 1779-1784.

Chan, H.S., and K.A. Dill. 1991. Polymer Principles in Protein-Structure and Stability. Annu Rev Biophys Biomol Struct. 20: 447-490.

Chance, B. 1951. Rapid and Sensitive Spectrophotometry. I. The Accelerated and Stopped-Flow Methods for the Measurement of the Reaction Kinetics and Spectra of Unstable Compounds in the Visible Region of the Spectrum. Rev. Sci. Instrum. 22(8): 619-627.

Chen, E., R.A. Goldbeck, and D.S. Kliger. 2003. Earliest Events in Protein Folding: Submicrosecond Secondary Structure Formation in Reduced Cytochrome c. J Phys Chem A. 107(40): 8149-8155.

Cho, J.H., S. Sato, and D.P. Raleigh. 2004. Thermodynamics and kinetics of non-native interactions in protein folding: a single point mutant significantly stabilizes the N-terminal domain of L9 by modulating non-native interactions in the denatured state. J Mol Biol. 338(4): 827-837.

Cho, J., and D.P. Raleigh. 2005. Mutational analysis demonstrates that specific electrostatic interactions can play a key role in the denatured state ensemble of proteins. J Mol Biol. 353(1): 174–185.

Clark, J. 2008. Single molecule studies of protein folding, aggregation and translocation.

Damaschun, G., H. Damaschun, K. Gast, and D. Zirwer. 1998. Denatured states of yeast phosphoglycerate kinase. Biochemistry (Mosc). 63(3): 259-275.

Deniz, A.A., M. Dahan, J.R. Grunwell, T. Ha, A.E. Faulhaber, D.S. Chemla, S. Weiss, and P.G. Schultz. 1999. Single-pair fluorescence resonance energy transfer on freely diffusing molecules: observation of Förster distance dependence and subpopulations. Proc. Natl. Acad. Sci. U.S.A. 96(7): 3670-3675.

Deniz, A.A., T.A. Laurence, G.S. Beligere, M. Dahan, A.B. Martin, D.S. Chemla, P.E. Dawson, P.G. Schultz, and S. Weiss. 2000. Single-molecule protein folding: diffusion fluorescence resonance energy transfer studies of the denaturation of chymotrypsin inhibitor 2. Proc. Natl. Acad. Sci. U.S.A. 97(10): 5179-5184.

Deniz, A.A., T.A. Laurence, M. Dahan, D.S. Chemla, P.G. Schultz, and S. Weiss. 2001. Ratiometric Single-Molecule Studies of Freely Diffusing Biomolecules. Annu. Rev. Phys. Chem. 52(1): 233-253.

Diez, M., B. Zimmermann, M. Börsch, M. König, E. Schweinberger, S. Steigmiller, R. Reuter, S. Felekyan, V. Kudryavtsev, C.A.M. Seidel, and P. Gräber. 2004. Proton-powered subunit rotation in single membrane-bound F0F1-ATP synthase. Nat. Struct. Mol. Biol. 11(2): 135-141.

Dill, K.A., and H.S. Chan. 1997. From Levinthal to pathways to funnels. Nat. Struct. Biol. 4(1): 10-19.

Dill, K.A., and D. Shortle. 1991. Denatured States of Proteins. Annu Rev Biochem. 60: 795-825.

Dimitriadis, G., A. Drysdale, J.K. Myers, P. Arora, S.E. Radford, T.G. Oas, and D.A. Smith. 2004. Microsecond folding dynamics of the F13W G29A mutant of the B domain of staphylococcal protein A by laser-induced temperature jump. Proc. Natl. Acad. Sci. U.S.A. 101(11): 3809-3814.

Dinner, A.R., A. Sali, L.J. Smith, C.M. Dobson, and M. Karplus. 2000. Understanding protein folding via free-energy surfaces from theory and experiment. Trends Biochem. Sci. 25(7): 331-339.

Dobson, C.M. 2003. Protein folding and misfolding. Nature. 426(6968): 884-890.

Doi, M., and S.F. Edwards. 1988. The Theory of Polymer Dynamics. Oxford University Press, USA.

Doose, S., H. Neuweiler, H. Barsch, and M. Sauer. 2007. Probing polyproline structure and dynamics by photoinduced electron transfer provides evidence for deviations from a regular polyproline type II helix. Proc. Natl. Acad. Sci. U.S.A. 104(44): 17400-17405.

Dyson, H., and P. Wright. 1998. Equilibrium NMR studies of unfolded and partially folded proteins. Nat Struct Biol. 5: 499-503.

Dyson, H., and P. Wright. 2005. Intrinsically unstructured proteins and their functions. Nat Rev Mol Cell Biol. 6(3): 197-208.

Edel, J.B., E.K. Hill, and A.J. de Mello. 2001. Velocity measurement of particulate flow in microfluidic channels using single point confocal fluorescence detection. Analyst. 126(11): 1953-1957.

Eggeling, C., S. Berger, L. Brand, J.R. Fries, J. Schaffer, A. Volkmer, and C.A.M. Seidel. 2001. Data registration and selective single-molecule analysis using multi-parameter fluorescence detection. J Biotechnol. 86(3): 163–180.

Fersht, A. 1999. Structure and mechanism in protein science. 7. ed. W.H. Freeman.

Fitzkee, N., and G. Rose. 2004. Reassessing random-coil statistics in unfolded proteins. Proc Natl Acad Sci U S A. 101(34): 12497-12502.

Flory, P.J. 1989. Statistical mechanics of chain molecules. Carl Hanser Verlag.

Flory, P. 1949. The Configuration of Real Polymer Chains. JCP. 17(3): 303-310.

Földes-Papp, Z. 2007. 'True' single-molecule molecule observations by fluorescence correlation spectroscopy and two-color fluorescence cross-correlation spectroscopy. Exp. Mol. Pathol. 82(2): 147-155.

Förster, T. 1948. Zwischenmolekulare Energiewanderung und Fluoreszenz. Ann Phys. 437(1-2): 55-75.

Frankenberg, N., C. Welker, and R. Jaenicke. 1999. Does the elimination of ion pairs affect the thermal stability of cold shock protein from the hyperthermophilic bacterium Thermatoga maritima? FEBS Lett. 454(3): 299-302.

Garcia-Mira, M., D. Boehringer, and F. Schmid. 2004. The folding transition state of the cold shock protein is strongly polarized. J Mol Biol. 339(3): 555-569.

Gellman, S.H. 1998. Minimal model systems for [beta]-sheet secondary structure in proteins. Curr Opin Chem Biol. 2(6): 717-725.

Grosberg, A.I., A.R. Khokhlov, and Y.A. Atanov. 1994. Statistical physics of macromolecules. Amer Inst of Physics.

Ha, T., T. Enderle, D.F. Ogletree, D.S. Chemla, P.R. Selvin, and S. Weiss. 1996. Probing the interaction between two single molecules: fluorescence resonance energy transfer between a single donor and a single acceptor. Proc. Natl. Acad. Sci. U.S.A. 93(13): 6264-6268.

Hänggi, P., P. Talkner, and M. Borkovec. 1990. Reaction-rate theory: fifty years after Kramers. Rev. Mod. Phys. 62(2): 251.

Henzler-Wildman, K.A., V. Thai, M. Lei, M. Ott, M. Wolf-Watz, T. Fenn, E. Pozharski, M.A. Wilson, G.A. Petsko, M. Karplus, C.G. Hübner, and D. Kern. 2007. Intrinsic motions along an enzymatic reaction trajectory. Nature. 450(7171): 838-844.

Hertzog, D.E., X. Michalet, M. Jäger, X. Kong, J.G. Santiago, S. Weiss, and O. Bakajin. 2004. Femtomole mixer for microsecond kinetic studies of protein folding. Anal. Chem. 76(24): 7169-7178.

Hillger, F., D. Nettels, S. Dorsch, and B. Schuler. 2007. Detection and analysis of protein aggregation with confocal single molecule fluorescence spectroscopy. J Fluoresc. 17(6): 759-765.

Hofmann, H., R.P. Golbik, M. Ott, C.G. Hubner, and R. Ulbrich-Hofmann. 2008. Coulomb forces control the density of the collapsed unfolded state of barstar. J Mol Biol. 376(2): 597-605.

Horn, G., R. Hofweber, W. Kremer, and H.R. Kalbitzer. 2007. Structure and function of bacterial cold shock proteins. Cell. Mol. Life Sci. 64(12): 1457-1470.

Huang, G.S., and T.G. Oas. 1995. Submillisecond folding of monomeric lambda repressor. Proc. Natl. Acad. Sci. U.S.A. 92(15): 6878-6882.

Jacob, M., M. Geeves, G. Holtermann, and F. Schmid. 1999a. Diffusional barrier crossing in a two-state protein folding reaction. Nat Struct Biol. 6(10): 923-926.

Jacob, M., G. Holtermann, D. Perl, J. Reinstein, T. Schindler, M. Geeves, and F. Schmid. 1999b. Microsecond folding of the cold shock protein measured by a pressure-jump technique. Biochemistry. 38(10): 2882-2891.

Jahn, T.R., and S.E. Radford. 2008. Folding versus aggregation: Polypeptide conformations on competing pathways. Arch Biochem Biophys. 469(1): 100-117.

Jia, Y., D. Talaga, W. Lau, H. Lu, W. DeGrado, and R. Hochstrasser. 1999. Folding dynamics of single GCN4 peptides by fluorescence resonant energy transfer confocal microscopy. Chem Phys. 247(1): 69-83.

Junker, J.P., F. Ziegler, and M. Rief. 2009. Ligand-Dependent Equilibrium Fluctuations of Single Calmodulin Molecules. Science. 323(5914): 633-637.

Kazmirski, S.L., K.B. Wong, S.M. Freund, Y.J. Tan, A.R. Fersht, and V. Daggett. 2001. Protein folding from a highly disordered denatured state: the folding pathway of chymotrypsin inhibitor 2 at atomic resolution. Proc Natl Acad Sci U S A. 98(8): 4349–4354.

Kimura, T., T. Uzawa, K. Ishimori, I. Morishima, S. Takahashi, T. Konno, S. Akiyama, and T. Fujisawa. 2005. Specific collapse followed by slow hydrogen-bond formation of beta-sheet in the folding of single-chain monellin. Proc Natl Acad Sci U S A. 102(8): 2748-2753.

Klein-Seetharaman, J., M. Oikawa, S. Grimshaw, J. Wirmer, E. Duchardt, T. Ueda, T. Imoto, L. Smith, C. Dobson, and H. Schwalbe. 2002. Long-range interactions within a nonnative protein. Science. 295(5560): 1719-1722.

Kohn, J.E., I.S. Millett, J. Jacob, B. Zagrovic, T.M. Dillon, N. Cingel, R.S. Dothager, S. Seifert, P. Thiyagarajan, T.R. Sosnick, M.Z. Hasan, V.S. Pande, I. Ruczinski, S. Doniach, and K.W. Plaxco. 2004. Random-coil behavior and the dimensions of chemically unfolded proteins. Proc Natl Acad Sci U S A. 101(34): 12491-12496.

Korzhnev, D.M., X. Salvatella, M. Vendruscolo, A.A. Di Nardo, A.R. Davidson, C.M. Dobson, and L.E. Kay. 2004. Low-populated folding intermediates of Fyn SH3 characterized by relaxation dispersion NMR. Nature. 430(6999): 586-590.

Kremer, W., B. Schuler, S. Harrieder, M. Geyer, W. Gronwald, C. Welker, R. Jaenicke, and H. Kalbitzer. 2001. Solution NMR structure of the cold-shock protein from the hyperthermophilic bacterium Thermotoga maritima. Eur J Biochem. 268(9): 2527-2539.

Krieger, F., B. Fierz, O. Bieri, M. Drewello, and T. Kiefhaber. 2003. Dynamics of unfolded polypeptide chains as model for the earliest steps in protein folding. J Mol Biol. 332(1): 265-274.

Kubelka, J., J. Hofrichter, and W.A. Eaton. 2004. The protein folding 'speed limit'. Curr Opin Struct Biol. 14(1): 76-88.

Kuhn, W. 1934. Über die Gestalt fadenförmiger Moleküle in Lösungen. Colloid & Polymer Science. 68(1): 2-15.

Lakowicz, J.R. 2006. Principles of Fluorescence Spectroscopy. 3. ed. Springer, Berlin.

Lapidus, L.J., W.A. Eaton, and J. Hofrichter. 2000. Measuring the rate of intramolecular contact formation in polypeptides. Proc. Natl. Acad. Sci. U.S.A. 97(13): 7220-7225.

Lapidus, L.J., S.H. Yao, K.S. McGarrity, D.E. Hertzog, E. Tubman, and O. Bakajin. 2007. Protein hydrophobic collapse and early folding steps observed in a microfluidic mixer. Biophys J. 93(1): 218-224.

Lipari, G., and A. Szabo. 1980. Effect of librational motion on fluorescence depolarization and nuclear magnetic resonance relaxation in macromolecules and membranes. Biophys. J. 30(3): 489-506.

Lipman, E.A., B. Schuler, O. Bakajin, and W.A. Eaton. 2003. Single-molecule measurement of protein folding kinetics. Science. 301(5637): 1233-1235.

Magg, C., J. Kubelka, G. Holtermann, E. Haas, and F. Schmid. 2006. Specificity of the initial collapse in the folding of the cold shock protein. J Mol Biol. 360(5): 1067-1080.

Magg, C., and F. Schmid. 2004. Rapid collapse precedes the fast two-state folding of the cold shock protein. J Mol Biol. 335(5): 1309-1323.

Marme, N., J. Knemeyer, M. Sauer, and J. Wolfrum. 2003. Inter- and Intramolecular Fluorescence Quenching of Organic Dyes by Tryptophan. Bioconjug Chem. 14(6): 1133-1139.

McCarney, E.R., J.E. Kohn, and K.W.&.C.M.M. Plaxco. 2005. Is there or isn't there? The case for (and against) residual structure in chemically denatured proteins. Crit Rev Biochem Mol Biol. 40(4): 181–189.

van der Meer, B.W., G.I. Coker, and S.S. Chen. 1994. Resonance Energy Transfer: Theory and Data. 1. ed. John Wiley & Sons.

Meier, S., M. Blackledge, and S. Grzesiek. 2008. Conformational distributions of unfolded polypeptides from novel NMR techniques. J Chem Phys. 128(5).

Merchant, K.A., R.B. Best, J.M. Louis, I.V. Gopich, and W.A. Eaton. 2007. Characterizing the unfolded states of proteins using single-molecule FRET spectroscopy and molecular simulations. Proc. Natl. Acad. Sci. U.S.A. 104(5): 1528-1533.

Minton, A.P. 2005. Models for excluded volume interaction between an unfolded protein and rigid macromolecular cosolutes: Macromolecular crowding and protein stability revisited. Biophys J. 88(2): 971-985.

Murphy, M., I. Rasnik, W. Cheng, T. Lohman, and T. Ha. 2004. Probing single-stranded DNA conformational flexibility using fluorescence spectroscopy. Biophys J. 86(4): 2530-2537.

Myers, J.K., and T.G. Oas. 2001. Preorganized secondary structure as an important determinant of fast protein folding. Nat Struct Mol Biol. 8(6): 552-558.

Neri, D., M. Billeter, G. Wider, and K. Wuthrich. 1992. NMR determination of residual structure in a urea-denatured protein, the 434-repressor. Science. 257(5076): 1559-1563.

Nettels, D., S. Müller-Späth, F. Küster, H. Hofmann, D. Haenni, S. Ruegger, L. Reymond, A. Hoffmann, J. Kubelka, B. Heinz, K. Gast, R. Best, and B. Schuler. 2009. Single-molecule spectroscopy of the temperature-induced collapse of unfolded proteins. Proc Natl Acad Sci U S A. 106(49): 20740-20745.

Nölting, B., R. Golbik, and A.R. Fersht. 1995. Submillisecond events in protein folding. Proc. Natl. Acad. Sci. U.S.A. 92(23): 10668-10672.

Ohnishi, S., A. Lee, M. Edgell, and D. Shortle. 2004. Direct demonstration of structural similarity between native and denatured eglin C. Biochemistry. 43(14): 4064-4070.

Pabit, S.A., H. Roder, and S.J. Hagen. 2004. Internal friction controls the speed of protein folding from a compact configuration. Biochemistry. 43(39): 12532-12538.

Palmer, A.G. 2001. Nmr probes of molecular dynamics: overview and comparison with other techniques. Annu Rev Biophys Biomol Struct. 30: 129-155.

Pande, V.S., Grosberg AYu, T. Tanaka, and D.S. Rokhsar. 1998. Pathways for protein folding: is a new view needed? Curr. Opin. Struct. Biol. 8(1): 68-79.

Perl, D., C. Welker, T. Schindler, K. Schroder, M. Marahiel, R. Jaenicke, and F. Schmid. 1998. Conservation of rapid two-state folding in mesophilic, thermophilic and hyperthermophilic cold shock proteins. Nat Struct Biol. 5(3): 229-235.

Phadtare S., Alsina J., and Inouye M.[1]. 1999. Cold-shock response and cold-shock proteins. Curr Opin Microbiol. 2: 175-180.

Plaxco, K.W., and D. Baker. 1998. Limited internal friction in the rate-limiting step of a two-state protein folding reaction. Proc Natl Acad Sci U S A. 95(23): 13591-13596.

Potapov, V., M. Cohen, and G. Schreiber. 2009. Assessing computational methods for predicting protein stability upon mutation: good on average but not in the details. Protein Eng Des Sel. 22(9): 553-560.

Prakash, S., and A. Matouschek. 2004. Protein unfolding in the cell. Trends Biochem Sci. 29(11): 593-600.

Prakash, S., L. Tian, K. Ratliff, R. Lehotzky, and A. Matouschek. 2004. An unstructured initiation site is required for efficient proteasome-mediated degradation. Nat Struct Mol Biol. 11(9): 830-837.

Pryse, K.M., T.G. Bruckman, B.W. Maxfield, and E.L. Elson. 1992. Kinetics and mechanism of the folding of cytochrome c. Biochemistry. 31(22): 5127-5136.

Qiu, L., C. Zachariah, and S. Hagen. 2003. Fast chain contraction during protein folding: "Foldability" and collapse dynamics. Phys Rev Lett. 90(16)Available at (verified 5 March 2010).

Rasnik, I., S.A. McKinney, and T. Ha. 2006. Nonblinking and longlasting single-molecule fluorescence imaging. Nat Methods. 3(11): 891-893.

Ratner, V., D. Amir, E. Kahana, and E. Haas. 2005. Fast collapse but slow formation of secondary structure elements in the refolding transition of E. coli adenylate kinase. J. Mol. Biol. 352(3): 683-699.

Ratner, V., and M.&.H.E. Sinev. 2000. Determination of intramolecular distance distribution during protein folding on the millisecond timescale. J Mol Biol. 299(5): 1363–1371.

Regenfuss, P., R.M. Clegg, M.J. Fulwyler, F.J. Barrantes, and T.M. Jovin. 1985. Mixing liquids in microseconds. Rev. Sci. Instrum. 56(2): 283-290.

Rösgen, J., B.M. Pettitt, and D.W. Bolen. 2005. Protein folding, stability, and solvation structure in osmolyte solutions. Biophys J. 89(5): 2988-2997.

Sali, A., E. Shakhnovich, and M. Karplus. 1994. How does a protein fold? Nature. 369(6477): 248-251.

Schellman, J.A. 2002. Fifty years of solvent denaturation. Biophys Chem. 96(2-3): 91-101.

Schindler, T., M. Herrler, M.A. Marahiel, and F.X. Schmid. 1995. Extremely rapid protein folding in the absence of intermediates. Nat Struct Mol Biol. 2(8): 663-673.

Schuler, B., E. Lipman, and W. Eaton. 2002. Probing the free-energy surface for protein folding with single-molecule fluorescence spectroscopy. Nature. 419(6908): 743-747.

Schuler, B. 2006. Application of Single Molecule Förster Resonance Energy Transfer to Protein Folding. p. 115-138. *In* Protein Folding Protocols.

Schuler, B., and W.A. Eaton. 2008. Protein folding studied by single-molecule FRET. Curr. Opin. Struct. Biol. 18(1): 16-26.

Schuler, B., E.A. Lipman, P.J. Steinbach, M. Kumke, and W.A. Eaton. 2005. Polyproline and the "spectroscopic ruler" revisited with single-molecule fluorescence. Proc. Natl. Acad. Sci. U.S.A. 102(8): 2754-2759.

Scott, K.A., S. Batey, K.A. Hooton, and J. Clarke. 2004. The folding of spectrin domains I: wild-type domains have the same stability but very different kinetic properties. J. Mol. Biol. 344(1): 195-205.

Shastry, M.C.R., and H. Roder. 1998. Evidence for barrier-limited protein folding kinetics on the microsecond time scale. Nat Struct Biol. 5(5): 385-392.

Shortle, D. 1996. The denatured state (the other half of the folding equation) and its role in protein stability. FASEB J. 10(1): 27-34.

Shortle, D., and M. Ackerman. 2001. Persistence of native-like topology in a denatured protein in 8 M urea. Science. 293(5529): 487-489.

Silow, M., and M. Oliveberg. 2003. High concentrations of viscogens decrease the protein folding rate constant by prematurely collapsing the coil. J Mol Biol. 326(1): 263-271.

Smith, L., K. Fiebig, H. Schwalbe, and C. Dobson. 1996. The concept of a random coil - Residual structure in peptides and denatured proteins. Fold Des. 1(5): R95-R106.

Socci, N., J. Onuchic, and P. Wolynes. 1996. Diffusive dynamics of the reaction coordinate for protein folding funnels. J Chem Phys. 104(15): 5860-5868.

Stone, H., A. Stroock, and A. Ajdari. 2004. Engineering flows in small devices: Microfluidics toward a lab-on-a-chip. Annu Rv Fluid Mech. 36: 381-411.

Stryer, L., and R. Haugland. 1967. Energy Transfer - A Spectroscopic Ruler. Proc Natl Acad Sci U S A. 58(2): 719-&.

Szabo, A., K. Schulten, and Z. Schulten. 1980. First passage time approach to diffusion controlled reactions. J. Chem. Phys. 72(8): 4350-4357.

Talaga, D.S., W.L. Lau, H. Roder, J. Tang, Y. Jia, W.F. DeGrado, and R.M. Hochstrasser. 2000. Dynamics and folding of single two-stranded coiled-coil peptides studied by fluorescent energy transfer confocal microscopy. Proc. Natl. Acad. Sci. U.S.A. 97(24): 13021-13026.

Tanford, C., K. Kawahara, and S. Lapanje. 1967. Proteins as Random Coils. I. Intrinsic Viscosities and Sedimentation Coefficients in Concentrated Guanidine Hydrochloride1a. J Am Chem Soc. 89(4): 729-736.

Tcherkasskaya, O., and V. Uversky. 2001. Denatured collapsed states in protein folding: Example of apomyoglobin. Proteins. 44(3): 244-254.

Teilum, K., F.M. Poulsen, and M. Akke. 2006. The inverted chevron plot measured by NMR relaxation reveals a native-like unfolding intermediate in acyl-CoA binding protein. Proc Natl Acad Sci U S A. 103(18): 6877-6882.

Uversky, V. 2009. Intrinsically Disordered Proteins and Their Environment: Effects of Strong Denaturants, Temperature, pH, Counter Ions, Membranes, Binding Partners, Osmolytes, and Macromolecular Crowding. Protein J. 28(7-8): 305-325.

Vogelsang, J., R. Kasper, C. Steinhauer, B. Person, M. Heilemann, M. Sauer, and P. Tinnefeld. 2008. A reducing and oxidizing system minimizes photobleaching and blinking of fluorescent dyes. Angew. Chem. Int. Ed. Engl. 47(29): 5465-5469.

Wahl, M. 2004. Time Tagged Time-Resolved fluorescence data collection. Available at www.picoquant.com (verified 9 April 2010).

Wahl, M., R. Erdmann, K. Lauritsen, and H. Rahn. 1998. Hardware solution for continuous time-resolved burst detection of single molecules in flow. p. 173-178. *In* Cohn, G.E. (ed.), Systems and Technologies for Clinical Diagnostics and Drug Discovery. SPIE, San Jose, CA, USA.

Walther, K., F. Grater, L. Dougan, C. Badilla, B. Berne, and J. Fernandez. 2007. Signatures of hydrophobic collapse in extended proteins captured with force spectroscopy. Proc Natl Acad Sci U S A. 104(19): 7916-7921.

Wassenberg, D., C. Welker, and R. Jaenicke. 1999. Thermodynamics of the unfolding of the cold-shock protein from Thermotoga maritima. J Mol Biol. 289(1): 187-193.

Watkins, L.P., H. Chang, and H. Yang. 2006. Quantitative single-molecule conformational distributions: a case study with poly-(L-proline). J Phys Chem A Mol Spectrosc Kinet Environ Gen Theory. 110(15): 5191-5203.

Wensley, B.G., S. Batey, F.A.C. Bone, Z.M. Chan, N.R. Tumelty, A. Steward, L.G. Kwa, A. Borgia, and J. Clarke. 2010. Experimental evidence for a frustrated energy landscape in a three-helix-bundle protein family. Nature. 463(7281): 685-688.

Widengren, J., A. Chmyrov, C. Eggeling, P.A. Lofdahl, and C.A.M. Seidel. 2007. Strategies to improve photostabilities in ultrasensitive fluorescence spectroscopy. J Phys Chem A. 111(3): 429-440.

Wilkins, D., S. Grimshaw, V. Receveur, C. Dobson, J. Jones, and L. Smith. 1999. Hydrodynamic radii of native and denatured proteins measured by pulse field gradient NMR techniques. Biochemistry. 38(50): 16424-16431.

Xie, X.S., P.J. Choi, G. Li, N.K. Lee, and G. Lia. 2008. Single-molecule approach to molecular biology in living bacterial cells. Annu Rev Biophys. 37: 417-444.

Young, T.S., and P.G. Schultz. 2010. Beyond the Canonical 20 Amino Acids: Expanding the Genetic Lexicon. J Biol Chem. 285(15): 11039-11044.

Zander, C., J. Enderlein, and R.A. Keller. 2002. Single-Molecule Detection in Solution Methods and Applications. 1. ed. Wiley-VCH.

Zhou, H. 2004. Polymer Models of Protein Stability, Folding, and Interactions†. Biochemistry. 43(8): 2141-2154.

Zhou, H., and F. Dong. 2003. Electrostatic Contributions to the Stability of a Thermophilic Cold Shock Protein. Biophys J. 84(4): 2216-2222.

Zhou, H., and K. Dill. 2001. Stabilization of proteins in confined spaces. Biochemistry. 40(38): 11289-11293.

Zumofen, G., J. Hohlbein, and C.G. Hübner. 2004. Recurrence and photon statistics in fluorescence fluctuation spectroscopy. Phys. Rev. Lett. 93(26 Pt 1): 260601.

Zwanzig, R. 1988. Diffusion in a rough potential. Proc Natl Acad Sci U S A. 85(7): 2029-2030.

6.3 ACKNOWLEDGEMENTS

Numerous people contributed to this work. I would like to thank:

- Prof. Ben Schuler for giving me the opportunity to work in his group, introducing me to the exciting field of single molecule spectroscopy, providing a very pleasant and professional environment, and supporting me throughout the years.
- Prof. Amedeo Caflisch and PD Ilian Jelezarov for joining my thesis committee.
- The former and current members of the Schuler group – Sonja, Daniel, Frank and Frank, René, Dominik, Luc, Bengt, Hagen, Philipp, Ruth, Jef, Stephan, Alessandro, Andrea and Andrea, and all the master and project students – not only for their collaboration in very exciting projects, numerous discussions and inputs on technical and scientific topics, but also for a very nice atmosphere and all the 'coffees in the sun'.
- Dr. Daniel Nettels for (among many other things) providing excellent analysis tools and – together with Dr. Hagen Hofmann – for revising my thesis.
- Dr. Jennifer Clark and Dr. Alessandro Borgia for providing FRET labeled protein A and spectrin R15 samples, respectively.
- The Department of Biochemistry at the University of Zurich for providing an excellent infrastructure, and especially the IT-service, our administrative assistant Mrs. Magrit Mathys Würfl, and the student advisor Prof. Heinz Gehring for their support.
- The Functional Genomics Center Zurich for providing mass-spectrometry analysis and Dr. Thomas Meier from ETH Zurich for allowing me to use his fermenter.
- Dr. Shawn Pfeil and Prof. Everett Lipman from UCSB for sharing their excellent microfluidic mixing system with us and hosting me in Santa Barbara.
- Dr. Peter Baumgärtel and Prof. Robert Seckler from the University of Potsdam, Dr. Avinash Kane and Prof. Olgica Bakajin from Lawrence Livermore National Laboratories, and Dr. Gerd Reichardt from BESSY for their efforts on the SRCD project.
- And the members of the group of Prof. Robert Seckler for hosting me in the start of my PhD in Potsdam, especially Jana Kramer for her technical assistance with my first production and labeling of cold shock protein.

Finally, I would like to thank all my friends, my family, and especially Marion for their indispensible support.

6.4 CURRICULUM VITAE

Personal Information

Name	**Armin Hoffmann**
Date of birth	May 28, 1978
Nationality	German

Education and Employment

Ph.D.

2004 – Present	Research group of B. Schuler, University of Zurich, Switzerland “Structure and Dynamic of Unfolded Proteins Probed with Advanced Spectroscopic Techniques and Microfluidic Mixing”
June 2008	Scientific visit in the research group of E. A. Lipman, UCSB, USA
2006 – 2008	Scientific visits at BESSY, synchrotron facility in Berlin, Germany (about a month each year)
2004 – 2005	Studies in Biochemistry at the University of Zurich

Studies in Biotechnology

1999 – 2004	Hochschule Mannheim, Germany Final degree: Dipl.-Ing. (FH) Biotechnologie
August 2003 – January 2004	Diploma Thesis at Sanofi-Aventis GmbH, Frankfurt a. M., Germany “Investigation of Insulin Folding Intermediates with Spectroscopic Methods”

Internships

May – June 2003	Research group of C. Frech, Hochschule Mannheim, Germany *Refolding, purification, and quality control of proteins and investigation of alternative purification techniques*
March – August 2002	BioReliance Manufacturing GmbH, Heidelberg, Germany *Protein production, refolding, purification and quality control in 1* m^3 *scale under GMP conditions*
September 2000 – February 2001	Research group of C.-H. Schröder at DKFZ, Heidelberg, Germany *Characterization of hepatitis B virus-related nucleic acids isolated from human blood*